Star formation across cosmic time and its influence on galactic dynamics

Jonathan Freundlich

THÈSE DE DOCTORAT
DE L'UNIVERSITÉ PIERRE ET MARIE CURIE

École Doctorale d'Astronomie & Astrophysique d'Île-de-France

LERMA, Observatoire de Paris

STAR FORMATION ACROSS COSMIC TIME AND ITS INFLUENCE ON GALACTIC DYNAMICS

Présentée par

Jonathan FREUNDLICH

Et soutenue publiquement le 1er décembre 2015 devant un jury composé de :

Françoise COMBES	Directrice de thèse
Carlos DE BREUCK	Rapporteur
Jean-Marc HURÉ	Rapporteur
Gary MAMON	Président du Jury
Linda TACCONI	Examinatrice
Frederic BOURNAUD	Examinateur
Amr EL-ZANT	Membre invité
Philippe SALOMÉ	Membre invité

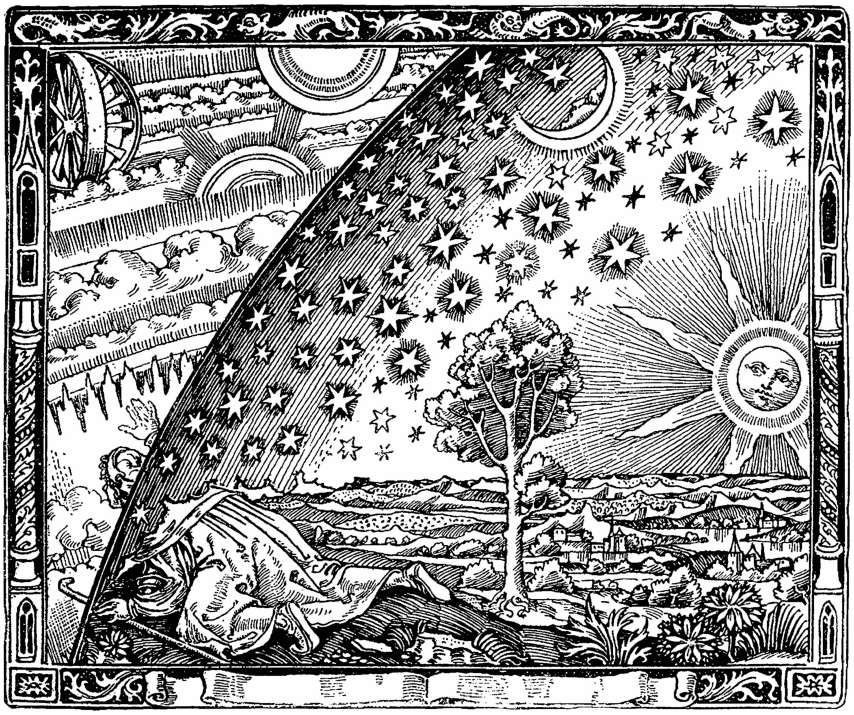

Back: Wood engraving appearing in Camille Flammarion's 1888 book *"L'atmosphère: météorologie populaire"*.

Résumé

Les observations montrent qu'il y a dix milliards d'années, les galaxies formaient bien plus d'étoiles qu'aujourd'hui. Comme les étoiles se forment à partir de gaz moléculaire froid, cela signifie que les galaxies disposaient alors d'importants réservoirs de gaz, et c'est ce qui est observé. Mais les processus de formation d'étoiles pourraient aussi avoir été plus efficaces : qu'en est-il ? Les étoiles se forment dans des nuages moléculaires géants liés par leur propre gravité, mais les toutes premières étapes de leur formation demeurent relativement mal connues. Les nuages moléculaires sont eux-mêmes fragmentés en différentes structures, et certains scénarios suggèrent que les filaments interstellaires qui y sont observés aient pu constituer la première étape de la formation des coeurs denses dans lesquels se forment les étoiles. En quelle mesure leur géométrie filamentaire affecte-t-elle les coeurs pré-stellaires ? Des phenomènes de rétroaction liés à l'évolution des étoiles, comme les vents stellaires et les explosions de supernovae, participent à la régulation de la formation d'étoiles et peuvent aussi perturber la distribution de matière noire supposée entourer les galaxies. Cette thèse aborde l'évolution des galaxies et la formation des étoiles suivant trois perspectives : (i) la caractérisation des processus de formation d'étoiles à des échelles sous-galactiques au moment de leur pic de formation ; (ii) la formation des coeurs pré-stellaires dans les structures filamentaires du milieu interstellaire ; et (iii) les effets rétroactifs de la formation et de l'évolution des étoiles sur la distribution de matière noire des galaxies.

Abstract

Observations show that ten billion years ago, galaxies formed their stars at rates up to twenty times higher than now. As stars are formed from cold molecular gas, a high star formation rate means a significant gas supply, and galaxies near the peak epoch of star formation are indeed much more gas-rich than nearby galaxies. Is the decline of the star formation rate mostly driven by the diminishing cold gas reservoir, or are the star formation processes also qualitatively different earlier in the history of the Universe? Ten billion years ago, young galaxies were clumpy and prone to violent gravitational instabilities, which may have contributed to their high star formation rate. Stars indeed form within giant, gravitationally-bound molecular clouds. But the earliest phases of star formation are still poorly understood. Some scenarii suggest the importance of interstellar filamentary structures as a first step towards core and star formation. How would their filamentary geometry affect pre-stellar cores? Feedback mechanisms related to stellar evolution also play an important role in regulating star formation, for example through powerful stellar winds and supernovae explosions which expel some of the gas and can even disturb the dark matter distribution in which each galaxy is assumed to be embedded. This PhD work focuses on three perspectives: (i) star formation near the peak epoch of star formation as seen from observations at sub-galactic scales; (ii) the formation of pre-stellar cores within the filamentary structures of the interstellar medium; and (iii) the effect of feedback processes resulting from star formation and evolution on the dark matter distribution.

Research summary

Within the standard ΛCDM cosmological model, galaxies grew out of tiny inhomogeneities in the primordial Universe. They evolved with time, along with their gas and stellar contents. Observations show that ten billion years ago, galaxies formed their stars at rates up to 20 times higher than now. As stars are formed from cold molecular gas, a high star formation rate means a significant gas supply, and galaxies near peak epoch of star formation are indeed much more gas-rich than nearby galaxies. Is the decline of the star formation rate mostly driven by the diminishing cold gas reservoir, or are the star formation processes also qualitatively different earlier in the history of the Universe? Ten billion years ago, young galaxies were clumpy and prone to violent gravitational instabilities, which may have contributed to their high star formation rate. Stars indeed form from giant, gravitationally-bound molecular clouds. But the earliest phases of star formation are still poorly understood. Some scenarii suggest the importance of interstellar filamentary structures as a first step towards core and star formation. How would their elongated geometry affect pre-stellar cores? Feedback mechanisms related to stellar evolution also play an important role in regulating star formation, for example through powerful stellar winds and supernovae explosions which expel some of the gas and can even disturb the dark matter distribution in which each galaxy is assumed to be embedded.

This PhD work participates in studies aiming at better understanding galaxy evolution and the cosmic star formation history. It mainly focuses on three perspectives: (i) star formation near the peak epoch of star formation as seen from observations at sub-galactic scales; (ii) the formation of pre-stellar cores from filamentary structures in the interstellar medium; and (iii) the effect of feedback processes resulting from star formation and evolution on the dark matter density of galaxies. This work involves astronomical observations as well as analytical calculations and numerical modeling.

Resolved star formation laws at high redshift. In the Milky Way and nearby spiral galaxies, stars form out of dense gas clouds which collapse due to their own gravity. As stars are formed from cold molecular gas, the star formation rate is expected to depend significantly on the amount of molecular gas available. Observations of nearby galaxies have shown that the molecular gas and star formation rate densities were indeed empirically well correlated through a simple power-law relation, the Kennicutt-Schmidt relation, which characterizes the star formation efficiency. Spatially-resolved mapping of molecular gas and star formation in nearby disk galaxies has shown that this relation simplifies to a linear relation on smaller scales, with a constant molecular gas depletion time. At redshift $z > 1$ - i.e., more than 8 billion years ago -, recent observations were able to obtain galaxy-averaged molecular Kennicutt-Schmidt relations in typical massive galaxies, notably within the PHIBSS survey (Tacconi et al., 2010; Genzel et al., 2010; Tacconi et al., 2013). The PHIBSS and PHIBSS2 programs (Plateau de Bure High-z Blue Sequence Surveys, Principal Investigators: Françoise Combes, Santiago García-Burillo, Roberto Neri & Linda Tacconi, `http://www.iram-institute.org/~phibss2`) indeed investigate early galaxy evolution and star formation from the perspective of the galaxies' molecular gas reservoir in relation with observational programs at the *Institut de Radioastronomie Millimétrique* (IRAM) Plateau de Bure interferometer. Although direct

resolution of the star-forming regions of distant galaxies is still challenging, we were able to derive spatially-resolved Kennicutt-Schmidt relations at high redshift (z$\sim$1.2) for the first time (Freundlich et al., 2013; Genzel et al., 2013). The results of these molecular gas observations carried within the PHIBSS survey are compatible with a constant depletion time of 1.9 billion years, and fit well with the corresponding low redshift observations of nearby galaxies. These results seem to point towards similar star formation processes at high and low redshifts, but bigger statistical samples would be necessary to obtain more meaningful mean depletion times for the substructures of distant galaxies. This work should be continued with an *Atacama Large Millimeter/submillimeter Array* (ALMA) project aiming at investigating the star formation processes, the morphologies and the kinematics of galaxies after the peak epoch of star formation at the scales of the star-forming regions themselves (P. I.: Jonathan Freundlich).

Stability of self-gravitating filaments in the interstellar medium. Observations of the interstellar medium reveal complex networks of filaments and suggest that these filaments are the first step towards core and star formation. The densest filaments could indeed fragment into pre-stellar cores owing to gravitational instability. The standard Jeans instability describes the collapse of a spherical gas cloud when the inner pressure is not strong enough to support the self-gravitating gas, but the cylindrical case relevant to an interstellar filament is less straighforward. As part of a collaboration with Chanda Jog at the Indian Institute of Science, Bangalore, India, we considered idealized self-gravitating filaments and derived dispersion relations describing the growth of perturbations within them. Assuming small local perturbations leads to a dispersion relation analogous to the spherical Jeans case: perturbations of size greater than the Jeans length collapse, and their growth rates display asymmetries only because of rotation (Freundlich et al., 2014a). But for perturbations of arbitrary size, the dispersion relation retains its complex terms: all modes are potentially unstable, and elongated perturbations near the axis of the cylinder grow faster. Prolate substructures and global collapse seem to be favored, which would be corroborated by most observations of interstellar filaments. As filamentary structures are also ubiquitous on cosmological scales, forming a cosmic web that connects galaxies to one another, our calculations could also apply on bigger cosmological scales. I started simulating idealized interstellar filaments with the adaptive mesh refinement code RAMSES (Teyssier, 2002) in order to test our results and to better understand the formation of pre-stellar cores within filamentary structures of the interstellar medium, but the results are yet only preliminary.

Effects of baryonic density fluctuations on the dark matter distribution. The current standard cosmological model assumes the existence of a cold dark matter that would mostly interact gravitationally and would represent 85 % of the total matter content of the Universe. In this model, galaxies are embedded in spherical dark matter haloes. But while dark-matter-only simulations predict dark matter haloes with steep, 'cuspy' inner density profiles, observations of dwarf galaxies show that the central dark matter profiles are shallower, or 'cored'. Introducing baryonic (i.e., non-dark-matter) physics in the simulations is essential to resolve this core-cusp discrepancy. Gravitational interactions between the baryonic and dark matter components can notably occur from the different feedback processes related to star formation or active galactic nuclei. Collaborating with

Amr El-Zant at the British University of Cairo, we carried out analytical calculations and numerical simulations, with the dark-matter-only self-consistent field (SCF) code developed by Hernquist & Ostriker (1992), in order to test a model in which the different feedback processes result in stochastic fluctuations in the gas density field and lead to the formation of cored density profiles (El-Zant et al., in prep.). We assume density perturbations with a power-law power-spectrum, and derive the expression of the velocity dispersion and of the associated relaxation time. In the simulations, the effects of such perturbations are modeled through their influence on the gravitational potential. We show that these density fluctuations are able to flatten significantly the inner part of the dark matter halo density profile, leading to cores instead of cusps. The next stage of this work would consist in using inputs from hydrodynamical simulations that include star formation and feedback mechanisms in order to constrain better and refine our model.

Acknowledgements

First of all, I would like to warmly thank Françoise Combes to have allowed me to do this work, for her precious opinions, for her guidance, and for her all-time availability to answer my questions and comment on my work. I would also like to thank Philippe Salomé for his support and advice, my friendly office mates Benjamin L'huillier, Anaelle Halle, Charlene Lefèvre and Quentin Salomé, and the different students and post-docs who passed through the LERMA: Martin Stringer, Greg Novak, Pedro Beirao, Kalliopi Dasyra, Julia Scharwächter, Celia Verdugo, Jeanne Treutel, Maxime Bois, and Antoine Radiguet. I would like to thank Martin Stringer in particular for the precise proofreading of my first articles. I am also indebted to the care of the administrative wing of the LERMA, in particular to Viviane Bigot, Valérie Audon and Laurent Girot, and to Djilali Zidani and Mouad Bahi for the numerical part. Additionally, the LERMA wouldn't be the same without Michel Caillat, Alain Coulais, François Viallefond, Laurent Maestrini and Benoit Semelin. I am also thankful to people who advised me during the course of my PhD and before, and in particular to Gary Mamon, who has always been keen to answer my questions and to talk about his research.

I am grateful to Carlos de Breuck and Jean-Marc Huré to have accepted to be the referees of my PhD work, and to the other members of the jury to have devoted some of their time to it.

I would like to thank the members of the PHIBSS and PHIBSS2 teams to have welcomed me in their midst, and in particular Linda Tacconi, Reinhard Genzel, Natasha Förster-Schreiber and Luis Colina. My attempts at dealing with RAMSES were helped by discussions with Frederic Bournaud, Yohann Dubois, Florent Renaud, Valentin Perret and Rebekka Bieri, while my second ALMA proposal benefited from a workshop organized by Raphael Moreno and Philippe Salomé. I am also thankful to Doris Arzoumanian for the few exchanges we had about interstellar filaments.

I am grateful to Chanda Jog, whom I enjoyed working with at the Indian Institute of Science (IISc), Bangalore, and to the astrophysics team there: Tarun Deep Saini, Prateek Sharma, Banibrata Mukhopadhyay, Arnab Rai Choudhuri, Arunima Banerjee, Indrani Banerjee, Moupiya Maji, Upasana Das, Rathul Nath, Soumavo Ghosh, Sujit Kumar Nath and Sumedh Anathpindika. I would also like to thank all the members of my foster lab at the Center for Ecological Sciences: Joy, Mahua, Pratibha, Laksh, Thejashwini, Kanchan, Srini, Yathi, Vignesh, Kruti, Nikita, Ananya, Satya, etc. I am also thankful to my welcoming hosts at IUCAA and NCRA, Pune: Kanak Saha, Ajit Kembhavi, Jayaram Chengalur, Gopal Krishna, Kandaswamy Subramanian and Charles Jose; and to my editors at The Hindu - In School: Suhel Quader and Keerthana Raj.

I am grateful to the teams which welcomed me heartfully at the Racah Institute of Physics, Hebrew University of Jerusalem, Israel, and at the British University of Cairo, Egypt: Avishai Dekel, Nir Mandelker, Colin Degraf, Joanna Woo, Elad Zinger, Re'em Sari, Amr El-Zant, Adel Awad, Sherif Elgammal, Yasser Abdella and Walaa Tarek. It

was a real pleasure to work with Amr El-Zant and to discover Egypt through his eyes. I also thank him for his careful proofreading and his suggestions.

This work was enabled by an ENS-specific PhD grant from the French *Ministère de l'Enseignement Supérieur et de la Recherche* and by an *Attaché temporaire d'enseignement et de recherche* (ATER) position at the *Collège de France* for the last few months. My four-months stay in Bangalore in January-April 2014 was made possible by a Raman-Charpak fellowship from the *Indo French Centre for the Promotion of Advanced Research* (IFCPAR/CEFIPRA), while the collaboration with Amr El-Zant at the British University of Cairo benefited from the Franco-Egyptian *Partenariat Hubert Curien* (PHC) Imhotep. This work was also largely facilitated by the ERC-Momentum-267399.

I am indebted to the great teachers I had all along, and in particular to Anne Leroi-Gourhan and Prebagaran Mouttou, who fed my interest for sciences and physics in the very beginning, to Steven Balbus and Luc Blanchet for having introduced me to astrophysics and general relativity, and to Gary Mamon and Avishai Dekel, who introduced me to the field of galaxy formation and evolution.

All of this probably wouldn't have been possible if I wasn't surrounded by amazing friends and family. Amongst them, I would like to thank in particular those who proofread parts of this manuscript.

Contents

List of Figures

Introduction

CHAPTER 1

Galaxy formation

Clear desert nights, far away from city lights, reveal a milky white glowing band across the sky: our Galaxy, the Milky Way. All visible stars including our Sun belong to the Milky Way, which comprises tens of billions of other stars. A galaxy can be simply defined as a gravitationally bound system that contains many stars. Although various scientists and philosophers including Democritus, Giordano Bruno and Immanuel Kant had suggested that the Universe comprised an infinity of worlds analogous to ours, it is only at the beginning of the 20th century that our Universe was empirically realized to extend far beyond our Milky Way and to contain hundreds of billions of other galaxies.

Studying galaxies, their formation and their evolution not only informs us about the history of the Universe and about our own cosmic origins, but also provides tools to trace the structure of the Universe as a whole and to test our understanding of the world. Such a study is particular in many ways. Indeed, our Universe is unique by definition and we are bound to observe it from inside at a specific position in space and time. Almost all the information we can get about distant astronomical objects comes from the light that our telescopes collect, and astrophysics is based on the assumption that phenomena are ruled by the same physical laws here and there - on Earth as well as at the far reaches of the Universe. Studying galaxies thus requires a multidisciplinary approach and calls on different fields of physics: amongst others, mechanics and hydrodynamics to study the movements of stars and gas within galaxies, electromagnetism and quantum physics to describe the atomic and molecular processes of emission and absorption at stake during the light travel path, or nuclear physics to understand the fusion reactions taking place in stellar cores. The time scales describing the evolution of galaxies are much larger than a human lifetime, and it is thus impossible to follow the actual evolution of an individual galaxy. Nevertheless, as the speed of light is finite, the further we look in space, the more distant in the past galaxies are. This enables us to reconstitute the evolution of galaxies' properties at different epochs of the history of the Universe, albeit in a statistical sense.

This chapter introduces some aspects of galaxy formation and evolution. The first section provides an historical perspective on observations of nearby and distant galaxies, from early speculations to the Hubble classification in the beginning of the 20th century. The history of nebulae observations and extragalactic speculations presented here

benefited particularly from *"Conceptions of Cosmos. From Myths to the Accelerating Universe: A History of Cosmology"* by Kragh (2007), while the description of the Milky Way benefited from *"Galaxies in the Universe: An Introduction"* by Sparke & Gallagher (2007). The second section comes back to the formation and evolution scenario for galaxies within the standard ΛCDM cosmological model: how small perturbations at the early stages of the Universe lead to highly inhomogeneous structures, the role of dark matter, and how galaxies get their gas. The last section focuses more specifically on the different stellar and gas cycles taking place during a galaxy's lifetime: stars are formed from cold molecular gas, but star formation in turn results in powerful feedback mechanisms that disturb subsequent star formation. As gas is continuously supplied to galaxies through mergers and smooth accretion from the cosmic web, there is a continuous cycle of star formation, outflows and gas replenishment. Parts of this chapter were inspired by the reading of *"Galaxy Formation and Evolution"* by Mo et al. (2010), *"The First Galaxies in the Universe"* by Loeb & Furlanetto (2013) and *"Galaxies et cosmologie"* by Combes et al. (1991).

Contents

1.1 Island worlds in the cosmos

1.1.1 From nebulae to galaxies – a historical perspective

The scientific recognition that our Milky Way is just one galaxy amongst a vast number of other galaxies only dates back to the beginning of the 20th century. How hazy cloud-like *nebulae* observed in the sky were realized to be *galaxies* analogous to our Milky Way is a long history of speculations about the size of the Universe, growing knowledge about the Milky Way, observations, and theoretical debates. The term *nebula*, originally used to designate all diffuse astronomical objects, comes from the Latin word meaning cloud, while evoking a *galaxy* already implies an analogy with the Milky Way: the word comes from the Ancient Greek γαλαξίας, which precisely designates the Milky Way. In the following historical presentation, we will use the word *nebula* in its original meaning, thus not restrictively referring to interstellar clouds of dust and gas as it is usually the case now.

The first observations of nebulae date back to Antiquity, with Ptolemy mentioning five nebulous stars in his *Almagest* around 150 A.D. The Persian astronomer Abd al-Rahman al-Sufi, also known in the West as Azophi, observed what is now known as Andromeda Galaxy for the first time in 964 and described it as a small cloud in his *Book of fixed stars*. While the German Simon Marius measured the diameter of this nebula in 1612, different catalogs as those by Johannes Hevelius (1665), Edmund Halley (1715), William Derham (1733) or Nicolas Louis de La Caille (1755) added to the number of known nebulae, as indicated in Table 1.1. But the nature of these astronomical objects was still unknown, and it is the German philosopher Immanuel Kant who seems to have suggested for the first time in his 1755 *Universal Natural History and Theory of Heaven* that nebulae were not individual stellar objects but vast ensembles of stars analogous to the Milky Way, scattered in an infinite Universe (Kant, 1755).

Kant's island universe theory

Kant was not the first to imagine an infinite Universe with an infinite number of worlds analogous to ours. As early as in the fourth century B.C., the Presocratic atomist philosopher Democritus had speculated that our Solar System was just one out of an infinite number of similar systems (Kragh, 2007). Atomists postulated that material objects were formed by chance congregations of atoms, infinite in shape and number, and their cosmological view thus only extended this postulate beyond our planetary system. The idea of an infinity of worlds analogous to our Solar System was taken over by Titus Lucretius Carus in his famous *De rerum natura* (first century B.C.) and much later by Giordano Bruno in his book *On the Infinite Universe and Worlds* (1584), in which he wrote: "There are innumerable suns, and an infinite number of earths revolve around those suns, just as the seven we can observe revolve around the Sun which is close to us" (Singer, 1950). Bruno further stated that the celestial bodies were made of the very same elements as those found on Earth, and believed that each of the infinite number of earths was inhabited.

<370 B.C.	The Presocratic atomist philosopher Democritus speculates an infinite Universe with an infinite number of worlds analogous to our Solar System, a conception which is further described in Titus Lucretius Carus' *De rerum natura* (first century B.C.)
∼150 A.D.	Claudius Ptolemaeus (Ptolemy) records the existence of five nebulous stars in his *Almagest*
964	The Persian astronomer Abd al-Rahman al-Sufi (Azophi) describes the Andromeda Galaxy as a small cloud in his *Kitab suwar al-kawakib al-thabita (Book of fixed stars)*
1584	Giordano Bruno argues in favour of an infinite Universe containing an infinity of worlds in *De l'infinito universo et mondi (On the Infinite Universe and Worlds)*
1610	Galileo Galilei relates the stellar structure of the Milky Way observed with his telescope in *Sidereus Nuncius (The Starry Messenger)*
1612	Simon Marius measures the diameter of the Andromeda Nebula
1665	Johannes Hevelius reports a dozen nebulae in his *Prodromus astronomiae*
1715	Edmund Halley describes six nebulae in *Of Nebulae or lucid spots among the Fix'd Stars*
1732	Pierre-Louis Moreau de Maupertuis discusses the shapes of the nebulous objects in *Discours sur la figure des astres*
1733	William Derham lists 16 nebulae in his article *Observations of the Appearances among the Fix'd Stars, Called Nebulous Stars*
1734	Emanuel Swedenborg suggests that many stellar systems as our own could exist in the Universe
1750	Thomas Wright of Durham describes the Milky Way as a rotating ensemble of stars for the first time in *An original theory or new hypothesis of the Universe* and states that other stellar systems exist in the Universe
1755	Nicolas Louis de La Caille catalogues 42 nebulae from the Cape of Good Hope
1755	The philosopher Immanuel Kant suggests that Milky Way has a flattened disk-like structure and that the diffuse nebulae are distant structures analogous to the Milky Way in his *Allgemeine Naturgeschichte und Theorie des Himmels (Universal Natural History and Theory of Heaven)*
1761	Johann Heinrich Lambert adopts a picture of the nebulae similar to that proposed by Kant in his *Cosmologische Briefe* (*Cosmological Letters*), although assuming a finite Universe
1781	Charles Messier compiles a catalog of 103 nebulae
1785	William Herschel confirms from observations that the Milky Way is a disk-shaped ensemble of stars and thus gives the first observational support for Kant's island universe theory in *The Construction of the Heavens*
1786	William and Caroline Herschel publish their *Catalogue of One Thousand New Nebulae and Clusters of Stars*
1845	William Parsons, Earl of Rosse, resolves most nebulae into stars and observes the first spiral nebula (M51, or the Whirlpool Galaxy)
1852	Stephen Alexander suggests that the Milky Way is a spiral nebula
1864	Observations of gaseous spectral lines in some nebulae by William Huggins seem to disprove the island universe theory
1899	Julius Scheiner obtains the spectrum of the Andromeda Nebula and finds it surprisingly similar to the solar spectrum. He interprets it as an argument in favor of the spiral nebula being a stellar cluster analogous to the Milky Way
1900	Cornelis Easton proposes a theory in which the Milky Way is a spiral nebula with the Solar System at its centre
1912	Henrietta Swan Leavitt shows that Cepheid stars can be used to determine cosmological distances
1917	Vesto Melvin Slipher discovers that most nebulae are redshifted
1918	Harlow Shapley prones that the Milky Way is an all-comprehending system
1920	The "Great Debate" between Harlow Shapley and Heber Doust Curtis, the latter claiming that spiral nebulae were extra-galactic island universes
1922	Ernst Julius Öpik does the first relevant estimate of the distance between the Andromeda Galaxy and the Milky Way and shows that the Andromeda Galaxy is well outside the Milky Way
1926	Edwin Powell Hubble confirms Öpik's results by identifying Cepheid variable stars in the Andromeda Galaxy and its companion galaxy, the Triangulum Galaxy (M33)

Table 1.1 – *A selective history of discoveries related to extragalactic nebulae and the existence of worlds analogous to our Milky Way in the vastness of the Universe*

One of the originalities of Kant's insight is that he related the structure of the Milky Way with the observed nebulae. Galileo had resolved the stellar structure of the Milky Way with his telescope in the beginning of the seventeenth century (*The starry messenger*, 1610) and the Swedish Emanuel Swedenborg had suggested in 1734 that there could be stellar systems similar to ours in the Universe. At the same time, Pierre-Louis Moreau de Maupertuis was studying the shapes of observed nebulae, but he did not imagine that they had so much to do with the Milky Way. In 1750, Thomas Wright of Durham published *An original theory or new hypothesis of the Universe* in which he described the Milky Way as a structured ensemble of stars rotating around a centre and not just as an indiscriminate scattering of stars. His work was infused with theology and identified the centre of the structure with the place from which God's infinite power emanated. Nevertheless, it decisively inspired Kant's *Universal Natural History and Theory of Heaven*. Kant adopted Wright's model of a structured ensemble of stars for the Milky Way, but correctly gave it a flattened disk-like shape. He suggested that nebulae were not individual stellar objects but huge unresolved congeries of stars of the same type and structure as the Milky Way: island worlds floating in an immense sea of void space. He further imagined that these islands were not isolated, but parts of even larger structures in an incredibly huge hierarchical arrangement within the infinite Universe he assumed. The possibility of island worlds in the cosmos was however not incompatible with the idea of a finite Universe, and was notably adopted in such a framework by Johann Heinrich Lambert in 1761.

The first observational evidence

Wiliam Herschel, helped by his sister Caroline, was the first astronomer to support the island universe theory with observational evidence. In his important 1785 paper, *The Construction of the Heavens*, Herschel presented his ambitious observational program aiming at understanding the structure of the Milky Way. His analysis resulted in a picture of the Milky Way as a "very extensive, branching, compound Congeries of many millions of stars" with the Solar System near the centre of the giant structure (Herschel, 1785). That the Solar System was at the centre of the congeries was due to the assumption that Herschel's telescope could reach the farthest limits of the Milky Way, an assumption

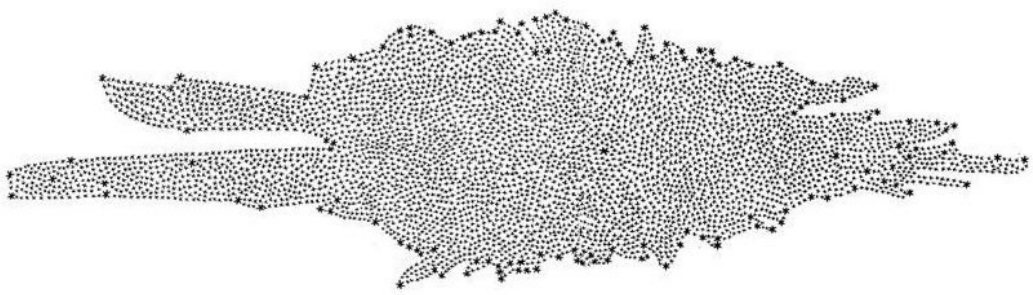

Figure 1.1 – *William Herschel's 1785 map of the Milky Way (Herschel, 1785).*

he himself had to abandon when he started to use a 40-foot telescope instead of a 20-foot reflector and began to see more stars. Herschel's view of our Galaxy was that of a flattened stellar system aligned with the hazy Milky Way appearing in the night sky, as shown in Figure 1.1. Herschel had also started observing nebulae a few years earlier, and he published his *Catalogue of One Thousand Nebulae and Clusters of Stars* in 1786. He had been able to resolve many nebulae into stars, and imagined that the others might just be too distant to be resolved. In *The Construction of the Heavens*, he concluded that our Milky Way was only one nebula among many others.

Although he initially thought that all nebulae were clusters of stars, William Herschel later identified some objects as "nebulous stars" and interpreted them as hot gaseous clouds that would only later turn into stellar objects. This nebular hypothesis in which the different types of nebulae constituted different stages of the evolution of stellar compounds got wide acceptance in the beginning of the 19th century. Such an hypothesis was in accordance with the popular view of the time, in which nature was in a state of continual evolution, but as such, also triggered an opposition: for some, it was associated with "dangerous" views such as Darwinian evolutionism and materialism. William Parsons, the Earl of Rosse, had built a giant 54-foot mirror telescope (nicknamed the "Leviathan of Parsonstown") with which he observed nebulae. As shown in Figure 1.2, he discovered in 1850 the spiral structure of the M51 nebula catalogued by Charles Messier in 1781, and the more nebulae he observed, the more he was able to resolve into stars. It was tempting to conclude that all nebulae were stellar clusters, and although Rosse himself was aware that such a conclusion was too general to be justified from his observations, the claim got wide acceptance among astronomers.

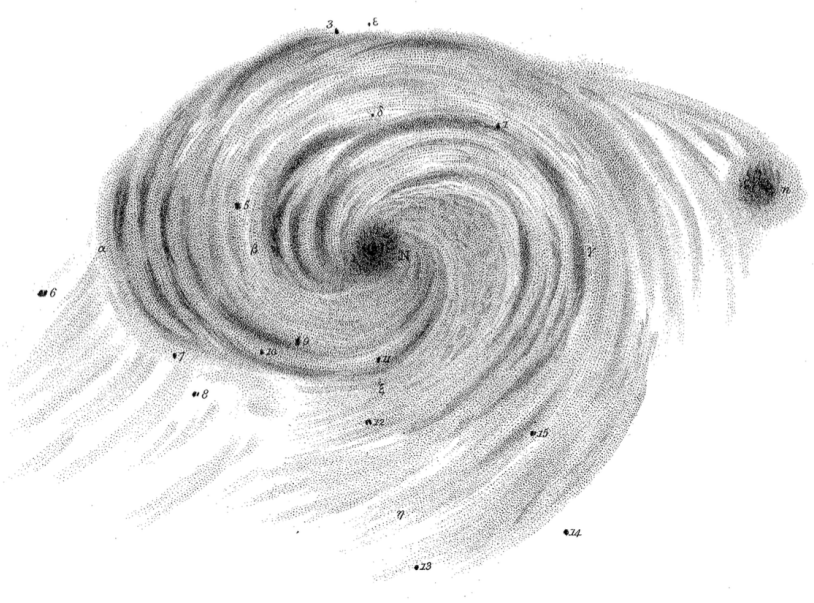

Figure 1.2 – *The Whirlpool Galaxy M51 as observed by Lord Rosse in 1850 (Rosse, 1850).*

The Great Debate

The onset of spectroscopy in the middle of the 19th century revived the nebular hypothesis. In 1864, William Huggins indeed observed a bright line in the spectrum of a nebula, which could only be explained if the astronomical object was made of gas. But on the other hand, the Andromeda Nebula was shown to have a continuous spectrum surprisingly similar to the solar spectrum in 1899. Julius Scheiner suggested from this observation that spiral nebulae were all huge stellar clusters analogous to the Milky Way, which supported the island universe theory. But the size and structure of our Galaxy still seemed uncertain by the end of the 19th century. The debate about the nature of the nebulae, namely whether they were structures similar to the Milky Way or smaller objects within it, was also a debate about the size of the Universe. Was the Universe limited to our Milky Way, or did it extend much beyond it?

Regarding the shape of the Milky Way, an American astronomer named Stephen Alexander had already suggested that our Galaxy was just another spiral nebula in 1852, but it is only in the beginning of the 20th century that the idea became more popular. In 1900, the Dutch journalist and amateur astronomer Cornelis Easton proposed a theory in which our Milky Way had a spiral structure with our Solar System at its centre. Figure 1.3 shows how he envisioned the Milky Way. He later revised the position of the solar system to place it further away from the centre. But comparing the Milky Way to spiral nebulae did not mean that Easton supported the island universe theory: to him, the other spirals were just "small eddies in the convolutions of the great one" and were thus part of our galactic system. At the same epoch, the German and Dutch astronomers Hugo von Seelinger and Jacobus Kapteyn both attempted to obtain a more precise, scientifically-motivated picture of the Milky Way. While Seelinger's method was

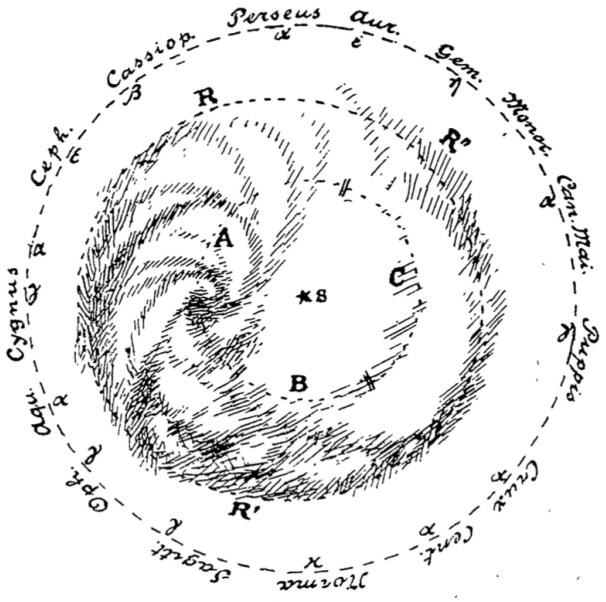

Figure 1.3 – *Cornelis Easton's representation of the Milky Way as a spiral nebula in 1900, with the Sun at its center (Easton, 1900).*

based on star counts and stellar magnitudes, Kapteyn used the proper motions of the stars. They both concluded that our Galaxy was a Sun-centered, flattened ellipsoid in which the density of stars decreased with radius. Kapteyn's Milky Way covered a distance of 59,000 light-years across the galactic plane ($\sim$18 kpc[1]) and 7,800 light-years between the poles ($\sim$2.4 kpc). As Easton before, Kapteyn later modified the position of the Sun to put it slightly away from the centre.

But both astronomers were assuming that stellar light was not absorbed in the interstellar medium, which soon turned out to be an important issue: to obtain a reliable picture of the Milky Way and the spiral nebulae, it was necessary to have a method to determine distances over long stretches of space. Cepheid stars turned out to provide such a method. Cepheids are variable stars whose luminosity changes periodically. Henrietta Swan Leavitt had shown in 1912 that the period associated to such a star was related to its maximum brightness, thus enabling one to measure the relative distance between cepheids by comparing their apparent magnitude. Harlow Shapley used this property to derive an operational method to determine distances on galactic scales: if a cepheid could be identified in a faraway object, it was possible to calculate the distance to that object. Using his cepheid distance ladder, Shapley determined the distance to a large number of globular stellar clusters and derived a model in which they were part of a nearly spherical system enveloping the plane of the Milky Way. The diameter of this system was more than 60 kpc (Shapley, 1918). For him, such a system was incompatible with the island universe theory: if spiral nebulae were outside of it, they would have to be at inconceivably large distances and would rotate at incredible speeds. Shapley's larger system in which the Milky Way was embedded was almost all-comprehending and identified with most of the material Universe. However, to evaluate the rotation speeds of spiral nebulae, he relied on erroneous measurements by Adriaan van Maanen.

On the other hand, the discovery of nebular redshifts by Vesto Melvin Slipher in 1917 was considered as a good support for the island universe theory. Slipher was aiming at measuring rotation in spiral nebulae when he found that the spectral lines of the majority of them were shifted towards higher or lower wavelengths than expected. Interpreting the results in terms of Doppler shift, it meant that the spirals were moving at large velocities relative to the Milky Way, up to about 700 km/s. These high velocities favored the idea that spiral nebulae were outside of the Milky Way. But as distance measurements to the spirals were still lacking, it did not allow to reach a decisive conclusion. Incidentally, the majority of the spiral nebulae that Slipher observed were redshifted rather than blueshifted, which would later turn out to be a most important result.

On 26 April 1920, a public debate took place at the National Academy of Science in Washington between Shapley and his compatriot Heber Curtis, who advocated the island universe theory. Although the debate did not end the controversy, it later got to be known as the "Great Debate". While Curtis focused on spiral nebulae, Shapley emphasized on globular clusters and the structure of the Milky Way. Both had good observational

[1]Galactic distances are usually measured in kpc: 1kpc = 10^3 parsecs, i.e., about 3. 10^{16} km. One parsec is the distance at which two astronomical objects separated by one Astronomical Unit (roughly the distance between the Earth and the Sun) would subtend a parallax angle of one arcsecond. 1Mpc = 10^6 parsecs.

arguments to support their theory, including a comparison between the magnitudes of supernovae within the Andromeda Nebula and elsewhere in the case of Curtis (Curtis, 1917), and none of them was entirely right or wrong: it was later shown that we do live in an island Universe, but that the size of the Milky Way is closer to Shapley's model. The estimation of the distance to the Andromeda Nebula was to be the decisive step to end the controversy.

The end of the controversy

The first convincing estimate of the distance between the Milky Way and the Andromeda Nebula was obtained by the Estonian astronomer Ernst Öpik in 1922. At that time, the luminosity of the Milky Way had been estimated from stellar counts and statistical estimates of the star distances. Its mass had been derived from the observed velocities of stars. Öpik calculated the mass-to-light ratio of the Milky Way, and assumed that spiral nebulae should have comparable mass-to-light ratios if they were ensembles of stars similar to the Milky Way. The mass of the Andromeda Nebula is related to its rotation velocity, which can be inferred from Doppler shift measurements, while its intrinsic luminosity depends on the observed luminosity and of the distance. Assuming a similar mass-to-light ratio for the Milky Way and the Andromeda Nebula enabled Öpik to obtain a distance estimate of 450 kpc (Opik, 1922) [2]. Öpik's estimate was below the modern value, which is around 770 kpc (e.g., Karachentsev et al., 2004), but clearly indicated that the Andromeda Nebula was well outside the Milky Way and gave credit to the hypothesis that the nebula was "a stellar universe comparable with our Galaxy" (Opik, 1922).

When Edwin Hubble discovered cepheid variable stars in the Andromeda Nebula and the Triangulum Nebula M33 in 1925, it confirmed Öpik's result and settled the controversy. Hubble had been studying novae in spiral nebulae when he observed two objects that had brightness variations similar to cepheids. Using Shapley's distance calibration, he found that the Andromeda Nebula had to be about 300 kpc away from the Milky Way (Hubble, 1925). The uncertainty on the measure notably came from the zero-point of Shapley's calibration, which underestimated the distance to the Magellanic Clouds. But given Hubble's evidence, the island universe theory finally got widely accepted. Spiral

[2] More precisely (cf. Peebles, 1993), the mass M of the nebula can be related to the linear speed v at radius r by:

$$\frac{GM}{r^2} = \frac{v^2}{r}$$

with $r = \theta D$, D being the distance to the nebula and θ the observed angular radius. This equation is just Newton's second law of motion applied to a star rotating at radius r with velocity v around the center of the nebula. If L is the intrinsic luminosity of the nebula, the observed energy flux on Earth is given by

$$F = \frac{L}{4\pi D^2}$$

so that

$$D = \frac{v^2\theta}{4\pi GF}\frac{L}{M}.$$

nebulae were recognized to be island worlds analogous to our Milky Way, while some of the original nebulae were identified as gas clouds belonging to our Galaxy. Spiral nebulae fully became *galaxies* like our own Milky Way, while the term *nebula* came to describe preferentially the interstellar gaseous clumps of our Galaxy. Hubble would show in 1929 that these galaxies are not only outside of our Milky Way, but are generally even drifting away from us due to the intrinsic expansion of the Universe. The redshifts initially observed by Slipher in 1917 are a consequence of this expansion, and the more a galaxy is redshifted, the further away it is. Redshift is thus a distance measurement. Since Slipher and Hubble, deep observations of the sky have revealed huge numbers of galaxies outside our Milky Way and their diversity is notably shown by the Hubble Ultra Deep Field (Fig. 1.4). One can still marvel at the immensity of the Universe and at the vast number of island worlds scattered in its vastness. However, these island universes are not independent. They indeed belong to even larger structures, groups and clusters of galaxies, are embedded within a cosmic web of overdense regions, and affect each other's development through their lives.

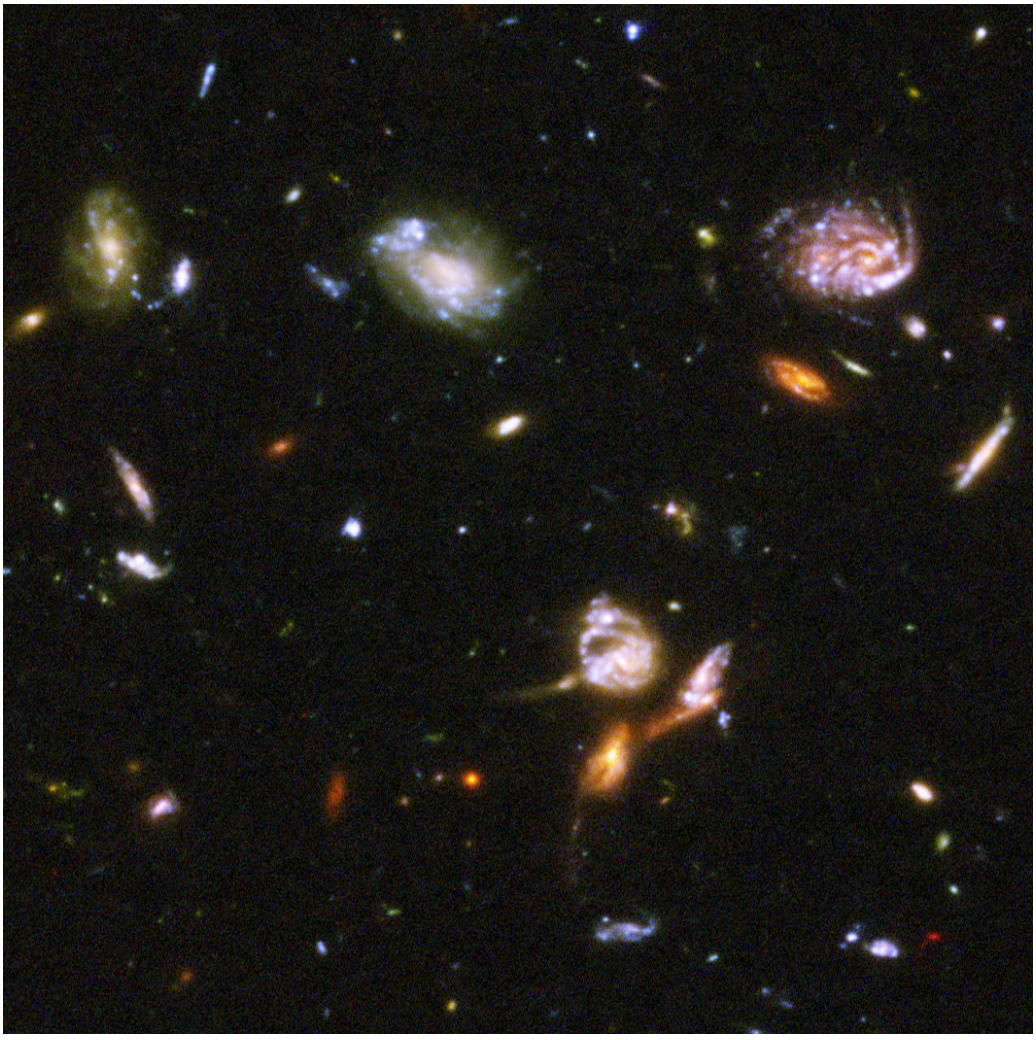

Figure 1.4 – *Galaxies from the Hubble Ultra Deep Field in a typical patch of the sky. Credits: NASA, ESA, S. Beckwith (STScI) and the HUDF Team.*

1.1.2 The Milky Way within the Local Group

The Milky Way

The modern picture of the Milky Way is not that far from that suggested by Cornelis Easton, Hugo von Seelinger or Jacobus Kapteyn at the beginning of the 20th century. Our Galaxy indeed seems to be a typical large spiral disk galaxy, and as such, not unlike its neighbor the Andromeda Galaxy. Fig. 1.5 from Sparke & Gallagher (2007) shows how the Milky Way could schematically be seen edge-on by an external observer. The Sun lies close to the mid-plane of the disk, at a distance $R_0 \simeq 8$ kpc from the Galactic center, and orbits around this center at a velocity of about 220 km.s^{-1} so that its complete orbit takes around 250 Myr (e.g., Mo et al., 2010). The Sun lies within the stellar disk of the Milky Way, which is thin and approximately circular. This prominent feature is what we can see as a milky white glowing band across the night sky. This disk has a diameter of about 30 kpc and weighs as much as $\sim 5\ 10^{10}$ M$_\odot$[3] (Licquia & Newman, 2015). It is itself embedded in a less massive thick disk, whose mass is about ten times less than the thin disk and whose width is approximately 1 kpc. Stars within the thick disk are generally older and poorer in heavy elements than stars in the thin disk. Stars are not homogeneously scattered in the disk, as their density is higher in the spiral arms, and they can regroup to form gravitationally-bound clusters of stars. In addition to the thin and thick disks, the Milky Way also contains a 'bulge' component, i.e., a more tightly packed central group of stars, of total mass $\sim 10^{10}$ M$_\odot$ (Licquia & Newman, 2015). However, while classical stellar bulges are characterized by random orbits and a spherical shape, the apparent bulge of the Milky Way seems to harbor orbiting stars and to consist of a bar (e.g., Binney et al., 1991; Stanek et al., 1994; Zhao et al., 1995; Shen et al., 2010), at least partially (Ness et al., 2013; Di Matteo et al., 2015; Saha, 2015). At the very center of the Milky Way lies a supermassive black hole whose mass is about $2\ 10^6$ M$_\odot$ and whose presence is inferred from stellar trajectories in its neighborhood (Genzel et al., 2000; Schödel et al., 2003; Ghez et al., 2005).

In addition to its stellar component, the Milky Way also contains gas and dust orbiting close to the plane of the disk, mostly a cold neutral and molecular gas component representing about $5\ 10^9$ M$_\odot$. The neutral gas is mostly constituted of atomic hydrogen and its surface density is roughly constant between 4 and 17 kpc. It drops at smaller and larger radii, and its distribution is warped in the outer part of the Galaxy as shown in the picture (Henderson et al., 1982). The molecular gas is located more towards the center of the galaxy, concentrated in a molecular ring between 4 and 8 kpc, and clumped in gravitationally bound molecular cloud complexes of masses between $10^5 - 10^7$ M$_\odot$ and typical densities of about 100 atoms per cm^3 (e.g., Combes, 1991; Dame et al., 2001). It is within these structures that stars are born, and young stars can ionize part of the gas owing to the ultraviolet (UV) radiation they emit. Stellar winds and supernovae explosions can further heat the gas locally. Overall, the gas mass fraction of the Milky Way disk with respect to the total gas and stellar components, $f_{gas} = M_{gas}/(M_{gas} + M_{stars})$, is about 10%. According to the standard ΛCDM cosmological model, the Milky Way disk

[3] A solar mass, M$_\odot$, is about 2.10^{30} kg.

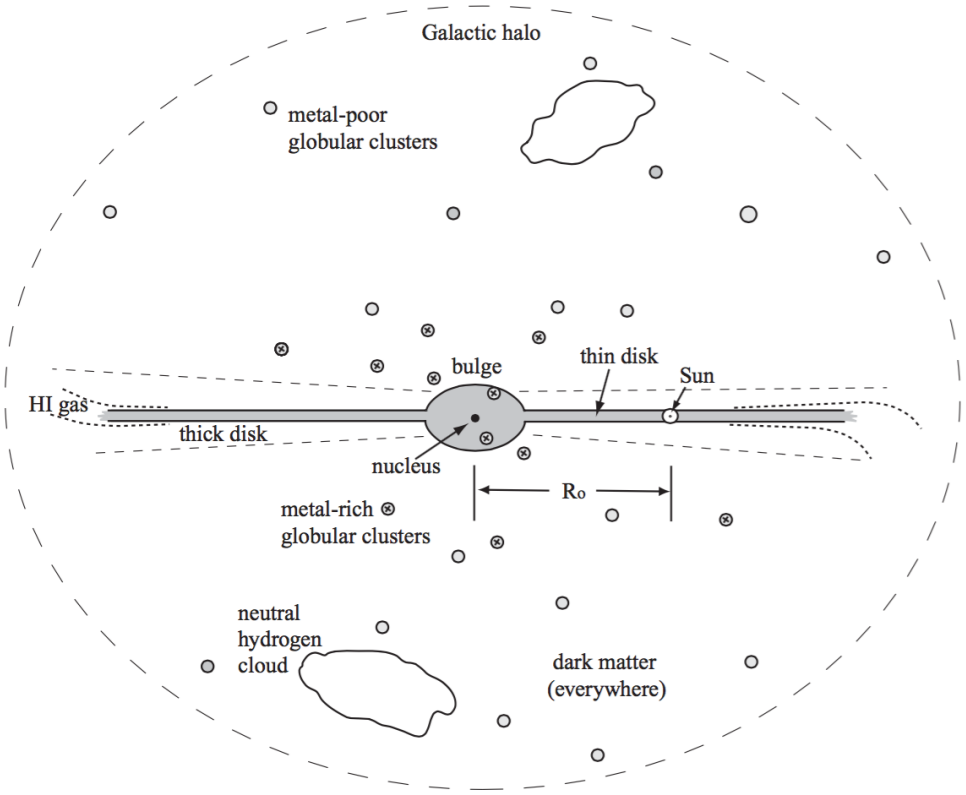

Figure 1.5 – *A schematic side view of the Milky Way, from Sparke & Gallagher (2007). Courtesy of Linda Sparke and Jay Gallagher.*

is further embedded in an invisible dark matter halo whose mass would be about 10^{12} $M_\odot$ and which would extend beyond 100 kpc of the Galactic center (e.g., McMillan, 2011). This dominant dark matter component is inferred from the rotation curves of stars in the periphery of the Milky Way, but has not yet been observed directly.

The Milky Way is not limited to a disk of stars, gas and dust embedded in a dark matter halo. Not all stars belong to the disk. In particular, numerous globular clusters of stars such as those shown on Fig. 1.5 scatter the Galactic halo (Harris, 1996). Those tightly gravitationally bound ensembles of stars have spherical shapes and orbit around the center of the Milky Way. But while open stellar clusters such as the Pleiades lie close to the plane of the disk, most globular clusters are high above it. They also contain more stars and are denser and older than their disk counterparts. Old metal-poor globular clusters are further away than the metal-rich ones, and while the latter have orbits similar to those of stars in the thick disk, the orbits of distant globular clusters are more eccentric and almost randomly oriented (e.g., Dauphole et al., 1996; Sparke & Gallagher, 2007).

Satellites of the Milky Way

Further away from the disk of the Milky Way lie smaller galaxies orbiting around it. These satellite galaxies are about a dozen and are approximately situated on a plane (Lynden-Bell, 1976; Kroupa et al., 2005; Metz et al., 2007), which suggests that they could stem

from material tidally stripped from another galaxy during an encounter with the young Milky Way (Pawlowski et al., 2011; Hammer et al., 2015), that they entered the Milky Way halo as a group (Li & Helmi, 2008), or that they were channeled through the cosmological overdense filaments which feed galaxy growth (Lovell et al., 2011). Among them, the Magellanic Clouds are a few tens of kpc away from our Galaxy and can be visible to the naked eye. These two gas-rich galaxies are actively forming new stars and host many stellar clusters, including globular clusters in the case of the Large Magellanic Cloud. The gravitational potential of the Milky Way also retains smaller, barely visible dwarf spheroidal companions. They are about hundred times less luminous than the Magellanic Clouds, and hardly contain any gas to make new stars. Tidal forces from the Milky Way's gravitational potential might be tearing them apart. The spheroidal dwarf satellites of the Milky Way are named after the constellations in which they appear: Sculptor, Fornax, Sagittarius, Ursa Minor, Ursa Major, Carina, Draco, etc. The smallest ones may not be more luminous than globular clusters, but they are still galaxies on their own. Fornax for example hosts its own globular clusters. All these dwarf spheroidals formed their stars over several Gyr (e.g., Hernandez et al., 2000) unlike globular clusters of the Milky Way, in which star formation was a punctual event.

The Local Group

As many galaxies, the Milky Way is not isolated. It belongs to a group of galaxies named the Local Group. Besides the Milky Way, this group comprises two other spiral galaxies: the Andromeda Galaxy, or M31, and the Triangulum Galaxy, M33. M31 is about 770 kpc away from the Milky Way (e.g., Ribas et al., 2005) while M33 is slightly further. The Andromeda Galaxy is bigger and more luminous than the Milky Way, and comprises at least 300 globular clusters and its own satellite galaxies. It has a large bulge and an extended atomic, molecular and dusty disk (Barmby et al., 2006). With a stellar mass of a little more than $10^{11}M_{\odot}$ (Geehan et al., 2006; Widrow et al., 2003), the Andromeda Galaxy is also more massive than the Milky Way. It is on a colliding course with our Galaxy, approaching at a velocity of about 120 $km.s^{-1}$: both galaxies are expected to merge in about 6 billion years from now (van der Marel et al., 2012). The third spiral galaxy of the Local Group, M33, is much less luminous than the Milky Way or the Andromeda Galaxy, and hosts a tiny bulge. It is however richer in atomic gas, and its outer disk is warped, probably due to tidal interactions with M31.

The Local Group is a gravitationally bound ensemble of galaxies. Besides the three spiral galaxies which make up most of its mass and emit about 90% of the visible light of the group, it contains a few tens of smaller galaxies (e.g., Sparke & Gallagher, 2007). Many of these are satellites of the Milky Way or of the Andromeda Galaxy. However, these dwarf galaxies can be divided into two main types: dwarf spheroidal galaxies such as most satellites of the Milky Way, and dwarf irregular galaxies. Dwarf spheroidals contain little gas and have old stellar populations, whereas dwarf irregulars are much more gas-rich and actively form stars. While most dwarf spheroidals are orbiting around one of the three main spiral galaxies of the Local Group, many of the dwarf irregulars are not satellites of larger systems.

Beyond the Local Group

The Local Group is but one example of a galactic system. Like the Milky Way, about half of the galaxies in the Universe are found in clusters or groups of a few Mpc in size and within which the gravitational attraction is strong enough to overcome the global expansion of the Universe. Outside the Local Group but still in its vicinity, the Virgo cluster and the Coma cluster, respectively at about 17 and 70 Mpc away, are examples of much larger clusters of galaxies. They are indeed assumed to have masses of a few 10^{14} $M_\odot$ and to be constituted by more than a thousand galaxies. The Local Group and the Virgo and Coma clusters are themselves part of a giant supercluster of mass $\sim 10^{17}$ $M_\odot$ which has been named the Laniakea Supercluster from the Hawaiian words meaning "sky" and "wide" (Tully et al., 2014). The vastness of such a cluster and of the Universe beyond allows a great diversity of galaxy types and properties.

At even larger scales, galaxies and clusters are often gathered in groups or along filaments, leaving large regions of the Universe empty. Galaxies are not spread uniformly through space and their distribution resembles a huge cosmic web of galaxies. Fig. 1.6 shows slices of the large scale structure of the Universe as observed from the 2dF Galaxy Redshift Survey (Peacock et al., 2001). Dense linear features as well as walls and elongated cosmological filaments are visible, with rich clusters of galaxies at their intersections. The voids between these structures can be tens of Mpc wide, sparsely populated by 'field' galaxies. Such a galaxy distribution is consistent with a universe in which the growth of structures is triggered by a competition between the gravitational attraction and the expansion of the Universe: from largely homogeneous initial conditions, overdense regions collapse while underdense regions become expanding voids.

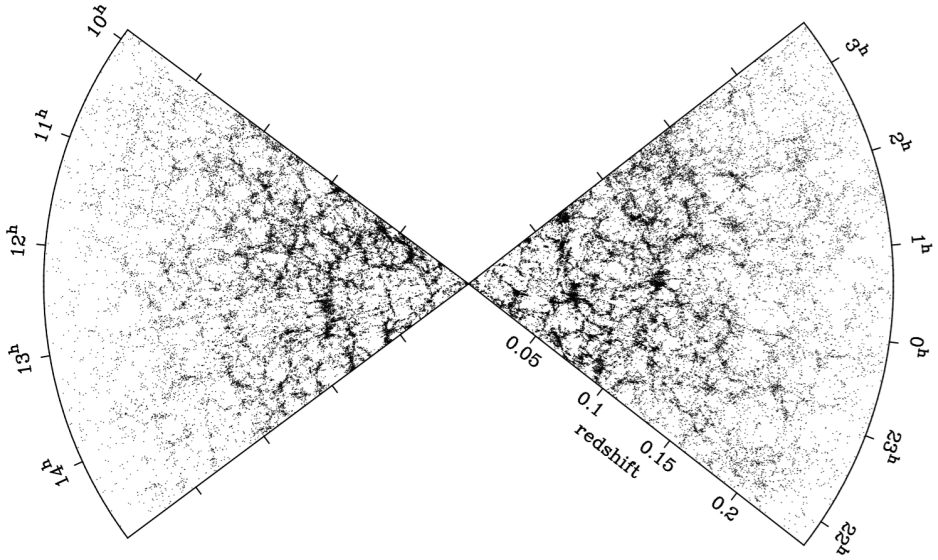

Figure 1.6 – *Slices of the distribution of galaxies from the 2dF Galaxy Redshift Survey (Peacock et al., 2001). The two slices are 4° thick, centered on the Milky Way, and respectively point north (left) and south (right) of the Galactic plane. Redshift 0.2 corresponds to a comoving distance of about 800 Mpc, or 2.6 billion light years.*

1.1.3 The Hubble classification of galaxies

The Hubble Sequence

Nebulae were cataloged long before some of them were realized to be galaxies outside of the Milky Way. Hence, the Messier (1781) catalog only contains 39 galaxies out of 109 nebulous objects, while the New General Catalogue (NGC, Dreyer, 1888) and the Index Catalogue (IC, Dreyer, 1895, 1908) respectively contain 3200 galaxies out of 7840 objects and 2400 galaxies out of 5836 (Combes et al., 1995). The realization that these objects were extragalactic island worlds lead to their separation from Galactic nebulae, and morphological classifications from observations have been crucial to sort them out and better understand their formation and evolution. In his book *"The Realm of Nebulae"* (1936), Hubble initiated a classification that would later be added to and modified but which is still in use today. This classification, shown in Fig. 1.7, distinguishes galaxies through their morphology, which Hubble thought reflected their time evolution. In this classification, Hubble separated three main types of galaxies: elliptical galaxies (E), spiral galaxies (S), and lenticular galaxies (S0). A fourth category of irregular galaxies included those which could not fit in any other category. Merger remnants such as the Antennae Galaxies, characterized by long tidal tails resulting from the strong gravitational interactions taking place during the merger, usually belong to this latter category of irregulars. The terms 'early type' and 'late type' are sometimes used to refer to the position of galaxies in the Hubble classification, from ellipticals to spirals. However, as the Hubble classification actually does not reflect a temporal evolution, we will avoid this denomination here. In fact, 'early-type' galaxies are full of 'late-type' stars, and vice-versa.

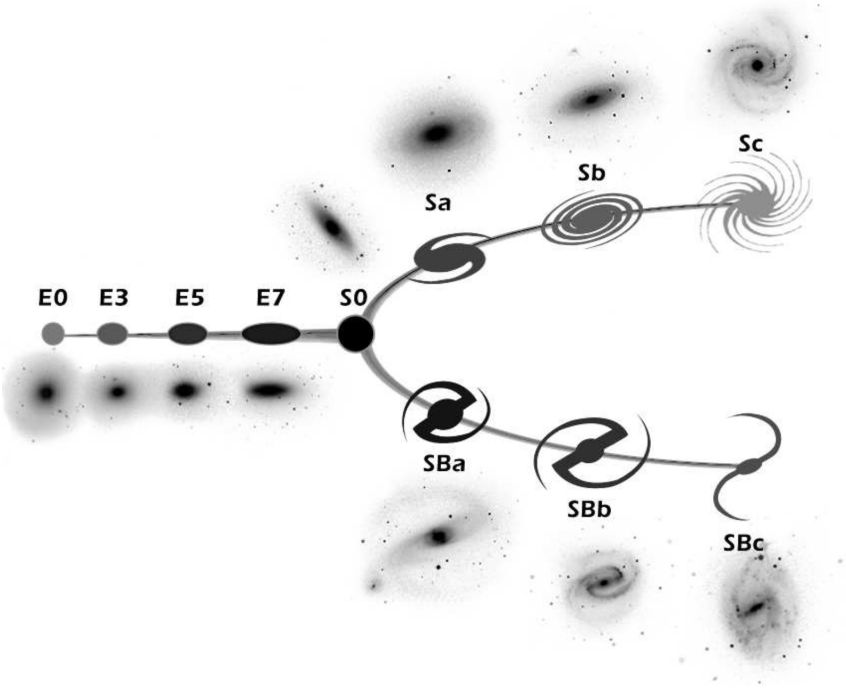

Figure 1.7 – *The Hubble Sequence. Credits: NASA & ESA, adapted by Anaelle Halle.*

Elliptical galaxies

Elliptical galaxies on the left of the Hubble classification are usually smooth and almost featureless. They are devoid of picturesque spiral arms and obscuring dust lanes. In the Hubble Sequence, they are sorted according to their ellipticity $\epsilon = 1 - b/a$, where a is the major axis and b the minor axis, and their names state the closest integer to 10ϵ from E0 to E7. An E0 galaxy is spherical, while increasing numbers up to E7 correspond to more and more elongated ellipsoids. Elliptical galaxies usually have less cold gas than spiral galaxies, and hence fewer young blue stars. They indeed appear redder than spiral galaxies, which indicate older stellar populations. Their stellar masses range from $\sim 10^6$ $M_\odot$ for dwarf ellipticals to $\sim 10^{12}$ $M_\odot$ for the most massive. Ellipticals are particularly numerous in big clusters of galaxies and the largest of them are found in the densest parts of these clusters. Giant ellipticals can be up to hundred times more luminous than the Milky Way, and their stars orbit around the galactic center in random directions. In less massive ellipticals, stars have more rotation and less random motion, and there are often signs of a disk hidden within the elliptical body. Fig. 1.8 show two different types of ellipticals.

The stellar density distributions of galaxies are often described in terms of a Sérsic surface brightness profile (Sérsic, 1963; Sersic, 1968; Caon et al., 1993)

$$I(R) = I_0 \exp\left(-\mathrm{b_n}\left(\frac{\mathrm{R}}{\mathrm{R_e}}\right)^{1/\mathrm{n}}\right), \tag{1.1}$$

Figure 1.8 – *Left: the giant elliptical galaxy M87, surrounded by a number of globular clusters. M87 belongs to the Virgo Cluster, its diameter is about 300 kpc, and more than ten thousands globular clusters orbit around it. Credits: Chris Mihos (Case Western Reserve University)/ESO. Right: the dwarf elliptical galaxy M110, which is a satellite of the Andromeda Galaxy containing 10 billion stars whose major axis is about 5 kpc. Credits: Adam Block/NOAO/AURA/NSF.*

where I_0 is the central surface brightness, R_e the effective radius and b_n can be chosen so that R_e corresponds to the radius encircling half of the total luminosity. To describe giant elliptical galaxies, de Vaucouleurs (1948) originally used a formula corresponding to a Sérsic index $n = 4$, but this value is only a first order approximation for the variety of elliptical galaxies. 'Boxy' giant elliptical galaxies whose shapes result from anisotropic random motions of stars have notably larger Sérsic indices than faint 'disky' elliptical galaxies whose random movements are isotropic but potentially flattened by rotation, the index n ranging from 0.5 to 16 (Caon et al., 1993).

Spiral galaxies

Spiral galaxies on the right of the Hubble classification are named for their bright spiral arms. These arms display clumps of bright young stars surrounded by dusty gas. While elliptical galaxies are supported against gravitational collapse by the random motions of stars, rotation plays an important role in spiral galaxies: most of their stars lie in a thin rotating disk whose characteristic height is much smaller than its radial length and which is stabilized by the centrifugal force. Atomic and molecular gas are concentrated in the disk, the molecular gas distribution being more clumped than the atomic gas (e.g., Schinnerer et al., 2013). About half of all spiral galaxies have a central bar-shaped structure composed of stars at the edge of which the spiral arms begin. The bar rotates but not necessarily together with the rest of the disk. In the Hubble classification, barred spirals are denoted SB and form the lower part of the 'fork'. Spiral galaxies also often present a stellar central ellipsoidal component, the 'bulge'. Bulges can be broadly separated in two types: 'classical bulges' on one side, which are spheroidal in shape and supported by random motions as elliptical galaxies, and 'pseudo-bulges' on the other, which can be 'boxy' to disky but are primarily supported by rotation (Kormendy & Kennicutt, 2004). It is often assumed that classical bulges are built by mergers (Baugh et al., 1996; Hopkins et al., 2009) while pseudo-bulges result either from secular evolution of the galaxy under the influence of the bar (Combes & Sanders, 1981; Athanassoula, 2005) or are due to the migration of clumps towards the center of the disk (Genzel et al., 2008; Elmegreen et al., 2008; Dekel & Krumholz, 2013; Bournaud et al., 2014). The sequence from Sa towards Sc is defined according to the relative size of the bulge as compared to the disk and to the shape of the spiral arms. Sa and SBa galaxies have large bulge components and tightly wound spiral arms, while types b and c have progressively smaller bulge-to-disk ratios and more loosely wound spiral arms. Hubble's original sequence was extended to Sd and Sm galaxies by de Vaucouleurs (1959, 1974), where Sm and SBm Magellanic spiral galaxies are analogous to the Magellanic Clouds. They are more ragged and less well ordered than other spirals and thus form the transition between spirals and irregular galaxies. As the Milky Way seems to have a central bar extending 3-4 kpc from the center, it would probably be an SBc galaxy in the Hubble classification scheme. Fig. 1.9 displays two other spiral galaxies, while Fig. 1.10 pictures the Large Magellanic Cloud.

Spiral galaxies generally have lower stellar masses than ellipticals, only up to a few 10^{11} $M_\odot$. Their density profiles can usually be decomposed into a central spheroidal

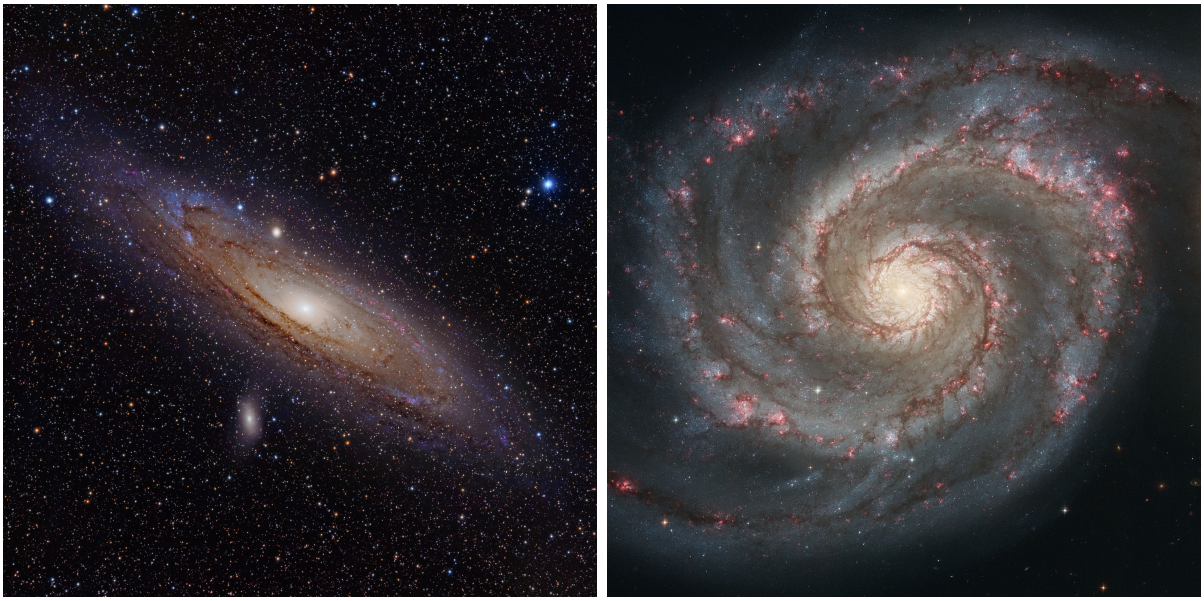

Figure 1.9 – *Left: the Andromeda Galaxy, ∼ 67 kpc in diameter and 2.5 million light-years away from the Milky Way. The nebulous object below it is M110, shown in Fig. 1.8. Credit: Adam Evans. Right: The Whirlpool Galaxy M51 drawn by Lord Rosse in 1850 (cf. Fig. 1.2). Its diameter is about 25 kpc. Credits: NASA, ESA, S. Beckwith (STScI), and the Hubble Heritage Team STScI/AURA.*

component described by a Sérsic surface brightness profile corresponding to the bulge, and an exponential disk

$$I(R) = I_0 \exp\left(-\frac{\mathrm{R}}{\mathrm{R_d}}\right), \tag{1.2}$$

where I_0 is the central density and R_d a characteristic disk radius. This characteristic radius typically ranges from a few hundreds of parsecs to about 10 kpc (e.g., de Jong, 1996). In an edge-on disk, the luminosity also decreases exponentially from the plane of the disk and the corresponding vertical luminosity profile can usually be decomposed in two exponential components corresponding to the thin disk and to the thick disk as in the case of the Milky Way. While the vertical scale length is a few hundreds of parsecs for the thin disk, it reaches about 1 kpc for the thick disk (e.g., Sparke & Gallagher, 2007, p. 72).

Lenticular galaxies

Lenticular galaxies have a flattened rotating disk and a very large central elliptical bulge, but lack any spiral arms or dust lanes. They constitute an intermediate class of galaxies between ellipticals and spirals and are named S0 in the Hubble classification. Like ellipticals, they are mostly found in regions of space that are relatively densely populated with galaxies, such as clusters of galaxies. A lenticular galaxy with a large oval shape but dust lanes indicating a disk can be seen in Fig. 1.10.

Figure 1.10 – *Left: the lenticular galaxy NGC6861. The fuzzy oval shape is typical of an elliptical galaxy, while the dark dust lanes indicate a dusty disk. Credits: ESA/Hubble & NASA, Acknowledgement: J. Barrington. Right: the Large Magellanic Cloud, which is an irregular galaxy orbiting around the Milky Way. Credit: Skatebiker.*

Extensions and other classifications

Albeit necessarily imperfect, the Hubble classification of galaxies has the merit to retain the main morphological features of the various types of galaxies: their overall ellipsoidal or flattened shape, the presence of a disk, of spiral arms and of a bulge, and the relative importance of the latter two. However, dwarf ellipticals and spheroidals as well as extra large diffuse galaxies, low surface brightness galaxies, or active and interacting galaxies do not always fit in the original classification used by Hubble (1936) and Sandage (1961). Other classifications have been proposed, including the extension by de Vaucouleurs (1959, 1974). In addition to the Magellanic galaxies Sm and SBm, this extension introduces an intermediate category of weakly barred or distorted oval spirals SAB between the normal and barred spiral sequences, and indicates the presence of internal or external rings. Among other variations on the Hubble Sequence, van den Bergh (1976) proposed a new classification in which normal gas-rich spirals and gas-poor S0 lenticular galaxies formed parallel sequences whose progression is determined by their bulge-to-disk ratio and in which a third sequence of intermediate 'anemic' spiral galaxies was added. More recently, Kormendy & Bender (2012) added to this latter classification by bridging the spiral and lenticular sequences with spheroidal and irregular galaxies. The ATLAS^{3D} team focuses specifically on elliptical and lenticular galaxies and classifies them according to their kinematics, distinguishing 'slow rotators' from 'fast rotators' (Cappellari et al., 2011). Physical properties of galaxies such as their luminosity, color, gas fraction or star formation rate can also serve as basis for classification.

Although it is no longer thought that galaxies evolve in time specifically from one end of the Hubble Sequence to the other end, the different morphologies do relate to the

particular history of each galaxy and its environment. The Hubble Sequence was mostly designed to describe nearby, low redshift galaxies, which were logically the first to be studied. However, the Universe is not static and galaxies evolve with time. As stars form and die, galaxies evolve and change. Distant high redshift galaxies, i.e., earlier in the history of the Universe, are indeed much more perturbed, less regular and more clumpy than their low redshift counterparts. Also, while elliptical galaxies appear early in the history of the Universe, disks only settle later, when star formation is already declining (Kassin et al., 2012). The second chapter of this thesis, p. 45, is specifically focusing on such distant galaxies.

1.2 A brief history of galaxy growth

How do galaxies form? The current standard Big Bang model assumes a very homogeneous Universe at early times, an assumption which is confirmed by the observations of the Cosmic Microwave Background. However, today's galaxy distribution is highly inhomogeneous and one can observe structures on all scales below ~ 10 Mpc - from planets and stars to galaxies, clusters of galaxies and enormous voids between them. The scenario leading to these huge inhomogeneities is based on the simple gravitational instability and on its interplay with the expansion of the Universe. It relies on a specific cosmological model.

1.2.1 Cosmological context

Cosmological models

Cosmological models aim at describing the structure of the Universe. They usually rely on Einstein's general relativity (Einstein, 1916) and the first cosmological model was proposed by Einstein himself in 1917 (Einstein, 1917). General relativity relates the structure of space-time with its mass and energy contents: gravitational fields intrinsically affect the curvature of space-time. Consequently, the matter distribution of the Universe determines its global geometry. The Einstein equations of general relativity can be written:

$$G^{\mu\nu} = E^{\mu\nu} + \Lambda g^{\mu\nu}, \tag{1.3}$$

where $G^{\mu\nu}$ is a tensor corresponding to the distribution of matter, $E^{\mu\nu}$ is the Einstein tensor, related to the curvature of space-time, and the last term is proportional to the metric $g^{\mu\nu}$ and implies a cosmological constant Λ. This tensorial equation fundamentally relates the content of the Universe (on the left side) to its structure (on the right). A non zero cosmological constant was initially suggested by Einstein to allow a static Universe, but was removed when Hubble showed that the Universe was expanding rather than static (Hubble, 1929). This integration constant arising from the equations of general relativity

seemed unnecessary. However, it needed to be reintroduced when the acceleration of the expansion was observed and is now thought to be non-zero.

The main assumption in cosmology is the 'cosmological principle': the Universe is assumed to be homogeneous and isotropic on large scales. There is no preferred place to observe the laws of nature, which are assumed to be the same everywhere and at all times. At very large scales, the Universe is smooth: averaged over large enough scales, its density does not fluctuate much. General relativity additionally assumes that space-time is simply connected (it could be filled with observers), locally flat (special relativity is locally valid) and that there is a means to synchronize all clocks in space.

The structure of space-time can be generally described by its metric, which is a quadratic form analog to distance in an Euclidean space. In the framework of general relativity, assuming a homogeneous and isotropic Universe leads to the Friedmann-Lemaître-Robertson-Walker metric

$$ds^2 = -c^2dt^2 + a(t)^2\left(\frac{dr^2}{1-kr^2} + r^2d\Omega^2\right) \tag{1.4}$$

where k describes the spatial curvature, $d\Omega^2 = d\theta^2 + sin^2\theta d\phi^2$ is the solid angle, and $a(t)$ is the time-dependent scale factor expressing the relative expansion or compression of the Universe. In an expanding Universe, physical distances will expand proportionally to $a(t)$ and this scale factor is determined by the Friedmann equations:

$$\begin{cases} \left(\frac{\dot{a}}{a}\right)^2 = \frac{8\pi G}{3}\rho - \frac{kc^2}{a^2} + \frac{\Lambda c^2}{3} \\ \frac{\ddot{a}}{a} = -\frac{4\pi G}{3}\left(\rho + \frac{3P}{c^2}\right) + \frac{\Lambda c^2}{3}. \end{cases} \tag{1.5}$$

These equations are the basis of the different models for the Universe, as they give the evolution of the scale factor as a function of time. Even if the Universe is not rigorously homogeneous and isotropic, the Friedmann-Lemaître-Robertson-Walker model is used as a first approximation. The Hubble parameter $H(t) = \dot{a}/a$ is the rate at which the Universe expands, as Hubble was the first to observe this expansion and to derive an estimate of $H_0 = H(0)$ (Hubble, 1929). Because of its expansion, the Universe was surely denser and hotter in earlier times. Accordingly, Big Bang models assume that the Universe started in a very hot and dense phase. The first Friedmann equation can be rewritten in terms of density parameters as

$$H^2 = H_0^2\left[\Omega_{r,0}a^{-4} + \Omega_{m,0}a^{-3} + \Omega_{k,0}a^{-2} + \Omega_{\Lambda,0}\right], \tag{1.6}$$

where $\Omega_{m,0} = \rho_{m,0}/\rho_c$ is the current matter density parameter, defined as the ratio of the matter density $\rho_{m,0}$ to the critical density of an Einstein-de Sitter universe[4] $\rho_c = 3H_0^2/8\pi G$, $\Omega_{r,0} = \rho_{r,0}/\rho_c$ is the radiation density parameter, $\Omega_{k,0} = -kc^2/H_0^2$ is associated to the spatial curvature, and $\Omega_{\Lambda,0} = \Lambda c^2/3H_0^2$ is linked to the value of the cosmological constant. The different density parameters add up to 1 by construction. They are some of the cosmological parameters describing the properties of the Universe and defining its cosmological model.

[4]An Einstein-de Sitter universe is a flat universe with no spatial curvature and no cosmological constant.

The ΛCDM model

Relatively recent observation programs have placed different constraints on the cosmological parameters, leading to the emergence of ΛCDM cosmology as the preferred cosmological model. The parameters of this model are particularly well constrained by measurements of the Cosmic Microwave Background, which is the closest we can get to an image of the Universe as it was right after the Big Bang about 14 billion years ago. Space missions such as NASA's WMAP (e.g., Komatsu et al., 2011) and ESA's Planck (e.g., Planck Collaboration et al., 2014, 2015) enabled precise determinations of these parameters, whose values are indicated in Table 1.2. The ΛCDM model is a Friedmann-Lemaître-Robertson-Walker model which assumes the existence of a cosmological constant Λ and of cold dark matter (CDM). It is a Big Bang model where the expansion is accelerated but space remains Euclidean, with a flat geometry (k=0), and where the Universe is 13.8 billion years old. According to the ΛCDM model, the mass and energy content of the Universe is composed for about two thirds of 'dark energy' characterized by its current density parameter $\Omega_{\Lambda,0} = 0.6911$, one quarter of cold dark matter with $\Omega_{cdm,0} = 0.259$ and about 5% or ordinary, 'baryonic' matter with $\Omega_{b,0} = 0.0486$ (Planck Collaboration et al., 2015). In this cosmological context, the term 'baryons' designates all matter formed out of protons, neutrons and electrons, thus all atoms and molecules composing the visible structures of the Universe. Neutrinos constitute a warm dark matter but their low masses reduce their contribution to the total mass and energy content of the Universe to only a few tenth of percents.

H_0	67.74 ± 0.46 kms^{-1}Mpc^{-1}	Hubble parameter
t_0	13.799 ± 0.021 Gyr	Age of the Universe
$\Omega_{\Lambda,0}$	0.6911 ± 0.0061	Dark energy density parameter
$\Omega_{m,0}$	0.3089 ± 0.0062	Total matter density parameter
$\Omega_{b,0}$	0.0486 ± 0.0003	Baryon density parameter
$\Omega_{cdm,0}$	0.259 ± 0.002	Cold dark matter density parameter

Table 1.2 – *Some of the ΛCDM cosmological parameters as recently measured by Planck (Planck Collaboration et al., 2015). The errors correspond to 68% confidence limits.*

Dark matter

The ΛCDM model assumes the existence of a cold, non baryonic dark matter. The observed phenomena which lead to this assumption are the radial line-of-sight velocities of stars and gas in galaxies. Indeed, Newtonian dynamics relates the rotation velocity of an object around a central mass to the distance between the two objects and to the mass of the central one. As he was trying to determine the mass of the Coma cluster in 1933,

the Swiss astronomer Fritz Zwicky was surprised to find that 100 to 500 times more mass than observed would be needed to explain the high velocities he observed (Zwicky, 1933). The same phenomenon was later observed by Sinclair Smith in 1936 for the Virgo cluster (Smith, 1936), but the problem did not trigger much interest at that time. It reappeared in the seventies when the American astronomer Vera Rubin studied the rotation of spiral galaxies: stars far from the center of the galaxy seemed to be rotating so fast that the rotation curve of most spiral galaxies was flat (Rubin & Ford, 1970; Rubin et al., 1982). According to Newtonian dynamics, the rotation velocity should decrease when moving away from the center of the galaxy, as most of the visible matter is concentrated around the center. As the density decreases approximately exponentially from the center, the velocity of the stars in the spiral arms of the galaxy should also decrease, which is not observed.

To explain the dynamics of these galaxies, one could imagine the existence of a halo made of non visible matter, in which the visible matter would be embedded and whose mass would be more than five times higher. Fig. 1.11 shows the flat rotation curve of a spiral galaxy, which is fitted by a model combining a spherical dark matter halo with the exponential disk (van Albada et al., 1985). The dark matter was originally expected to be constituted of ordinary baryonic matter, like interstellar gas, asteroids, extrasolar planets or neutron stars. But later studies have shown that it is not possible: the Big Bang theory precisely predicts the quantity of baryons present at the first epochs of the Universe, and dark matter has therefore to be explained with a different type of matter. The first candidates were neutrinos, which are neutral particles weakly interacting with ordinary matter. But we now know that their mass would have been too small to explain the masses of galactic haloes and their velocities too big to enable structures to form: the

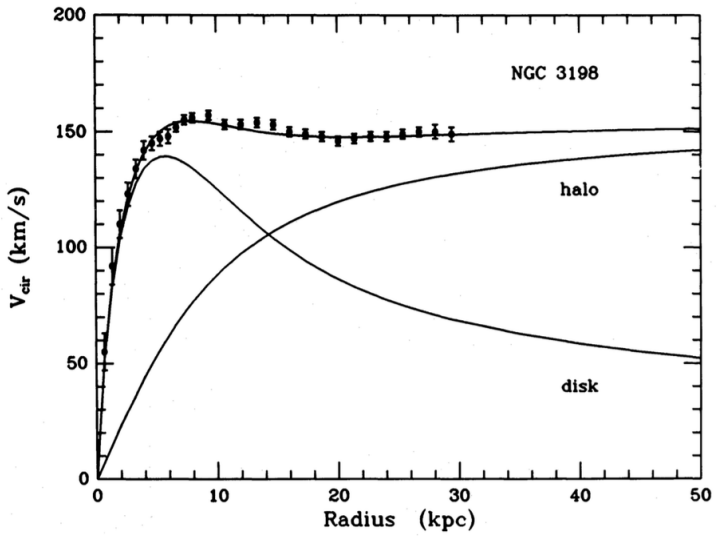

Figure 1.11 – *The rotation curve of the spiral galaxy NGC 3198 can be reproduced by introducing a spherical dark matter halo in addition to the exponential disk (van Albada et al., 1985). The error bars correspond to the observed data points, while the solid lines indicate the model. The line that fits the data corresponds to the combination of an exponential disk and a spherical halo.*

high velocities of these hot dark matter particles would have dispersed the little primordial inhomogeneities which then led to the formation of galaxies and clusters of galaxies. Most of the dark matter thus has to be 'cold', which implies that its mean velocity at the first stages of cosmic history was much smaller than the speed of light. Particle physicists are searching for such a particle, which would weakly interact with ordinary matter and would be much more slower and massive than the neutrino. Some extensions of the standard model of particle physics, such as supersymmetry, offer possible candidates in the form of Weakly Interacting Massive Particles (WIMPs). They would be difficult to detect directly because they would experience no electromagnetic interactions, and their indifference to the strong nuclear interaction would prevent them to react with atomic kernels. Within the supersymmetric theory, the neutralino would be a good candidate for dark matter: this particle would be the fermionic superpartner of both the photon (boson which transmits the electromagnetic force) and the Z^0 boson (which transmits the weak nuclear interaction). The neutralino would be more massive than all known particles but the lightest supersymmetric particle, which would assure its stability. Current searches, notably carried at the CERN Large Hadron Collider (LHC), have however ruled out large portions of parameter space corresponding to the simplest such models.

Even if the ΛCDM model seems to be the most accurate model to describe our Universe nowadays, dark matter has not been directly detected so far. The assumption of its existence is not the only possible answer to the incompatibility between the observed galactic orbits and Newtonian predictions. Alternatives include forms of dark matter that are fundamentally different from the usual cold dark matter, such as self-interacting dark matter (e.g., Spergel & Steinhardt, 2000), and models that change the gravitational law itself like Mordechai Milgrom's MOND theory (Milgrom, 1983a,b,c). This latter model notably explains extremely well the rotation curves of galaxies, without introducing cold dark matter. However, it lacks an underlying theory which would explain the suggested empirical modification of Newton's law. Section 4.1.4 (p. 137) elaborates further on potential alternatives to the cold dark matter paradigm.

An accelerated expansion

Measurements of the velocities of standard supernovae of type Ia have shown that the Hubble constant was lower earlier in the history of the Universe so that the expansion of the Universe is accelerating (e.g., Riess et al., 1998). This can be achieved with a non-zero positive cosmological constant. The observed expansion implies that the vacuum contributes through $\Omega_{\Lambda,0}$ to about 70% of the present mass and energy content of the Universe. This contribution can be described in terms of 'dark energy'. The cosmological constant Λ can be interpreted as a property of space-time itself, as if it had an intrinsic repulsive action. However, the fundamental cause of this acceleration remains unsure.

The accelerated expansion of the Universe stipulated by the ΛCDM model may incidentally have an important consequence for the distant future of cosmology and astrophysics: as the expansion of the Universe accelerates, extragalactic sources of light will slowly move out of the observable volume of the Universe, and the merger remnant of the Milky

Way and Andromeda galaxies will be the only galaxy remaining within Earth's horizon in another hundred billion years (Loeb, 2011). If such predictions of the ΛCDM model are correct, future cosmologists - if there are any - might have to rely on ancient textbooks to understand the Big Bang and distant galaxies: what would be the future of cosmology in such conditions? Hypervelocity stars escaping from the only remaining visible galaxy might serve as tracers to test cosmological models, but the lack of direct evidence might require an act of faith to believe in the existence of other galaxies in the distance.

Missing baryons

Analysis of the Cosmic Microwave Background power spectrum and primordial nucleosynthesis in the ΛCDM model yield a mean cosmic baryonic density of $0.0486\rho_c$ (Planck Collaboration et al., 2015). However, inventories of the baryonic budget in galaxies and galaxy clusters are only able to account for about 10% of this value. Indeed, stars and stellar remnants represent about 5% of the mean cosmic baryonic density, cool gas less than 2% and hot gas in clusters and ellipsoids a bit less than 4% (Fukugita et al., 1998; Fukugita & Peebles, 2004). Gas from cosmic filaments revealed by Lyman-α absorbers could account for $\gtrsim$ 20% of the mean cosmic baryonic density (Lehner et al., 2007), while numerical simulations show that a gaseous warm-hot intergalactic medium (WHIM) notably produced by shocks during the formation of large-scale structure could account for about 30-40% of all baryons (Cen & Ostriker, 1999; Davé et al., 2001). However, only a small fraction of the expected WHIM gas has been detected, representing only about 3-10% of the baryons (Danforth & Shull, 2005). A large fraction of the baryons is still missing from an observational point of view.

1.2.2 Structure formation in the Universe

Early history of the Universe

The basic process involved in galaxy formation is the gravitational instability: a local excess of matter will attract the neighboring matter due to its gravitational potential and will thus grow. Over-dense regions pull matter towards them and become even more dense, while underdense regions become less and less dense as matter flows away from them. In the standard cosmological model, density fluctuations were created very early in the history of the Universe and later condensed to form the structured objects we now see. Quantum fluctuations at the very first moments were the seeds for the future growth of structure in the Universe. The current standard cosmological model assumes that the nascent Universe passed through a phase of exponential expansion, named inflation and driven by the negative-pressure vacuum energy density or one or more quantum fields, in which the microscopic quantum fluctuations were magnified to cosmic size. As the Universe expanded, temperature decreased and formation of structured matter became possible after the epoch of matter radiation equality. At that time, the Universe was still

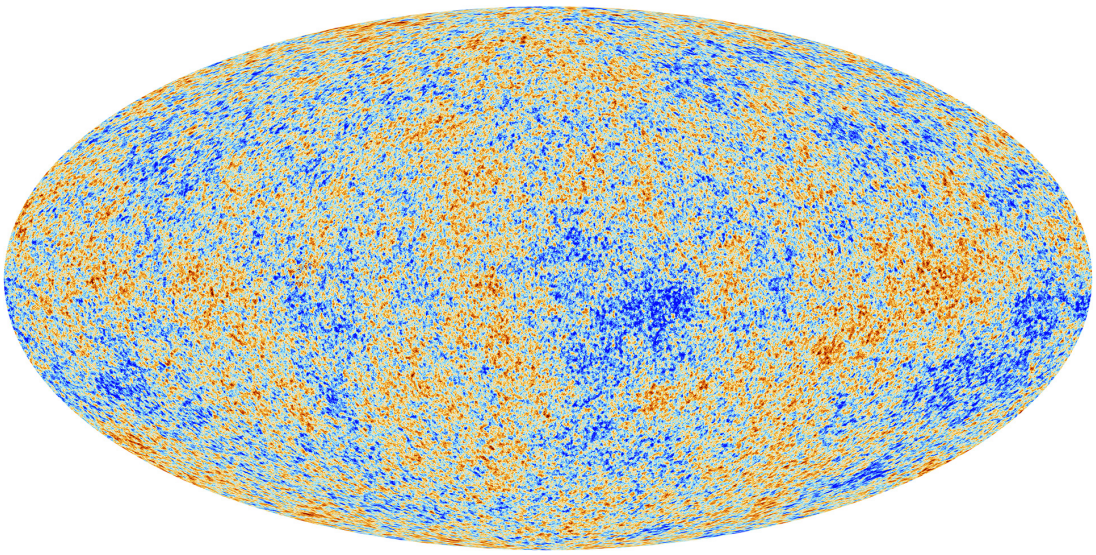

Figure 1.12 – *The Cosmic Microwave Background as observed by the Planck telescope. The color scale highlights the tiny* 10^{-5} *level inhomogeneities in temperature and density. Credits: ESA and the Planck Collaboration.*

opaque: there was an equilibrium between electromagnetically-interacting matter and radiation, as free electrons ceaselessly absorbed and re-emitted photons. As the Universe continued to cool, electrons had no longer enough energy to overcome the attractive force of atomic nuclei, and became bound to atoms. Light could now stream forth unimpeded. This process is called recombination, and the 'first light' enabled to stream is what we now see as the Cosmic Microwave Background radiation. As a relic of the earliest moments of the Universe, the Cosmic Microwave Background (CMB) shows how homogeneous the Universe was 380,000 years after the Big Bang, with inhomogeneities at the level of about 10^{-5}. Fig. 1.12 displays the CMB as observed by the Planck telescope.

Growth of perturbations through gravitational instability

Formation of structures is essentially driven by the competition between the gravitational growth of fluctuations and the expansion of the Universe, which tends to dilute each local overdensity. The first study of the gravitational instability was carried out by the British physicist James Jeans in 1902: his theory took into account gravity and pressure and assumed a static medium. Gravity tends to condense matter, whereas pressure diminishes inhomogeneities: the more the mass of a fluctuation is, the more gravity is important compared to pressure. Taking the expansion of the Universe into account and assuming a uniform background, the Friedmann equations in an Einstein-de Sitter universe yield for non-relativistic matter and for perturbations smaller than the horizon[5]

$$\ddot{\delta} + 2H(t)\dot{\delta} = 4\pi G\rho_u(t)\delta + a(t)^{-2}c_s^2\nabla^2\delta \tag{1.7}$$

[5]The horizon at a given cosmological time corresponds to the maximum distance at which two regions can be causally connected, i.e., between which light may have traveled within the finite lifetime of the Universe and given its expansion. The horizon consequently defines the observable Universe: no information can reach us from beyond it.

where $a(t)$ is the scale factor of the Universe, $\rho(t,\vec{r}) = \rho_u(t)[1+\delta(t,\vec{x})]$ with $\rho_u(t)$ the mean density of the Universe at time t, $\delta(t,\vec{x})$ the overdensity and $\vec{x} = \vec{r}/a(t)$ the comoving coordinates (Peacock, 1999). An Einstein-de Sitter universe is indeed a good approximation of our Universe at early times. This equation assumes that the fluctuations are small enough to use a linear approximation, and $c_s^2 = \partial P/\partial\rho$ designates the sound speed. The right side of the equation shows the competition between gravity and pressure, whereas on the left side, the Hubble flow seems to slow down the perturbation growth as a friction force, which is an artifact of the comoving coordinates. The first stage of fluctuation growth can be described by the linear approximation, but this approximation becomes inaccurate when fluctuations have developed up to $\delta \gtrsim 1$. The linear phase leads to a non linear phase whose analytic treatment is more difficult and requires additional assumptions such as the Zel'dovich approximation (Zel'dovich, 1970; Shandarin & Zeldovich, 1989), or a statistical approach (Press & Schechter, 1974). Cosmological structures being formed out of a distribution of matter which is almost homogeneous but most likely non rigorously spherical, the collapse is faster along the shortest axis and leads structures shaped as pancakes and filaments (e.g., Lin et al., 1965; Peebles, 1993; Springel et al., 2005; Boylan-Kolchin et al., 2009).

1.2.3 Major mergers versus smooth accretion

Hierarchical clustering

Instead of using the spatial distribution of the overdensity $\delta(t,\vec{x})$, it is possible to consider its Fourier transform $\delta_{\vec{k}}(t)$ and power spectrum $\left\langle|\delta_{\vec{k}}|^2\right\rangle$. The evolution of the power spectrum of the fluctuations depends on the properties of matter: if matter had been mostly constituted of adiabatic baryons or hot dark matter (neutrinos), the spectrum would have been cut at small scales and galaxies would have formed by fragmentation of huge structures. But in the ΛCDM model, most of the matter is assumed to be made of cold dark matter: structure formation is mostly determined by dark matter dynamics, in which small structures form first and larger structures assemble by successive mergers. Galaxies are assumed to form within the potential wells of dark matter haloes (White & Rees, 1978). Indeed, as dark matter does not lose energy by radiation, it can't condense as efficiently as baryonic matter and is organized in more diffuse structures. Cosmological simulations allow to follow the formation of each dark matter halo or of each galaxy and to reconstruct the history of its progenitors and of the successive mergers in 'merger trees' such as the one shown in Fig. 1.13. Collisions and close interactions between galaxies lead to tidal forces which distort and strip galaxies: their morphology is not fixed and notably evolves under the influence of the environment and of the successive mergers. Mergers are also expected to trigger bursts of star formation, as inferred from observations of merging galaxies (e.g., Sanders et al., 1988; Elbaz & Cesarsky, 2003) and from numerical simulations (e.g., Di Matteo et al., 2007, 2008; Martig & Bournaud, 2008). This enhancement of star formation notably results from tidal torques depleting the angular momentum of the gas in the inner half of the galactic disk, leading this gas to fall in and to increase the central density of the galaxy (Barnes & Hernquist, 1991).

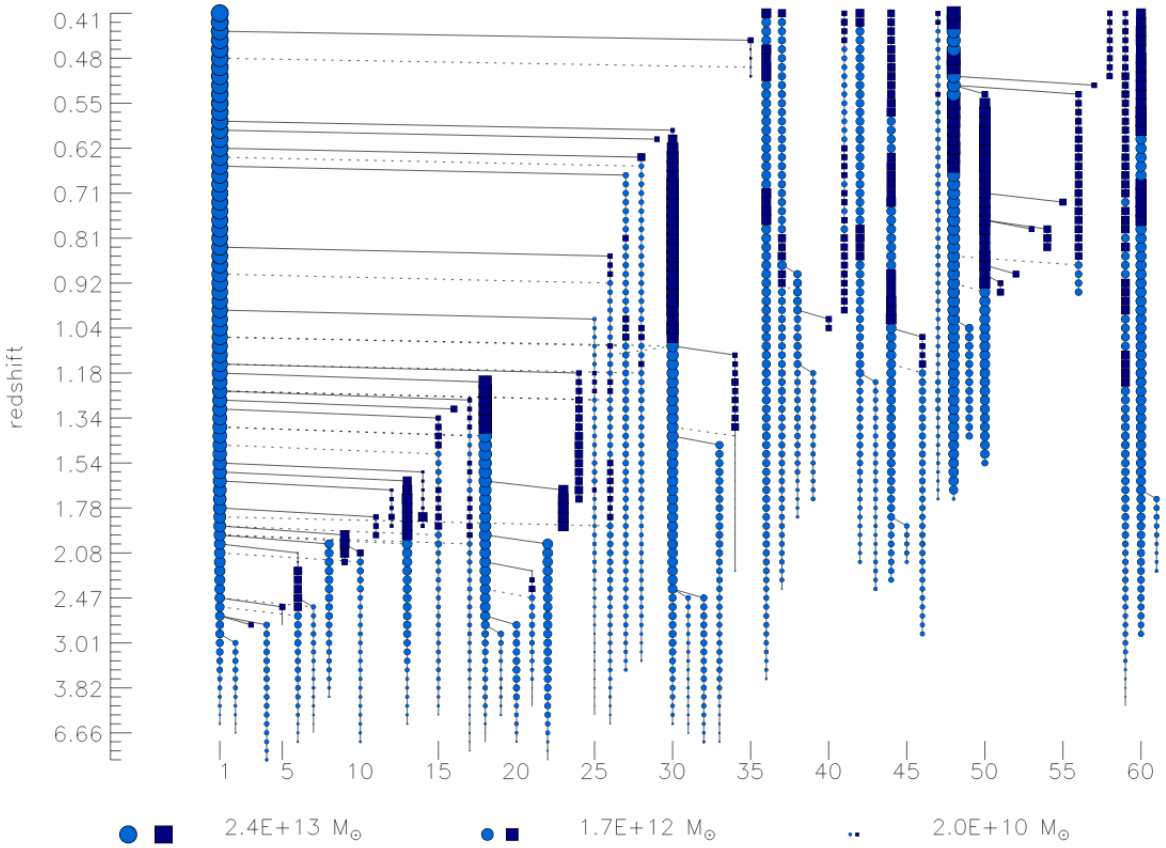

Figure 1.13 – *Baryonic merger tree of a galaxy and of its satellites from L'Huillier et al. (2012). The evolution with time goes from bottom to top. Dark blue circles are galaxies while bright blue squares are satellites. Some of the satellites eventually merge with the main galaxy on the left.*

Accretion from the cosmic web

Present-day galaxies like the Milky Way were constructed over billions of years by the assembly of a million building blocks constituted by the earliest dwarf galaxies. The fuel for the formation of stars and of the central black hole is provided by gas accretion onto the halo, either through major mergers of galaxies or through relatively smooth and steady accretion. In the case of spherical gaseous accretion onto the halo, an accretion shock forms near the virial radius of the galaxy[6] and the incoming gas is heated up to high temperatures before being able to cool down and descend into the inner galaxy (Rees & Ostriker, 1977; Birnboim et al., 2007). However, while such a shock seems to be the predominant accretion mode for large haloes, cold gas can penetrate deep inside smaller haloes along cosmological filaments, directly to the central galaxy, and typical galaxies at redshifts $z \gtrsim 2$ contain hot gas in virial equilibrium punctured by cold dense streams stemming from the cosmic web (Birnboim & Dekel, 2003; Kereš et al., 2005; Dekel & Birnboim, 2006; Ocvirk et al., 2008; Dekel et al., 2009a; Kereš et al., 2009). Fig. 1.14 from Dekel et al. (2009a) shows a simulated galaxy fed by such cold streams. Two

[6]The virial radius of a galaxy is defined page 133.

streams harbor gas clumps whose mass is on the order of one-tenth of the mass of the central galaxy, but the streams are otherwise rather smooth. The presence of asymmetrical and warped galaxies that are apparently isolated would also be an argument in favour of a smooth accretion of gas from the cosmic web (e.g., Combes, 2009). These steady flows are crucial for star formation as a continuous supply of cold gas, and their angular momentum contributes to the build-up of a rotating disk within the galaxy.

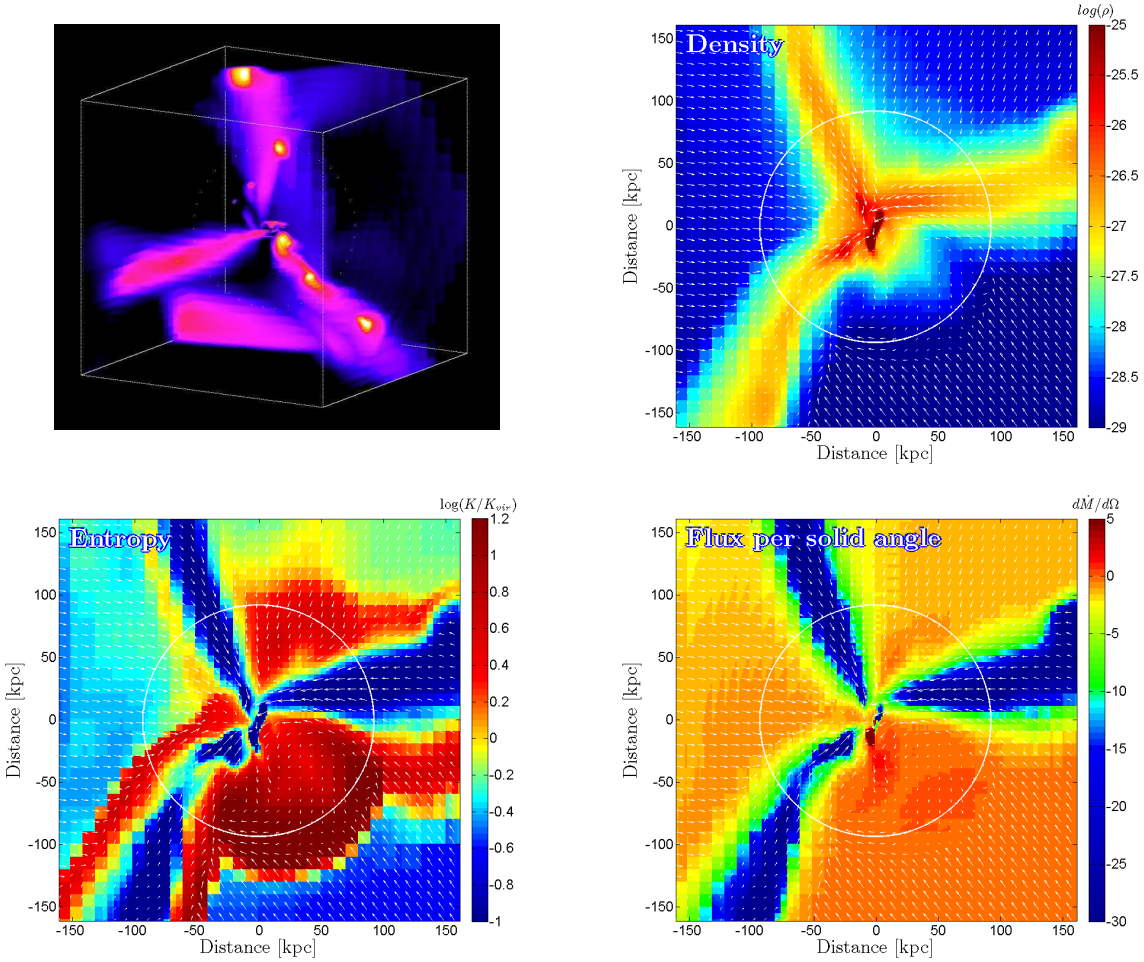

Figure 1.14 – *Three dimensional view and slices of a simulated galaxy fed by cold streams at $z = 2.5$ (Dekel et al., 2009a). The colors in the 3D view refer to the inflow rate per solid angle while the slices display the density ρ, the entropy[7] $log(T/\rho^{2/3})$ and the radial flux $\dot{m} = r^2 \rho v_r$, thus highlighting the penetrating low-entropy gas streams. The small arrows correspond to the velocity field, the dotted circles to the virial radius. The pictured galaxy has a viral mass of 10^{12} $M_\odot$ as the Milky Way.*

[7]Defining the entropy as $log(K) = log(T/\rho^{2/3})$ is common in astrophysics. It corresponds to the entropy of an ideal monoatomic gas with adiabatic index $\gamma = 5/3$, $K = PV^\gamma$ being the adiabatic constant.

1.3 Star formation and its regulation

Although gravity determines the large-scale evolution of structures in the Universe, intricate baryonic processes affect morphology and structure on galactic scales. Indeed, galaxy formation and evolution are driven by a complex interplay between the hierarchical merging of dark matter haloes, gas accretion, and baryonic processes such as cooling and gravitational fragmentation, the formation of molecular clouds, star formation, stellar nucleosynthesis and outflows driven by stellar winds, supernovae or Active Galactic Nuclei. Within haloes, ordinary matter can cool, losing energy by radiation, and fall to the center of the potential well. There, the gas can fragment into small, high-density cores that may eventually form stars. At the end of their evolution, the most massive stars explode as supernovae and eject their gas and the heavy elements formed at their core in the interstellar medium. The accretion onto the central black hole of the galaxy releases energy in the interstellar medium as well. Both phenomena can produce powerful galactic winds which heat the disk and inhibit subsequent star formation. Baryonic processes play an important role in shaping galaxies.

1.3.1 Giant molecular clouds in the interstellar medium

Structures of the interstellar medium

Observations show that, in the Milky Way, star formation occurs in dense molecular clouds whose typical density is about hundred particles per cubic centimeter and whose temperatures are usually around 10 K (Blitz, 1993; Williams et al., 2000). Therefore, the overall star formation rate (SFR) of a galaxy is related to its ability to form such dense molecular clouds in the interstellar medium (ISM). In the Milky Way, the ISM constitutes a flattened disk predominantly made of cold gas. Most of this gas is made of neutral hydrogen, but about 20% of its mass is in molecular form, mainly as molecular hydrogen (H_2). The ISM also comprises a small fraction of dust grains, amounting for about 1% of the total mass. Observations show that the distribution of molecular gas in the Milky Way is highly clumpy: most of it is distributed over giant molecular clouds (GMCs), which have masses between $10^5 - 10^7$ $M_\odot$ and sizes of over a few tens of parsecs. GMCs are themselves structured at smaller scales and composed of numerous spherical or filamentary substructures (Blitz, 1993; Bally et al., 1987), from molecular 'clumps' with masses between $10^2 - 10^4$ $M_\odot$ and sizes of about 10 parsecs to $0.1 - 10$ $M_\odot$ 'cores'. Star formation occurs in the denser parts of these substructures. While the protostellar cores may form single stars, the most massive clumps can form stellar clusters.

Equilibrium of GMCs

GMCs are correlated with young stellar clusters with ages $\lesssim 10^7$yr but not significantly with older clusters, which indicates that their lifetimes are around 10^7 yr (e.g, Leisawitz

et al., 1989; Fukui et al., 1999). Such a time scale is short compared to the lifetime of a galaxy. If GMCs were only supported against gravitational collapse by thermal pressure, they should collapse and form stars on a free-fall time

$$t_{ff} \simeq \frac{1}{\sqrt{G\rho}} \simeq 3.6 \times 10^6 \mathrm{yr} \left(\frac{\mathrm{n_{H_2}}}{100 \mathrm{cm}^{-3}} \right) \tag{1.8}$$

where ρ is their mean density and $n_{\mathrm{H_2}}$ the corresponding number density. Indeed, the Jeans mass for a self-gravitating, homogeneous, isothermal sphere of gas is

$$M_J = \frac{\pi^{5/2}}{6} \frac{c_s^3}{(G^3\rho)^{1/2}} \simeq 40 \ \mathrm{M}_\odot \left(\frac{\mathrm{c_s}}{0.2 \mathrm{km\ s}^{-1}} \right)^3 \left(\frac{\mathrm{n_{H_2}}}{100 \mathrm{cm}^{-3}} \right)^{-1/2} \tag{1.9}$$

where c_s is the sound speed (Mo et al., 2010), and structures of masses above this mass should collapse on a free-fall time[8]. GMCs have number densities above 100 cm^{-3}, so their Jeans mass is orders of magnitude smaller than their mass. As the free fall time on which the gravitational collapse should happen is significantly smaller than the inferred lifetimes of GMCs, they should additionally be supported against gravitational collapse by non-thermal pressure. Turbulence and magnetic fields are consequently expected to play a significant role in star formation, as they would provide the additional pressure support. Both phenomena should affect the efficiency of star formation.

Larson's relation

Despite the fact that GMCs are usually complex structures, they obey to relatively simple scaling relations over wide orders of magnitudes. In particular, the masses and velocity dispersions of individual molecular clouds and clumps of masses between $10^2 - 10^6$ $\mathrm{M}_\odot$ are observed to be tightly correlated with their size R:

$$M \propto R^2 \tag{1.10}$$

$$\sigma \propto R^{1/2} \tag{1.11}$$

(Larson, 1981; Solomon et al., 1987; Myers & Fuller, 1992; Heyer & Brunt, 2004; Heyer et al., 2009; Lombardi et al., 2010). Except for protostellar cores, the observed velocity dispersions are much larger than what would be expected from thermal broadening, reaching about 10 kms^{-1} on the scale of a GMC while a temperature of 10 K would only yield a thermal line broadening of about 0.2 kms^{-1}. Consequently, GMCs and molecular clumps have high levels of supersonic turbulence. The empirical relation involving the velocity dispersion and initially identified by Larson (1981) characterizes this turbulence. A Kolmogorov subsonic turbulence would yield $\sigma \propto R^{1/3}$ and is therefore insufficient to explain the slightly higher observed exponent. The relation between mass and size also suggests a fractal hierarchy of clouds, allowing a turbulent energy cascade from large to small scales (Falgarone & Puget, 1986; Combes, 1991). This relation further implies that

[8] In fact, it would be more appropriate to consider the Bonnor-Elbert mass instead of the Jeans mass, but both masses are of the same order of magnitude for molecular clouds (Mo et al., 2010, p. 420). Cf. section 3.1.3 for a more detailed description of the Jeans stability criterion.

the surface density of molecular cloud structures is approximately constant, which is verified by observations (e.g., Solomon et al., 1987; Blitz et al., 2007). However, it does not hold when considering different radii within a single molecular cloud (Lombardi et al., 2010).

1.3.2 Star formation and stellar evolution

From giant molecular clouds to proto-stars

Stars form in the densest regions of GMCs, where gravity pulls gas particles together. Parts of the clouds fragment and form high density cores which will later turn into stars (e.g., Iben, 1965; Larson, 1969; Stahler et al., 1980). As the free-fall time is inversely proportional to the square root of the density, the denser central regions collapse more rapidly and their density becomes more and more peaked. When the density reaches a certain threshold, a core arises, in which gas has stopped collapsing. However, gas continues to accrete onto the proto-stellar core from the outside. A shock develops, which heats the gas. The gravitational potential energy loss of the infalling gas is radiated away: the luminosity of pre-stellar cores in their earliest stages is not due to nuclear reactions but to this conversion of gravitational potential energy. Because the parent cloud had most likely some rotation, the conservation of angular momentum leads upon contraction to the formation of a disk around the core. Parts of this disk may later become planets orbiting around the star. The proto-stellar core continues to grow by

Figure 1.15 – *The Orion Nebula, a stellar nursery. Thousands of stars of various sizes and ages are embedded in a giant cloud of gas and dust. Credits: NASA,ESA, M. Robberto (Space Telescope Science Institute/ESA) and the HST Orion Treasury Project Team.*

accretion and its radius expands. Inside, temperature and pressure rise, along with the degree of ionization. When the pre-stellar core is dense enough, deuterium fusion reactions ignite, followed by hydrogen fusion reactions. However, stars with masses smaller than ~ 0.08 $M_\odot$ can't ignite hydrogen and become brown dwarfs. Hydrogen fusion reactions make typical main sequence stars shine, and young stars are particularly vigorous. They emit highly energetic ultraviolet light and generate strong winds that blow away their surroundings. In the Orion Nebula for example, the winds generated by the bright young stars at the center of the stellar nursery have carved a huge oval cavity visible in Fig. 1.15. These outflows and the associated radiation constitute a proto-stellar feedback loop as they disperse the gas around the proto-star and hence reduce or even terminate further accretion.

Stellar nucleosynthesis

The Sun is an incredibly hot sphere of gas, mostly made of hydrogen, and the temperature in its core can reach millions of degrees. Such a star is powered by nuclear fusion, through which light elements synthesize heavier ones. Hundreds of millions of tons of hydrogen atoms fuse together each second to form elements like helium in the core of the Sun. Fusion reactions are very energetic and generate most of the Sun's intense energy. But these reactions slowly drain the available hydrogen reservoir: in another five billion years, the core of the Sun will run out of fuel. The nuclear reactions will stop in the core and start around it, where there will still be some hydrogen left. The Sun will become a red giant star. Its core will again contract and heat up, until the helium atoms start to fuse to form carbon in an explosive reaction. Eventually, the nuclear reactions in and around the core of the Sun will stop and the star will become a cold white dwarf. But fusion reactions can produce elements up to iron in bigger stars. Indeed, the binding energy per nucleon increases up to iron so that fusion reactions are thermodynamically advantageous up to this heavy element. Cosmological primordial nucleosynthesis only produces light elements, so all elements heavier than helium and lithium are believed to have been synthesized inside stars. Light elements can be converted successively into heavier and heavier elements inside stars, depending on the stellar mass.

Metal enrichment

When the outer layers of a star are ejected at the end of the star's life, for example if it explodes as a supernova, heavy elements are released in the interstellar medium. This 'metal enrichment' affects subsequent star formation, as the cooling efficiency of the gas depends strongly on its 'metallicity': metal-enriched gas cools faster (e. g., Mo et al., 2010). In this context, the term 'metal' collectively designates elements heavier than helium. If metal enrichment is expected to increase the star formation efficiency, stars also generate strong winds which remove part of the gas from the interstellar medium and consequently hamper further star formation. Such feedback processes are crucial to regulate star formation.

1.3.3 Feedback processes

Early models of galaxy formation in the ΛCDM model predicted that most baryonic material should cool efficiently and form stars. However, only a small fraction of baryons are found to be in the form of stars or cold gas (cf. paragraph 1.2.1). Indeed, the stellar to dark matter ratio within galaxies is only a few percent, well below the cosmological baryon fraction. This suggests the existence of physical processes that would prevent the gas from cooling or that would reheat the cold gas.

Stellar feedback mechanisms

Stars release energy and momentum in their surrounding medium in different ways, namely through radiation, neutrino emission and mass flows. The first generations of stars therefore affect subsequent star formation in a variety of stellar feedback mechanisms.

First of all, stars emit strong radiation fields which travel over vast distances in the interstellar medium. A typical Sun-like star notably emits about 10^{51} erg[9] in radiation during its life, which contributes to heating the interstellar medium (ISM). Ultraviolet ionizing background radiation from young stars can indeed heat the interstellar gas up to 10^4 K (e.g., Gnedin & Ostriker, 1997) and reduce the cooling efficiency in low density environments (Efstathiou, 1992). The H_2 molecule is also relatively fragile and can be easily photodissociated by this energetic radiation (e.g., Stecher & Williams, 1967; Haiman et al., 1997). These effects all hamper star formation in the ISM. But radiation also has mechanical effects on interstellar particles. Indeed, the heating of the gas by young stars can lead to its photoevaporation: the surface of a heated gaseous cloud can expand and disperse in its surrounding medium (Oort & Spitzer, 1955; Bertoldi, 1989; Walch et al., 2012). Additionally, a gaseous cloud unevenly subject to radiation can benefit from a 'rocket effect' due to gas evaporating specifically out of the side facing the stars and being accelerated towards the opposite direction (Oort & Spitzer, 1955). Radiation also directly exerts a substantial force on the gas through radiation pressure, which is expected to be particularly important around stellar clusters (Krumholz & Matzner, 2009). Radiation pressure is indeed able to accelerate atoms within a star-forming cloud up to velocities of a few km s^{-1}, namely of the order of magnitude of the escape velocity (Loeb & Furlanetto, 2013, p. 192). Consequently, although the velocity induced by radiation pressure is not high *per se*, it can eject gas from the star-forming region, slow down accretion, and contribute to inhibiting further star formation. Murray et al. (2010) notably estimate that high redshift star forming clumps can be disrupted by radiative pressure as soon as 20% of their mass has turned into stars, expelling the remaining gas back in the disk.

Through their lives, stars also emit neutrinos and generate strong winds, while the most massive of them ultimately explode as supernovae, directly injecting substantial

[9]The erg is an energy unit equals to 10^{-7} J, or 1 g cm^2 s^{-2}. The most powerful thermonuclear bomb ever tested (Tsar Bomba, 1961) released about 2 10^{24} erg, or 50 megaton TNT.

amounts of mass, momentum and kinetic energy into the ISM. A supernova explosion typically accelerates about 10 $M_\odot$ of gaseous material to velocities of about 2000 km s^{-1}, injecting a few 10^{50} erg in the ISM (Mo et al., 2010, p. 493). Supernova-driven winds and shock waves are expected to remove a significant fraction of the gas from galaxies and hence suppress part of the fuel for further star formation (e.g., Larson, 1974; Dekel & Silk, 1986; Efstathiou, 2000; Greif et al., 2007). These processes also generate powerful outflows, and should enrich the gas with heavy elements formed inside stars. Numerical simulations including different forms of stellar feedback (e.g., Guedes et al., 2011; Agertz et al., 2013; Ceverino et al., 2014; Hopkins et al., 2014; Agertz & Kravtsov, 2015) indeed show that these processes are able to reduce star formation and its efficiency and to produce realistic galaxies. In a simulation code such as the one used by Agertz et al. (2013), the different stellar feedback mechanisms are implemented by injecting energy, momentum, mass and metals in the cells surrounding stars. However, the combination of all the different stellar feedback processes seems to be necessary to obtain realistic stellar masses inside dark matter haloes (Hopkins et al., 2014). The different feedback mechanisms also drive supersonic turbulence in the ISM, (Krumholz & Thompson, 2012), which plays an important role in the evolution of GMCs and the formation of stars within them.

Star formation feedback is not limited to negative feedback hampering further star formation. Indeed, stellar winds and supernovae inject heavy elements in the ISM, which enhance cooling and subsequent star formation. Winds and supernovae blast waves also locally compress the diffuse gas, increase its density, and can thus facilitate its gravitational collapse. Additionally, the dense shell that accumulates behind the shock can itself be unstable and fragment (Loeb & Furlanetto, 2013, p. 201). X-ray background radiation can also constitute a positive feedback source, as by ionizing hydrogen and helium atoms, this radiation releases free electrons catalyzing H_2 formation, which is a crucial molecule for star formation (Haiman et al., 1997).

AGN feedback

Accretion onto the central black hole of a galaxy generates very energetic feedback processes which influence star formation. Paradoxically, black hole environments are indeed some of the brightest and most energetic objects in the Universe. Bright quasars powered by supermassive black holes with masses $\gtrsim 10^9$ $M_\odot$ in the early Universe can indeed have luminosities up to $\gtrsim 10^{16}$ $L_\odot$ (e.g., Mortlock et al., 2011). These huge maelstroms attract matter towards them, and the infalling gas heats up and shines as it spirals towards the center. Fluid elements rubbing against each other heat up through frictional shear dissipation while their orbital energy is radiated away (Lynden-Bell, 1969; Rees, 1984). More than 10% of the mass-energy of the infalling material can be converted into radiation, which is more than what is needed to completely expel the gas out of a galaxy (Silk & Rees, 1998; Fabian, 2012). These highly energetic processes in a very concentrated region generate outflowing winds and highly collimated relativistic jets (e.g., Aalto, 2015). Outflow velocities can reach tens of thousands of kms^{-1} (e.g., Pounds & Page, 2006), and observations of galaxy clusters reveal bubbles of hot gas blown away by the central black

holes (e.g., Fabian et al., 2003; Salomé et al., 2006; Randall et al., 2015). Radiation, jets and winds from these active galactic nuclei (AGN) affect star formation in a similar way as stellar feedback does, and the quenching of the gas supply at the center of the galaxy can further terminate the AGN. Semi-analytical models and hydrodynamical simulations reproduce the negative feedback resulting from AGN activity (e.g., Croton et al., 2006; Bower et al., 2006; Di Matteo et al., 2005; Somerville et al., 2008; Booth & Schaye, 2009), and observations show that the energy associated with AGN-induced bubbles is sufficient to significantly reduce or quench cooling flows (e.g., Bîrzan et al., 2004).

As for stellar feedback, AGNs can also positively influence further star formation. Indeed, AGN jets and winds compress the interstellar gas as supernova blast waves do, which can enhance star formation locally (e.g., Silk, 2005; Silk & Norman, 2009; Gaibler et al., 2012; Nayakshin & Zubovas, 2012; Bieri et al., 2015a,b; Salomé et al., 2015). This effect could notably be relevant to explain the high star formation rates observed at high redshift. Also, although AGN-driven outflows can affect star formation in the long run by removing substantial amounts of gas, they might not directly affect the star formation efficiency given that star-forming clouds could be too dense to be significantly affected (Gabor & Bournaud, 2014; Roos et al., 2015).

Outflows

Feedback mechanisms give rise to powerful ionized and neutral gas outflows observed both at low redshift (e.g., Heckman et al., 1990; Veilleux et al., 1994; Lehnert & Heckman, 1996; Rupke et al., 2005a,b; Strickland & Heckman, 2009) and high redshift (e.g., Pettini et al., 2000; Shapiro et al., 2009; Weiner et al., 2009; Genzel et al., 2011; Förster Schreiber et al., 2011; Newman et al., 2012a,b; Maiolino et al., 2012; Lehnert et al., 2013; Förster Schreiber et al., 2014; Geach et al., 2014). The outflowing material can be widespread within galactic disks and related to star formation as expected from stellar feedback (e.g., Lehnert & Heckman, 1996; Pettini et al., 2000; Shapiro et al., 2009; Newman et al., 2012a), or induced by AGNs and concentrated in the central regions (e.g., Förster Schreiber et al., 2011, 2014). Outflows notably appear in observations as slightly blue-shifted broad emission line wings. Feedback mechanisms indeed accelerate parts of the gas to velocities of a few hundreds up to $1000 - 2000$ km s^{-1}, resulting in a broad component in the emission lines. This component is usually slightly blue-shifted as the backside of the galaxy (where the gas should be redshifted from the outflow) is obscured by dust. Outflows from individual star-forming clumps have been detected up to high redshifts (Genzel et al., 2011; Newman et al., 2012b) as expected from theoretical models and simulations (e.g., Dekel et al., 2009b; Bournaud et al., 2014). Fig. 1.16 displays the blue-shifted broad component observed in the Hα+[NII] emission lines of an individual bright star-forming clump at high redshift (Genzel et al., 2011), revealing significant ionized outflows. When sensitivity is insufficient, the broad wing associated to outflows can potentially be revealed by stacking different clumps, as suggested in the ALMA proposal briefly presented in section 2.4.4.

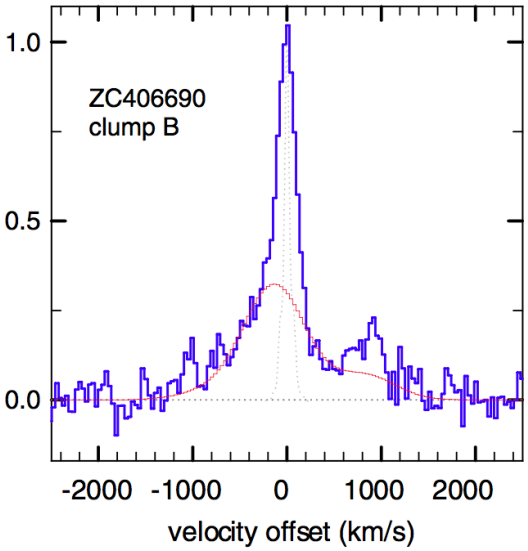

Figure 1.16 – *Broad component in the Hα+[NII]emission lines of an individual clump from a $z = 2.2$ star-forming galaxy (Genzel et al., 2011). The broad wing (in red) is slightly blue-shifted towards negative line-of-sight velocities, as expected for outflowing material.*

The gaseous material ejected by outflows is not necessarily lost and some of it can remain bound to the galaxy and be recycled when it falls back towards the disk. The conservation of the gas mass in a galaxy can be schematically expressed to take stellar feedback and outflows into account as

$$\dot{M}_{gas} = \dot{M}_{gas,in} - \dot{M}_{\star} - \eta\dot{M}_{\star} + R\dot{M}_{\star} \tag{1.12}$$

where $\dot{M}_{gas}$ is the growth rate of the gas mass, $\dot{M}_{gas,in}$ the gas accretion rate, $\dot{M}_{\star}$ the star formation rate (SFR), η the mass-loading factor of the outflows lost in the intergalactic medium, and R corresponds to the recycled gas mass loading-factor (Bouché et al., 2010; Dekel & Mandelker, 2014). The last two terms are proportional to the SFR as outflows resulting from stellar feedback depend on the amount of stars that are created. This 'bathtub' model represents a galaxy as a gas reservoir fed by accretion, for example through smooth streams stemming from the cosmic web, and emptied through star formation and outflows. Once the characteristic time scale associated to star formation becomes shorter than the accretion time scale, the galaxy settles in a steady-state in which its gas content is constant and the SFR set by the inflow rate (Bouché et al., 2010). The galaxy can be seen as a factory processing stars: the inflowing gas is the raw material, stars are the processed goods, and there is some waste on the way, corresponding to outflows. The amount of waste is proportional to the quantity of goods processed, and part of it can be recycled and reused, corresponding to $R\dot{M}_{\star}$. However, Eq. 1.12 notably does not take into account the fact that the recycled gas is 'polluted' by metals, which should influence the star formation efficiency. It nevertheless allows to represent in a simple way the gas and stellar cycles taking place in a galaxy.

Shaped by feedback

Feedback processes from stars and AGNs are able to unbind and expel large amounts of gas from galaxies, thus explaining the small fraction of baryons constituted by gas and stars within galaxies. However, while stellar feedback depends on the star formation history and the total mass of stars which were formed, the energy injected into the ISM by AGNs depends on the black hole mass. The fraction of gas that is eventually removed also depends on the binding energy of the gas, hence of the density distribution (e.g., Shankar et al., 2006). Consequently, the efficiency of the different feedback mechanisms varies with galaxy mass. This is particularly visible when comparing the luminosity function of galaxies with the halo mass function. The luminosity function of galaxies, $dn(L) = \Phi(L)dL$, is a statistical observable describing the number of galaxies per comoving volume within luminosity bins $[L,\ L + dL]$. It can also be expressed in terms of a galaxy mass function $\Phi(m)$, where m is the stellar mass. On the other hand, the halo mass function $N(M)$ describes the number of haloes per halo mass M expected from ΛCDM cosmology (e.g., Mo et al., 2010). If each dark matter halo hosted one galaxy and if the stellar-to-halo mass ratio was constant, the luminosity function of galaxies should be a rescaled version of the halo mass function. However, as shown in Fig. 1.17, this is not the case. In this figure from Moster et al. (2010), symbols indicate the observed galaxy mass function

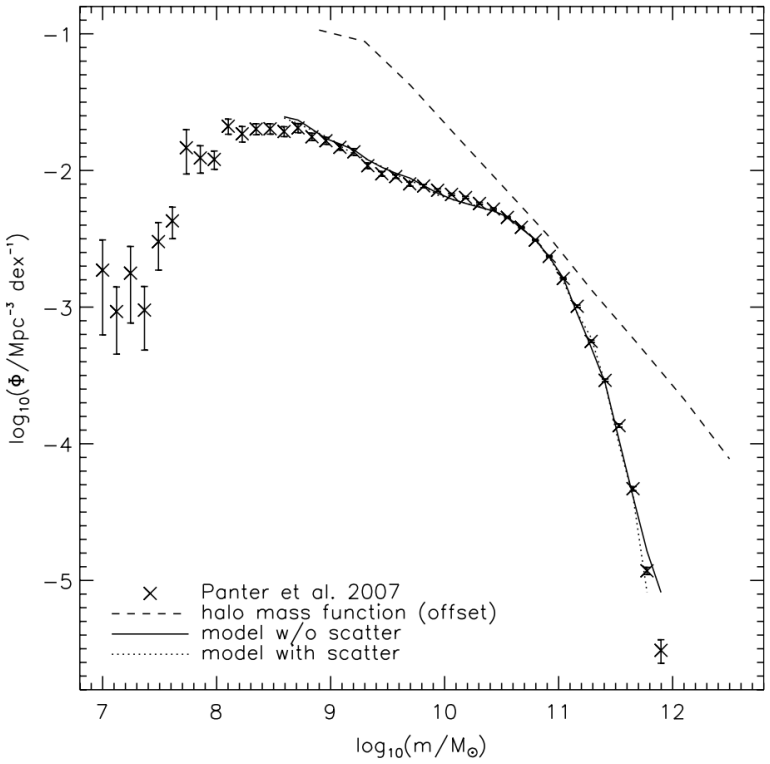

Figure 1.17 – *Comparison between the observed galaxy mass function and the halo mass function, from Moster et al. (2010). Symbols correspond to the observed galaxy mass function from the SDSS (Panter et al., 2007) while the dashed line corresponds to the mass function that would be expected from the theoretical halo mass function with a constant stellar-to-halo mass ratio* $m/M = 0.05$.

from the *Sloan Digital Sky Survey*[10] (SDSS), while the dashed line corresponds to the mass function that is expected from the halo mass function with a constant stellar-to-halo mass ratio $m/M = 0.05$. This indicates that the stellar-to-halo mass ratio varies with halo mass, first increasing from low mass up to a halo mass of about $10^{12}M_{\odot}$ (about $5\ 10^{10}$ in stellar mass), and then dropping at higher masses. This is consistent with the feedback processes regulating star formation: the star formation efficiency at low galaxy mass is hampered by stellar feedback (e.g., Dekel & Woo, 2003; Benson et al., 2003; Ceverino et al., 2014; Hopkins et al., 2014), as the first generations of stars can blow away most of the remaining gas during their lifetime, while massive galaxies host supermassive black holes suppressing star formation and thus explaining the drop in the galaxy mass function (e.g., Shankar et al., 2006; Croton et al., 2006; Bower et al., 2006; Somerville et al., 2008). Star formation and feedback processes from stars and AGNs shape the galaxy luminosity function and are crucial to explain the observed properties of galaxies.

[10]The *Sloan Digital Sky Survey* is a spectroscopic redshift survey started in 2000 which created the most detailed three dimensional map of the Universe ever made. It includes photometric observations of about 500 million astronomical objects, and spectra for more than 3 million of them.

Part One

The star formation efficiency at high-redshift

CHAPTER 2

Towards resolved Kennicutt Schmidt relations at high redshift

Star formation and the associated feedback mechanisms participate in shaping galaxies. But these processes are not set once and for all: they evolve with time across the history of the Universe. Indeed, our Milky Way only forms a few stars per year (Licquia & Newman, 2015), similarly to most nearby spiral galaxies, while observed galaxies ten billion years ago formed their stars at rates up to 20 times higher (Noeske et al., 2007; Daddi et al., 2007; Bouché et al., 2010; Lilly et al., 2013). Studying the evolution of the star formation rate (SFR) in the Universe is particularly important to better understand the formation and evolution of galaxies, and notably the complex phenomena occurring in the interstellar medium, the internal dynamics of galaxies, their interaction with their environment, and the feedback processes from stars and active galactic nuclei (AGN). As stars are formed from cold molecular gas, a high star formation rate means a significant gas supply: galaxies near the star formation peak are found to be much more gas-rich than local galaxies, with molecular gas fractions as high as 30-50% (Tacconi et al., 2010, 2013; Daddi et al., 2010a) when they only reach 7-10% in local giant spirals (Leroy et al., 2008; Saintonge et al., 2011a). The disks of such gas-rich galaxies are expected to be highly turbulent and gravitationally unstable, inducing the presence of giant gaseous clumps in which a significant part of the stars form (Elmegreen et al., 2008; Dekel et al., 2009b). Is the evolution of the cosmic star formation rate mostly driven by the available cold gas reservoir, or are the star formation processes in high redshift clumps qualitatively different than in their low redshift counterparts?

The Kennicutt-Schmidt (KS) relation between the molecular gas and star formation rate densities enables to characterize the star formation efficiency at low and high redshift (Schmidt, 1959; Kennicutt, 1998b). However, resolved measurements at the scale of the star-forming regions are still challenging at high redshift. Molecular gas observations carried out at the IRAM Plateau de Bure interferometer within the PHIBSS program (Tacconi, Combes et al.) permit us to study the star formation efficiency at sub-galactic scales around redshifts z=1.2 and 1.5 for a limited sample of galaxies, and thus help us characterize the star formation processes at the corresponding epoch. Our results lay in

the continuation of the resolved low redshift measurements, but further studies would be necessary to complement our sample and validate our conclusions.

After an introduction presenting the cosmic star formation history of the Universe and its characterization through the Kennicutt-Schmidt relation, this chapter mainly follows the article by Freundlich et al. (2013) *"Towards a resolved Kennicutt-Schmidt law at high redshift"*. This article aims at obtaining a Kennicutt-Schmidt relation for ensembles of clumps within a set of four galaxies at $z = 1.2$, taking advantage of the different kinematics of the clumps. Such a relation was also obtained on a pixel basis for another galaxy of the PHIBSS sample, which is the object of an article by Genzel et al. (2013), *"Phibss: Molecular Gas, Extinction, Star Formation, and Kinematics in the z = 1.5 Star-forming Galaxy EGS13011166"*. Some of its results are added to this chapter (section 2.3.3) for a more complete overview of the PHIBSS resolved measurements regarding the star formation efficiency.

Contents

Related publications and conference proceedings

- **Freundlich, J.**, Combes, F., Tacconi, L. J., Cooper, M. C., Genzel, R., Neri, R., Bolatto, A., Bournaud, F., Burkert, A., Cox, P., Davis, M., Förster Schreiber, N. M., Garcia-Burillo, S., Gracia-Carpio, J., Lutz, D., Naab, T., Newman, S., Sternberg, A., Weiner, B., 2013, A&A, 553, 130, *Towards a resolved Kennicutt-Schmidt law at high redshift*
- **Freundlich, J.**, Combes, F., Tacconi, L. J., Cooper, M. C., Genzel, R., Neri, R., 2013, SF2A Proceedings, 343-346, *Star formation efficiency at high z and subgalactic scales*

- Genzel, R., Tacconi, L. J., Kurk, J., Wuyts, S., Combes, F., **Freundlich, J.**, Bolatto, A., Cooper, M. C., Neri, R., Nordon, R., Bournaud, F., Burkert, A., Comerford, J., Cox, P., Davis, M., Förster Schreiber, N. M., García-Burillo, S., Gracia-Carpio, J., Lutz, D., Naab, T., Newman, S., Saintonge, A., Shapiro Griffin, K., Shapley, A., Sternberg, A., Weiner, B., 2013, ApJ, 773, 68, *Phibss: Molecular Gas, Extinction, Star Formation, and Kinematics in the z = 1.5 Star-forming Galaxy EGS13011166*

- **Freundlich, J.**, Salomé, P., Combes, F., Tacconi, L., Neri, R., Garcia-Burillo, S., Genzel, R., Contini, T., Lilly, S., 2014, SF2A Proceedings, 387-390, *High-redshift star formation efficiency as uncovered by the IRAM PHIBSS programs*

- Genzel, R., Tacconi, L. J., Lutz, D., Saintonge, A., Berta, S., Magnelli, B., Combes, F., García-Burillo, S., Neri, R., Bolatto, A., Contini, T., Lilly, S., Boissier, J., Boone, F., Bouché, N., Bournaud, F., Burkert, A., Carollo, M., Colina, L., Cooper, M. C., Cox, P., Feruglio, C. Förster Schreiber, N. M., **Freundlich, J.**, Gracia-Carpio, J., Juneau, S., Kovac, K., Lippa, M., Naab, T., Salomé, P., Renzini, A., Sternberg, A., Walter, F., Weiner, B., Weiss, A., Wuyts, S., 2015, accepted by ApJ, *Combined CO & Dust Scaling Relations of Depletion Time and Molecular Gas Fractions with Cosmic Time, Specific Star Formation Rate and Stellar Mass*

- **Freundlich, J.**, Combes, F., Tacconi, L., Cooper, M., Genzel, R., Neri, R., 2015, IAU General Assembly, Meeting 29, 2247399, *Resolved star formation relations at high redshift from the IRAM PHIBSS program*

2.1 Star formation processes across cosmic time

2.1.1 The cosmic star formation history

Global time evolution

It could be possible to reconstruct the history of the Milky Way and of its neighboring galaxies from what can be observed today, as archaeologists do with ancient history. Astronomical objects indeed bear traces of their past: for example, the Orion Nebula shown in Fig. 1.15 reveals the star-formation history of this specific region of the Milky Way, with young stars, ionized gas, and expanding outflow-driven shocks. But as the speed of light is constant, observing distant galaxies directly uncovers the past history of the Universe. Indeed, the further we look in space, the further we look back in time. This does not permit to reconstruct the time evolution of an individual galaxy, but it enables to follow their global evolution by averaging over the whole population of galaxies. Such a statistical approach ignores the specific history, morphology and environment of each galaxy in order to highlight the global trends. By doing so, it also avoids the selection bias that an individual observation would have. Studying the global evolution of star formation across cosmic time smooths out the particularities of individual galaxies and implicitly assumes that the SFR averaged over the whole population only depends on cosmic time. Different observations since the 1990s enabled to characterize the global evolution of the SFR, exploring higher and higher redshifts with different techniques and tracers.

Measuring the star formation rate

As individual stars are not resolved in all but the closest galaxies, the star formation activity has to be assessed from the overall light emitted by the galaxy or a subregion of the galaxy. Star formation tracers aim at selectively probing newly or recently formed stars. However, as short-lived stars are usually the most massive and as different stars do not contribute equally to the observed light, assessing the SFR requires an assumption on the specific mass distribution of the newly-formed stars in order to recover the whole stellar population and the total SFR. This distribution is given by the initial mass function (IMF), and different IMFs can be inferred from observations, such as the Salpeter (1955), Scalo (1986), Kroupa (2001, 2002) or Chabrier (2003) IMFs.

Very massive young stars of masses > 10 $M_\odot$ emit strong ionizing photons up to 10 Myr after the star formation burst. The Hα recombination line is the most traditional indicator of the resulting photoionized gas (Kennicutt, 1992, 1998a; Kennicutt & Evans, 2012). Indeed, an hydrogen atom looses its electron when ionized, and can emit an Hα photon of rest wavelength 656.28 nm when both particles recombine together and the electron cascades down from an excited energy level to the ground level of minimal

energy[1]. Different calibrations enable to calculate the SFR from the Hα line luminosity, and such a calibration was notably used by Gallego et al. (1995) to determine the SFR of a few hundred galaxies at redshift $\lesssim 0.05$. The collisionally excited [OII] line is less directly related to star formation but can also be empirically calibrated to trace the SFR (Kennicutt, 1998a). Early measurements using Hα or [OII] lines seemed to point towards an increase of the star formation activity between redshifts $z = 0$ and $z = 1$ (Songaila et al., 1994; Colless, 1995; Ellis et al., 1996; Cowie et al., 1996).

Young stars emit most of their light in the energetic ultraviolet (UV) domain, so the UV luminosity is also one of the main SFR tracers (Madau, 1997; Kennicutt, 1998a; Kennicutt & Evans, 2012; Loeb & Furlanetto, 2013; Madau & Dickinson, 2014). High-mass (> 5 M$_\odot$) main-sequence stars emit UV light over timescales of about 100-200 Myr, after which the UV luminosity fades quickly. It thus provides a good measure of the 'instantaneous' SFR on a 100-200 Myr timescale. Determining the SFR from the UV light is however particularly sensitive to interstellar reddening and extinction (e.g., Buat, 1992): interstellar dust and gas absorb and reemit blue light more than they do with red light, so stars appear redder than they are and their light is attenuated. This effect is analogous to atmospheric diffusion, which makes sunsets look red because of the thicker atmospheric layer the Sun's light has to cross when low in the horizon. Lilly et al. (1996) showed that the UV luminosity density averaged over a comoving volume decreased rapidly from $z = 1$ to $z = 0$, so that the SFR was about 15 times higher at $z = 1$ as compared to now. Similar measurements at even higher resdhifts hinted that star formation actually experienced a peak around $z = 1.5$ (Madau et al., 1996; Connolly et al., 1997).

In addition to emission lines and UV luminosity, other methods to determine the SFR include evolutionary synthesis models of galaxy colors, especially used in early times, infrared (IR) continuum light, or combinations of different methods. Emission lines such as Hα and [OII] are indeed also subject to extinction, which can lead to systematic errors in the SFR if not assessed properly. Interstellar dust absorbs mainly at UV wavelengths and re-emits in the IR between $10 - 300$ μm. As most UV radiation comes from star formation, the IR luminosity often results from dust-obscured star formation regions and can be used to trace dust-embedded star formation (e.g., Bell et al., 2005; Calzetti et al., 2007). However, AGNs also produce strong UV emission in dusty environments and old stellar populations can heat the interstellar dust, both potentially contributing to the total IR luminosity. Some tracers include a combination of UV and IR light in order to trace unobscured and obscured star formation at the same time (e.g., Wuyts et al., 2011a; Leroy et al., 2012). Radio emission can also measure the synchrotron radiation emitted by relativistic electrons produced in supernova remnants and hence trace the production rate of massive stars (> 8 M$_\odot$). As such stars are short-lived, their production rate can be used as a SFR tracer. In the absence of an X-ray emitting AGN, X-rays can also be used to trace star formation as young stellar populations also emit X-rays (e.g., Kennicutt & Evans, 2012).

[1]More precisely, the Hα photon is emitted when the electron transitions from the $n = 3$ to the $n = 2$ levels, with n being the principal radial quantum number of the atomic orbitals describing the hydrogen atom. The Hα line is one of the characteristic Balmer lines of atomic hydrogen.

A star formation peak

Adding to earlier measurements, more recent observations have enabled to get a fuller picture of the evolution of the cosmic SFR up to redshift ~ 8, i.e., up to less than a Gyr after the Big Bang (e.g., Giavalisco et al., 2004; Daddi et al., 2004; Reddy & Steidel, 2009; Bouwens et al., 2010, 2011, 2012a,b; Finkelstein et al., 2012; Madau & Dickinson, 2014). Fig. 2.1 from Madau & Dickinson (2014) compiles different measurements of the cosmic SFR density per comoving volume. It clearly shows a peak around redshift $z \sim 2$ and a subsequent decrease by about an order of magnitude. This decrease might seem sharp in redshift, but as redshift does not linearly depend on time, $z \sim 2$ already corresponds to a relatively early epoch in the history of the Universe, namely when it was about 3.5 Gyr. Observations beyond $z > 8$ confirm the decreasing trend at high redshift (e.g., Oesch et al., 2014). Given this cosmic star formation history, half of the stellar mass observed today was formed before $z = 1.3$, i.e., at least 9 Gyr ago. About 25% of the stellar mass was formed before the peak at $z > 2$, and another 25% after $z = 0.7$, so half of the stellar mass was formed during the peak epoch of star formation (Madau & Dickinson, 2014). Interestingly, the AGN activity has cosmic time evolution similar as that of the cosmic SFR (Madau & Dickinson, 2014).

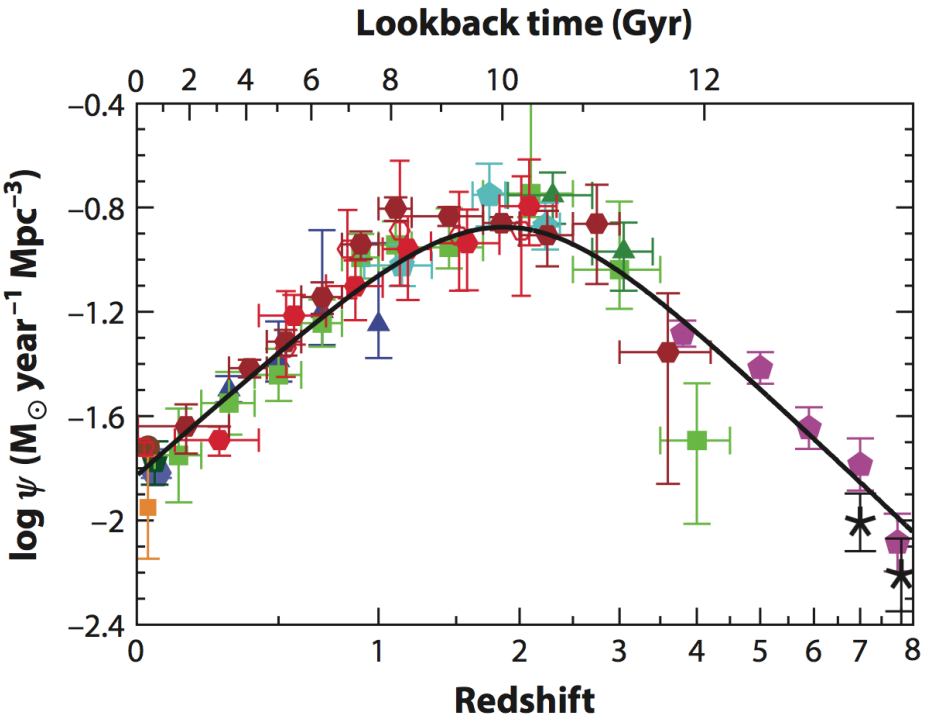

Figure 2.1 – *The cosmic star formation history up to resdhift $z \sim 8$, from Madau & Dickinson (2014). The data points come from different surveys and include UV and IR measurements. The IR measurements are in orange and red, while the other data points correspond to UV observations.*

The main sequence of star formation

The cosmic star formation history shown in Fig. 2.1 averages the SFR over the whole population of galaxies at each epoch. But the galaxy distribution is far from homogeneous. More precisely, there is a bimodality between blue star-forming galaxies on one side and red passive galaxies on the other (e.g., Baldry et al., 2004; Bell et al., 2005; Noeske et al., 2007; Elbaz et al., 2007; Daddi et al., 2007; Damen et al., 2009; Santini et al., 2009; Wuyts et al., 2011b). The color of a galaxy indeed relates to its stellar population and SFR, as young stars are typically bluer than old ones: the blue sequence corresponds to active star-forming galaxies with high SFR while red sequence galaxies have lower SFR or even stopped forming stars. This galaxy bimodality is also a bimodality in morphology, as the blue sequence corresponds to disk galaxies and the red sequence to ellipticals. Fig. 2.2 highlights this morphological difference by representing the galaxy distribution in the stellar mass - SFR plane in terms of Sérsic index. MS galaxies have Sérsic indexes close to 1 while red sequence galaxies have higher indexes. As shown in this figure, the bimodality holds at least from redshift $z = 0$ to $z \approx 2.5$, i.e., over the past 10 Gyr. The blue star-forming galaxies lie on a tight relationship between their stellar mass M_{star} and their SFR, the 'main sequence of star formation' (MS). About 90% of the cosmic star formation history since $z \lesssim 2.5$ took place near this MS (Rodighiero et al., 2011; Sargent et al., 2012). Coherently with the evolution of the global SFR shown in Fig. 2.1, the SFR on the MS drops by a factor ~ 20 from $z \sim 2$ to present time at any given stellar mass. Typical star-forming galaxies are expected to follow the MS until their star formation activity is quenched, and then to rapidly transit down to the red sequence (e.g., Bouché et al., 2010). This transition is still poorly understood.

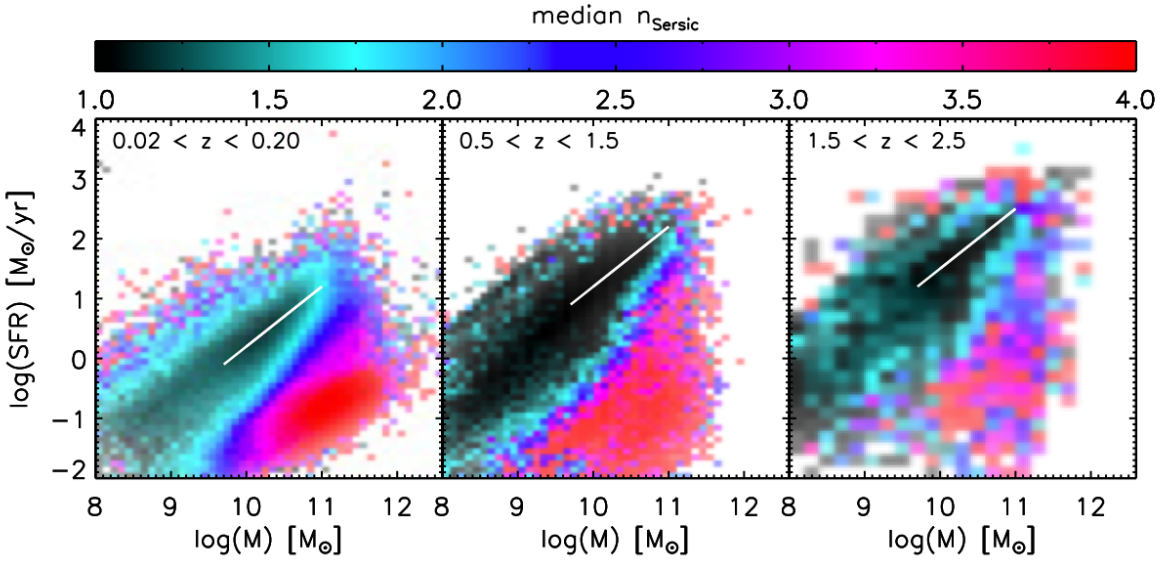

Figure 2.2 – *The main sequence of star formation shown in terms of Sérsic index in the stellar mass - SFR plane, from Wuyts et al. (2011b). A Sérsic index $n_{Sersic} = 1$ corresponds to an exponential disk, while the de Vaucouleurs (1948) profile with $n_{Sersic} = 4$ usually describes elliptical galaxies.*

The star formation peak and the subsequent decrease of the cosmic SFR was initially attributed to a period rich in major mergers of galaxies (e.g., Larson & Tinsley, 1978; Mihos & Hernquist, 1996; Elbaz & Cesarsky, 2003). However, the absence of classical bulges in a majority of galaxies today seem to indicate that most galaxies did not experience major mergers since $z = 4$ (Weinzirl et al., 2009). Long star formation cycles inferred from the number of star-forming galaxies observed between $z = 1 - 2$ (Daddi et al., 2005; Caputi et al., 2006; Daddi et al., 2007) also argue in favor of a more quiescent mode of star formation, as merger-induced starbursts would be short-lived and hence less numerous in the observed samples - unless mergers were very frequent. The tightness of the main sequence of star formation, with an rms scatter smaller than 0.3 dex, similarly seems to indicate that the evolution of the SFR is not driven by violent mergers but rather by a continuous replenishment of the gas reservoir, declining with time. Mergers would indeed yield a bigger scatter. The cold gas streams stemming from the cosmic web that feed galaxies (Birnboim & Dekel, 2003; Kereš et al., 2005; Dekel & Birnboim, 2006; Cattaneo et al., 2006; Ocvirk et al., 2008; Dekel et al., 2009a; Kereš et al., 2009) could provide such a steady gas supply and fuel the high SFR at the peak epoch of star formation without disturbing significantly the morphology of star-forming disk galaxies. In the 'bathtub' model (Bouché et al., 2010, cf. section 1.3.3, p. 38), the SFR is accordingly driven by the accretion rate. According to such a scenario, the small scatter in the main sequence would be associated with minor mergers or clumpy accretion (e.g., Dekel et al., 2009b). But many parameters other than the gas supply may intervene to account for the evolution of galaxies since then, from environmental effects, secular evolution and internal dynamics, feedback mechanisms from stars and AGNs, to the star formation efficiency itself (SFE = SFR/M_{gas}, where M_{gas} is the gaseous mass of the galaxy). This latter quantity has notably been shown to decrease significantly after $z = 1$ (Combes et al., 2011, 2013) and could thus contribute substantially to the evolution of the cosmic SFR. As stars form from cold molecular gas, the relationship between molecular gas and SFR densities characterizes the star formation efficiency.

2.1.2 The Kennicutt-Schmidt relation

A power law to describe the star formation efficiency

The SFR is an extensive variable which is a priori expected to grow with galaxy mass, others things being equal. The interest of an intensive quantity such as the star formation efficiency is that it enables to characterize the star formation processes irrespective of the size of the gaseous reservoir which is considered. As the quantity of stars that can form in a galaxy is determined by the amount of gas available, it is logical to assume that the SFR volume density ρ_{SFR} depends crucially on the gas density ρ_{gas}. The relationship between these two quantities can characterize the efficiency at which a galaxy transforms its gaseous reservoir into stars. Since Schmidt (1959), it is common to assume a simple power-law between the two quantities:

$$\rho_{SFR} \propto \left(\rho_{gas}\right)^n \tag{2.1}$$

where n is a characteristic exponent to be derived from observations. By comparing the distributions of atomic hydrogen and young stars in the Milky Way, Schmidt (1959) obtained an exponent $n \approx 2$.

However, astronomical observations yield surface densities instead of volume densities as all astronomical objects are projected in the plane of the sky. Hence, it is usually more common to consider surface densities and to assume a relation analogous to Eq. 2.1 between the SFR and gas mass surface densities $\Sigma_{\rm SFR}$ and $\Sigma_{\rm gas}$:

$$\Sigma_{\rm SFR} \propto \left(\Sigma_{\rm gas}\right)^N . \tag{2.2}$$

In the case of galaxies with constant thickness along the line of sight, the exponents n and N are equal. While Schmidt's measurements dealt with regions of the Milky Way, Kennicutt (1998b) showed that the SFR and gas surface densities of nearby galaxies were correlated through a power-law of exponent $N = 1.40 \pm 0.15$ over various orders of magnitude. His sample included 61 spiral galaxies and 36 starburst galaxies, whose data points can be seen Fig. 2.3. The scatter in the relation is relatively small, although the logarithmic scales tend to contract distances on the plot. This was not the first measurement of the kind outside of the Milky Way, but it bore a convincing statistical significance and was explicitly expressed in terms of SFR and gas mass. The previous measurements similarly yielded exponents between 0.9 and 3.5 (Sanduleak, 1969; Hartwick, 1971; Madore et al., 1974; Tosa & Hamajima, 1975; Hamajima & Tosa, 1975; Newton, 1980; Buat et al., 1989; Buat, 1992; Deharveng et al., 1994).

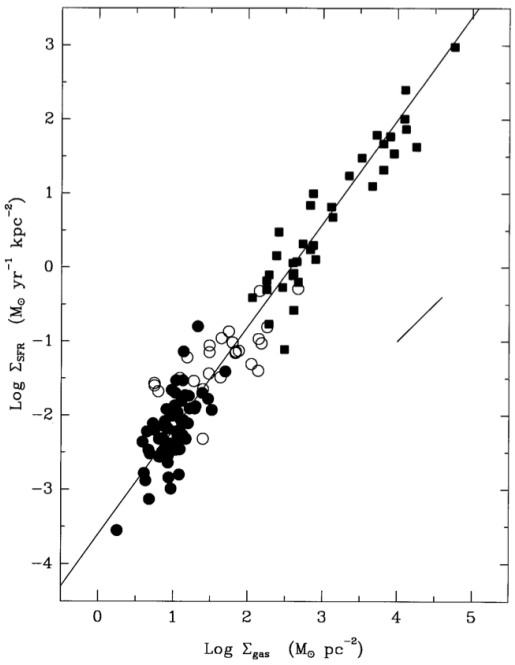

Figure 2.3 – *The Kennicutt-Schmidt law in nearby star-forming galaxies, from Kennicutt (1998b). The filled circles correspond to the 61 spiral galaxies of the sample, the empty circles to their central regions, and the black squares to the 36 starburst galaxies. The line corresponds to the best linear fit, with slope* $N = 1.40$.

The molecular KS relation at sub-galactic scales

Different studies refined the Kennicutt-Schmidt (KS) relation between the SFR and gas surface densities in nearby galaxies since Kennicutt's article, using different SFR tracers and notably targeting sub-galactic scales (Wong & Blitz, 2002; Boissier et al., 2003; Heyer et al., 2004; Misiriotis et al., 2006; Schuster et al., 2007; Crosthwaite & Turner, 2007; Kennicutt et al., 2007; Wyder et al., 2009; Bigiel et al., 2008; Heiderman et al., 2010; Schruba et al., 2011; Kennicutt & Evans, 2012; Leroy et al., 2013). These studies obtain exponents in a large range between 1 and 3 owing to different methodologies, in particular different SFR tracers and spatial resolution. Bigiel et al. (2008) derive a resolved KS relation on a pixel-by-pixel basis at a scale of about 750 parsecs and separate the atomic and molecular gas components. Fig. 2.5 shows the KS relations they obtain when considering solely the atomic gas surface density $\Sigma_{\rm HI}$, the molecular gas density $\Sigma_{\rm H2}$, and both. The linear correlation with the SFR surface density $\Sigma_{\rm SFR}$ is much better for the molecular gas, with an exponent $N = 1.0 \pm 0.2$, which confirms the crucial role of giant molecular clouds in the formation of stars. The striking correlation between the SFR and the molecular gas density can also be seen on the maps of the galaxies studied by Bigiel et al. (2008), as shown in Fig. 2.4.

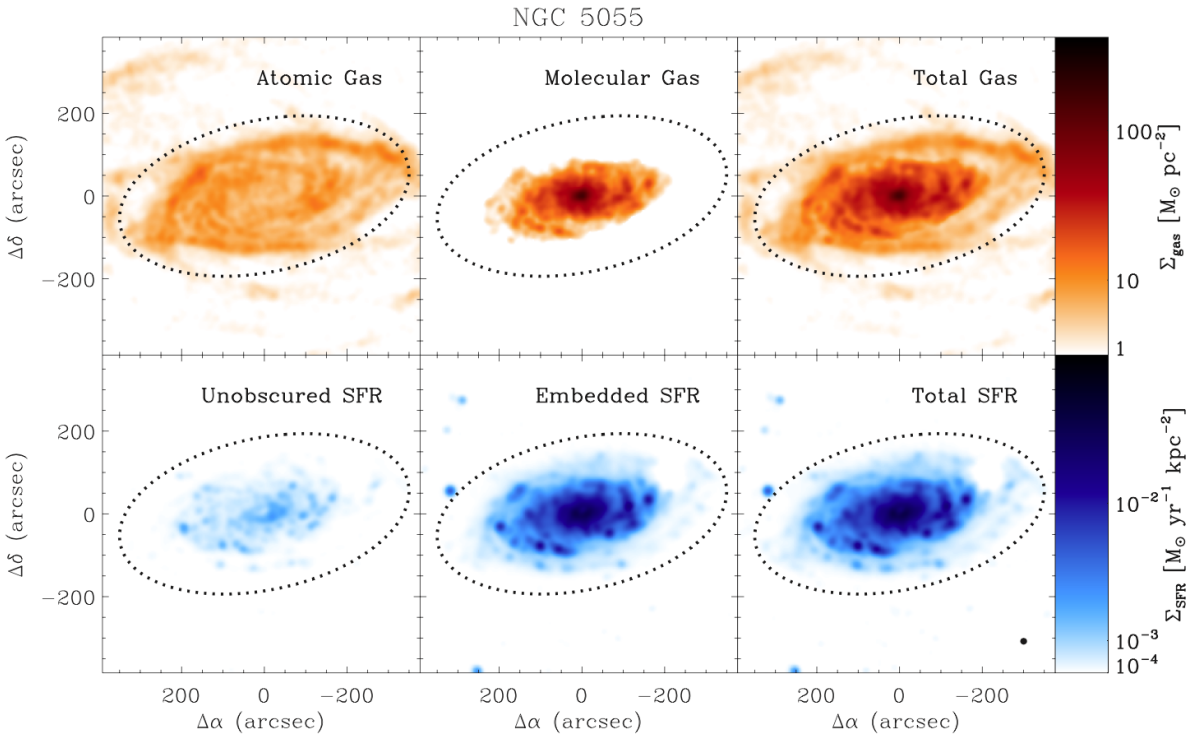

Figure 2.4 – *Maps of the atomic, molecular and total gas density along with the unobscured, dust-embdedded and total SFR in one of the galaxies studied by Bigiel et al. (2008), from Leroy et al. (2008). The atomic gas is traced through the 21-cm line of neutral hydrogen due to the hyperfine transition of the atom's ground energy level, while the molecular gas is traced by the carbon monoxide CO molecule. The SFR measurements combine UV data tracing unobscured star formation and IR data corresponding to dust-embedded star formation.*

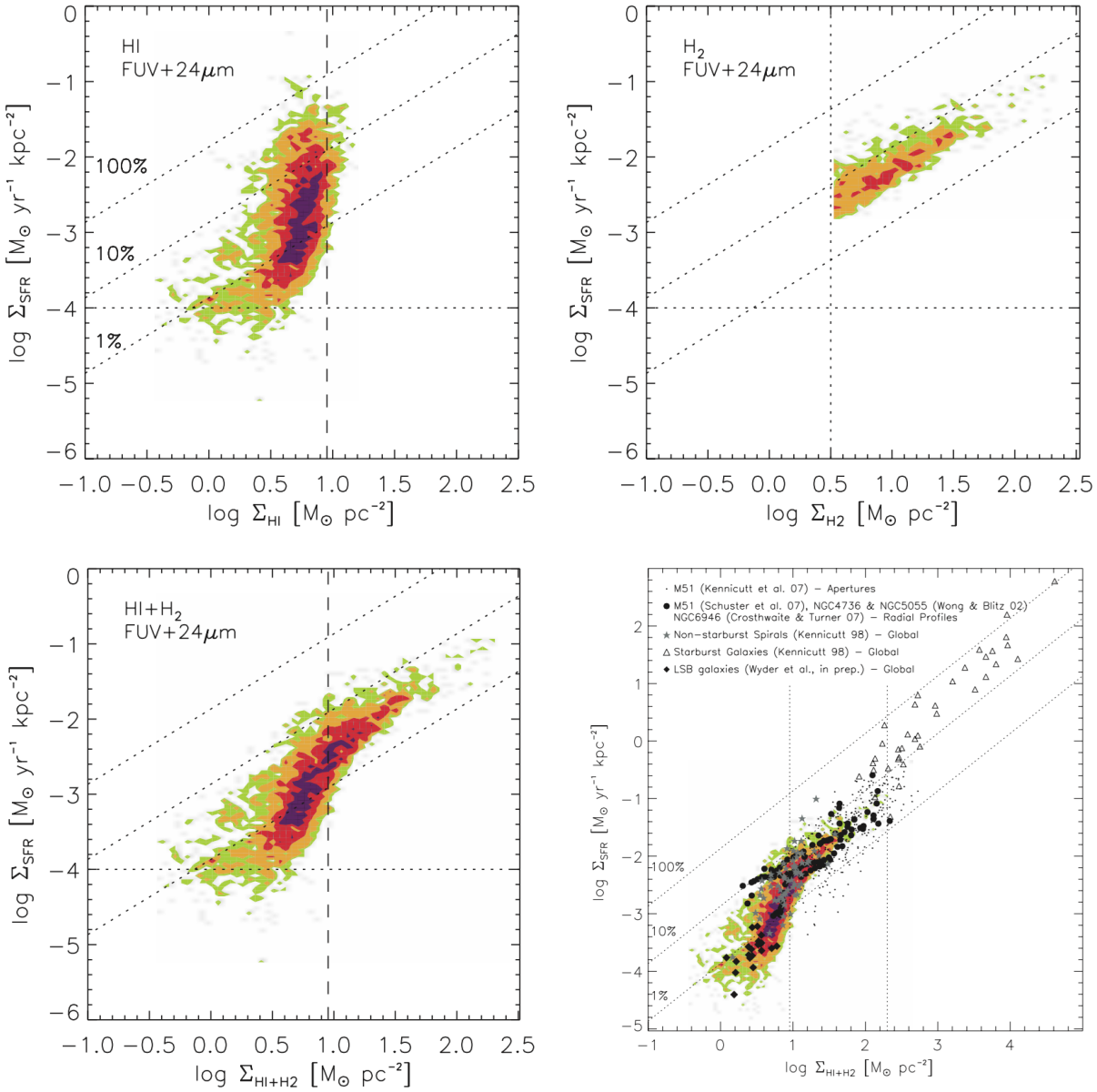

Figure 2.5 – *The resolved atomic and molecular Kennicutt-Schmidt relation from Bigiel et al. (2008). The color contours correspond to a pixel-by-pixel analysis of 18 nearby galaxies at a spatial resolution of 750 parsecs carried out by Bigiel et al. (2008) while the data points shown in the lower right panel correspond to earlier measurements in nearby galaxies. The upper left panel shows the KS relation in terms of the atomic gas surface density* $\Sigma_{\rm HI}$*, the upper right in terms of the molecular gas surface density* $\Sigma_{\rm H2}$*, the lower left is the combination of both, and the lower right adds other measurements to compare with. The diagonal dotted lines correspond from bottom to top to constant depletion times respectively equal to 10, 1 and 0.1 Gyr. The fraction of gas depleted to form stars in 0.1 Gyr along these lines would respectively be 1%, 10% and 100%. The best fit to the molecular data yield a constant depletion time of 2 Gyr.*

A linear relation between the SFR and molecular gas surface densities means a constant star formation efficiency, which can also be described in terms of depletion time. The depletion time is the inverse of the star formation efficiency, namely

$$\mathrm{t_{depl}} = \frac{1}{\mathrm{SFE}} = \frac{\mathrm{M_{gas}}}{\mathrm{SFR}}, \tag{2.3}$$

and corresponds to the time needed for a gas reservoir to turn all its gas into stars. The measurements by Bigiel et al. (2008) yield a constant depletion time of about 2 Gyr. The KS relation in terms of the total gas mass has an inflexion around a surface density of 9 $\mathrm{M_\odot pc^{-2}}$, which is the density at which atomic gas seems to saturate and above which the excess gas is found in the molecular phase. The scatter of about 0.2 dex in the KS relation allows some variability between a region and another, which could be explained by the different evolutionary stages of the molecular clouds (e.g., Lada et al., 2010; Lombardi et al., 2010; Zamora-Avilés et al., 2012; Zamora-Avilés & Vázquez-Semadeni, 2014; Utomo et al., 2015).

Theoretical arguments to justify the KS relation

Gravitational collapse. Different arguments can justify the observed values for the KS exponent N, and notably for values between 0.75 and 2 (e.g., Bigiel et al., 2008). Assuming that stars are formed from the gravitational collapse of a giant molecular cloud (GMC) can suggest to write that the SFR volume density is proportional to the gas density divided by the free-fall time $\mathrm{t_{ff}}$ (e.g., Madore, 1977; Krumholz et al., 2012),

$$\rho_{\mathrm{SFR}} \propto \frac{\rho_{\mathrm{gas}}}{\mathrm{t_{ff}}}. \tag{2.4}$$

As $\mathrm{t_{ff}} \propto 1/\sqrt{G\rho_{gas}}$ for the gaseous clump, it would yield $\rho_{\mathrm{SFR}} \propto \left(\rho_{\mathrm{gas}}\right)^{1.5}$. Consequently, if the gas line-of-sight scale height is constant,

$$\Sigma_{\mathrm{SFR}} \propto \left(\Sigma_{\mathrm{gas}}\right)^{1.5} \tag{2.5}$$

and the KS exponent should be around 1.5, which is relatively close to the initial measurements by Kennicutt (1998b).

Constant GMC surface densities. Instead of assuming constant scale heights, it is possible to use the fact that GMCs are observed to have constant surface densities (e.g., Solomon et al., 1987; Blitz et al., 2007). In this case, the GMC mass $\mathrm{M_{gas}} \propto \mathrm{R}^2$ with R the size of the cloud, or equivalently, $\mathrm{R} \propto \left(\mathrm{M_{gas}}\right)^{1/2}$. Consequently,

$$\rho_{\mathrm{gas}} \propto \frac{\mathrm{M_{gas}}}{\mathrm{R}^3} \propto \left(\mathrm{M_{gas}}\right)^{-1/2}. \tag{2.6}$$

Still considering that GMCs turn their gas into stars in a free-fall time would hence lead to

$$\mathrm{SFR} \propto \frac{\mathrm{M_{gas}}}{\mathrm{t_{ff}}} \propto \mathrm{M_{gas}}\sqrt{\rho_{gas}} \propto \left(\mathrm{M_{gas}}\right)^{0.75} \tag{2.7}$$

(Krumholz & McKee, 2005) so that when taking the surface densities, the KS exponent should be about 0.75.

Uniform GMC population. If we instead consider that all GMCs are similar and that the SFR only reflects the number of GMCs that are forming stars at the same rate, we would expect it to be simply proportional to the number of GMCs, i.e., to the total gas mass. In this case, the exponent would be $N \approx 1$.

Star formation as a collisional process. If we assume that star formation results from a collisional process, for example by considering that it depends on the formation rate of an H_2 molecule out of two hydrogen atoms or on the collision of two small gaseous clouds to form a bigger one, we would expect

$$\rho_{\mathrm{SFR}} \propto \left(\rho_{\mathrm{gas}}\right)^2 \tag{2.8}$$

so the KS exponent would be $N \approx 2$ for a system with constant line-of-sight scale height.

The role of previous star formation

The KS relation assumes that the SFR only depends on the mass of gas, through a simple power-law relation. Such a description necessarily smooths part of the complexity of the star formation processes at stake. For example, the free-fall time should theoretically not only depend on the gas mass, but also on the mass of stars that already formed. More generally, the presence of stars should significantly affect star formation. Indeed, stars release metals in the interstellar medium, which enhance star formation, but also generate powerful feedback mechanisms (cf. section 1.3.3, p. 36). In addition to the mass of gas, the SFR is thus expected to depend on different parameters such as the metallicity or the stellar mass (e.g., Mannucci et al., 2010), which leads to various 'extended' KS relations. For example, Shi et al. (2011) take into account the stellar surface density Σ_{stars} and model its influence on Σ_{SFR} as another power-law. Assuming that Σ_{SFR} is the product of two power-laws respectively implying Σ_{gas} and Σ_{stars}, they obtain the following fit:

$$\Sigma_{\mathrm{SFR}} \propto \left(\Sigma_{\mathrm{gas}}\right)^{1.13\pm0.05} \left(\Sigma_{\mathrm{stars}}\right)^{0.36\pm0.04}. \tag{2.9}$$

This modelisation enables to represent the contribution of the newly formed stars, which here seem to slightly enhance star formation. Shi et al. (2011) show that this relation holds over a few orders of magnitude in stellar surface density and can reproduce the MS of star formation when introduced in analytical models.

However, we will not focus here on such refinements of the KS relation and we will rather concentrate on its evolution with redshift in order to better understand the cosmic star formation history. Bigiel et al. (2008) showed that the molecular KS relation averaged at sub-galactic scales was linear at low redshift, yielding a constant depletion time of about 2 Gyr. Are the star formation processes qualitatively different at high redshift? More efficient? Does the KS relation varies with cosmic time?

2.1.3 Star formation at high redshift

Clumpy gas-rich galaxies

As stars are formed from cold molecular gas, the high SFR observed in high redshift galaxies require a significant gas content. Observations show that galaxies near the star formation peak are indeed much more gas rich than their low redshift counterparts, with gas amounting for about 30-50%, or even more, of all baryons at redshifts $z = 1 - 2$ (e.g., Erb et al., 2006; Daddi et al., 2010a; Tacconi et al., 2010, 2013). Tacconi et al. (2013) notably obtain mean gas fractions $f_{gas} = M_{gas}/\left(M_{gas} + M_{stars}\right)$ of 33% at $z = 1.2$ and 47% at $z = 2.2$, while gas only represents about 8% of all baryons at low redshift (Leroy et al., 2008; Saintonge et al., 2011a). The gas fraction is additionally shown to decrease with stellar mass, in accordance with feedback models in which the first generations of stars inhibit further star formation by removing part of the gas from the galaxy (e.g., Davé et al., 2011a). The extent of the molecular gas emission in high redshift galaxies is shown to be comparable with the optical emission from their stars (Tacconi et al., 2013), which suggests that these galaxies are in a steady equilibrium state in which they regularly form stars rather than out-of-equilibrium.

Most star-forming galaxies at high redshift are shown to be rotationnally supported disks (e.g., Förster Schreiber et al., 2006; Genzel et al., 2006; Stark et al., 2008; Förster Schreiber et al., 2009; Daddi et al., 2010a; Tacconi et al., 2010, 2013). Resolved galaxy kinematics indeed give access to the rotation curve of such galaxies and to their velocity dispersion. Fig. 2.6 displays the molecular gas map and the associated velocity and velocity dispersion maps of a typical massive, main sequence, star-forming galaxy at $z = 1.12$ (Tacconi et al., 2010). The molecular gas lies in an extended disk comparable in size to the stellar disk of the galaxy revealed in the Hubble Space Telescope (HST) image, while the velocity field clearly shows a gradient along one direction, as expected from a rotating disk. The rotation curve confirms this rotation and is well fitted by an exponential disk model. The figure also shows that the disk is relatively turbulent, as most star-forming galaxies at high redshift (e.g., Genzel et al., 2008; Law et al., 2009; Tacconi et al., 2010, 2013; Swinbank et al., 2011; Genzel et al., 2011, 2013). The ratio of rotational motion to velocity dispersion v_{rot}/σ is indeed about 5-7 in such galaxies (Tacconi et al., 2013), while it reaches 10-20 in their low redshift counterparts (e.g., Dib et al., 2006). Such a result is coherent with theoretical models and numerical simulations in which high redshift gas-rich disks fed by cosmological streams are expected to be turbulent and highly gravitationally unstable, leading to enhanced star formation: the peak epoch of star formation might be a period of 'violent disk instabilities' (Elmegreen et al., 2008; Dekel et al., 2009b; Bournaud et al., 2009; Agertz et al., 2009; Ceverino et al., 2010; Dobbs & Pringle, 2013).

Gas-rich disks have high gas surface densities and are thus more likely to be gravitationally unstable. They are indeed found to be fragmented into a number of giant gaseous clumps of diameter up to 2.5 kpc, where most of the star formation occurs (e.g., Cowie et al., 1995; van den Bergh et al., 1996; Elmegreen et al., 2004; Conselice et al.,

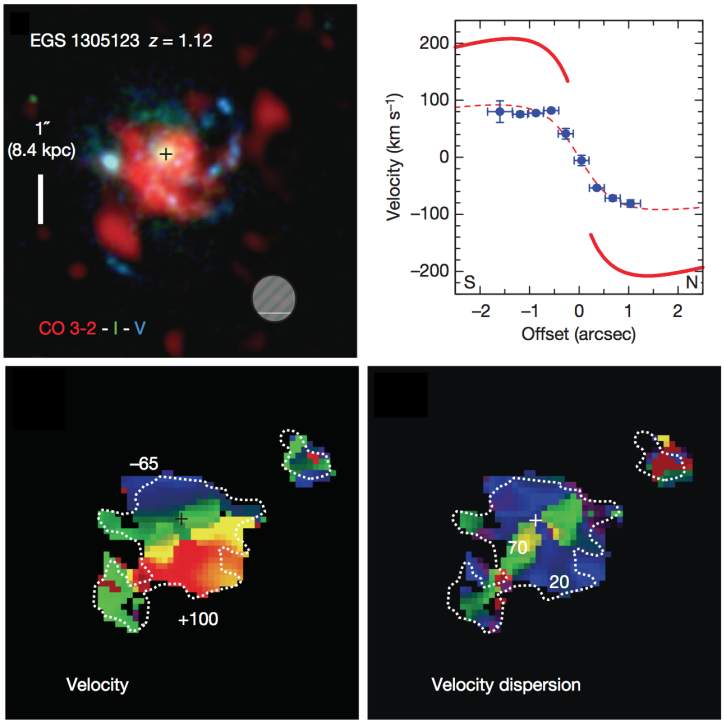

Figure 2.6 – *Molecular gas map and resolved kinematics for a massive star-forming galaxy at z=1.12, from Tacconi et al. (2010). The upper left panel superimposes the CO line luminosity tracing the molecular gas with a composite HST image, while the lower panels show the velocity and velocity dispersion maps derived from the CO observations. The velocity dispersion is derived by subtracting an exponential disk best-fit model to the velocity field. This model is shown on the upper right panel (dashed red line) displaying the rotation curve of the galaxy. An inclination of 27 ° has been assumed, so the intrinsic rotation curve (solid red line) has a wider span.*

2004; Elmegreen & Elmegreen, 2005; Förster Schreiber et al., 2006; Elmegreen et al., 2007; Kriek et al., 2009; Elmegreen et al., 2009; Förster Schreiber et al., 2009; Swinbank et al., 2010; Jones et al., 2010; Tacconi et al., 2010; Förster Schreiber et al., 2011; Genzel et al., 2011; Tacconi et al., 2013; Genzel et al., 2013). These clumps probably consist in loose ensembles of unresolved giant molecular clouds, and their added contribution to the total luminosity amount to 10-25% (Förster Schreiber et al., 2011). Fig. 2.7 shows six examples of such clumpy galaxies at high redshift. The star-forming complexes are found to have typical scales of about 1 kpc, masses up to 10^9 $M_\odot$, and they are responsible for about half of the star formation (e.g., Elmegreen et al., 2004; Elmegreen & Elmegreen, 2005; Elmegreen et al., 2009; Tacconi et al., 2010; Förster Schreiber et al., 2011; Genzel et al., 2011). Bound giant molecular gas complexes observed at low redshift are comparatively smaller, with masses between 1-6 10^7 $M_\odot$ and diameters around 500 parsecs (Rand & Kulkarni, 1990).

If they resist disruption by the feedback mechanisms resulting from star formation, the clumps are expected to interact, lose energy and angular momentum through dynamical friction, and migrate towards the center of the galaxy to form a bulge (Immeli et al., 2004;

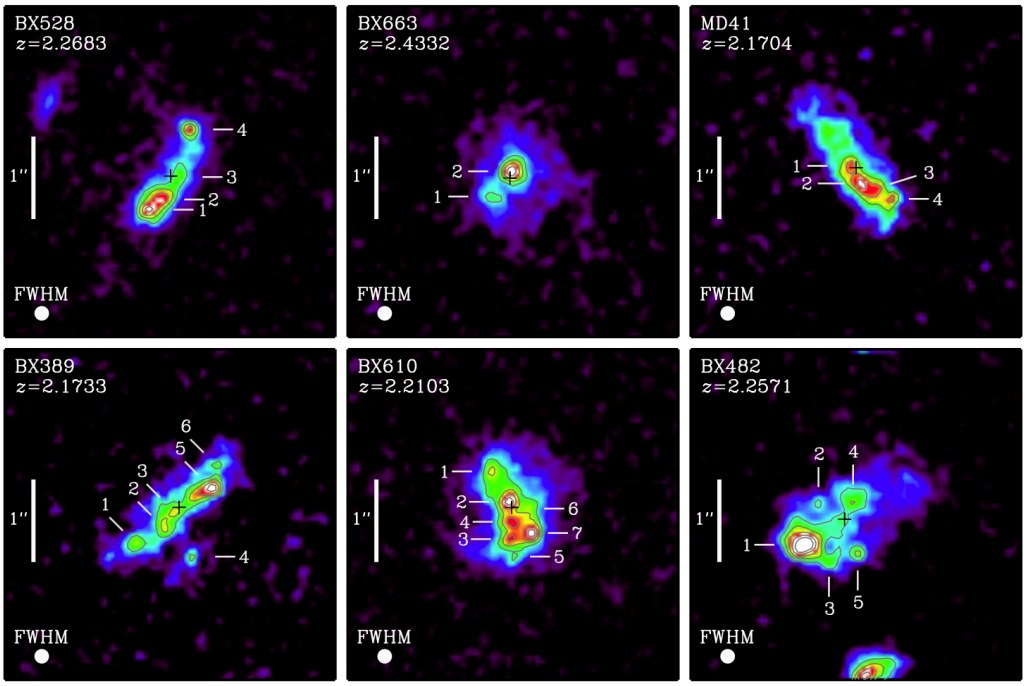

Figure 2.7 – *HST broad band images at* 5000 Å *of six clumpy galaxies at z = 2-2.5 from Förster Schreiber et al. (2011). Compact clumps are identified and numbered on the images. The angular scale of 1″ corresponds to about 8.4 kpc.*

Genzel et al., 2008; Bournaud et al., 2008; Dekel et al., 2009b; Dekel & Krumholz, 2013; Bournaud et al., 2014). Observations coherently find that older clumps are at smaller radii than younger ones (Förster Schreiber et al., 2011), but as bulgeless galaxies and tiny pseudobulges prevail in the local Universe (e.g., Kormendy et al., 2010), they might disrupt before reaching the center. Indeed, these clumps are expected to generate steady molecular gas outflows from the different feedback mechanisms (Dekel et al., 2009b; Genzel et al., 2011; Bournaud et al., 2014; Förster Schreiber et al., 2014). The fate of these clumps at the peak epoch of star formation and after is still poorly understood. More detailed observations of galaxies at intermediate redshifts, such as those proposed in an ongoing ALMA cycle 3 project (P.I.: Freundlich), would help understand the transition between thick turbulent disks to thinner disks stabilized by their stars, and help tackle issues like bulge growth, fragmentation, and the quenching of star formation.

The global KS relation at high redshift

In terms of star-formation efficiency, observations of the CO molecular gas have enabled to obtain galaxy-averaged KS relations for typical star-forming galaxies belonging to the massive tail of the MS at high redshift (e.g., Bouché et al., 2007; Daddi et al., 2010b; Genzel et al., 2010; Tacconi et al., 2013). At low redshift, the KS relation is shown to be near linear with constant depletion times between 0.5-3 Gyr and a scatter of about 0.3 dex (e.g., Leroy et al., 2008; Bigiel et al., 2008, 2011; Saintonge et al., 2011b). As shown in Fig. 2.8, the same linear trend is observed for galaxies from the PHIBSS sample

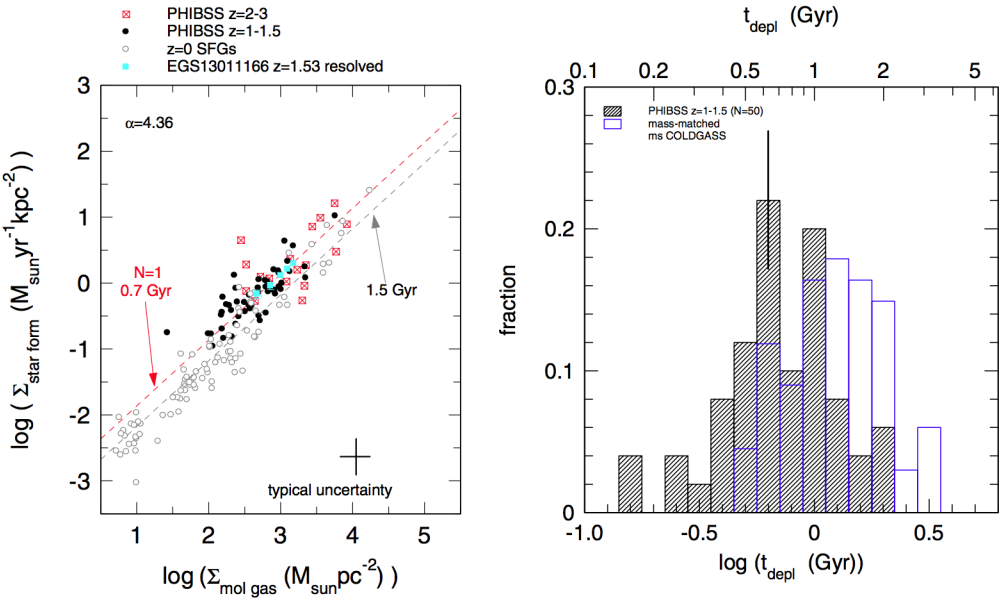

Figure 2.8 – *The near linear KS relation at high redshift and the distribution of depletion times from the PHIBSS sample (Tacconi et al., 2013). The PHIBSS z=1-3 measurements are compared to z=0 samples such as the COLDGASS sample (Saintonge et al., 2011a,b).*

at z=1-3 (Genzel et al., 2010; Tacconi et al., 2013). The high redshift measurements lie in continuity of the low redshift ones, and the depletion time only seems to vary slowly with redshift: star formation on the MS seems to be driven by the same physical processes across cosmic time. However, the mean depletion time of 0.7 Gyr observed in the PHIBSS sample at $z \sim 1$ is about half that a present time, suggesting that this quantity could vary with redshift as $t_{depl} \sim 1.5 \times (1+z)^{-1}$ Gyr and that the star formation efficiency could be proportional to $(1+z)$ (Tacconi et al., 2013). Genzel et al. (2015) further show that the depletion time of a galaxy varies according to its position relatively to the MS in terms of specific SFR (SSFR = SFR/M_{star}): galaxies with SSFR above the SSFR of the MS generally have smaller depletion times while galaxies with lower SSFR than on the MS have higher depletion times. As the depletion time is much smaller than the Hubble time (which is approximately the age of the Universe), there is in any case a need for gas replenishment to sustain star formation over cosmological timescales.

Towards a resolved KS relation at high-z with the PHIBSS program

The results by Tacconi et al. (2010, 2013) and Genzel et al. (2010, 2015) presented in the previous paragraph were carried out as part of the PHIBSS program. The Plateau de Bure High-z Blue Sequence Survey (PHIBSS) was an IRAM[2] Large Program (Tacconi, Combes et al.) which studied the molecular gas properties of star-forming galaxies on

[2]The *Institut de radioastronomie millimétrique* (IRAM) is a French-German-Spanish collaboration which operates two radiotelescopes and whose headquarters are situated in Grenoble, France. The two telescopes are the 30m single-dish telescope on Pico Veleta near Granada, Spain, and the Plateau de Bure interferometer in the French Alps.

the MS and aimed at better understanding the winding-down of star formation with a statistical sample of star-forming galaxies at high redshift. The IRAM Plateau de Bure interferometer indeed enables to observe the cold molecular gas through the CO rotational lines. At the time of the PHIBSS program, the interferometer consisted in six antennas, each of them being 15m wide. Since then, its NOEMA upgrade has increased the number of antennas, two of them being already at the Plateau de Bure and four more being planned: the full NOEMA project should in term double the number of antennas of the Plateau de Bure interferometer. The antennas are mounted on rails and can be as far as 760m from each other to achieve a maximum spatial resolution of about $0.4''$ (Winters & Neri, 2011). The main goals of the first PHIBSS program were to study the evolution with redshift of the molecular gas fraction f_{gas} and the star formation efficiency in normal MS star-forming galaxies, to characterize the dependence of these quantities on stellar mass and morphology in order to compare with feedback and quenching models, to examine the inner gas dynamics, and to probe the physical gas properties through multiple CO transitions. The program focused on the massive tail of the MS at $z = 1.2$ and 2.2, with $\log(M_{star}/M_{\odot}) \geqslant 10.4$ and $\log(SFR/M_{\odot}yr^{-1}) \geqslant 1.5$, and comprised 52 CO detections and 8 high-resolution imaging observations.

The PHIBSS program uncovered large molecular gas reservoirs at high redshift and participated in showing that typical star-forming galaxies in the distant Universe are turbulent rotating disks with a molecular gas distribution of the same size as the stellar distribution. In addition to the galaxy-averaged KS relation shown in Fig. 2.8, it showed that the cosmic evolution of the SSFR is mainly due to the diminishing gas fraction. The gas fraction was also shown to decrease with stellar mass, which is coherent with the picture in which massive galaxies are more quenched than others and in which part of their gas is removed due to stellar and AGN feedback mechanisms. Moreover, the vertical offset from the MS in the stellar mass - SFR plane seems to be mainly controlled by the molecular gas fraction (Tacconi et al., 2013).

Spatially resolved mapping of molecular gas and star formation in nearby disk galaxies has shown that the KS relation simplifies to a linear relation with a constant molecular gas depletion time of about 1-2 Gyr (Bigiel et al., 2008, 2011; Leroy et al., 2008, 2013; Schruba et al., 2011; Casasola et al., 2015). At high redshift, observations such as those by Genzel et al. (2010) and Tacconi et al. (2013) were able to obtain galaxy-averaged molecular KS relations in massive ($M_{star} > 3\ 10^{10}\ M_{\odot}$) main-sequence galaxies. But higher resolution observations are still challenging. How does the resolved KS relation, averaged over sub-galactic scales, vary with cosmic time? We present here a method to obtain the gas and SFR surface densities of ensembles of clumps within galaxies at $z = 1.2$ from the PHIBSS sample, and derive a KS relation spatially-resolved at a scale below the resolution limit of the IRAM Plateau de Bure measurements, namely below 8 kpc. This method rely on the rotating disk kinematics of star-forming galaxies at high redshift and is based on identifying the substructures in position-velocity diagrams corresponding to slices within the galaxies. This work is published in an article titled *"Towards a resolved Kennicutt-Schmidt law at high redshift"*, by Freundlich et al. (2013). Our results lie in the continuation of the resolved low redshift measurements, which seems to confirm the similar star formation processes at high and low redshifts, but further studies would be necessary to complement our sample and validate our conclusions.

2.2 A set of four galaxies from the PHIBSS sample

2.2.1 General characteristics and morphology

We use IRAM Plateau de Bure CO molecular gas observations from the PHIBSS survey (Genzel et al., 2010; Tacconi et al., 2010, 2013) and Keck DEEP2 optical and IR spectra (Newman et al., 2013) of four massive galaxies at redshift $z \sim 1.2$ in order to investigate the star formation efficiency within their clumps, or groups of clumps.

These galaxies were drawn from the All-wavelength Extended Groth strip International Survey (AEGIS), which provides deep imaging in all major wave bands from X-rays to radio, including Hubble Space Telescope (HST) images, and optical spectroscopy (DEEP2/Keck) over a large area of sky (Noeske et al., 2007; Davis et al., 2007; Cooper et al., 2011; Newman et al., 2013). They were further selected from the sample analyzed by Tacconi et al. (2010, 2013), which gathers non-major-merger, luminous, star-forming galaxies at $z\sim1.2$, with stellar masses $\gtrsim 3\ 10^{10}$ $M_\odot$ and SFR $\gtrsim 40$ $M_\odot$ yr^{-1}. These four galaxies - named EGS13003805, EGS13004291, EGS12007881, and EGS13019128 in the AEGIS terminology - belong to the massive end of the MS of star formation at $z\sim1.2$. Table 2.1 summarizes some of the general properties of these galaxies, while Fig. 2.9

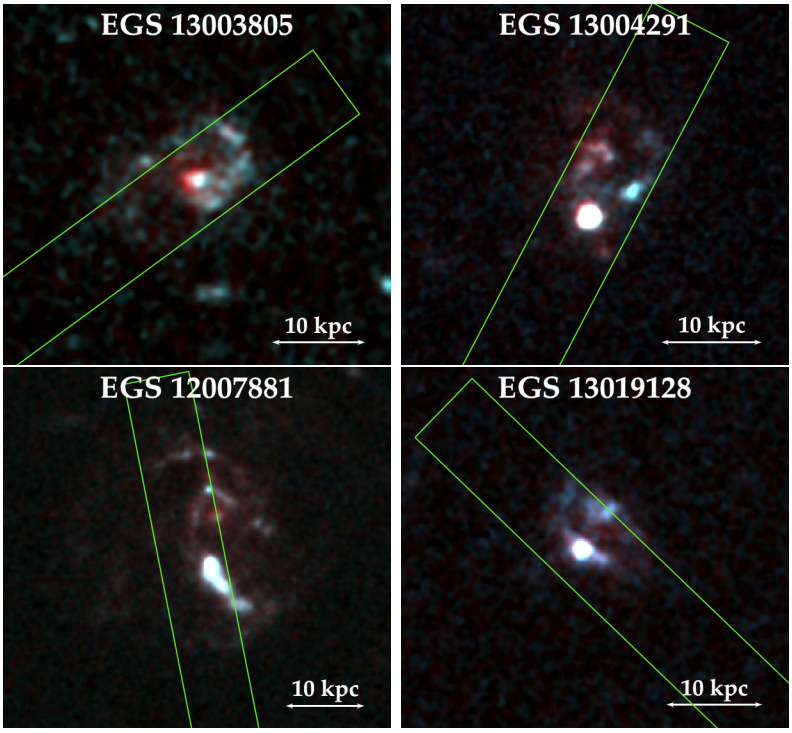

Figure 2.9 – *Composite HST images of the four galaxies of the sample, combining ACS I and V bands. The green box shows the DEEP2 slit used for each galaxy, whose size is indicated in Table 2.1. We assumed that the DEEP2 survey measured the position of the center of the galaxy more accurately than the HST, and shifted the HST image accordingly. North is up, east is left.*

Table 2.1 – *Global properties and observational details for the four galaxies of the sample.*

EGS identifier	13003805	13004291	12007881	13019128
z (1)	1.2318	1.19705	1.16105	1.3494
D_A [Mpc] (2)	1753.0	1745.3	1736.4	1772.8
D_L [Mpc] (2)	8731.5	8424.7	8108.8	9785.1
Scale [kpc/"]	8.50	8.46	8.42	8.60
DEEP2 slit size	$6.863'' \times 1''$	$5.149'' \times 1''$	$5.762'' \times 1''$	$10.343'' \times 1''$
DEEP2 slit orientation (PA)	$-53.858°$	$-27.649°$	$11.142°$	$46.142°$
IRAM CO(3-2) beam	$0.8'' \times 0.6''$	$0.6'' \times 0.5''$	$1.1'' \times 0.9''$	$1.6'' \times 1.4''$
$SFR_{[OII]}$ [$M_\odot yr^{-1}$] (3)	98	182	119	202
$SFR_{UV+24\mu m}$ [$M_\odot yr^{-1}$] (4)	200	630	94	87
$SFR_{[OII],B}$ [$M_\odot yr^{-1}$] (5)	63	231	265	213
M_{gas} [10^{11} $M_\odot$] (6)	2.2	2.8	1.3	1.2
M_{stars} [10^{11} $M_\odot$] (7)	3.4	5.0	5.0	3.8
f_{gas} (8)	0.39	0.36	0.21	0.24
$R_{1/2}$ [kpc] (9)	5.7	3.1	5.7	5.2
$\log_{10}(\Sigma_{gas}/[M_\odot pc^{-2}])$ (10)	3.03	3.67	2.80	2.86
$\log_{10}(\Sigma_{SFR}/[M_\odot yr^{-1} kpc^{-2}])$ (10)	-0.193	0.604	-0.095	0.204
$\log_{10}(\Sigma_{stars}/[M_\odot pc^{-2}])$ (10)	3.22	3.92	3.39	3.36
$A_{H\alpha}$ (11)	1.25	1.28	1.06	1.21
A_V (11)	1.56	1.60	1.30	1.50
$A_{[OII]}$ (11)	2.28	2.26	2.04	2.19
$A_{[OII]}/A_{H\alpha}$ (12)	1.82	1.77	1.92	1.81

Notes: (1) the redshift, as determined in the AEGIS catalogues from the [OII] line using DEEP2 spectra; (2) the angular distance D_A and the luminosity distance D_L; (3) the SFR from the [OII] line luminosity in the galaxy-integrated "1D" spectrum, obtained according to Kewley et al. (2004) calibration; (4) the extinction-corrected SFR obtained from 24 μm and UV continuum by Tacconi et al. (2013); (5) the SFR extrapolated from the empirical calibration of Moustakas et al. (2006); (6) the gas mass derived from the IRAM Plateau de Bure observations; (7) the total star mass obtained by SED fittings from CFHT B, R, and I bands photometric data using `kcorrect` (Blanton & Roweis, 2007), corrected for a Universe with $H_0 = 70$ km.s^{-1}.Mpc^{-1}; (8) the gas fraction $f_{gas} = M_{gas}/(M_{gas} + M_{stars})$; (9) the optical half light radius $R_{1/2}$ as indicated in Tacconi et al. (2013); (10) the surface densities associated to the gas mass, the SFR, and the star mass, calculated within $R_{1/2}$, for example as $\Sigma_{gas} = 0.5\ M_{gas}/\pi R_{1/2}^2$; (11) H$\alpha$, visible, and [OII] extinctions as derived from the `kcorrect` SED reconstruction ; and (12) the extinction ratio $A_{H\alpha}/A_{[OII]}$. A_V, $A_{[OII]}$, $A_{H\alpha}/A_{[OII]}$, $SFR_{24\mu m+UV}$ and $SFR_{[OII],B}$ are given for information only. O'Donnell (1994) predicts that $A_{H\alpha}/A_{[OII]}$ is around 1.86 for a diffuse interstellar medium, and the variations here observed from one galaxy to the other are representative of the quality of the `kcorrect` fit. The comparison between $SFR_{[OII]}$, $SFR_{24\mu m+UV}$, and $SFR_{[OII],B}$ gives an idea of the uncertainties in the SFR.

shows them in the I and V bands of the HST Advanced Camera for Surveys (ACS). To compute the physical distances, we adopt a cosmology with $\Omega_\Lambda = 0.73$, $\Omega_m = 0.27$, and $H_0 = 70$ km s^{-1}Mpc^{-1}. As expected for such high redshift MS galaxies, the four galaxies of the sample have clumpy features in the HST images, and they are less well ordered than low redshift Hubble Sequence galaxies.

2.2.2 Total molecular gas mass

CO as molecular gas tracer

Molecular hydrogen in the form of H_2 is the most abundant molecule in the Universe, playing a key role in all molecular processes and in star formation in particular. However, this molecule is highly symmetrical, without dipole moment, and is consequently difficult to observe directly from Earth (e.g., Habart et al., 2005). Indeed, its electronic transitions are in the UV domain, which is absorbed by the Earth's atmosphere, while its vibrational and rotational transitions are faint because of the absence of dipole moment. By contrast, a rotating dipolar molecule would emit electromagnetic radiations as any other oscillating electrical dipole. As carbon and oxygen are the most abundant elements after hydrogen and helium in the Universe, carbon monoxide CO is the second most abundant molecule after H_2, with an abundance between 10^{-5} and 10^{-4} relative to H_2 (e.g., Tielens, 2013). This asymmetric molecule with non-zero dipole moment is excited rotationally through collisions in the interstellar medium, and the resulting radiation can be observed. As most collisions are due to H_2 molecules, it provides a good tracer of molecular hydrogen in galaxies (e.g., Combes, 1991; Young & Scoville, 1991; Solomon & Barrett, 1991; Dame et al., 2001). Its rotational energy levels E_J are quantified, with

$$E_J = J(J+1)\frac{\hbar^2}{2I} \tag{2.10}$$

where J is the angular momentum quantum number and I the moment of inertia of the molecule. The frequency associated to the CO(1-0) transition, i.e., from the J=1 to the J=0 energy level, is for example 115.27 GHz, while it is 230.54 GHz for CO(2-1) and 345.80 GHz for CO(3-2). However, although CO is the most easily observed molecular line, the conversion factor between the CO luminosity and the H_2 mass is subject to uncertainties (e.g., Dickman et al., 1986; Solomon et al., 1987; Combes, 1991; Solomon et al., 1997).

Derivation of the total molecular mass

We use high resolution observations of the CO(3-2) transition shifted into the 2 mm band for $z\sim1.2$ sources carried at the IRAM Plateau de Bure, including its most extended 'A' configuration. The angular resolution obtained is between $0.5''$ and $1.5''$ for all galaxies (cf.

Table 2.1), corresponding to physical scales between 4 and 13 kpc. The CO luminosity associated to any region of flux can be expressed as

$$\left(\frac{\mathrm{L'_{CO}}}{\mathrm{K\ km\ s^{-1} pc^2}}\right) = \frac{3.25\times10^7}{(1+z)^3}\ \left(\frac{S_{\mathrm{CO}}\Delta V}{\mathrm{Jy\ km\ s^{-1}}}\right)\ \left(\frac{\nu_{obs}}{\mathrm{GHz}}\right)^{-2}\ \left(\frac{\mathrm{D_L}}{\mathrm{Mpc}}\right)^2 \tag{2.11}$$

where $S_{CO}\Delta V$ is the velocity integrated flux, ν_{obs} the observed frequency, and D_L the luminosity distance (Solomon et al., 1997). To derive H_2 masses, we follow the approach used by Tacconi et al. (2010). This assumes a Milky-Way-like conversion factor of $\alpha = 3.2\ \mathrm{M_\odot}\ (\mathrm{K\ km\ s^{-1}\ pc^2})^{-1}$ between the CO(1-0) luminosity and the H_2 mass, a factor 1.36 to account for interstellar helium, and a further correction by a factor 2 for the CO(3-2)/CO(1-0) luminosity ratio. The total gas masses of the four studied galaxies are indicated in Table 2.1.

2.2.3 The star formation rate

The Hα recombination line is the most direct and reliable tracer of young massive stars, and thus of the SFR (e.g., Kennicutt, 1998a). Since this line lies in the middle of a low atmospheric transmission band for the four galaxies considered here, ground-based Hα spectroscopy is impossible, and we estimate the SFR from the collisionally excited [OII] line (rest frame wavelength 3727 Å, shifted around 8200 Å for $z\sim1.2$ sources).

An empirical calibration from the [OII] line

Although the [OII] forbidden line luminosity is not directly associated to the ionizing luminosity, it is possible to establish it empirically as a quantitative SFR tracer. The Kennicutt (1998a) [OII] SFR calibration has been broadly used, but does not take reddening and metallicity into account. Here we use the calibration proposed by Kewley et al. (2004), which includes these two effects. The four galaxies studied here are particularly massive and should thus belong to the observed metallicity plateau at 12+log(O/H) = 9.07 (Mannucci et al., 2010). Assuming this metallicity for all galaxies, the Kewley et al. (2004) [OII] SFR calibration gives

$$\left(\frac{\mathrm{SFR}}{\mathrm{M_\odot yr^{-1}}}\right) \simeq 3.5\ 10^{-8}\ \left(\frac{\mathrm{L_{[OII]}}}{\mathrm{L_\odot}}\right) \tag{2.12}$$

where $L_{[OII]}$ is the intrinsic [OII] line luminosity. This calibration is expected to follow the reliable standard Kennicutt (1998a) Hα SFR calibration with a scatter of 0.03-0.05 dex (Kewley et al., 2004).

To determine $L_{[OII]}$, we use spectra provided by the Keck DEEP2 survey, obtained with the high spectral resolution DEIMOS spectrograph (Faber et al., 2003) and taken along slits with a typical size of $5'' \times 1''$. The data was reduced using a dedicated pipeline (Newman et al., 2013; Cooper et al., 2012), and a velocity resolution of about 50 km s^{-1} ($R = \lambda/\Delta\lambda \approx 5000$) enables resolving the [OII] line (Davis et al., 2003). DEEP2 spectra are not flux-calibrated, and we use CFHT I band magnitudes (CFH12K camera) to calibrate the galaxy-integrated "1D" spectrum (Coil et al., 2004).

Dust extinction

The value of $L_{[OII]}$ has to be corrected for dust extinction. The Galactic extinction is taken into account in the CFHT magnitudes, since they already include the dust corrections of Schlegel et al. (1998), but the dust present in the galaxies themselves is an even greater cause of extinction. Indeed, the observed flux in a given band X is attenuated by interstellar dust as

$$F_{obs}^X = F_0^X \ 10^{-0.4A_X} \tag{2.13}$$

where F_0^X is the intrinsic flux of the source and A_X the extinction in the considered band. In a potentially misleading way, the empirical Kennicutt (1998a) [OII] calibration has to be corrected from extinction at the Hα wavelength because it derives from an Hα calibration. On the contrary, the SFR calibration from Eq. 2.12 has to be corrected more straightforwardly from the $A_{[OII]}$ extinction at the [OII] wavelength (Kewley et al., 2004).

The dust distribution is derived from the spectral energy distribution (SED) of the galaxies, obtained from the B, R, and I band CFHT magnitudes with the `kcorrect` software developed by Blanton & Roweis (2007) (version `v4_2`). This software finds the best non-negative linear combination of a number of template star formation histories fitting the CFHT magnitudes. The templates are based on stellar population synthesis models, which enables the software to provide approximate physical quantities related to the star formation history. It notably provides SED curves with and without extinction, from which we can deduce the extinction $A_{[OII]}$ at the [OII] wavelength. Such an SED can be seen for one of the galaxies of the sample in Fig. 2.10.

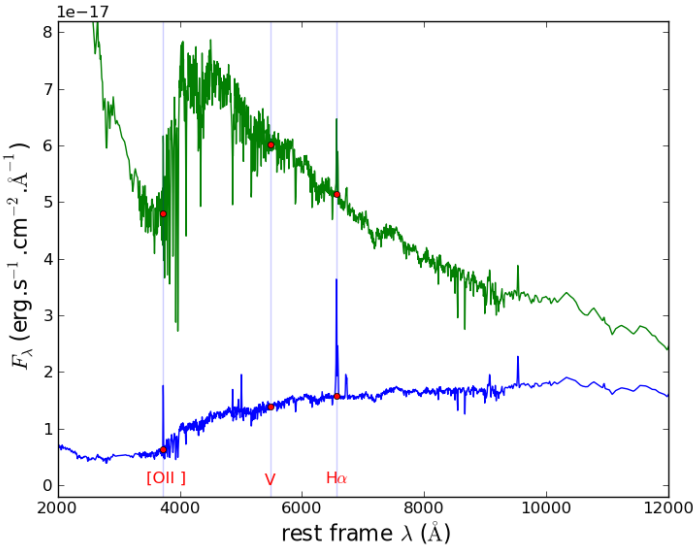

Figure 2.10 – *SED of EGS 13004291 with and without extinction as reconstituted by* `kcorrect` *(Blanton & Roweis, 2007) from CFHT B, R, and I band magnitudes. The intrinsic SED without extinction is on top (in green) while the dust attenuated SED is below (in blue).*

The values for $A_{[OII]}$ are indicated in Table 2.1, along with the visible extinction A_V and the extinction $A_{H\alpha}$ at Hα wavelength, obtained from the SED curves. The $A_{H\alpha}/A_{[OII]}$ ratio varies up to 10% from galaxy to galaxy but remains comparable to the value predicted by O'Donnell (1994) for a diffuse interstellar medium: $A_{H\alpha}/A_{[OII]} = 1.86$. Since this ratio should remain constant for the different galaxies, the variations give an idea of the quality of the `kcorrect` fit. The obtained extinctions are in approximate agreement with observations (e.g., Förster Schreiber et al., 2011), and the SFR deduced from the [OII] luminosity with this empirical calibration are given in Table 2.1 as $SFR_{[OII]}$.

Other determinations of the SFR

Moustakas et al. (2006) present an alternative empirical [OII] SFR calibration parametrized in terms of the B-band luminosity. This calibration is intended to remove, on average, the systematic effects of reddening and metallicity, as well as to reduce the scatter in the resulting SFR values.

The SFR of the four galaxies studied here were also determined from UV and IR luminosities by Tacconi et al. (2013). Because UV light directly traces unobscured star formation and IR 24 μm emission originates in small dust grains mainly heated by UV photons from young stars, the combination of the two is a sensitive tracer of the global SFR (Leroy et al., 2008, 2012). Tacconi et al. (2013) derive the global SFR of the four galaxies studied here from a combination of UV and Spitzer 24 μm luminosities with the methods of Wuyts et al. (2011b).

The SFR obtained through these two calibrations are given for information in Tables 2.1 and 2.2. The values differ up to 3σ between the three methods, which gives an idea of the uncertainty of the SFR measurements. Since it yields a lower standard deviation, we use the Kewley et al. (2004) calibration in our study. However, [OII] measurements may not reveal some dust-embedded star-forming regions, which probably explains the higher values of the SFR traced by UV and IR luminosities determined by Tacconi et al. (2013) for some of the galaxies.

SFR calibration	13003805	13004291	1200	7881	13019128
Kewley et al. (2004)	131	242		164	272
Moustakas et al. (2006)	63	231		265	213
Tacconi et al. (2013)	200	630		94	87

Table 2.2 – *SFR values from different calibrations, in* $M_\odot yr^{-1}$.

2.3 A resolved Kennicutt-Schmidt relation

2.3.1 Beating the resolution limit with the kinematics

The HST images shown in Figure 2.9 reveal kpc-sized clumps within diffuse regions, but these clumpy features ($\sim 0.1''$) are smoothed out at DEEP2 and IRAM resolutions, whose ranges are respectively $0.6 - 1.0''$ and $0.5 - 1.6''$. Spectroscopy, however, helps separate different components, thanks to their kinematics. Three galaxies of the sample have indeed been shown to be rotating disks while the last one, EGS 13004291, is a late-stage merger whose spectrum reveals substructures (Tacconi et al., 2013). DEEP2 spectra correspond to position-velocity diagrams (PV diagrams) along the galaxy major axis (Davis et al., 2007), and there is a good qualitative correspondence between the [OII] ionized gas structures observed in these diagrams and the CO molecular gas structures seen in the corresponding slices of the IRAM observations. The relative amplitudes in ionized and molecular gas may vary from one structure to another, but we are precisely interested in better understanding the interplay between the two components through the KS relation. Figures 2.11 and 2.12 compare the [OII] position-velocity diagrams with the corresponding slices in CO(3-2), both with the same $1''$ width. Smoothed $1''$-sized ensembles of clumps are separated by eye along the velocity axis of the PV diagrams in this pilot study. The characteristics of these ensembles are given in Table 2.3, and we aim at describing the star formation efficiency within them. We tried to compensate for the substructure separation by eye by taking all identifiable structures into account.

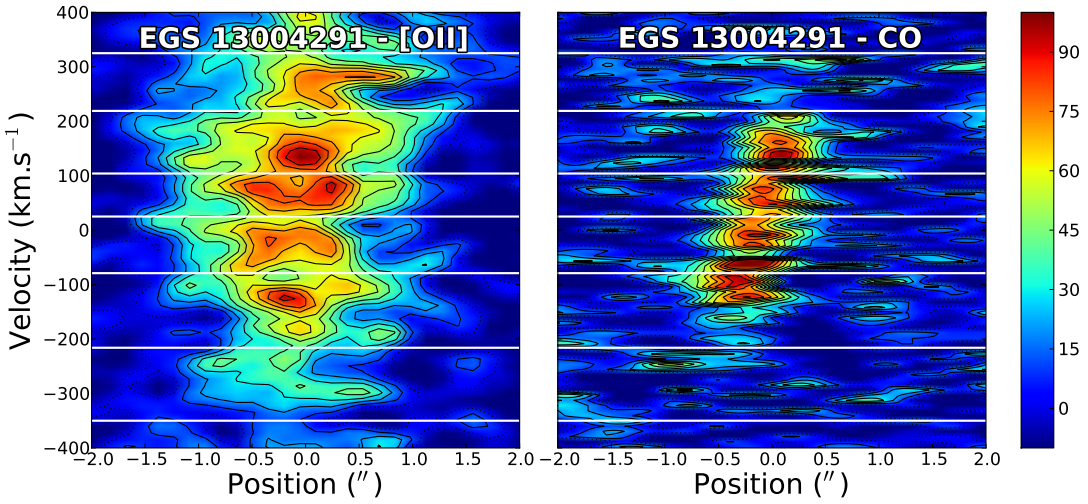

Figure 2.11 – *[OII] line and CO luminosities (respectively left and right panels for each galaxy) in position-velocity planes corresponding to the DEEP2 slit. Smoothed ensembles of clumps are separated by eye along the vertical axis, as shown with the white horizontal lines. The [OII] diagram was normalized in order to have fluxes proportional to the SFR, but all galaxies presented here and in Fig. 2.12 share the same arbitrary color scales. One arcsecond corresponds approximately to 8.5 kpc (cf. Table 2.1).*

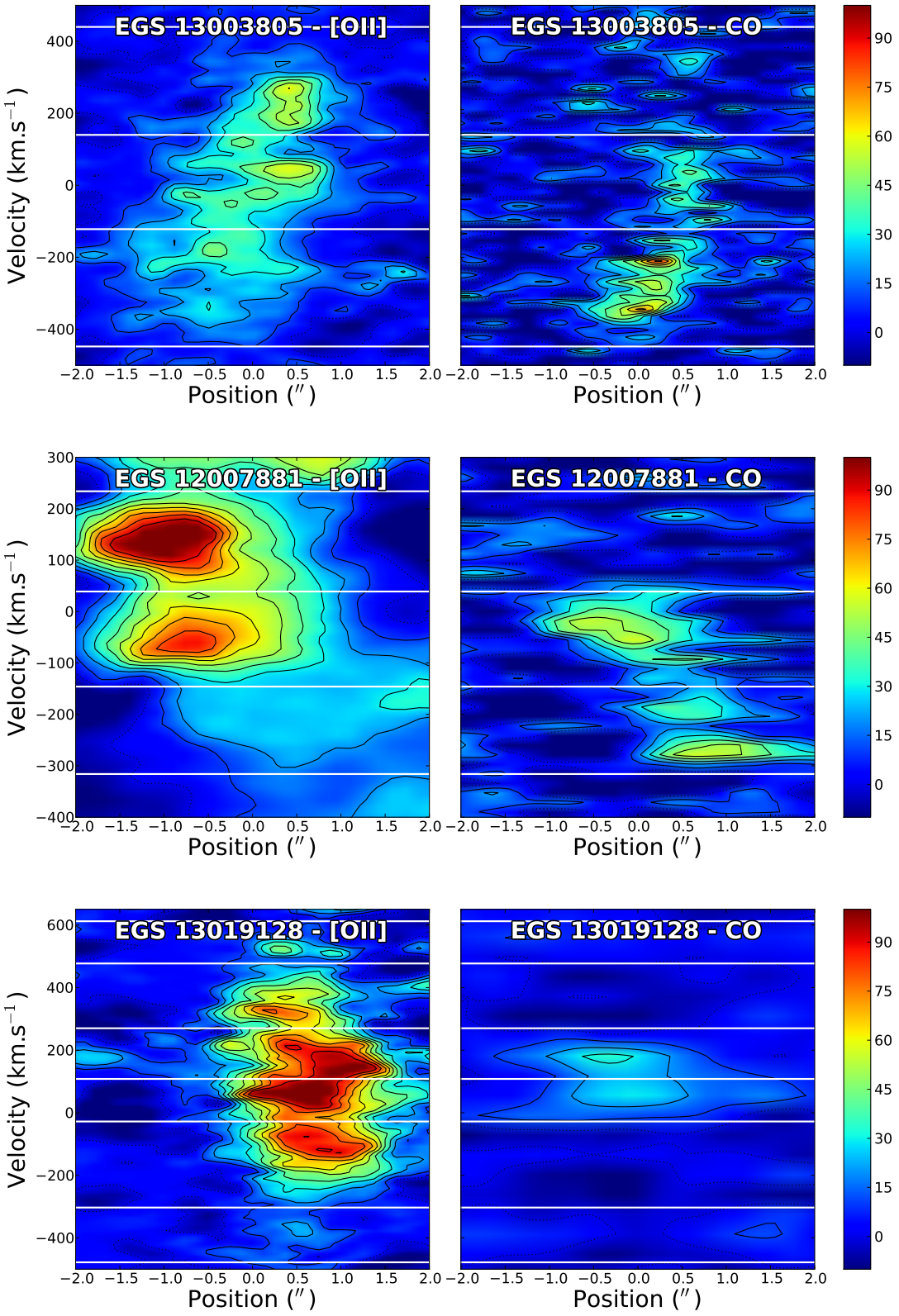

Figure 2.12 – *Continuation of Fig. 2.11 for the three other galaxies of the sample.*

Table 2.3 – *Some properties of the clumps of EGS 13004291 (A), EGS 13003805 (B), EGS 12007881 (C), and EGS 13019128 (D) obtained from measurements in the position-velocity diagrams.*

Clump	M_{gas} (1)	SFR (2)	$\log_{10}\left(\frac{\Sigma_{gas}}{M_\odot\ pc^{-2}}\right)$ (3)	$\log_{10}\left(\frac{\Sigma_{SFR}}{M_\odot\ yr^{-1}\ kpc^{-2}}\right)$ (3)	t_{depl} (4)	FWHM (5)
A-I	11.85	38.23	3.019	−0.473	3.10	0.93
A-II	6.92	34.75	2.785	−0.514	1.99	0.78
A-III	3.18	24.99	2.447	−0.657	1.27	0.63
B-I	2.37	11.37	2.324	−0.995	2.09	0.78
B-II	5.80	27.08	2.713	−0.618	2.14	0.64
B-III	7.75	26.16	2.838	−0.633	2.96	0.74
B-IV	4.96	23.92	2.644	−0.672	2.07	0.79
B-V	6.28	33.83	2.761	−0.522	1.92	0.61
B-VI	3.99	23.45	2.550	−0.681	1.70	1.1
C-I	5.33	25.38	2.680	−0.642	2.10	1.35
C-II	7.26	41.88	2.814	−0.425	1.73	1.36
C-III	1.41	51.05	2.10	−0.339	0.28	1.57
D-I	1.70	4.03	2.165	−1.460	4.22	0.83
D-II	0.58	57.23	1.697	−0.307	0.10	1.14
D-III	7.08	52.78	2.785	−0.342	1.34	1.67
D-IV	5.25	47.51	2.655	−0.388	1.10	1.60
D-V	0.78	32.32	1.828	−0.555	0.24	1.62
D-VI	2.60	5.89	2.351	−1.295	4.42	1.86

Notes: (1) the gas mass obtained as a fraction of the total mass of the galaxy from the CO position-velocity diagram, in units of 10^{10} $M_\odot$; (2) the SFR obtained similarly from the [OII] position-velocity diagram, normalized with the total SFR determined according to section 2.2.3, in $M_\odot$ yr^{-1} ; (3) the derived gas mass and SFR surface densities averaged over the same area of 1″ in diameter; (4) the depletion time $t_{depl} = M_{gas}/SFR$, in Gyr; and (5) the FWHM obtained from the IRAM position-velocity diagram with a Gaussian fit in the direction of the slice (for information only), in arcseconds. The FWHM roughly corresponds to the IRAM beam size, so we preferred to use the same 1″ size for all clumps in the different calculations. Using the FWHM instead of a constant 1″ diameter to calculate the surface densities gives a much larger scatter, but actually does not change the constant depletion time fit and the values of t_{depl}. The clumps are numbered from bottom to top according to the horizontal separation lines of Figure 2.11.

2.3.2 Depletion time and KS relation

From the CO and [OII] lines, we estimate the gas mass and the SFR contained in areas of 1″ in diameter (corresponding to the width of the slice and approximately to the size of the ensembles of clumps), and obtain the corresponding averaged surface densities, Σ_{gas} and Σ_{SFR}. As shown in Figure 2.13, the depletion time ($t_{depl} = M_{gas}/SFR$) is equal to 1.9 ± 0.3 Gyr, to be compared with results for samples of whole galaxies (2.1 Gyr at $z = 0$ in Kennicutt (1998a), 0.5-1.5 Gyr from $z \sim 2$ to $z \sim 0$ in Genzel et al. (2010), 1.05 ± 0.74 Gyr in Saintonge et al. (2011a), ∼0.7 Gyr at $z = 1 - 3$ in Tacconi et al. (2013)) and samples of subgalactic regions at low redshift (2.0 ± 0.8 Gyr in Bigiel et al.

(2008) and 2.35 Gyr in Bigiel et al. (2011)). The resulting KS diagram is displayed in Fig. 2.14. The data points scatter around the line of constant depletion time equal to 1.9 Gyr (such a line corresponding to a power law $\Sigma_{\rm SFR} \propto \Sigma_{\rm gas}^{N}$ of exponent N=1). However, the depletion time is locally very different from one data point to the other, suggesting that the star formation scaling laws are different from one ensemble of clumps to the next within a galaxy. The scatter is comparable to the ∼0.3 dex scatter observed for resolved local galaxies (Bigiel et al., 2008, 2011). The corresponding values obtained with the SFR from Tacconi et al. (2013) and through the B-band calibration of Moustakas et al. (2006) are indicated in Table 2.4, and give an idea of the uncertainties due to the SFR calibration method. Our sample is too incomplete to compute a best fit slope, but the method developed here could be applied to more high redshift galaxies.

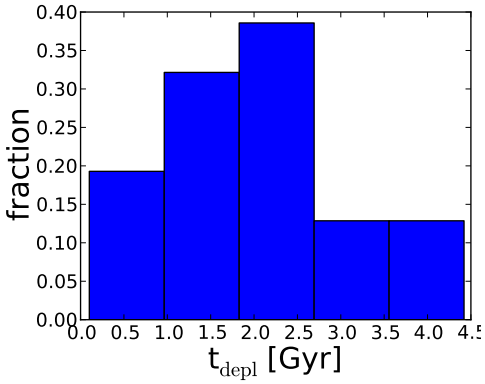

Figure 2.13 – *Distribution of the depletion time for the 16 regions identified in the four galaxies studied by Freundlich et al. (2013), using the Kewley et al. (2004) [OII] SFR calibration. The distribution has a mean of* $t_{\rm depl} = 1.9$ *Gyr and a standard deviation of 1.2 Gyr, for a median value of 2.0 Gyr. Since we identified 18 ensembles of clumps, the standard error of the mean is 0.3 Gyr.*

SFR calibration	Depletion time [Gyr]		
	mean	median	std. dev.
Kewley et al. (2004)	1.9	2.0	1.2
Tacconi et al. (2013)	2.1	0.7	2.9
Moustakas et al. (2006)	1.8	1.6	1.3

Table 2.4 – *Mean, median, and standard deviation of the depletion time of the clumps obtained through three different calibrations of the SFR: Kewley et al. (2004) [OII] calibration, UV+24μm calibration from Tacconi et al. (2013) and Moustakas et al. (2006) [OII] B-band calibration.*

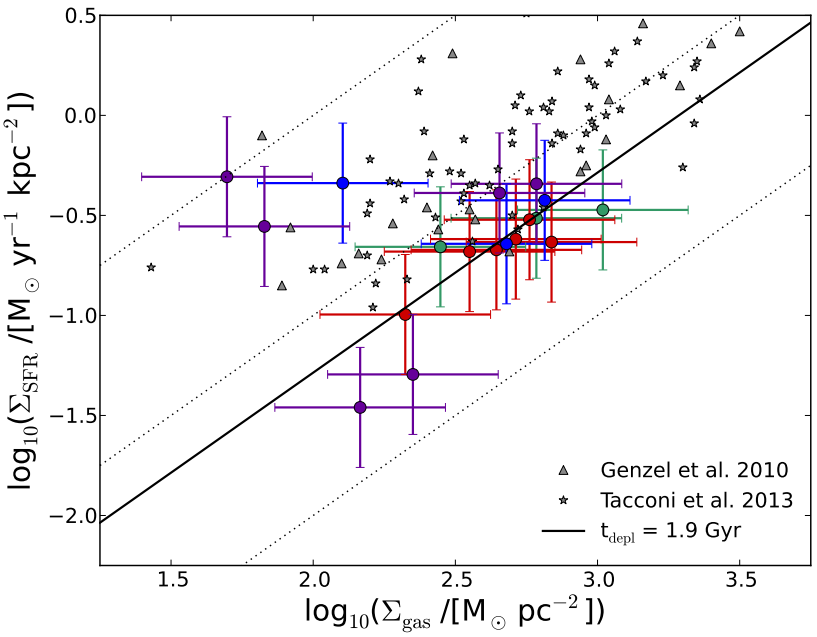

Figure 2.14 – *Molecular KS diagram for ensembles of clumps of EGS13003805 (green), EGS13004291 (red), EGS12007881 (blue), and EGS13019128 (purple), using the Kewley et al. (2004) [OII] SFR calibration. The dotted diagonal lines correspond to constant gas depletion times of 0.1, 1, and 10 Gyr from top to bottom, and the solid black line to a constant depletion time equal to the mean depletion time of the clumps,* $t_{\rm depl}$*=1.9 Gyr. The error bars of* 0.3 *dex yield a reduced* χ^2 *close to* 1 *and correspond to a factor 2 uncertainty, which is a lower estimate. The gray data points from Genzel et al. (2010) and Tacconi et al. (2013) are indicated for comparison with whole galaxies.*

2.3.3 The case of EGS 13011166

For one $z = 1.53$ massive star-forming galaxy of the PHIBSS sample, namely EGS 13011166, Genzel et al. (2013) further obtain a pixel-by-pixel molecular KS relation. They combine high-resolution IRAM Plateau de Bure observations of the CO molecular gas with Large Binocular Telescope (LBT) Hα spectroscopy and Hubble Space Telescope (HST) broad-band images to obtain the molecular gas and SFR distributions and kinematics as well as stellar and extinction maps. As shown on the left panel of Fig. 2.15, EGS 13011166 belongs to the massive end of the MS with $\log(M_{\rm star}) = 11.1$, slightly above the mean MS SFR. The HST image shown in the right panel of this figure reveals a highly clumpy morphology, with a dozen bright clumps of kpc size. The galaxy is shown to have a regular velocity field corresponding to a rotating disk, with a ratio between rotation and velocity dispersion $v_{\rm rot}/\sigma \approx 6$, further indicating a turbulent medium. Broad-band emission in Hα might indicate the presence of outflows of velocity ~ 600 km s^{-1}, as would be expected from stellar feedback mechanisms.

The HST broad-band images and SED fitting enable to derive extinction maps of the galaxy. Correcting the Hα distribution pixel-by-pixel with these extinction maps yields a resolved molecular KS relation at a spatial resolution of about 6 kpc, corresponding to the IRAM Plateau de Bure and LBT resolutions. The relation is plotted in Fig. 2.16

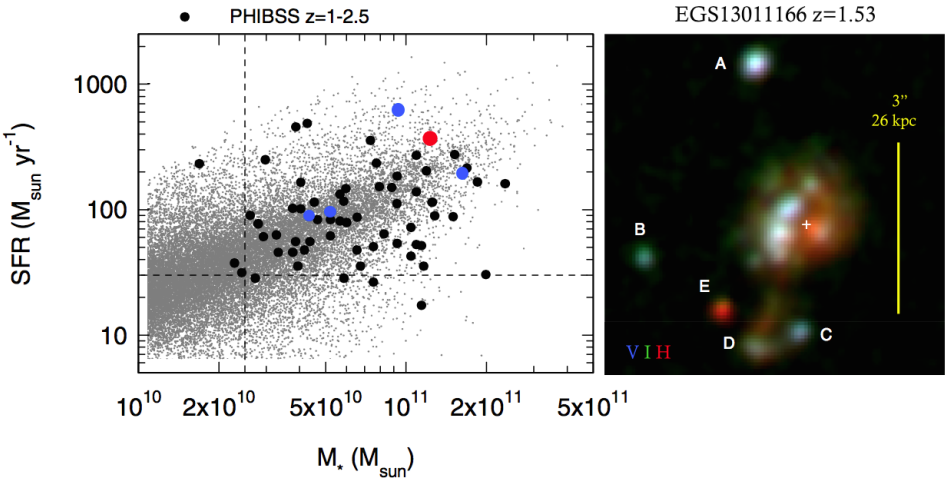

Figure 2.15 – *Position in the stellar mass - SFR plane (left) and composite HST image (right) of EGS 13011166 (Genzel et al., 2013). The filled circles in the left panel indicate the other galaxies from the PHIBSS sample (Tacconi et al., 2013) for comparison, EGS 13011166 being indicated in red and the four galaxies studied by Freundlich et al. (2013) in blue.*

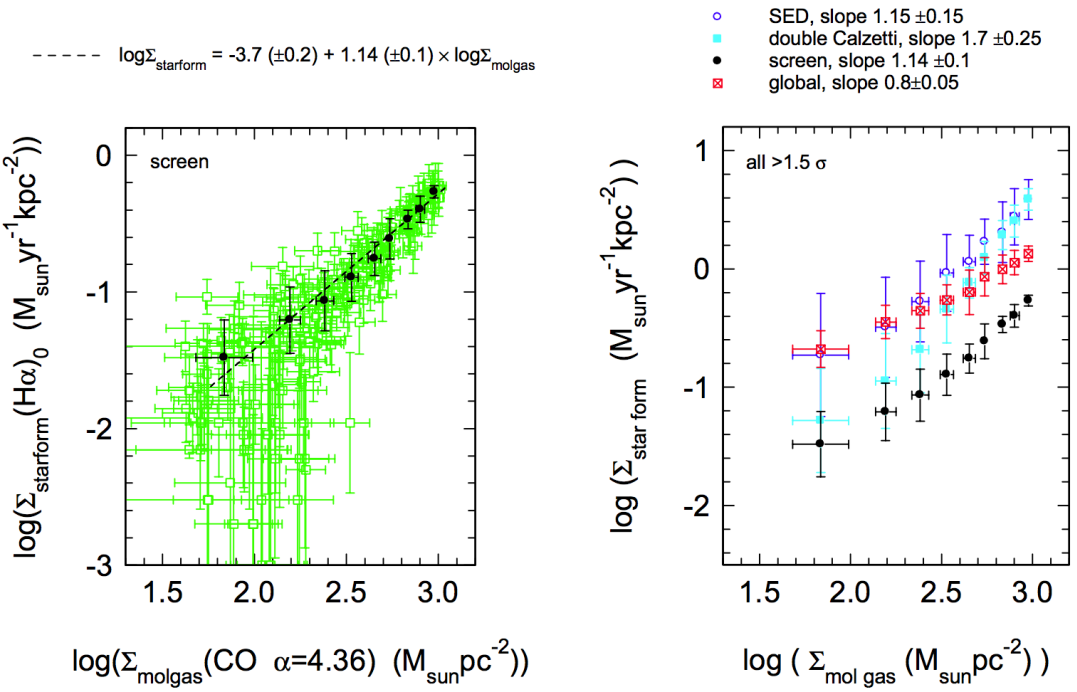

Figure 2.16 – *Spatially resolved molecular KS relation in EGS 13011166, from Genzel et al. (2013). The left panel displays the pixel-by-pixel measurements with a resolved 'screen' extinction correction (Calzetti et al., 2000) in green and binned medians over groups of 10-30 pixels in black. The right panel compares different extinction correction models. In particular, the resolved extinction correction plotted on the left panel is indicated in black, while the red points correspond to a unique extinction correction for the whole galaxy.*

and yields a KS exponent N = 1 − 1.5, which is broadly consistent with low redshift measurements. However, as displayed on the right panel of the figure, Genzel et al. (2013) also show that the shape and the slope of the KS relation depend strongly on the extinction correction that is applied: using resolved extinction maps instead of a single value for the whole galaxy significantly changes the depletion times that are obtained from sub-galactic observations.

2.4 Discussion and perspectives

2.4.1 Advantages of the method

Beating the resolution limit

In this pilot study, we have shown how various ensembles of clumps could be separated by their kinematics in PV diagrams, even though the angular resolution of molecular gas and SFR data was not able to separate them in integrated intensity. As such, a KS diagram can be obtained within regions below the resolution size ($\sim 1''$).

Direct observations

Previous resolved KS work at high redshift was only obtained using serendipitous amplification by gravitational lenses. Decarli et al. (2012) carried out one of the first spatially resolved studies in high redshift galaxies, using [NII], FIR, and CO observations for two gravitationally lensed $z \sim 3.9$ galaxies. They obtain a steep relation of slope N = 1.4±0.2 between the dust continuum and the molecular gas surface brightness. Strong lenses are rare, and determination of the clumps physical parameters depend on the lensing model. Our method is probably more appropriate for a systematic study of the star formation at high redshift, until higher resolution instruments resolve the clumps.

In the absence of high resolution molecular gas data, (Swinbank et al., 2010) notably report adaptive optics Hα observations of eleven kpc-scale star-forming regions identified in $z = 0.84 - 2.23$ galaxies and measure the velocity dispersion of the ionized gas σ and the star formation surface density $\Sigma_{\rm SFR}$. By assuming that σ also corresponds to the dispersion of the cold clumps and that the clumps are marginally stable with a Toomre parameter $Q \simeq 1$, they claim a correlation between the gas surface density $\Sigma_{\rm gas}$ and $\Sigma_{\rm SFR}$. But the method is highly indirect, relies on many assumptions, and underestimates beam-smearing effects in the determination of σ.

2.4.2 Biases and uncertainties

Selection bias

The four galaxies studied here are particularly luminous and were selected from a sample Tacconi et al. (2010) with stellar masses and star formation rates that are respectively higher than 3. 10^{10} $M_\odot$ and 40 $M_\odot$ yr^{-1}. A high luminosity was also needed to visualize and isolate the clumps in the PV diagrams, so this method is intrinsically biased towards massive galaxies.

Separating substructures in PV diagrams

In this pilot study involving only four galaxies, we separated substructures by eye on the PV diagrams. A more systematic method to separate substructures, or just a pixel-by-pixel analysis would probably be more relevant with bigger samples. We also assumed that the luminosities associated to the substructures were proportional to the integrated luminosity in the PV diagrams, which is a significant assumption in itself.

Uncertainties from the SFR and CO calibrations

The main uncertainties for estimating gas and SFR surface densities come from the SFR calibration and from the values used for $\alpha = M_{H_2}/L'_{CO}$, for the CO(3-2)/CO(1-0) luminosity ratio, and for the extinction $A_{[OII]}$. These quantities could vary significantly from one galaxy to another and within each galaxy, thus increasing the scatter and the uncertainty of our measurements. For example, the CO(3-2) transition is less directly related to the molecular gas mass than the CO(1-0), and variations in the CO luminosity ratios as high as of a factor $\sim$2 can be observed within a single galaxy (e.g., Koda et al., 2012). Significant variations in extinction values from one substructure to another within each galaxy are also expected, as observed in local galaxies (e.g., Scoville et al., 2001) and high redshift galaxies. Genzel et al. (2013) notably uses the CO(3-2) and Hα lines, as well as HST multiband images of a high redshift galaxy belonging to the same sample as ours to show that the methodology used to correct for extinction has a certain influence on the shape of the KS relation, especially on its slope. We thus expect that using a resolved extinction map instead of a single value would significantly change the depletion time we obtain. Nevertheless, identifying the ensembles of clumps in PV diagrams and the low spatial resolution of the [OII] and CO measurements prevent us from finding the corresponding structures in two-dimensional images and deriving extinction maps for our ensembles of clumps. As seen in section 2.2.3, the values of the SFR are highly dependent on the calibration and, since the scatter in the observed [OII]/Hα flux ratio is always higher than 32% (Moustakas et al., 2006), this remains a lower limit of the uncertainty in the SFR determined from [OII]. We expect our final values for the mass of gas and the SFR to be determined with uncertainty factors at least as high as 2 or 3.

2.4.3 Comparison with low redshift observations

The resolved molecular KS relations obtained by Freundlich et al. (2013) and Genzel et al. (2013) for high redshift galaxies within the PHIBSS sample can be plotted against those at low redshift, as shown in Fig. 2.17 (Freundlich et al., 2014b). Our results, as well as most other high redshift observations (e.g., Genzel et al., 2010; Tacconi et al., 2010, 2013; Decarli et al., 2012; Swinbank et al., 2012), indicate that the star formation scaling law between SFR and gas surface densities is not significantly different at high redshift than in the local Universe. Indeed, our limited sample of five galaxies at $z = 1.2$ and $z = 1.5$ is compatible with a constant depletion time of about 1.9 Gyr, which is of the same order of magnitude as measurements at lower redshift. This adds to the growing evidence that the star formation processes ten billion years ago were similar to the ones that are observed in the local Universe.

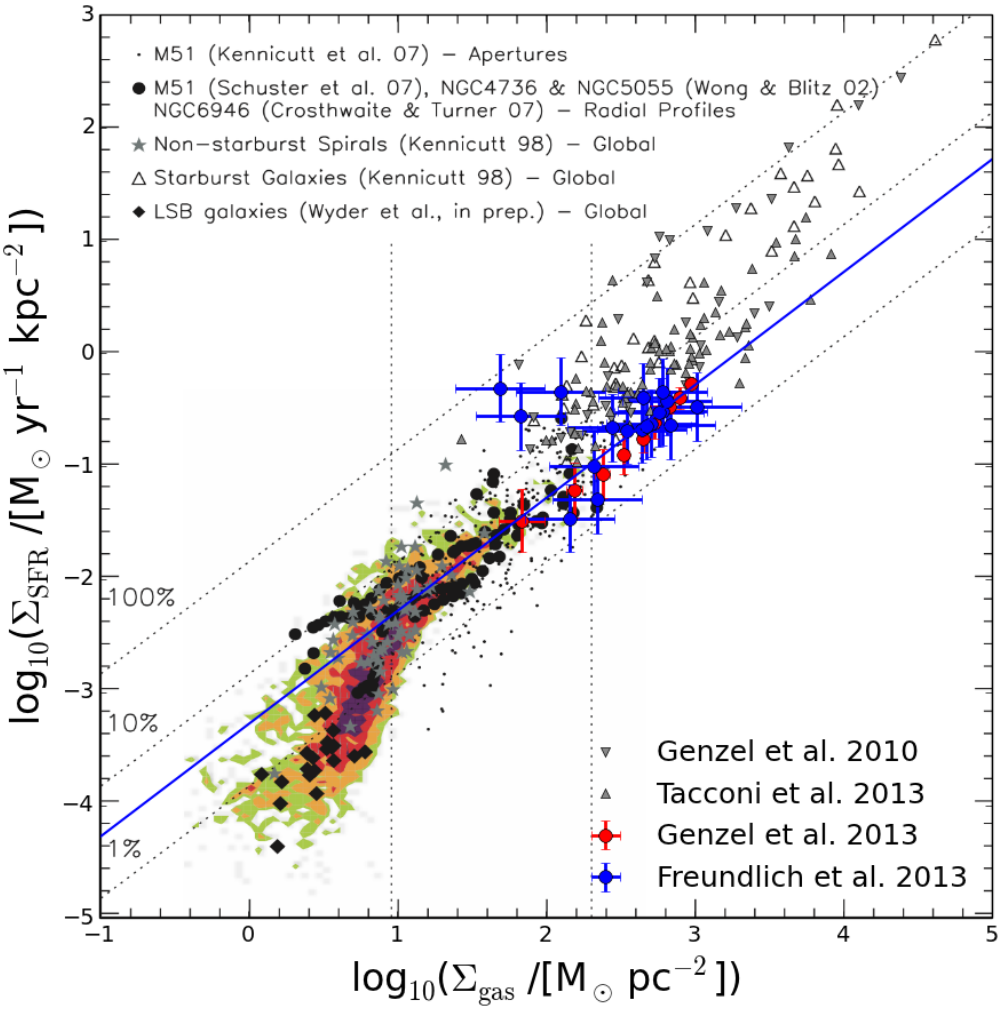

Figure 2.17 – *Spatially resolved molecular KS relation from the PHIBSS sample (Freundlich et al., 2013; Genzel et al., 2013) superimposed on the sub-galactic KS diagram obtained at low redshift by Bigiel et al. (2008). The solid blue line corresponds to a constant depletion time tdepl = 1.9 Gyr, and the grey data points to galaxy-averaged measurements.*

However, there might be some hints that the star formation efficiency could be higher at high redshift, with smaller depletion times. This is notably suggested by the comparison shown in Fig. 2.8 between the PHIBSS and COLDGASS measurements (Saintonge et al., 2011a; Tacconi et al., 2013). More recent observations might confirm the trend, notably from high-resolution measurements in gravitationally-lensed galaxies at even higher redshift than the PHIBSS sample (Swinbank et al., 2010; Danielson et al., 2011; Decarli et al., 2012; Sharon et al., 2013; Rawle et al., 2014). Fig. 2.18 summarizes some of these measurements, including direct kpc-scale observations at $z \approx 4$ by Hodge et al. (2012, 2015). While MS galaxies in the local Universe and from the PHIBSS sample at $z = 1-2$ have molecular gas depletion timescales close to a Gyr, resolved higher-redshift measurements seem to yield lower depletion times. But the results from Fig. 2.18 should be handled carefully, as the observed higher redshift galaxies might be starbursts and not normal star-forming galaxies. Using dust continuum observations, Scoville et al. (2015) study galaxy-averaged star formation for a large sample of galaxies at $z = 1-6$ on and above the MS and obtain a near-linear KS relation with a characteristic depletion time of about 0.1 Gyr. Comparing this timescale to the corresponding value at low redshift, they argue in favor of a different mode of star formation in the distant Universe. As already noticed by Magdis et al. (2012) and Tacconi et al. (2013), they also find that the principal difference between galaxies on and above the MS at a given stellar mass seems to be their gas fraction, not their star formation efficiency.

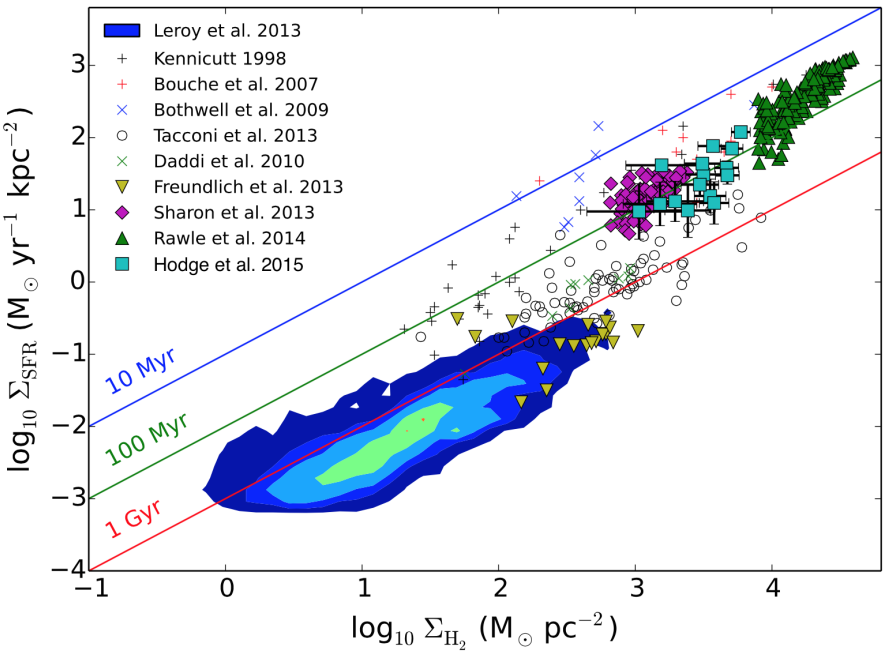

Figure 2.18 – *Molecular KS relation for different measurements at low- and high redshift, from Hodge et al. (2015). Filled data points indicate resolved measurements. The data shown here include observations at different redshifts, from the local Universe (Kennicutt, 1998a; Bothwell et al., 2009; Leroy et al., 2013) to* $z = 0.5-3$ *(Bouché et al., 2007; Daddi et al., 2010a; Tacconi et al., 2010; Freundlich et al., 2013; Sharon et al., 2013) up to* $z = 4-5.5$ *(Rawle et al., 2014; Hodge et al., 2015). The solid lines indicate constant molecular gas depletion timescales.*

But observations use different tracers and calibrations for the molecular gas and the SFR, which sometimes makes comparisons difficult. More statistically robust observations at high redshift would help constrain the evolution of the star formation efficiency. The work shown here presents a method to reach sub-galactic scales in high redshift galaxies owing to their kinematics, and as such, constitutes a pilot study that could be applied to more galaxies in the distant Universe.

2.4.4 Perspectives

PHIBSS2

Better understanding the build-up and the winding-down of star formation in the Universe is an important issue that involves observers as well as theorists. The ongoing IRAM PHIBSS2 Legacy Program (Combes, Garcia-Burillo, Neri, Tacconi, et al.) will more than triple the number of high redshift normal star-forming galaxies with CO measurements, extend the redshift range of the available sample, and include galaxies below the main sequence of star formation. This four-year program is phased to optimize and exploit the NOEMA capabilities as they come online at the Plateau de Bure: the smaller integration times and the increased sensitivity will permit a statistical gain and a better sampling of the stellar mass - SFR plane. The program is more focused on galaxy-averaged measurements, but might also imply high-resolution follow-up observations of some galaxies of the sample, in which resolved KS measurements taking advantage of the kinematics such as those presented by Freundlich et al. (2013) should be possible.

ALMA programs

The PHIBSS2 Legacy Program is complemented by ALMA[3] programs which will further contribute to extend the sample owing to an even higher sensitivity (Genzel et al.), probe higher CO transitions to study the gas excitation and the physical conditions of the gas in early star-forming systems (Weiss et al.), and possibly obtain high-resolution images and kinematics of the molecular gas in galaxies at intermediate redshifts (Freundlich et al.). This latter ALMA cycle 3 proposal, which was rated B and is currently being observed, precisely aims at investigating the star formation processes and the fate of the star-forming regions after the peak epoch of star formation, at $z = 0.7$. It would enable us to characterize star formation on subgalactic scales, notably through a spatially-resolved KS relation, to observe the inner morphology of the disk, and to test the virialization of the star-forming clumps.

[3] The *Atacama Large Millimeter/submillimeter Array* (ALMA) is a radio interferometer located in the Atacama desert of Chile, which is an international collaboration among Europe, the United States, Canada, East Asia and the Republic of Chile. For its 2015 – 2016 cycle 3, it will comprise of at least 38 12m and 10 7m antennas and reach spatial resolutions of about $0.03''$ in the most extended configurations.

Part Two

Star formation in the filamentary structures of the interstellar medium

CHAPTER 3

An analytical approach to the stability of interstellar filaments

In the previous chapter, we aimed at characterizing star formation in distant galaxies. As individual stars and giant molecular clouds are not resolved in all but the closest galaxies, the star formation activity had to be assessed from quantities averaged over whole galaxies or large subregions within them. Scaling relations such as the Kennicutt-Schmidt (KS) relation describe star formation and its efficiency from a global point of view, without resolving the smaller-scale structures and processes at stake during star formation. High-resolution observations of molecular gas clouds and star-forming complexes in our Milky Way enable us to better understand how stars are formed in the interstellar medium (ISM). Observations notably show that the interstellar medium hosts complex networks of filamentary structures. The formation of turbulence-driven filaments and their subsequent gravitational fragmentation could represent an important step towards core and star formation (e.g., André et al., 2010, 2014). Gravitational instabilities could indeed lead these filaments to clump into a series of bead-like structures which would then turn into stars. More generally, filamentary structures are very common in astrophysics and are observed at various scales. The elongated spiral arms of some galaxies can be seen as filaments, and giant molecular clouds are often aligned along them (e.g., Elmegreen & Elmegreen, 1983). Close interactions between galaxies can also lead to stretched tidal tails, which can host beads of star-forming complexes with young stellar populations (e.g., Olave-Rojas et al., 2015). On a cosmological scale, simulations notably show that matter is usually distributed along filaments, forming a cosmic web that connects galaxies to one another and provides the gas reservoir from which they grow and accrete (e.g., Springel et al., 2005; Dekel et al., 2009a). The inner core of many of these cosmological filaments may be predominantly made of gas (e.g., Harford & Hamilton, 2011), and matter can possibly contract and seed galaxy formation within them.

To investigate the growth of gravitational instabilities within filamentary structures, we consider idealized self-gravitating filaments and derive the dispersion relation for small perturbations within them. The standard Jeans instability describes the collapse of a spherical gas cloud, but the cylindrical case is less straightforward and has not been fully investigated yet. Assuming local perturbations leads to a dispersion relation analogous to

the spherical case, but all modes are potentially unstable for perturbations of arbitrary size. Elongated perturbations near the axis of the filament should grow faster so prolate substructures and global collapse seem to be favored, which would be corroborated by most observations.

After a short introduction on filamentary structures in the interstellar medium and beyond, section 3.2 follows the article by Freundlich et al. (2014a) *"Local stability of a gravitating filament: a dispersion relation"*. This article focuses on local perturbations within an infinite, self-gravitating and rotating cylinder with pressure and density related by a barotropic equation of state. Further work investigated the more general case of large-scale perturbations in a non-rotating filament, whose results are presented in section 3.3. We also started some preliminary work to simulate the growth of perturbations within idealized filaments of the interstellar medium with the RAMSES simulation code (Teyssier, 2002), which we mention briefly among the perspectives. This work was carried out in collaboration with Chanda Jog at the Indian Institute of Science, Bangalore, and benefited from a *Raman-Charpak fellowship* delivered by the *Indo French Centre for the Promotion of Advanced Research* (IFCPAR/CEFIPRA).

Contents

Related publications and conference proceedings

- **Freundlich, J.**, Jog, C. J., Combes, F., 2014, A&A, 564, 7, *Local stability of a gravitating filament: a dispersion relation*
- **Freundlich, J.**, Jog, C. J., Combes, F., Anathpindika, S., 2014, SF2A Proceedings, 325-328, *On the stability of self-gravitating filaments*
- **Freundlich, J.**, Jog, C. J., Combes, F., 2015, IAU General Assembly, Meeting 29, 2247395, *Perturbation growth within self-gravitating interstellar filaments*

3.1 Filamentary structures in the ISM and beyond

3.1.1 Star formation and interstellar filaments

The filamentary structure of the ISM

The giant molecular clouds in which stars are formed are not smooth, regular features and they are themselves highly structured at smaller scales. In particular, they host complex networks of filamentary structures, which are ubiquitous in the interstellar medium (e.g., Schneider & Elmegreen, 1979; Bally et al., 1987; Mizuno et al., 1995; Falgarone et al., 2001; Hatchell et al., 2005; Goldsmith et al., 2008; André et al., 2010, 2014; Men'shchikov et al., 2010; Arzoumanian et al., 2011; Jackson et al., 2010; Kirk et al., 2013; Palmeirim et al., 2013; Konyves et al., 2015). Fig. 3.1 displays *Herschel*[1] images of the Aquila molecular cloud complex, which is one of the nearest star-forming regions of the Milky Way, and the right panel highlights networks of filaments in a subregion of the molecular cloud. These filaments have typical lengths of a few parsecs and widths of about 0.1 parsec. This characteristic width seems to be universal (Arzoumanian et al., 2011; Palmeirim et al., 2013; Alves de Oliveira et al., 2014; André et al., 2014), but its origin remains unclear.

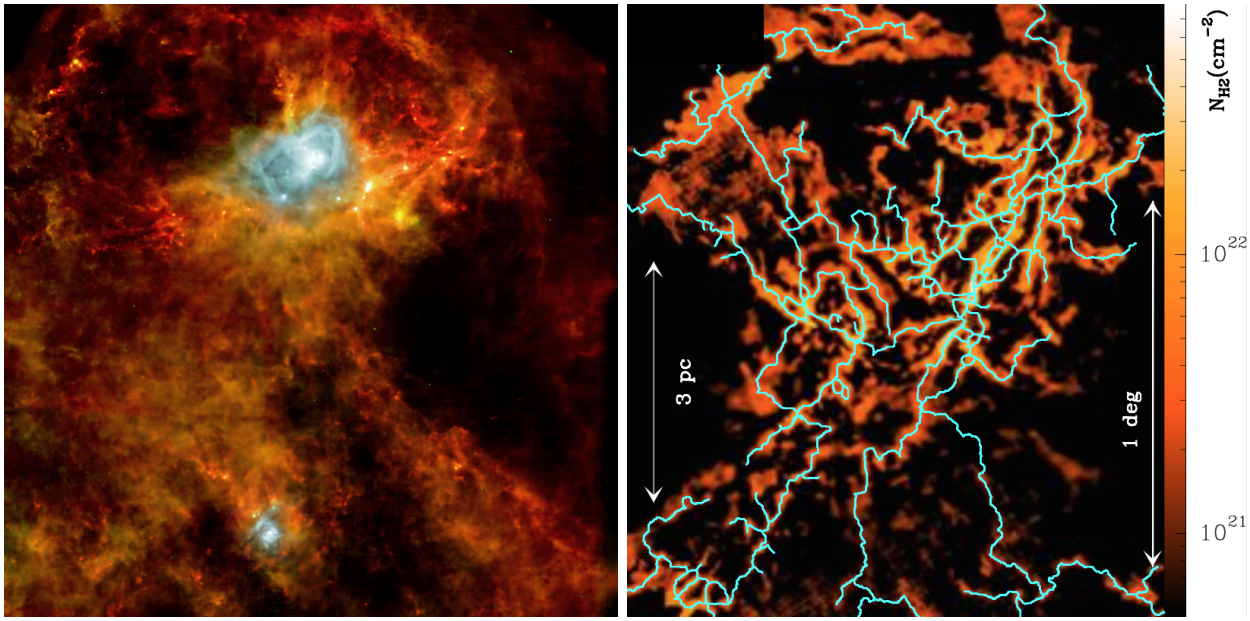

Figure 3.1 – *Composite Herschel image of the Aquila star-forming complex (left) and detail of one subregion whose column density* N_{H2} *reveals large networks of interstellar filaments (right). The left image covers an area whose width is about 50 pc. Crédits: ESA/Herschel/SPIRE/PACS/"Gould Belt survey" Key Programme/P. André & D. Arzoumanian.*

[1] *Herschel* is a European Space Agency (ESA) space observatory which carried the largest, most powerful infrared telescope ever launched in space and was active from 2009 to 2013. The observatory was named after William Herschel and his sister and collaborator Caroline Herschel, who pioneered the observation of the heavens (cf. page 7).

The complex geometry of the filaments and their characteristic width seem to indicate that they originate from large-scale interstellar turbulence. Indeed, 0.1 parsec corresponds approximately to the sonic scale, which is the characteristic scale below which interstellar turbulence becomes subsonic (Arzoumanian et al., 2011). Intersecting shock waves due to supersonic turbulent flows could account for the formation of filaments and for their width (e.g., Padoan et al., 2001; Klessen et al., 2004; Pudritz & Kevlahan, 2013). But other mechanisms could also play an important role in their formation, such as magnetic fields and dissipation by ion-neutral friction (Nakamura & Li, 2008; Hennebelle, 2013; Hennebelle & André, 2013; Ntormousi et al., 2015), or simple gravitational instabilities in self-gravitating sheets and clouds (e.g., Larson, 1985; Miyama et al., 1987a,b; Nagai et al., 1998; Burkert & Hartmann, 2004; Gómez & Vázquez-Semadeni, 2014). Filaments are indeed shown to correlate strongly with interstellar magnetic fields (e.g., McClure-Griffiths et al., 2006; Goldsmith et al., 2008). A characteristic width of about 0.1 parsec also arises when considering an isothermal self-gravitating cylinder in pressure equilibrium with its ambient medium (Fischera & Martin, 2012). More generally, some filaments might be transient turbulent features while others became gravitationally-bound structures.

Filaments are observed in star-forming clouds such as the Aquila complex, but also in regions that are not forming stars, such as the Polaris Flare cirrus cloud (André et al., 2010; Ward-Thompson et al., 2010; Miville-Deschênes et al., 2010). Nevertheless, they seem to be intimately related to star formation. As shown in Fig. 3.2, a large majority of pre-stellar cores and proto-stellar cores lie within the filamentary structures. A pre-stellar core is defined here as a gravitationally-bound, starless dense core, while a proto-stellar core hosts a proto-star. As much as 75% of the pre-stellar cores of the Aquila complex lie within filaments (Konyves et al., 2015).

Star formation within filaments

The fact that pre-stellar cores lie within the filaments of the interstellar medium (Mizuno et al., 1995; Hartmann, 2002; Könyves et al., 2010; André et al., 2010; Men'shchikov et al., 2010; Konyves et al., 2015) suggests that these filaments play an important role during star formation. Accordingly, André et al. (2010, 2014) propose a scenario in which the formation of turbulence-driven filaments in the interstellar medium represents the first step towards core and star formation. Complex networks of filaments form within molecular clouds, and the densest of them then fragment into pre-stellar cores owing to gravitational instability. The fact that filamentary structures are present in non star-forming regions indeed seems to indicate that they precede star formation (Miville-Deschênes et al., 2010; Men'shchikov et al., 2010). The scenario is further justified by the fact that most pre-stellar and proto-stellar cores lie in filaments whose mass per unit length is larger than the theoretical critical mass per unit length above which filaments are expected to be gravitationally unstable. Inutsuka & Miyama (1992, 1997) indeed show through analytical calculations and numerical simulations that in the absence of magnetic fields, isothermal filaments are gravitationally unstable for masses per unit length above

$$\mathrm{M_{line,crit}} = \frac{2\mathrm{c_s^2}}{\mathrm{G}}, \tag{3.1}$$

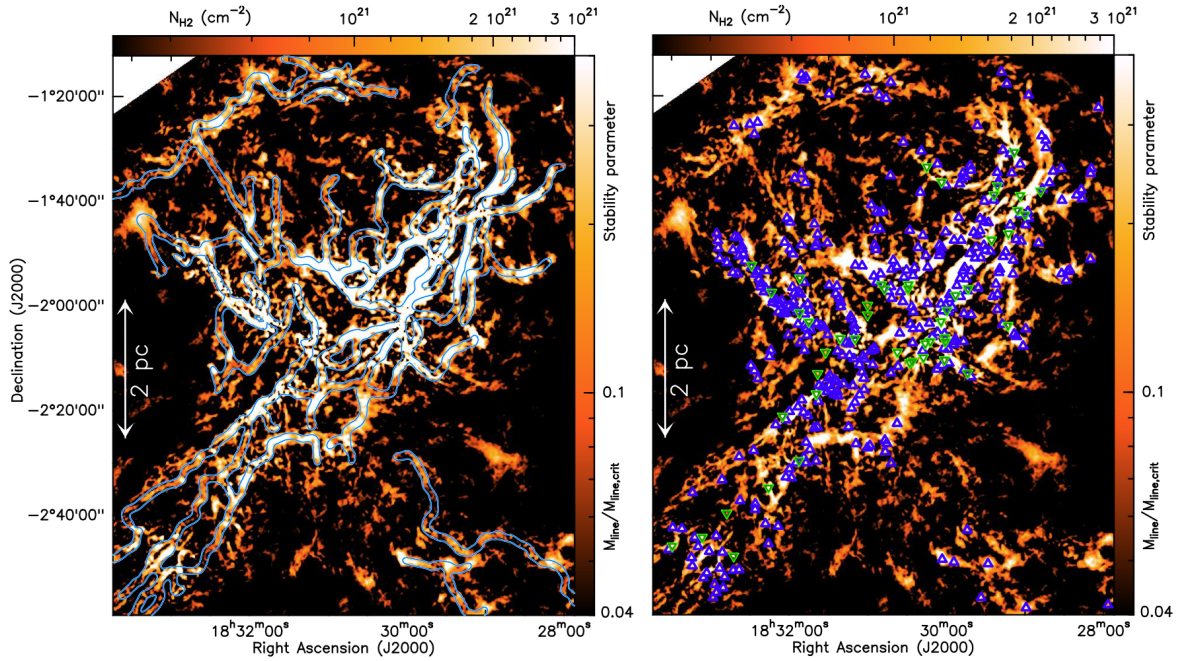

Figure 3.2 – *Herschel high-resolution column density maps of a subregion of the Aquila star-forming complex comparing the filamentary structures (left) and the locations of pre-stellar and proto-stellar cores (right), from Konyves et al. (2015). The subregion corresponds to that displayed on the right panel of Fig. 3.1. The blue contours on the left outline 0.1 pc-wide filaments while the blue and green triangles on the right correspond respectively to the locations of pre-stellar and proto-stellar cores. 75% of the pre-stellar cores lie within the 0.1 pc-wide filaments.*

where c_s is the sound speed, and fragment into bead-like spherical structures when marginally critical. This critical mass per unit length only depends on the temperature of the filament through the sound speed, and is equal to 16 $M_\odot$ pc^{-1} for a temperature of 10 K. Assuming a constant 0.1 parsec width for the filaments enables to express the column density map of Fig. 3.2 in terms of mass per unit length along the filaments, M_{line}. This is indicated in the color scale on the right. The white areas highlight regions in which $M_{line} > 0.5\ M_{line,crit}$, and they correlate very well with the positions of pre-stellar and proto-stellar cores. More generally, the filament population seems to be divided between supercritical, self-gravitating, star-forming filaments with high column densities, and subcritical, unbound, quiescent filaments with lower column density (e.g., André et al., 2010; Konyves et al., 2015).

Moreover, the fragmentation of interstellar filaments into these dense cores seem to determine the stellar initial mass function (IMF) and thus control the properties of the newly formed stars. Indeed, the observed pre-stellar core mass function ressembles the IMF of stars, albeit slightly shifted as would be expected if the star formation efficiency within an individual star-forming core $\epsilon_{core} = M_{star}/M_{core}$, i.e., the mass of the resulting stellar system divided by the core mass, was around 40% (e.g., André et al., 2010, 2014; Könyves et al., 2010; Konyves et al., 2015). Studying the growth of gravitational instabilities within the filamentary structures of the ISM is consequently crucial to better understand the star formation processes and their efficiency.

3.1.2 The ubiquity of filamentary structures

Spiral arms

The giant molecular clouds in which stars are formed host filamentary structures shaped by their inner turbulence, but they are themselves potentially embedded in the spiral structure of the galaxies they belong to. Observations show that giant gaseous clouds and bright stellar complexes are often regularly-spaced along the spiral arms of galaxies, like 'beads on a string' (e.g., Elmegreen & Elmegreen, 1983; Boulanger & Viallefond, 1992; Engargiola et al., 2003; Gusev & Efremov, 2013; Schinnerer et al., 2013). Simulations such as that carried out by Renaud et al. (2013) and shown in Fig. 3.3 reproduce this feature. This hydrodynamical simulation of a Milky Way-like galaxy carried out with the RAMSES simulation code (Teyssier, 2002) at a high-resolution of 0.05 parsec takes into account star formation and stellar feedback, and yields regularly-spaced overdense clumps along the bar and the spiral arms. Their number might be overestimated as compared to the Milky Way, but processes such as stellar feedback are expected to decrease their mass and size with time and hence to improve the match with the real Galaxy at later stages. Spiral arms also often appear bluer and with stronger Hα emission than the rest of the disk, indicating the presence of short-lived massive young stars and active star formation (e.g., van den Bergh, 1964; Schweizer, 1976; Knapen & Beckman, 1996; Sparke & Gallagher, 2007, p. 225). However, spiral arms are not material arms containing a fixed population of stars and gas. Differential rotation would indeed rapidly disrupt such a structure. Instead,

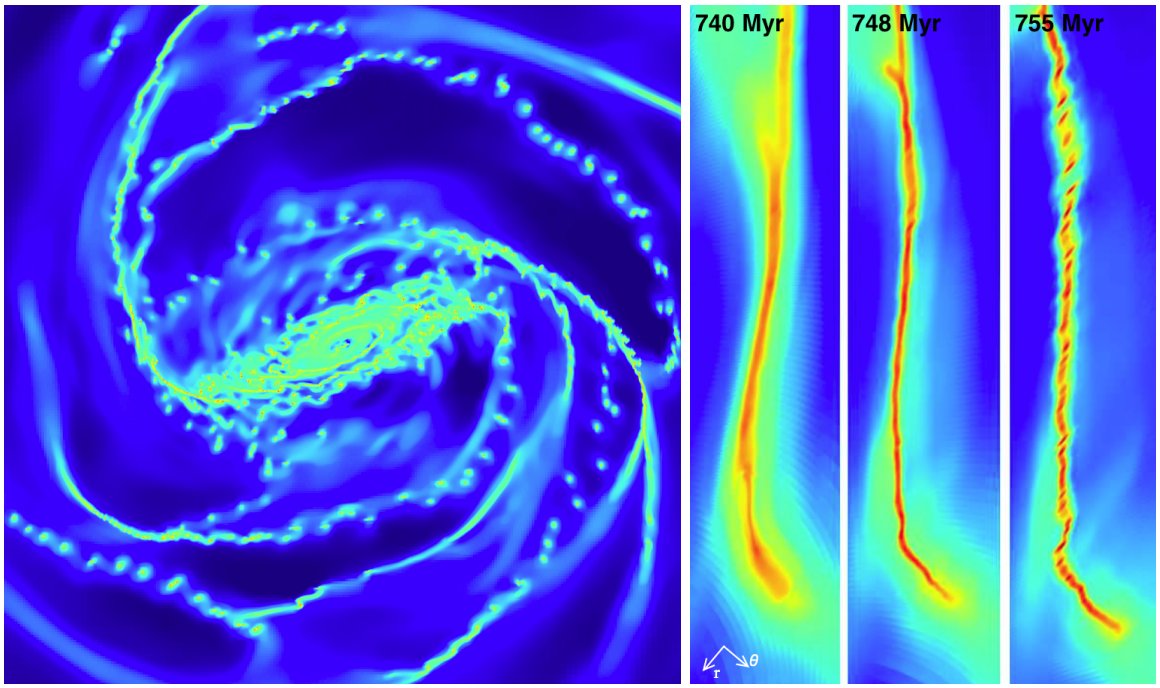

Figure 3.3 – *Gas surface density for a Milky-Way-like simulated galaxy by Renaud et al. (2013). The bar and the spiral arms host dense clumps distributed as 'beads on a string'. The three panels to the right focus on the first stages leading to the formation of such beads along one of the spiral arms.*

most of them correspond to density waves within the disk (e.g., Lindblad, 1963; Lin & Shu, 1964, 1966; Combes et al., 1995; Sparke & Gallagher, 2007). When the gas enters the potential well associated to the density wave, it is shocked and the compression can trigger gravitational instabilities (e.g., Roberts, 1969; Bonnell et al., 2006). The passage within the spiral arm lasts a few tens of Myr, depending notably on the radius and the rotation velocity, which enables gravitationally-bound structures to develop locally. The formation of giant molecular clouds can stem from gravitational instabilities or cloud-cloud collisions, both processes being favored inside spiral arms, where the gas density is higher (e.g., Elmegreen, 2011; Dobbs & Pringle, 2013). Because of their elongated shape, spiral arms can be seen as overdense cylinders at first approximation, in which the standard formalism for spherical gravitational collapse does not apply. However, the large scale dynamics of the galactic disk is expected to affect the gravitational stability of these filamentary structures, notably through velocity gradients and gravitational torques.

Tidal tails

Interactions and close encounters between galaxies generate elongated tidal tails as part of the material of a galaxy is stripped towards the other (Toomre & Toomre, 1972). Such an elongated tidal tail can be seen in the optical and far ultraviolet (FUV, 130-180 nm in the case of the GALEX FUV band) images of Fig. 3.4, between NGC 6845A and NCG 5845B. Tidal interactions between galaxies trigger star formation in the disk (cf. section 1.2.3, p. 29), but tidal tails themselves are often seen to be fragmented into bead-like clumps (e.g., Combes et al., 1999; Odenkirchen et al., 2002; Espada et al., 2012; Whitmore et al., 2014). Quillen & Comparetta (2010) and Comparetta & Quillen (2011) argued that the such condensations observed in the spectacularly-long Palomar 5 tidal tail of the Milky Way were caused by gravitational instabilities within the filamentary

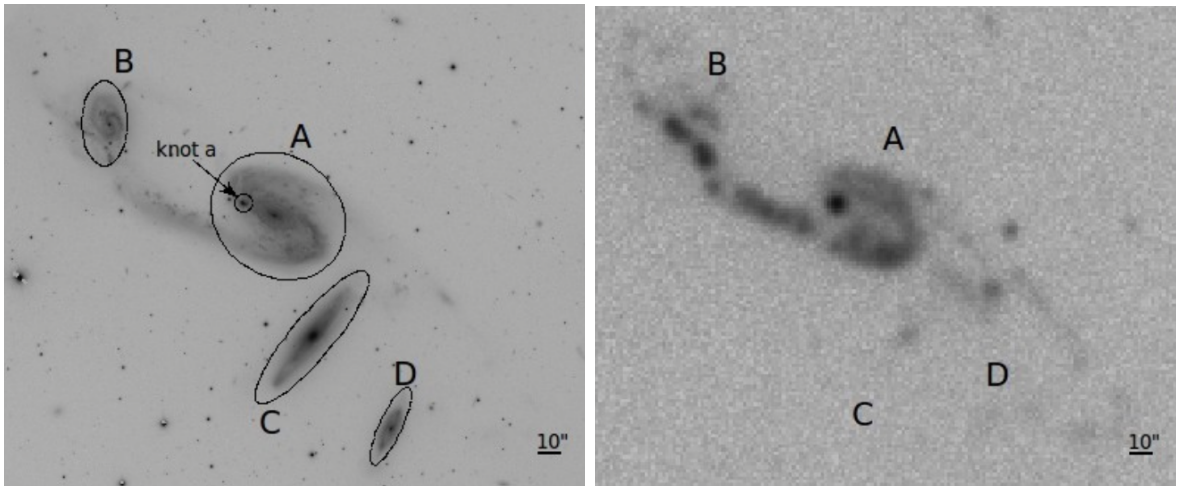

Figure 3.4 – *Star-forming tidal tail between NGC 6845A and NGC 6845B seen in the optical Gemini r' (left) and GALEX FUV (right) bands, from Olave-Rojas et al. (2015). The FUV light traces young stellar populations. The black ellipses correspond to the optical radius for each galaxy.*

structure. They modeled the tidal tail as a static, homogeneous cylinder and considered perturbations depending on the axial z coordinate. They concluded that the regularly-spaced clumps observed in the tidal tail could be due to gravitational instability. However, they considered a static cylinder and did not take into account its expansion and stretching due to the opposite gravitational forces on both sides and the effect it has on the velocity dispersion. By adding such effects, Schneider & Moore (2011) conclude that the Palomar 5 tidal tail should not be directly gravitationally unstable, which is further confirmed by numerical simulations (Mastrobuono-Battisti et al., 2012). Nevertheless, the compression occurring during tidal interactions could trigger or enhance star formation, and elongated tidal tails indeed seem to host star-forming complexes with young stellar populations of age $\lesssim$ 10 Myr (Rodrigues et al., 1999; Chien et al., 2007; de Mello et al., 2008; Smith et al., 2008; Torres-Flores et al., 2014; Olave-Rojas et al., 2015). In Fig. 3.4, the FUV image indeed reveals several knots of young stellar complexes along the tidal tail, which are thought to have formed *in situ* given their ages (Olave-Rojas et al., 2015). The cylindrical geometry of such a tidal tail may influence the formation of stellar clusters, although large-scale velocity fields affect its stability.

Cosmological filaments

Filamentary structures are also ubiquitous on cosmological scales, forming a cosmic web that connects galaxies to one another (e.g., Bond et al., 1996; Springel et al., 2005; Fumagalli et al., 2011) and provides a gas reservoir from which galaxies grow and accrete (e.g., Kereš et al., 2005; Dekel et al., 2009a). This is particularly visible in the *Millenium* cosmological simulation, shown in Fig. 3.5. Sheets ('pancakes') and filaments arise naturally as a consequence of asymmetrical gravitational collapse, because ellipsoidal maxima collapse at different speeds along the three unequal axes (Lin et al., 1965). Cosmological simulations show that most of the dark matter mass in the Universe is concentrated in the filaments of the cosmic web (e.g., Aragón-Calvo et al., 2010), which could host a significant part of the missing baryons: about half of the warm gas may indeed reside in these filaments as a warm hot intergalactic medium (WHIM, cf. section 1.2.1, p. 27; Fukugita et al., 1998; Cen & Ostriker, 1999; Viel et al., 2005). However, this gas is difficult to detect (e.g., Turnshek et al., 2004; Cantalupo et al., 2012; Planck Collaboration et al., 2013; Beygu et al., 2013; Cantalupo et al., 2014; Finley et al., 2014). The baryon distribution is expected to follow the dark matter distribution on large scales, but to differ on smaller scales. Simulations by Harford et al. (2008) and Harford & Hamilton (2011) have shown that intergalactic gas tends to concentrate towards the inner parts of filaments and sheets, with quasi-spherical dark matter structures at the intersections of the filaments. The inner core of many of these cosmic filaments is thus expected to be predominantly composed of gas, justifying models that treat them as self-gravitating isothermal or barotropic cylinders in hydrostatic equilibrium. Simulations show that when the cooling time is short enough, the inner part of the filament collapses to form dense cold cores that contain a substantial fraction of the gas (Gray & Scannapieco, 2013). Within cosmological filaments, gravity is however challenged by the expansion of the Universe, implying that Newtonian physics might not be sufficient to fully describe the condensations occurring at such large scales.

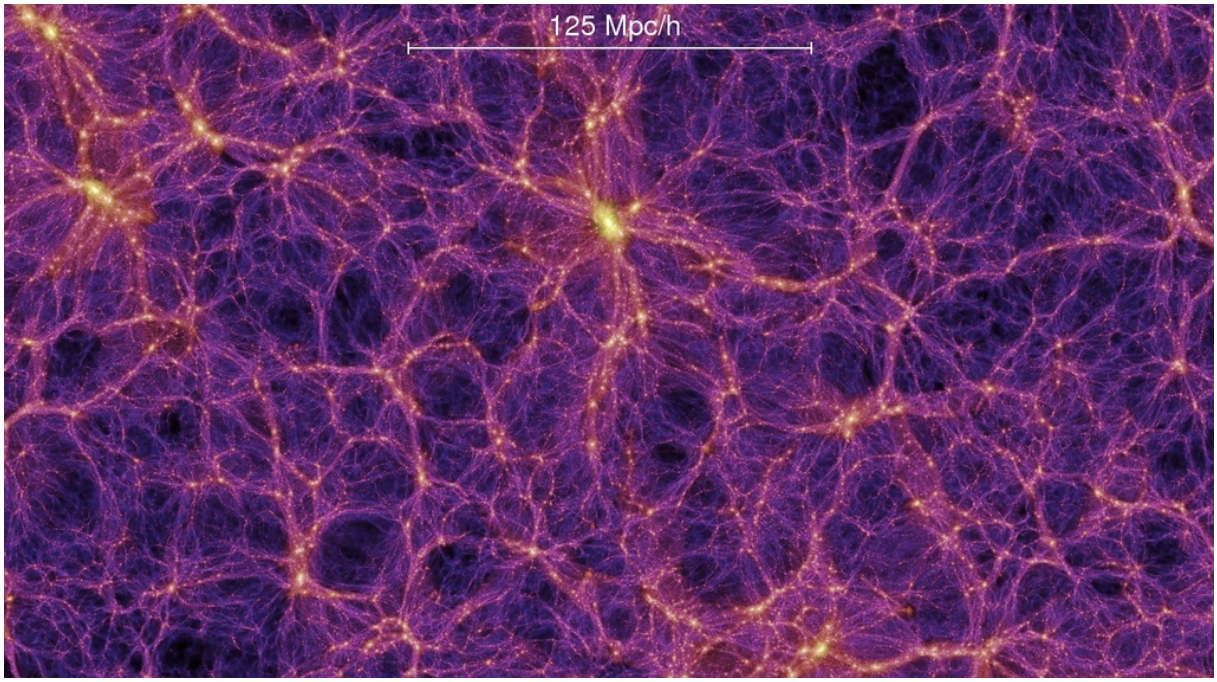

Figure 3.5 – *The Millenium simulation reveals a cosmic web of dark matter filamentary structures in the Universe (Springel et al., 2005). Each tiny yellow dot is a galaxy.*

3.1.3 Describing the growth of perturbations

Whether regarding the filamentary structures of the interstellar medium, spiral arms, tidal tails or even the filaments of the cosmic web, the nearly cylindrical geometry of the elongated overdensities in which gravitational instabilities are expected to develop should play an important role. The standard Jeans instability describes the collapse of a spherical gas cloud when the inner pressure is not strong enough to support the self-gravitating gas. Gravity tends to condense the matter, while pressure tends to reduce the inhomogeneities. In the spherical case, small perturbations are amplified when their size is larger than a specific length, the Jeans length (e.g., Binney & Tremaine, 1987). The cylindrical case is less straightforward and has not been fully investigated yet. But before considering perturbations within cylindrical structures, let us remind the standard spherical case initially worked on by Jeans (1902).

The standard Jeans instability

Hydrodynamic equations. For a continuous distribution of matter such as a gaseous cloud, the density $\rho(\vec{r},t)$, the pressure $p(\vec{r},t)$, the gravitational potential $\Phi(\vec{r},t)$ and the velocity $\vec{v}(\vec{r},t)$ are very generally related by Euler's equation of motion

$$\frac{\partial \vec{v}}{\partial t} + (\vec{v}.\vec{\nabla})\vec{v} = -\frac{1}{\rho}\vec{\nabla}p - \vec{\nabla}\Phi, \tag{3.2}$$

the continuity equation enforcing the conservation of mass

$$\frac{\partial \rho}{\partial t} + \vec{\nabla}.(\rho \vec{v}) = 0, \tag{3.3}$$

and Poisson's equation

$$\nabla^2 \Phi = 4\pi G \rho. \tag{3.4}$$

Additionally, we can assume a barotropic fluid in which pressure is only a function of density so that

$$\frac{1}{\rho}\vec{\nabla} p = \vec{\nabla} h \tag{3.5}$$

where h is the specific enthalpy of the gas. In this case, Euler's equation can be expressed in terms of h instead of p.

Linear equations. We consider an unperturbed barotropic fluid described by the quantities $\rho_0(\vec{r})$, $h_0(\vec{r})$, $\Phi_0(\vec{r})$ and $\vec{v}_0(\vec{r})$ and we would like to describe its behavior when a small perturbation occurs. This perturbation can be described by first order corrections to the different physical quantities:

$$\begin{aligned} \rho(\vec{r},t) &= \rho_0(\vec{r}) + \rho_1(\vec{r},t) \\ h(\vec{r},t) &= h_0(\vec{r}) + h_1(\vec{r},t) \\ \Phi(\vec{r},t) &= \Phi_0(\vec{r}) + \Phi_1(\vec{r},t) \\ \vec{v}(\vec{r},t) &= \vec{v}_0(\vec{r}) + \vec{v}_1(\vec{r},t) \end{aligned} \tag{3.6}$$

where the infinitesimal disturbances are denoted by an index 1 so that $\rho_1/\rho_0 \ll 1$ and similar relations for the other quantities. Assuming that equations 3.2 to 3.5 are valid for the unperturbed as well as for the perturbed gas yields the linear equations that govern the response of the barotropic fluid to the perturbations:

$$\begin{cases} \dfrac{\partial \vec{v_1}}{\partial t} + (\vec{v_0}.\vec{\nabla})\vec{v_1} + (\vec{v_1}.\vec{\nabla})\vec{v_0} = -\vec{\nabla}(h_1 + \Phi_1) \\ \dfrac{\partial \rho_1}{\partial t} + \vec{\nabla}.(\rho_0 \vec{v_1}) + \vec{\nabla}.(\rho_1 \vec{v_0}) = 0 \\ \nabla^2 \Phi_1 = 4\pi G \rho_1 \\ h_1 = c_0^2 \dfrac{\rho_1}{\rho_0}, \end{cases} \tag{3.7}$$

where the speed of sound in the uniform medium is defined as

$$c_0^2 = \left(\frac{dp}{d\rho}\right)_{\rho_0}. \tag{3.8}$$

Growth of perturbations. In the case of an infinite, homogeneous, unperturbed system, the hydrodynamic equations can't be verified simultaneously, as Poisson's equation requires $\nabla^2 \Phi_0 = 4\pi\rho_0$ but $\vec{\nabla}\Phi_0 = 0$ for a uniform gravitational potential and $\rho_0 \neq 0$.

The 'Jeans swindle' artificially lets us assume that Poisson's equation properly describes the relation between the perturbed density and potential, while some unspecified source cancels the unperturbed term in $\nabla^2\Phi_0$. The linear equations describing small perturbations in the case of an infinite, immobile, unperturbed medium of constant density ρ_0, where $\vec{v_0} = \vec{0}$, are

$$\begin{cases} \dfrac{\partial \vec{v_1}}{\partial t} = -\vec{\nabla}(h_1 + \Phi_1) \\ \dfrac{\partial \rho_1}{\partial t} + \rho_0 \vec{\nabla}.\vec{v_1} = 0 \\ \nabla^2\Phi_1 = 4\pi G\rho_1 \\ h_1 = c_0^2 \dfrac{\rho_1}{\rho_0}. \end{cases} \tag{3.9}$$

As each signal can be Fourier decomposed into normal modes proportional to $e^{-i\omega t + \vec{k}.\vec{r}}$, we can consider perturbations of the kind without losing any generality. For such a normal mode, the previous equations lead to the following complex equations:

$$\begin{cases} -i\omega\vec{v_1} = -i\vec{k}(c_0^2\dfrac{\rho_1}{\rho_0} + \Phi_1) \\ -i\omega\rho_1 + i\rho_0\vec{k}.\vec{v_1} = 0 \\ -k^2\Phi_1 = 4\pi G\rho_1. \end{cases} \tag{3.10}$$

Combining these equations yields the dispersion relation describing the potential modes,

$$\omega^2 = c_0^2k^2 - 4\pi G\rho_0. \tag{3.11}$$

For wavenumbers k above $k_J = \sqrt{4\pi G\rho_0/c_0^2}$, $\omega^2 > 0$ and the solutions are oscillatory, while for wavenumbers below this value, the solutions are exponentially growing or decaying. However, the presence of a growing solution in the latter case implies that the system is gravitationally unstable. Perturbations of size larger than the Jeans length

$$\lambda_J = \sqrt{\frac{\pi c_0^2}{G\rho_0}}, \tag{3.12}$$

are amplified while smaller perturbations fade away. For a gaseous cloud, it means that a spherical overdensity of size larger than the Jeans length will be unstable gravitationally and collapse.

Timescales. The Jeans instability can be interpreted in terms of timescales. Indeed, a spherical gaseous cloud of initial density ρ_0 will collapse when its radius r verifies

$$\frac{r}{c_0} > \sqrt{\frac{\pi}{G\rho_0}}. \tag{3.13}$$

The left-hand term corresponds to the time needed for a sound wave to propagate through the cloud, the sound-crossing time, while the right-hand term is approximately the free-fall time, i.e., the time for the cloud to collapse under its own gravitational attraction. The sound-crossing time corresponds to the time needed by the system to re-establish the pressure equilibrium when a perturbation arises, so when it is bigger than the free-fall time, the system does not have the time to re-adjust itself against gravitational collapse.

Previous work on filamentary structures

In the following work, we aim at obtaining a dispersion relation analogous to Eq. 3.11 for the perturbations arising in a cylindrical filament. The standard Jeans instability assumes an infinite, uniform, unperturbed medium, which corresponds to spherical symmetry, while elongated structures introduce a fundamental anisotropy in the equations. Early studies mostly considered cylindrical structures from a theoretical point of view. Chandrasekhar & Fermi (1953) notably studied the dynamics of a homogeneous and incompressible, infinite, self-gravitating cylinder with a constant axial magnetic field, while Simon (1963) and Ostriker (1964a) generalized their calculations to a homogeneous compressible cylinder. Stodólkiewicz (1963) further considered an isothermal cylinder embedded in different types of magnetic fields and derived criteria for the critical length of the perturbations. Remarkably, Ostriker (1964b) derived an analytical expression for the density profile and the gravitational potential of a self-gravitating cylinder with an isothermal equation of state:

$$\rho_0(R) = \rho_c \frac{1}{\left(1 + \frac{1}{8}\left(\frac{R}{R_s}\right)^2\right)^2} \tag{3.14}$$

$$\Phi_0(R) = 2c_0^2 \ln\left(1 + \frac{1}{8}\left(\frac{R}{R_s}\right)^2\right) \tag{3.15}$$

where $\rho_c = \rho_0(0)$ is the central density, c_0 the constant speed of sound, and $R_s = c_0/\sqrt{4\pi G\rho_c}$ a characteristic scale length. This expression is valid for a non-rotating isothermal cylinder, and notably differs from the spherical isothermal case through its behavior at large radii. Indeed, $\rho_0 \propto R^{-2}$ at large radii for isothermal spheres (e.g., Mo et al., 2010, p. 242) while this profile yields a steeper exponent, with $\rho_0 \propto R^{-4}$ at such radii.

In his seminal 1964 paper, Toomre carried out a perturbation analysis for a rotating disk and obtained a dispersion relation assuming local perturbations. The calculation applies to galactic disks, but not to elongated filaments. Mikhailovskii & Fridman (1972, 1973) and Fridman & Poliachenko (1984) later described the instability of a homogeneous gravitating cylinder of finite radius and infinite length, using a similar perturbation analysis. But a homogeneous density profile is very restrictive and does not even fit with an isothermal self-gravitating cylinder. The calculation should ideally be applicable to any type of density profile and equation of state. Hansen et al. (1976) examined the case of an infinite, isothermal, and uniformly rotating cylinder of finite radius, whereas more complex situations were investigated from a numerical perspective (Bastien & Mitalas, 1979; Bastien, 1983; Arcoragi et al., 1991; Bastien et al., 1991; Nakamura et al., 1993, 1995; Matsumoto et al., 1994; Tomisaka, 1995, 1996).

Nagasawa (1987) numerically obtained a dispersion relation in the case of an isothermal gas cylinder with an axial magnetic field, and found that such a cylinder was unstable to axisymmetric perturbations of wavelength higher than a particular one. This behavior is similar to the spherical Jeans case. Studying the stability of self-similar solutions for an

infinitively long isothermal filament, Inutsuka & Miyama (1992) found that filaments of mass per unit length close to the critical value required for equilibrium were unstable to axisymmetric perturbations (cf. Eq. 3.1). When the mass per unit length greatly exceeds the critical value, fragmentation does not occur and the entire filament globally collapses towards its axis. Fischera & Martin (2012) further characterized the gravitational state of isothermal gas cylinders with a finite radial boundary and a non-zero external pressure in terms of the ratio of their mass per unit length to the maximum possible value for a cylinder in vacuum. This maximum corresponds to the critical value of Inutsuka & Miyama (1992) when the effective temperature is equal to the thermal temperature. The comparison of their results with observations of interstellar filaments indicated good agreement and suggested a temperature of 10 K.

Interest in the growth of instabilities within filaments has been recently revived, notably motivated by observations and simulations of the interstellar medium and the cosmic web, with the need for a stability analysis compatible with more realistic densities and equations of state. In particular, Quillen & Comparetta (2010) and Comparetta & Quillen (2011) roughly estimated a dispersion relation inspired by Fridman & Poliachenko (1984) in order to explain the condensations observed in the Palomar 5 tidal tail of the Milky Way. They were followed and criticized by Schneider & Moore (2011), who carried out a perturbation analysis and used energetic arguments to find out that such a tidal stream should finally be stable gravitationally. Motivated by the cosmological filaments uncovered by numerical simulations, Breysse et al. (2014) carried out a detailed perturbation analysis for barotropic but non-rotating filaments.

Current motivation and hypotheses

We aim at obtaining a dispersion relation for density perturbations arising in filamentary structures with a minimal set of assumptions. Recent observations have shown that interstellar filaments are not isothermal, finding dust temperatures that tend to increase with radius (Stepnik et al., 2003; Palmeirim et al., 2013), and theoretical calculations inspired by Ostriker (1964a,b) show that such filaments are more stable than their isothermal counterparts (Recchi et al., 2013). This motivates us not to limit ourselves to the isothermal case, but to assume a more general barotropic equation of state, which can result in a temperature varying with radius. Not all density profiles would reproduce the observed trend for the temperature, but so as to keep the calculation as general as possible, we do not restrict ourselves to any specific density distribution. The pressure support could be due to thermal as well as turbulent pressure. In fact, in the interstellar medium the dominant term is the turbulent support (e.g., McKee & Ostriker, 2007; Hennebelle & Falgarone, 2012).

Our idealized picture consists of an infinite self-gravitating and rotating cylinder with pressure and density related by a barotropic equation of state. We neglect the role of magnetic fields for simplicity, although their influence may contribute to the formation and stabilization of the filaments observed in the interstellar medium (Nakamura & Li, 2008; Hennebelle, 2013; Hennebelle & André, 2013). We treat matter as an inviscid fluid and

use hydrodynamics to obtain the linearized equations that govern the local perturbations. Cylindrical symmetry involves no dependence on the axial and azimuthal coordinates z and ϕ for the unperturbed system, and we only consider axisymmetric perturbations. We further assume that there is no radial movement in the undisturbed system and that all particles initially share the same axial velocity. As filamentary geometry provides a favorable situation for small perturbations to grow before global collapse overwhelms them (Pon et al., 2011), we assume an unperturbed system at equilibrium and initially neglect the global collapse of the filamentary cloud.

3.2 Local perturbations in a rotating filament

3.2.1 Obtention of a dispersion relation

The unperturbed system

The unperturbed system is assumed to be infinite and cylindrically symmetric. The undisturbed density is thus written as $\rho_0(R)$, pressure as $p_0(R)$, and the resulting gravitational field as $\Phi_0(R)$, in cylindrical coordinates. We assume that there is no radial velocity in the undisturbed system and that all fluid particles share the same initial axial velocity. The velocity field can then be written in the reference frame of the cylinder as $\vec{v_0}(R,\phi) = R\Omega_0(R)\ \vec{e_\phi}$, where $\Omega_0(R)$ is the undisturbed angular velocity and $\vec{e_\phi}$ the azimuthal unit vector. This expression guarantees mass conservation, and all calculations will hereafter be carried in the reference frame of the unperturbed system, without loss of generality. We further assume the gas to be barotropic, so that its pressure only depends on the density and the pressure force can be expressed in terms of the enthalpy $h_0(R)$, which is defined by

$$dh_0 = \frac{1}{\rho_0} dp_0. \tag{3.16}$$

For the unperturbed system, the radial equation of motion and Poisson's equation can be written as

$$-R\Omega_0^2 = -\frac{\partial h_0}{\partial R} - \frac{\partial \Phi_0}{\partial R} \tag{3.17}$$

$$\nabla^2 \Phi_0 = 4\pi G \rho_0. \tag{3.18}$$

Linear perturbations

We study the growth of instabilities when the physical quantities deviate from their equilibrium values. The dynamics of the perturbed system is determined by the following set

of linearized first-order equations, where the infinitesimal disturbances are denoted by an index 1:

$$\begin{cases} \dfrac{\partial \vec{v_1}}{\partial t} + \left(\vec{v_0}.\vec{\nabla}\right)\vec{v_1} + \left(\vec{v_1}.\vec{\nabla}\right)\vec{v_0} = -\vec{\nabla}h_1 - \vec{\nabla}\Phi_1 \\ \dfrac{\partial \rho_1}{\partial t} + \mathrm{div}\left(\rho_1\vec{v_0}\right) + \mathrm{div}\left(\rho_0\vec{v_1}\right) = 0 \\ \nabla^2\Phi_1 = 4\pi G\rho_1. \end{cases} \tag{3.19}$$

These equations correspond respectively to the equation of motion, the continuity equation, and Poisson's equation. The linearized equation of state yields for its part (see Appendix E.1)

$$h_1 = c_0^2\,\frac{\rho_1}{\rho_0} \tag{3.20}$$

where $c_0(R)$ is the speed of sound, defined for the barotropic fluid by

$$c_0^2 = \left(\frac{\partial p}{\partial \rho}\right)_{\rho_0} = \left(\frac{dp}{d\rho}\right)_{\rho_0}. \tag{3.21}$$

For an isothermal cylinder, c_0 would be a constant related to the gas temperature, but the following calculations apply to any barotropic fluid. Assuming axisymmetric perturbations of the generic form $e^{-i\omega t}e^{ik_R R}e^{ik_z z}$ (normal modes), we obtain

$$\begin{cases} \omega v_{1R} - 2i\Omega_0 v_{1\phi} = -i\dfrac{\partial h_1}{\partial R} + k_R\Phi_1 \\ \omega v_{1\phi} - 2iBv_{1R} = 0 \\ \omega v_{1z} = k_z c_0^2\dfrac{\rho_1}{\rho_0} + k_z\Phi_1 \\ \omega\rho_1 + i\dfrac{1}{R}\dfrac{\partial}{\partial R}\left(R\rho_0 v_{1R}\right) - k_z\rho_0 v_{1z} = 0 \\ \dfrac{1}{R}\dfrac{\partial}{\partial R}\left(R\dfrac{\partial\Phi_1}{\partial R}\right) - k_z^2\Phi_1 = 4\pi G\rho_1 \end{cases} \tag{3.22}$$

where the equation of motion has been projected on the different cylindrical axes, and $B(R) = -\frac{1}{2}\left(\Omega_0(R) + \frac{\partial}{\partial R}\left(R\Omega_0(R)\right)\right)$ is one of Oort constants (e.g., Jog & Solomon, 1984).

Local perturbations

In this section, we assume local perturbations: the typical scale of the perturbations is small compared to that of the unperturbed quantities, i.e., $k_R R_0 \gg 1$, where R_0 is the typical radius for the unperturbed distribution within which the perturbations occur. This assumption was made in a seminal article by Toomre (1964), and is analogous to the Wentzel-Kramers-Brillouin approximation (WKB) used in quantum physics. Perturbed quantities X_1 oscillate rapidly with the radius R whereas unperturbed quantities X_0 change much more smoothly along the radial direction, so that

$$\left|X_1\frac{\partial X_0}{\partial R}\right| \ll \left|X_0\frac{\partial X_1}{\partial R}\right|.$$

This approximation yields up to the first order

$$\frac{\partial h_1}{\partial R} = \frac{\partial}{\partial R}\left(\frac{c_0^2}{\rho_0}\rho_1\right) = \frac{c_0^2}{\rho_0}\frac{\partial \rho_1}{\partial R} + \rho_1 \frac{\partial}{\partial R}\left(\frac{c_0^2}{\rho_0}\right) \simeq \frac{c_0^2}{\rho_0}\frac{\partial \rho_1}{\partial R} \tag{3.23}$$

$$\frac{1}{R}\frac{\partial}{\partial R}\left(R\rho_0 v_{1R}\right) = \rho_0 \frac{\partial v_{1R}}{\partial R} + v_{1R}\frac{1}{R}\frac{\partial}{\partial R}\left(R\rho_0\right) \simeq \rho_0 \frac{\partial v_{1R}}{\partial R} \tag{3.24}$$

$$\frac{1}{R}\frac{\partial}{\partial R}\left(R\frac{\partial \Phi_1}{\partial R}\right) = \frac{\partial^2 \Phi_1}{\partial R^2} + \frac{1}{R}\frac{\partial \Phi_1}{\partial R} \simeq \frac{\partial^2 \Phi_1}{\partial R^2} \tag{3.25}$$

and the linearized equations become

$$\begin{cases} \omega v_{1R} - 2i\Omega_0 \mathrm{v}_{1\phi} = k_R \dfrac{c_0^2}{\rho_0}\rho_1 + k_R \Phi_1 \\ \omega v_{1\phi} - 2iB v_{1R} = 0 \\ \omega v_{1z} = k_z \dfrac{c_0^2}{\rho_0}\rho_1 + k_z \Phi_1 \\ \omega \rho_1 - \rho_0 k_R v_{1R} - \rho_0 k_z v_{1z} = 0 \\ -k_R^2 \Phi_1 - k_z^2 \Phi_1 = 4\pi G \rho_1. \end{cases} \tag{3.26}$$

Combining these equations, we obtain the local dispersion relation,

$$\omega^4 + \omega^2\left(4\pi G\rho_0 - c_0^2 k^2 - \kappa^2\right) + \kappa^2 k_z^2\left(c_0^2 - \frac{4\pi G\rho_0}{k^2}\right) = 0 \tag{3.27}$$

where $k = \sqrt{{k_R}^2 + {k_z}^2}$ corresponds to the total wavenumber and κ is the epicyclic frequency, defined by $\kappa^2 = -4\Omega_0 B$. Note that this latter quantity, as well as ρ_0 and c_0, does depend on the position R at which the perturbations are considered.

When there is no rotation, $\kappa^2 = 0$ and the asymmetry between the different directions disappears in this dispersion relation valid for small local perturbations: the local WKB assumption prevents the perturbations feeling the large-scale geometry of the system. Eq. 3.27 reduces to the standard dispersion relation for collapsing spherical systems (cf. section 3.1.3 and Binney & Tremaine, 1987):

$$\omega^2 = c_0^2 k^2 - 4\pi G\rho_0. \tag{3.28}$$

Without rotation, we thus retrieve the Jeans criterion, perturbations larger than $\lambda_J = (\pi c_0^2/G\rho_0)^{1/2}$ being unstable.

3.2.2 Some properties of the dispersion relation

A condition for stability

Introducing the characteristic angular frequency $\omega_0 = \sqrt{4\pi G\rho_c}$, where $\rho_c = \rho_0(0)$ is the central density of the filament, the dispersion relation obtained in the previous section,

Eq. 3.27, can be written in terms of the dimensionless variable $x = \omega/\omega_0$ as a fourth order polynomial equation:

$$x^4 + \alpha x^2 + \beta = 0 \tag{3.29}$$

where

$$\alpha = \frac{\rho_0}{\rho_c} - \frac{c_0^2 k^2}{\omega_0^2} - \frac{\kappa^2}{\omega_0^2} \tag{3.30}$$

and

$$\beta = \frac{\kappa^2 k_z^2}{\omega_0^2}\left(\frac{c_0^2}{\omega_0^2} - \frac{1}{k^2}\frac{\rho_0}{\rho_c}\right). \tag{3.31}$$

This equation can also be considered as a second order polynomial expression in x^2, whose roots are

$$x_+^2 = \frac{-\alpha + \sqrt{\Delta}}{2} \tag{3.32}$$

and

$$x_-^2 = \frac{-\alpha - \sqrt{\Delta}}{2} \tag{3.33}$$

where $\Delta = \alpha^2 - 4\beta$ is the discriminant of the equation. It can be shown (Appendix E.2.1) that Δ is always positive, implying that x^2 is always real. Moreover, x_+^2 is always positive as well (Appendix E.2.2), so at least two of the four roots of Eq. 3.29 are real. Consequently, the system is stable to axisymmetric perturbations when $x_-^2 \geqslant 0$ and unstable when $x_-^2 < 0$, as growing modes require a non-zero imaginary part. This condition reduces to the standard Jeans criterion (Appendix E.2); i.e., all roots are real and the system is stable when

$$k^2 \geqslant 4\pi G\rho_0/c_0^2. \tag{3.34}$$

Introducing the critical wavenumber $k_{\rm crit} = \sqrt{4\pi G\rho_0}/c_0$, the filament is expected to be stable for wavenumbers $k \geqslant k_{\rm crit}$ and unstable below. This stability condition is symmetrical in k_R and k_z, does not depend on rotation, and depends on the radius R at which the perturbation occurs as $k_{\rm crit}$ is a function of ρ_0 and c_0. Symmetry arises because of the local WKB assumption, which prevents the space-limited perturbation feeling the larger scale behavior of the system. The result is consistent with observations of structures within an interstellar filament by Kainulainen et al. (2013), which show that the fragmentation more closely ressembles Jeans fragmentation at small scales than at higher scales. At small scales, fragmentation is insensitive to the large-scale geometry and only depends on local properties.

As this equation was established for a barotropic equation of state where c_0 could vary with radius, it can also describe filaments with a non-uniform temperature. Palmeirim et al. (2013) were notably able to reproduce the increasing temperature profile of a filament in the Taurus molecular cloud with a polytropic equation of state and a Plummer-like density profile

$$\rho_0(R) = \frac{\rho_c}{\left(1 + \left(\frac{R}{R_0}\right)^2\right)^p} \tag{3.35}$$

with ρ_c the central density, R_0 a characteristic radius and p the exponent of the generalized Plummer profile. In this case, the temperature is proportional to $\rho_0^{\gamma-1}$, which increases with radius for an adiabatic index $\gamma < 1$. For such filaments with temperature and sound speed increasing with radius, the critical wavenumber $k_{\rm crit}$ falls more rapidly with radius than in the isothermal case. Consequently, such filaments are expected to be more stable than their isothermal counterparts, which was also inferred by Recchi et al. (2013) by comparing the equilibrium structure of isothermal and non-isothermal filaments.

In the isothermal case, Nagasawa (1987) numerically computes the dispersion relation for axisymmetric perturbations within an infinite non-rotating gas cylinder, and obtains a critical wavenumber that is 0.561 the critical wavenumber derived from Eq. 3.34 at the center of a similar filament. The discrepancy is partly due to the simplification involved in the local assumption, and thus gives an idea of its limitations.

The fastest growing mode

The only solution of the dispersion relation that could be negative and give rise to unstable modes is x_-^2. For a given radius R, the distribution of x_-^2 in the plane (k_R, k_z) is a useful tool to study the properties of the instabilities that could form. As long as $k < k_{\rm crit}$, different unstable modes can grow and coexist. But the fastest growing mode, which minimizes the value of x_-^2 for a given k_R, will dominate the growth of instabilities and influence the shape of the resulting structures. At any given radius R, this fastest growing mode can be described by a polynomial equation in k^2 and k_R^2 (Appendix E.3.1):

$$\left(\frac{\rho_0}{\rho_c}\right)^2 \frac{k_R^2}{k^2} = \frac{c_0^2}{\kappa^2} k^2 \left[\left(\frac{c_0^2}{\omega_0^2}k^2 - \frac{\rho_0}{\rho_c}\right)^2 + \frac{\rho_0}{\rho_c}\frac{\kappa^2}{\omega_0^2}\right]. \tag{3.36}$$

For a given k_R, this equation can be rewritten as a polynomial expression in k/k_0, where $k_0 = \omega_0/c_0$ is a characteristic wavenumber, depending in principle on the position R through c_0:

$$\left(\frac{k}{k_0}\right)^8 - 2\frac{\rho_0}{\rho_c}\left(\frac{k}{k_0}\right)^6 + \frac{\rho_0}{\rho_c}\left(\frac{\rho_0}{\rho_c} + \frac{\kappa^2}{\omega_0^2}\right)\left(\frac{k}{k_0}\right)^4 - \frac{\kappa^2}{\omega_0^2}\left(\frac{\rho_0}{\rho_c}\right)^2\left(\frac{k_R}{k_0}\right)^2 = 0. \tag{3.37}$$

For an isothermal filament, k_0 corresponds to the critical wavenumber taken at the center of the filament. When the curve associated with Eq. 3.37 in the (k_R, k_z) plane is above the line $k_z = k_R$, the structure resulting from the perturbation is expected to be oblate, whereas when $k_z < k_R$, the structure is expected to be prolate. This curve meets the line $k_z = k_R$ when k_R satisfies (Appendix E.3.2):

$$\left(\frac{k_R}{k_0}\right)^6 - \frac{\rho_0}{\rho_c}\left(\frac{k_R}{k_0}\right)^4 + \frac{1}{4}\frac{\rho_0}{\rho_c}\left(\frac{\rho_0}{\rho_c} + \frac{\kappa^2}{\omega_0^2}\right)\left(\frac{k_R}{k_0}\right)^2 - \frac{1}{16}\left(\frac{\rho_0}{\rho_c}\right)^2\frac{\kappa^2}{\omega_0^2} = 0. \tag{3.38}$$

This polynomial equation can be solved numerically, and should give a threshold value for k_R separating prolate and oblate collapsed structures.

3.2.3 Application to a fiducial interstellar filament

TMC-1, or 'The Bull's Tail'

As an illustrative numerical application, we use a filament from the Taurus molecular cloud, TMC-1, also known as 'The Bull's Tail' (Nutter et al., 2008) and shown in Fig. 3.6. Recent *Herschel* observations were able to reveal the structure of interstellar filaments with unprecedented detail (cf. section 3.1.1 and, among others, André et al., 2010; Arzoumanian et al., 2011; Malinen et al., 2012; Palmeirim et al., 2013; Kirk et al., 2013), and the Taurus molecular cloud is one of the closest and most studied star-forming regions (e.g., Narayanan et al., 2008; Goldsmith et al., 2008). Malinen et al. (2012) fit the density profile of this filament with a Plummer-like profile of the form

$$\rho_0(R) = \frac{\rho_c}{\left(1 + \left(\frac{R}{R_0}\right)^2\right)^p}, \tag{3.39}$$

and notably obtain p = 1.1, $R_0 = 0.043$ pc, and $\rho_c = 7.0 \times 10^4$ cm^{-3} from *Herschel* dust emission observations. Such values are relatively typical for interstellar filaments, as shown for a larger sample by Arzoumanian et al. (2011). Noticeably, none of the filaments studied by Arzoumanian et al. (2011) had the steep $p = 2$ exponent expected

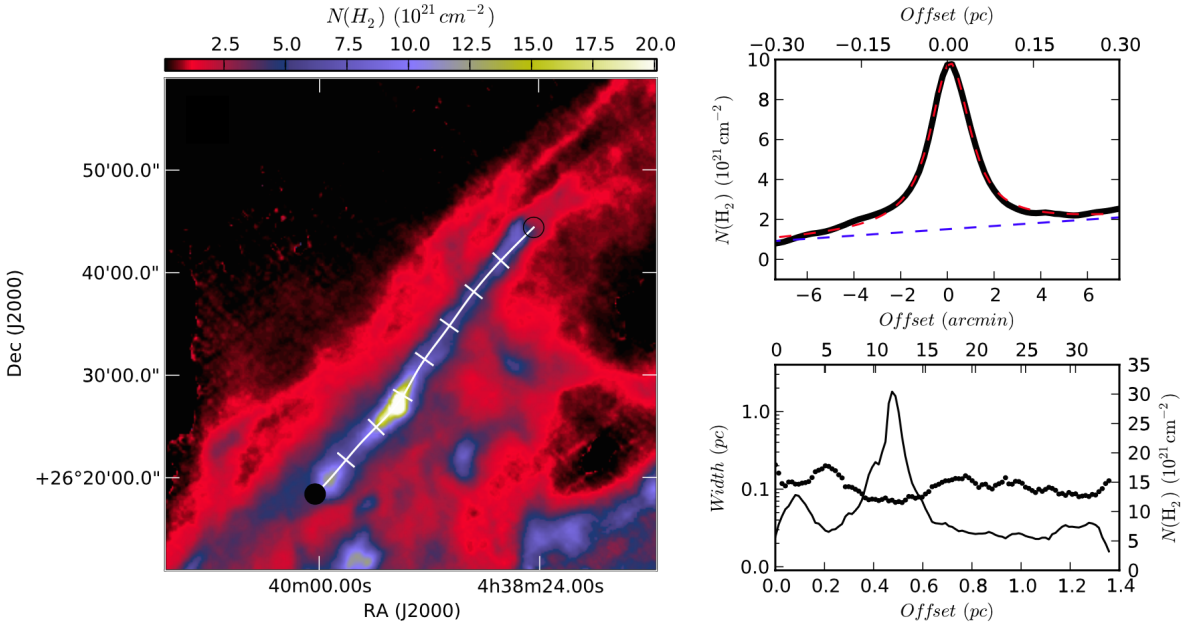

Figure 3.6 – *Herschel infrared column density map of the TMC-1 filament (left) along with its radial (upper right) and longitudinal (lower right) density profiles, from Malinen et al. (2012). The ridge of the filament is indicated as a white line on the column density map. The upper right panel displays the average column density profile (black line) and the fitted Plummer profile as in Eq. 3.39 (red dashed line). In the lower right panel, the FWHM of the filament is indicated as black circles (left-hand scale) while the column density along the ridge is plotted as a solid line (right-hand scale).*

for isothermal filaments (Ostriker, 1964b): their exponents ranged from 0.75 to 1.25, for a mean characteristic radius $R_0 = 0.03$ pc.

Here we consider an idealized filament whose density profile corresponds to the analytical Plummer-like profile found by Malinen et al. (2012) for the TMC-1 filament, and numerically solve the dispersion relation (3.27). We use a uniform thermal velocity $c_0 = 200$ m.s^{-1} for simplicity, which corresponds to a temperature of about 10 K for neutral molecular hydrogen.

Graphic representation of the dispersion relation

We obtain x_-^2 as a function of the wavenumbers k_R and k_z and of the radius R at which the perturbations are assumed to arise. x_-^2 is indeed the only solution of the dispersion relation that could be negative and give rise to unstable modes. Figure 3.7 shows the resulting distribution of x_-^2 projected in the planes $R = R_0$, $k_R = 0.2k_0$, and $k_z = 0.2k_0$, where $k_0 = \omega_0/c_0$ is the characteristic wavenumber, here equal to about 74 pc^{-1}. As expected from Eq. 3.34, while the boundary between the stable and unstable regimes is symmetrical in the plane (k_R, k_z), rotation and geometry introduce strong asymmetries in the unstable regime. These asymmetries could affect the shape of the prestellar cores that form within the filament. Notably, as the dashed line corresponds to the fastest growing instability, in the unstable regime we expect perturbations with a small k_R to be less elongated in the z direction than perturbations with a larger k_R. As shown by the figure and Eq. 3.38, this curve intersects the line $k_z = k_R$ around $k_{R,\mathrm{threshold}}/k_0 = 0.31$. We thus expect to observe

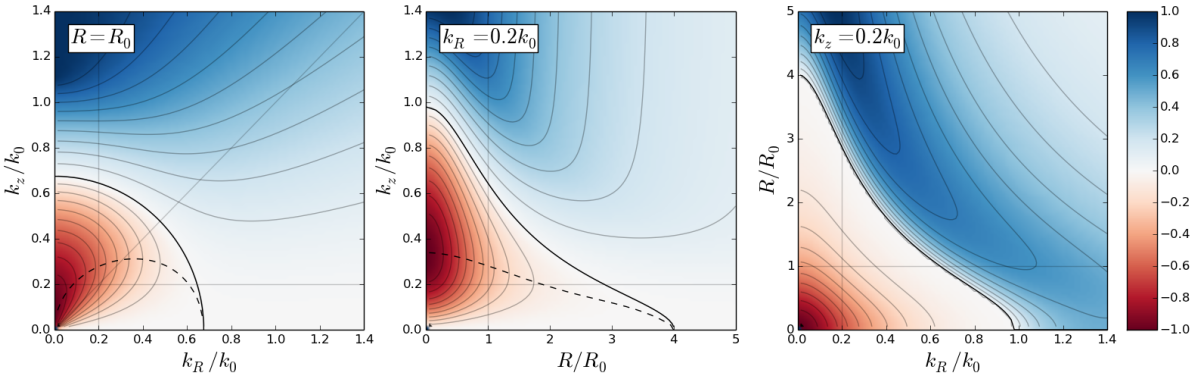

Figure 3.7 – *Projection of the distribution of the frequency x_-^2 in the planes $R = R_0$, $k_R = 0.2k_0$, and $k_z = 0.2k_0$ for an idealized filament inspired by TMC-1, with $R_0 = 0.043$ pc and $k_0 \approx 74$ pc^{-1}. The color scale is normalized to its maximum for positive values of x_-^2 and to its minimum for negative values. The contours are equally spaced. Negative values of x_-^2 correspond to an unstable filament, whereas the filament should be stable in the region where x_-^2 is positive. The solid black curve separates the stable and unstable regimes, and corresponds to $k = k_{\mathrm{crit}}$. This threshold corresponds to a length scale $\lambda_{\mathrm{crit}} = 2\pi/k_{\mathrm{crit}} = 0.13$ pc at $R = R_0$. The dashed line corresponds to the minimum value of x_-^2, i.e., to the most unstable mode, and is obtained from Eq. 3.37 for the first panel. It intersects the line $k_z = k_R$ at $k_{R,\mathrm{threshold}} = 0.31k_0$, which corresponds to $\lambda_{\mathrm{threshold}} = 0.28$ pc.*

oblate structures of radius greater than $\lambda_{\rm threshold} = 2\pi/k_{R,\rm threshold} = 0.28$ pc, and prolate structures below. The maps of the TMC-1 filament presented by Malinen et al. (2012) do reveal clumps along the ridge of the filament: some of them are visible in the *Herschel* image presented Fig. 3.6, others show more clumps at different wavelengths. Comparing their properties with our analytical results could enable to better understand the effect of the cylindrical geometry, albeit depending on the rotation state of the filament.

Comparison with observations

Comparing this result with observations of proto-stellar regions or molecular clouds is not straightforward, as most studies are more interested in the statistical distribution of shapes than in the correlation between shape and size, and as projected quantities are not fully reliable tracers of three dimensional shapes. Most observations in the Taurus molecular cloud or in other molecular clouds favor prolate structures within interstellar filaments and tend to show that cores are elongated along the direction of the filaments (e.g., Myers et al., 1991; Nozawa et al., 1991; Tatematsu et al., 1993; Onishi et al., 1996; Tachihara et al., 2000; Curry, 2002; Hartmann, 2002), which is expected in a picture where cores are formed by gravitational fragmentation of their host filament (e.g., Schneider & Elmegreen, 1979). Jones et al. (2001) and Jones & Basu (2002) also use catalogs of observations for molecular clouds, cloud cores, Bok globules, and condensations to characterize their shape and show that neither pure oblate nor pure prolate cores can account for the observed distribution, and that cores have intrinsically triaxial shapes, but tend to be more prolate on scales $\gtrsim 1$ parsec and closer to oblate between 0.01 and 0.1 parsec. Our result yields the opposite trend, but the comparison between the two studies may be ambiguous and using projected axis ratios not be the best method to distinguish between oblate and prolate structures, as it introduces systematic biases (Curry, 2002).

As our calculations are based on the local WKB assumption $k_R R_0 \gg 1$, the dispersion relation does not rigorously apply when the wavelength $2\pi/k_R$ is large compared to the typical size of the density distribution, and it is thus difficult to assess the relative importance of oblate and prolate cores from this dispersion relation. Moreover, observation of filaments with clumps of star formation whose size is comparable to the thickness of the filament could imply that the whole filament collapses along its axis into several clumps, which would not be a local collapse.

The discrepancies between the predicted and observed shapes could not only be the consequence of non-local perturbations, but could also be explained if observed structures have grown in the non-linear regime. A fastest growing mode that is an oblate perturbation in the linear regime could indeed further collapse to a more prolate structure within the embedding filament in the non-linear regime, as suggested by the numerical calculation carried out by Inutsuka & Miyama (1997) for isothermal filaments of mass per unit length close to the critical equilibrium value.

Rotation also logically tends to favor oblate perturbations. Underestimating the velocity scale appearing in the pressure term, for example by using a thermal velocity instead

of taking turbulence into account, consequently produce more oblate structures than it should. Further studies would be necessary to evaluate the match between observations and the dispersion relation we obtain, which is beyond the illustrative scope of this numerical application.

3.2.4 An order-of-magnitude estimate for cosmic filaments

Maps of the galaxy distribution in the Universe reveal large coherent structures such as filaments and walls (e.g., Geller & Huchra, 1989; Gott et al., 2005). Simulations explain these alignments and predict the existence of a dark matter and gaseous cosmic web that would connect galaxies one to another (cf. section 3.1.2 and for example Bond et al., 1996; Springel et al., 2005; Kereš et al., 2005; Dekel et al., 2009a; Fumagalli et al., 2011). Direct unequivocal evidence of the dark matter and gas filaments is still lacking, and we have to rely on simulations to describe them. Harford & Hamilton (2011) study a cosmological simulation at redshift $z = 5$ and show that the inner core of intergalactic filaments is predominantly made of gas and that a significant fraction of them can be described as isothermal gas cylinders. An effective sound speed c_s can be computed from the isothermal profile (Eq. 3.14), and this quantity is shown to correspond to the actual sound speed determined from the temperature for a significant fraction of the filaments. The central gas density of these filaments is about 500 times the mean cosmic density at the simulation redshift, i.e., about 0.1 cm^{-3}. Assuming that the inner part of these filaments is molecular and atomic, the temperatures of $(1-2)\ 10^4$ K obtained by Harford & Hamilton (2011) correspond to a sound speed between $6-12$ km s^{-1}. The stability threshold given by Eq. 3.34 applied at the center of such a filament leads to a characteristic scale $\lambda_{\rm crit} = 2-4$ kpc for the structures that would form within it, which corresponds approximately to the size of the filaments. This is consistent with a model in which cosmic filaments are shaped by gravity and are not merely intersections of sheets. In retrospect, this justifies modeling them as self-gravitating cylinders. However, we neglected here the influence of the expansion of the Universe, which should stabilize the cosmological filaments against gravitational collapse.

3.3 Large-scale perturbations in a static filament

3.3.1 Limits of the local dispersion relation

Assuming perturbations smaller than the typical size of the density distribution, we derived a dispersion relation for axisymmetric perturbations in an infinite, self-gravitating, and rotating filament (Eq. 3.27). This dispersion relation yields a symmetrical threshold in the axial and radial wavenumbers between the stable and unstable regions, but the fastest growing mode breaks this symmetry and should influence the shape of the resulting perturbations. However, the local WKB assumption prevents the perturbations feeling

the large-scale geometry of the system and thus leads to the standard spherical Jeans case when there is no rotation. The asymmetry of the fastest growing mode comes from the rotation of the filament. Gravitational collapse should enhance rotation in interstellar and cosmic filaments due to angular momentum conservation. But although signs of rotation such as transverse velocity gradients are observed for interstellar filaments, and notably for TMC-1 (Olano et al., 1988), there generally does not seem to be a global coherent rotation of such filaments, as assumed in our calculations (e.g., Loren, 1989; Tatematsu et al., 1993; Falgarone et al., 2001). Additionally, turbulent processes would probably disturb the rotation that may arise. Hence, our first calculations probably overestimate the effects of rotation when applied to interstellar filaments, and thus artificially favor oblate structures. They would however remain relevant in cases of coherently rotating filaments.

We now aim at obtaining a more general dispersion relation, that would better fit the observed properties of interstellar filaments. Removing the WKB assumption should enable to better understand the specific effects of cylindrical geometry, and we will further assume non-rotating filaments for simplicity as observations do not seem to indicate coherent rotation in the case of interstellar filaments.

3.3.2 A dispersion relation with complex terms

Full dispersion relation

Without the local WKB assumption $k_R R_0 \gg 1$, the derivatives present in the hydrodynamic equations yield additional terms that were neglected in Eqs. 3.23 to 3.25 and in the linearized system of equations 3.26. Adding these terms to the linear equations yield

$$\begin{cases} \omega v_{1R} - 2i\Omega_0 v_{1\theta} = k_R \dfrac{c_0^2}{\rho_0}\rho_1 - i\rho_1 \dfrac{\partial}{\partial R}\left(\dfrac{c_0^2}{\rho_0}\right) + k_R \Phi_1 \\ \omega v_{1\theta} - 2iBv_{1R} = 0 \\ \omega v_{1z} = k_z \dfrac{c_0^2}{\rho_0}\rho_1 + k_z \Phi_1 \\ \omega \rho_1 - \rho_0 k_r v_{1R} + i v_{1R} \dfrac{1}{R}\dfrac{\partial}{\partial R}(R\rho_0) - k_z \rho_0 v_{1z} = 0 \\ -k_R^2 \Phi_1 + i\dfrac{k_R}{R}\Phi_1 - k_z^2 \Phi_1 = 4\pi G \rho_1. \end{cases} \tag{3.40}$$

where the previously neglected terms have been highlighted in blue. Introducing the characteristic angular frequency $\omega_0 = \sqrt{4\pi G \rho_c}$ and the dimensionless variable $x = \omega/\omega_0$ as in section 3.2.2 again enables to express the resulting dispersion relation as a fourth order polynomial equation (cf. Appendix E.4)

$$x^4 + Ax^2 + B = 0 \tag{3.41}$$

with

$$A = \frac{\rho_0}{\rho_c}\left(1-i\frac{k_R}{k^2}\frac{1}{R\rho_0}\frac{\partial}{\partial R}\left(R\rho_0\right)\right)\left(1+i\frac{\frac{k_R}{R}}{k^2-i\frac{k_R}{R}}\right)$$

$$-\frac{c_0^2k^2}{\omega_0^2}\left(1-i\frac{k_R}{k^2}\frac{1}{Rc_0^2}\frac{\partial}{\partial R}\left(Rc_0^2\right)-\frac{1}{k^2}\frac{1}{Rc_0^2}\frac{\partial}{\partial R}\left(R\rho_0\right)\frac{\partial}{\partial R}\left(\frac{c_0^2}{\rho_0}\right)\right)-\frac{\kappa^2}{\omega_0^2} \tag{3.42}$$

and

$$B = \frac{\kappa^2k_z^2}{\omega_0^2}\left(\frac{c_0^2}{\omega_0^2}-\frac{1}{k^2}\frac{\rho_0}{\rho_c}\left(1+i\frac{\frac{k_R}{R}}{k^2-i\frac{k_R}{R}}\right)\right). \tag{3.43}$$

Without the local WKB assumption, the dispersion relation retains its complex terms and all modes are potentially unstable. This dispersion relation is valid in the case of an infinite barotropic gas filament with cylindrical symmetry. We assume no radial velocity and the same velocity along the direction of the cylinder for all particles in the unperturbed system. Perturbations are assumed to be small enough to linearize the equations and we use Fourier decomposition to consider modes proportional to $e^{-i\omega t}e^{ik_RR}e^{ik_zz}$.

Non-rotating filaments

As observations do not particularly favor coherently-rotating filaments, we neglect rotation. In this case, the dispersion relation yields

$$\omega^2 = -4\pi G\rho_0\frac{k^2}{k^2-i\frac{k_R}{R}}\left[1-i\frac{k_R}{k^2}\left(\frac{1}{R}+\frac{1}{\rho_0}\frac{\partial\rho_0}{\partial R}\right)\right]+c_0^2k^2$$

$$-ik_R\left[\frac{c_0^2}{R}+\frac{\partial c_0^2}{\partial R}\right]-\left[\frac{1}{R}+\frac{1}{\rho_0}\frac{\partial\rho_0}{\partial R}\right]\left[\frac{\partial c_0^2}{\partial R}-c_0^2\frac{1}{\rho_0}\frac{\partial\rho_0}{\partial R}\right], \tag{3.44}$$

from which we can separate the real and imaginary parts of the square of the pulsation frequency:

$$\mathrm{Re}(\omega^2) = c_0^2k^2\left[1+\frac{1}{k^2}\left(\frac{1}{\rho_0}\frac{\partial\rho_0}{\partial R}-\frac{1}{c_0^2}\frac{\partial c_0^2}{\partial R}\right)\left(\frac{1}{R}+\frac{1}{\rho_0}\frac{\partial\rho_0}{\partial R}\right)\right]$$

$$-4\pi G\rho_0\frac{k^4}{k^4+\left(\frac{k_R}{R}\right)^2}\left[1+\frac{k_R^2}{k^4}\frac{1}{R}\left(\frac{1}{R}+\frac{1}{\rho_0}\frac{\partial\rho_0}{\partial R}\right)\right] \tag{3.45}$$

$$\mathrm{Im}(\omega^2) = 4\pi G\rho_0\frac{k_Rk^2}{k^4+\left(\frac{k_R}{R}\right)^2}\frac{1}{\rho_0}\frac{\partial\rho_0}{\partial R}-k_R\left[\frac{c_0^2}{R}+\frac{\partial c_0^2}{\partial R}\right]. \tag{3.46}$$

3.3.3 Application to TMC-1

Representation of the growth rate in the plane (k_R, k_z)

We represent the effects of the imaginary terms of the dispersion relation by numerically evaluating $\mathrm{Im}(\omega/\omega_0)$ for an idealized filament inspired by TMC-1 as in section 3.2.3, and by plotting this quantity in the (k_R, k_z) plane at different radii R as shown in Fig. 3.8. The fiducial filament has a Plummer-like density profile with parameters as observed by Malinen et al. (2012) for TMC-1, i.e., $\rho_c = 7\ 10^4$ cm^{-3}, $R_0 = 0.043$ pc and an exponent

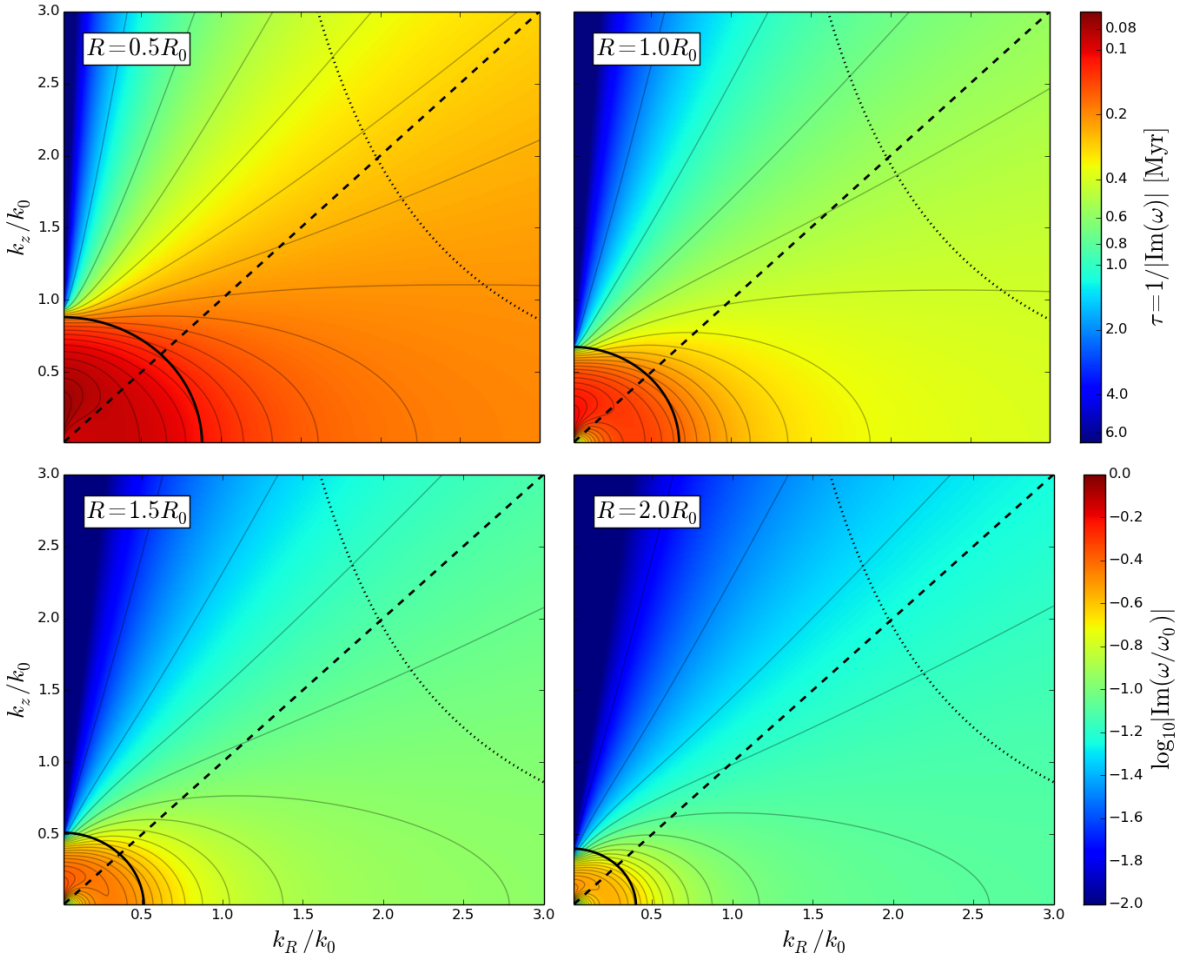

Figure 3.8 – *Imaginary part of the angular frequency resulting from the dispersion relation 3.44 for an idealized filament inspired by TMC-1 in the plane (k_R, k_z) at different radii. The plotted quantity is a measure of the growth rate of the perturbations, or alternatively, of its associated timescale τ. The black solid arc of a circle corresponds to $k = \sqrt{k_R^2 + k_z^2}$ equals $k_{\mathrm{crit}} = \sqrt{4\pi G\rho_0}/c_0$, the wavenumber separating the stable and unstable domains according to the local dispersion relation 3.27, while the black dashed line corresponds to $k_R = k_z$. The dotted line follows a set of modes with similar volumes in the plane (k_R, k_z), i.e., with $k_z \propto 1/k_R^2$.*

$p = 1.1$. Again, we further assume a constant thermal sound speed $c_0 = 200$ m s^{-1}, so the characteristic wavenumber $k_0 = \omega_0/c_0 \approx 74$ pc^{-1}. Physically, $\mathrm{Im}(\omega/\omega_0)$ corresponds to the growth rate of the unstable modes in units of $\omega_0 \approx 15$ Myr^{-1}, so it can also be translated into a timescale $\tau = 1/|\mathrm{Im}(\omega)|$. A perturbation mode of characteristic scale $R_0 = 0.043$ pc would have a wavenumber $2\pi/R_0 \approx 2k_0$ with these settings, so small perturbations compared to the size of the filament would have characteristic wavenumbers above this value. As shown in the figure, while the separation between stable and unstable modes was symmetrical in k_R, k_z when assuming small local perturbations with the WKB assumption (cf. section 3.2.2 and Fig. 3.7), the distribution of $\mathrm{Im}(\omega/\omega_0)$ here loses its symmetry without any rotation. In the region within the arc of circle $k = k_{\mathrm{crit}}$, the behavior of $|\mathrm{Im}(\omega/\omega_0)|$ is less regular than elsewhere, but this region corresponds to very large perturbations compared to the size of the filament and is thus less relevant physically.

Prolate substructures are favored

The solid black arc of a circle represents the symmetrical threshold of section 3.2.2, where the total wavenumber $k = \sqrt{k_R^2 + k_z^2}$ equals $k_{\mathrm{crit}} = \sqrt{4\pi G\rho_0}/c_0$. But instead of following this arc, the nearby lines of equal growth rate draw ellipses whose major axis coincides with the $k_z = 0$ line, thus favoring more prolate modes with $k_z < k_R$ than obtained in the previous section. At a given radial wavenumber k_R, the growth rate also generally increases with decreasing k_z, which again favor prolate collapsed substructures. Moreover, the growth rate generally increases for smaller radii, thus favoring perturbations near the axis of the filament.

If at a given radius we consider a set of individual modes with equal volumes, i.e., with their wavenumbers varying as $k_z \propto 1/k_R^2$, the growth rate associated to the different modes would increase with decreasing k_z and increasing k_R. The dotted curves of Fig. 3.8 correspond to modes with a constant volume such that

$$k_z k_R^2 = \left(\frac{2\pi}{R_0}\right)^3, \tag{3.47}$$

thus including the mode $k_R = k_z = 2\pi/R_0$ whose characteristic length scales all equal R_0. The growth rate of these modes increases along the curve from left to right, so such an evolution conserving the volume is more likely to produce more and more elongated structures.

As already mentioned, the fact that elongated substructures are favored is corroborated by most observations in the Taurus molecular cloud and elsewhere. Indeed, pre-stellar cores are often found to be stretched along the direction of the filaments in which they reside (e.g., Myers et al., 1991; Nozawa et al., 1991; Tatematsu et al., 1993; Onishi et al., 1996; Tachihara et al., 2000; Curry, 2002; Hartmann, 2002). Further work would be needed to better understand the general dispersion relation found here and its implications for observations. We are notably planning to carry out numerical simulations of idealized filaments such as the one inspired by TMC-1 that was considered here.

3.4 Discussion and perspectives

3.4.1 Summary

To investigate the growth of instabilities within filamentary structures and the properties of the resulting condensations, we considered idealized self-gravitating filaments and derived the dispersion relation for small linear perturbations within them. We assumed no specific density distribution, treated matter as a fluid, and used hydrodynamics to derive the linearized equations that govern the growth of perturbations. The fluid was assumed to be barotropic, which includes the narrower isothermal and polytropic cases, and the system cylindrically symmetric. We used an interstellar filament observed in the Taurus Molecular Cloud, TMC-1 (Nutter et al., 2008; Malinen et al., 2012), as fiducial numerical application, and notably represented the properties of the dispersion relation in the (k_R, k_z) phase plane. Assuming small local perturbations within a rotating filament leads to a dispersion relation analogous to the spherical Jeans case: perturbations of size higher than the Jeans length collapse and asymmetries regarding their growth rates arise because of rotation. The assumption of local perturbations prevents them from feeling the large-scale geometry of the system, hence leading to the standard spherical case when there is no rotation. For perturbations of arbitrary size, the dispersion relation retains its complex terms so all modes are potentially unstable. However, elongated perturbations near the axis of the cylinder grow faster. Prolate substructures and global collapse seem to be favored, which would be corroborated by most observations of interstellar filaments.

3.4.2 Discussion

Our calculations focus on the initial linear phase of the perturbations, implicitly assuming that this first evolution stage sets part of the properties of the resulting collapsed structures. We also rely on a number of simplifying assumptions, amongst them neglecting the magnetic fields and the environment surrounding the filaments as well as assuming that the filaments are bound and self-gravitating, which is probably not the case for all filaments of the interstellar medium (e.g., Falgarone et al., 2001).

Unperturbed velocity distribution and dispersion

We assumed the same initial axial velocity for all particles, which enabled us to remove the velocity dependence in the reference frame of the unperturbed system. Although there may be an average axial flow towards one edge of the filament, the initial velocity distribution of the particles is likely to be more complex than assumed here. For example, the case of a Maxwellian distribution could be studied in more detail, as well as the case of accelerated particles. Peretto et al. (2013) and Zernickel et al. (2013) indeed observe coherent velocity gradients along interstellar filaments and interpret them as

a large-scale longitudinal collapse. Filaments feel the gravitational acceleration from the structures onto which they are accreted, thus leading to accelerated particles. The longitudinal expansion of tidal tails has notably been shown to have a strong stabilizing effect (Schneider & Moore, 2011).

In our numerical applications, we invariantly assumed a constant speed of sound corresponding to a thermal sound speed. However, the pressure support is probably at least partly due to turbulence, notably as thermal support is insufficient to explain the observed lifetimes of giant molecular clouds (cf. section 1.3.1). Additionally, the turbulent velocity dispersion might vary with the radius of the filament. Indeed, the velocity dispersion σ is expected to increase with the size R of the filament, as given by Larson's relation $\sigma \propto R^{0.5}$ (cf. section 1.3.1 and Larson, 1981; Solomon et al., 1987; Blitz et al., 2007). This would supply an additional support against gravitational collapse for larger radii. The resulting stability gain could replace that due to rotation, with similar scale dependence, depending on the density distribution.

Magnetic fields

We neglected the role of magnetic fields in our calculations, although they are ubiquitous in the interstellar medium and could affect filament stability. Even a small magnetic field can generally play a significant role in gas dynamics, and moderate fields can have a strong impact on the fragmentation of gas clouds and on the formation of pre-stellar cores (McClure-Griffiths et al., 2006; Hily-Blant & Falgarone, 2007; Nakamura & Li, 2008; Tilley & Pudritz, 2007; Li et al., 2010; Hennebelle, 2013; André et al., 2014). The magnetic forces are indeed intrinsically anisotropic, which promotes fragmentation. By studying numerically the dispersion relation for magnetized and non-magnetized isothermal filaments, Nagasawa (1987) has shown that a uniform axial magnetic field does not change the critical wavenumber but efficiently stabilizes the filament by reducing the growth rate of the unstable modes. A generalization of our calculations including magnetic fields in different configurations would help us understand the formation of pre-stellar cores within interstellar filaments.

The role of the environment

Our model also implicitly assumes an isolated filament, surrounded by voids, whereas interstellar and cosmic filaments are typically embedded in intricate networks. Indeed, interstellar filaments tend to branch out from dense star-forming hubs (Myers, 2009) or to group in smaller-scale bundles of similar properties and common physical origin (Hacar et al., 2013). These bundles may result from the fragmentation of the initial cloud into different sub-regions, that further condense into velocity-coherent filaments. Gas accretion onto the filaments is also expected to play a major role, as it not only brings mass but also drives internal turbulence and affects the stability of the filament (Klessen & Hennebelle, 2010; Heitsch, 2013). Indeed, filaments are not static but highly

dynamical systems. They often show striations from which material can be added, and they are themselves feeding hubs in which clustered star formation occur (e.g., André et al., 2014). There are tendrils, knots and torsions affecting interstellar filaments, and potentially imposing torques and an angular velocity varying along the filament and its radius, $\Omega_0(R, z)$. Some of the filaments could also be out of equilibrium, and possibly expanding radially. Could collapse nevertheless occur locally in such a filament? The interaction between filaments and with their environment, including tidal fields as shown in the spherical Jeans case (Jog, 2013), is likely to influence their fragmentation, and should be further investigated. At cosmological scales, numerical simulations of structure formation in the Universe show that cosmological filaments often merge with each other to form bigger and bigger filaments, thus increasing the density contrast with the surrounding voids (e.g., Springel et al., 2008; Klypin et al., 2011; Vogelsberger et al., 2014).

Non-axisymmetric perturbations

While the study of the environmental effects on the formation of prestellar cores requires a more detailed study, some limited generalizations of our calculations could be achieved more easily. We notably limited ourselves to axisymmetric perturbations, while the case of non-axisymmetric perturbations could also be of interest. Such perturbations are notably envisaged numerically for an isothermal cylinder by Nagasawa (1987), which could provide a useful comparison. We could follow up some of these ideas in the future, as well as address the influence of magnetic fields on our results, and carry out a more detailed comparison of the local dispersion relation found here with observations and simulations.

3.4.3 RAMSES simulations

In order to better understand our analytical results and the fragmentation of elongated filaments into pre-stellar cores in the interstellar medium, we started to carry out numerical simulations of idealized filaments with the adaptive mesh refinement (AMR) code RAMSES (Teyssier, 2002). This numerical code solves the hydrodynamic equations on an adaptive Cartesian grid and allows a wide range of options for the simulated physical processes. The setup to simulate an idealized filament is almost in place, but the results yet very preliminary as not all relevant physical processes have been taken into account. The initial conditions are implemented as specific Fortran files `condinit.f90` and `units.f90` in the patch directory.

An idealized filament

The initial unperturbed conditions correspond to a non-rotating isolated filament with a Plummer-like density profile

$$\rho_0(R) = \frac{\rho_c}{\left(1 + \left(\frac{R}{R_0}\right)^2\right)^p}, \tag{3.48}$$

where ρ_c, R_0 and p enter in the parameter file of the simulation code. This filament is assumed to be in hydrostatic equilibrium so its unperturbed pressure $p_0(R)$ is defined from

$$\frac{dp_0}{dR} = -\rho_0 \frac{d\Phi_0}{dR}, \tag{3.49}$$

where $\Phi_0(R)$ is the gravitational potential. Poisson's equation yields for such a Plummer-like density profile a gravitational force

$$\frac{d\Phi_0}{dR} = \frac{2\pi G \rho_c R_0^2}{p-1} \frac{1}{R} \left(1 - \frac{1}{\left(1 + \left(\frac{R}{R_0}\right)^2\right)^{p-1}} \right) \tag{3.50}$$

when $p \neq 1$, and

$$\frac{d\Phi_0}{dR} = 2\pi G \rho_c R_0^2 \frac{1}{R} \ln\left(1 + \left(\frac{R}{R_0}\right)^2\right) \tag{3.51}$$

when $p = 1$ (cf. Appendix E.5). Given these expressions, the resulting pressure p_0 is computed as an integral from its radial derivative (Eq. 3.49). The corresponding energy density is the sum of the kinetic energy density and of the thermal internal energy density

$$u = \frac{p_0}{\gamma - 1} \tag{3.52}$$

where γ is the adiabatic index and the gas treated as an ideal gas. In the absence of perturbations and without additional forces, the filament defined here is stable.

We assume periodic boundary conditions in all directions, so the filament is infinite in the longitudinal z direction but not rigorously isolated: there is virtually an infinite number of replicates of the same filament in the x and y directions. The computational domain is chosen to be large enough to neglect the gravitational influence of these virtual replicates.

Density and velocity perturbations

In order to trigger gravitational instabilities within the filament, we introduce some stochasticity in the density field, namely by adding a small Gaussian perturbation in each cell. However, as the AMR cells have different sizes for different AMR levels l, the associated standard deviation σ_l should not be a constant because a bigger cell corresponds to an average over a large number of smaller cells and should thus yield a smaller standard deviation at constant density ρ. The relative standard deviation σ_l/ρ at a given level l should not be constant either: as the density varies, σ_l/ρ should depend on the number of particles N present in each cell and accordingly decrease as $1/\sqrt{N}$ when density increases.

To correctly model perturbations arising from the stochasticity of gas particles, we consider that a single such particle would result in an uncertainty σ_0 on the density,

which is an extensive quantity. Consequently, at the finest level l_{max} where the grid cell size is $\Delta x_{l_{max}}$, the total density ρ of a cell comprising

$$N = \frac{1}{m}\rho \ (\Delta x_{max})^3 \tag{3.53}$$

particles of mass m should have a standard deviation

$$\sigma_{l_{max}} = \sqrt{N} \ \sigma_0. \tag{3.54}$$

In particular, a similar cell at the center of the filament would comprise N_c particles and its density would have a standard deviation

$$\sigma_{l_{max},c} = \sqrt{N_c} \ \sigma_0. \tag{3.55}$$

Introducing the relative standard deviation at the center $s_{rc} = \sigma_{l_{max},c}/\rho_c$ yields

$$\sigma_{l_{max}} = \sqrt{\frac{N}{N_c}} \ \sigma_{l_{max},c} = \left(\frac{\rho}{\rho_c}\right)^{1/2} s_{rc} \ \rho_c = (\rho\rho_c)^{1/2} \, s_{rc}. \tag{3.56}$$

Now considering that a cell of size Δx_l at level l encompasses

$$N' = \left(\frac{\Delta x_l}{\Delta x_{l_{max}}}\right)^3 \tag{3.57}$$

cells of size $\Delta x_{l_{max}}$, the standard deviation in a cell of density ρ at level l should be

$$\sigma_l = \frac{\sigma_{l_{max}}}{\sqrt{N'}} = s_{rc} \ (\rho\rho_c)^{1/2} \ \left(\frac{\Delta x_{l_{max}}}{\Delta x_l}\right)^{3/2}. \tag{3.58}$$

The parameter s_{rc} controls the relative importance of the density fluctuations at the center of the filament, and constitutes one of the inputs of the model.

Similarly, we could also introduce a Gaussian random velocity to the different cells, corresponding to a Maxwell-Boltzmann distribution for the gas particles. The Gaussian random field would again depend on the density and the cell size. However, as the velocity is an intensive quantity, the dependence in the density ρ would be different: the standard deviation would be proportional to $1/\sqrt{\rho}$ instead of being proportional to $\sqrt{\rho}$. More precisely, the velocity standard deviation of a particle of mass m with a Maxwell-Boltzmann distribution is

$$\Delta v_0 = \sqrt{\frac{kT}{m}} \tag{3.59}$$

where T is the gas temperature. Consequently, the velocity standard deviation associated to a grid cell of size Δx_l and density ρ comprising $N = \rho \ (\Delta x_l)^3 / m$ particles should be

$$\Delta v_l = \frac{1}{\sqrt{N}} \ \Delta v_0 = \sqrt{\frac{kT}{\rho \, (\Delta x_l)^3}}. \tag{3.60}$$

But such a velocity standard deviation would be highly negligible given the involved scales and the fact that the AMR grid precisely adapts itself to the cell density in order to have a roughly constant mass per cell. Alternatively, it could be possible to introduce a velocity dispersion following Larson's relation (cf. section 1.3.1) in order to account for interstellar turbulence. But for the moment, we only include density fluctuations in our model.

Refinement strategy

The computational domain is chosen to be a cube of size $l_{box} = 10$ pc, which is much larger than the characteristic scale of the filament $R_0 = 0.1$ pc. The coarsest level of the AMR grid is $l_{min} = 4$, which corresponds to a Cartesian grid with $\left(2^4\right)^3$ elements and with a cell size of 0.625 pc. The grid resolution is adapted at each time step depending on the density between the low refinement level $l_{min} = 4$ and $l_{max} = 10$. At the highest level of refinement, the cell size is about 0.01 pc so as to resolve the central area of the filament within R_0 by at least 20 cells in the radial direction. At each timestep, an AMR cell is divided into eight smaller new cells if the mass within it exceeds $8 \times \texttt{mass\_sph} = 0.0008$ $M_\odot$. This threshold is chosen in order to reach the finest level before $\rho \gtrsim \rho_c/2$. A cell of density $\rho_c/2$ at level $l_{max} - 1$ will indeed be refined at level l_{max} if its mass

$$\frac{\rho_c}{2} \left(\Delta x_{l_{max}-1}\right)^3 \geqslant 8 \times \texttt{mass\_sph}, \tag{3.61}$$

which corresponds to $\texttt{mass\_sph} \leq 2.7\ 10^{-4}$ $M_\odot$ given ρ_c and $l_{max} = 10$. We chose a slightly lower value of `mass_sph` in order to reach the finest refinement level even before.

Avoiding artificial fragmentation

The standard Jeans instability within a gaseous cloud (Jeans, 1902, 1928) results in perturbations of scale larger than the Jeans length to be unstable: for such perturbations, the inner pressure is too weak to overcome self-gravity and the cloud collapses. Numerical methods always produce finite errors during the discretization process, and notably at the spatial resolution scale. These errors can act as perturbations to the exact solution and can thus lead to growing instabilities if larger than the Jeans length (Truelove et al., 1997). Interestingly, although such instabilities are triggered by numerical errors, the driver of their growth is a physical process, the Jeans instability. It would nevertheless lead to an artificial fragmentation, which is to be avoided - especially when aiming at better understanding gravitational instabilities. Truelove et al. (1997) show that always resolving the Jeans length by at least four cells is enough to prevent this artificial fragmentation. But since the Jeans length is defined as

$$\lambda_{\rm J} = \left(\frac{\pi c^2}{G\rho}\right)^{1/2} \tag{3.62}$$

where c and ρ are the local sound speed and gas mass density, it decreases progressively while the cloud collapses and can eventually fall below the resolution scale Δx. A method to ensure that $\lambda_{\rm J} \geq 4\ \Delta x$ consists in imposing a polytropic pressure floor (Robertson & Kravtsov, 2008; Teyssier et al., 2010). Indeed, a minimum pressure

$$p_{\rm min} = \frac{16 \Delta x^2 G \rho^2}{\pi \gamma} \tag{3.63}$$

enforces $\lambda_{\rm J} \geq 4\Delta x$, γ being the adiabatic index [2]. This pressure floor proportional to ρ^2 corresponds to a polytropic index `g_star` $= 2$ and can also be expressed as a temperature floor

$$T_{\rm min} = \frac{16\Delta x^2 G m \rho}{\pi \gamma k_B} \tag{3.66}$$

where $m = m_{\rm H}/{\rm X}$ is the mean mass per particle, with ${\rm X} = 0.75$. Such a temperature threshold can be introduced within RAMSES through the variables `g_star` $= 2$, `T2_star` and `n_star`. When the polytropic index equals 2, the minimum Jeans length is also conveniently constant.

Preliminary test results

As a first simulation attempt, we consider an idealized interstellar filament whose properties are of the same order of magnitude as those of TMC-1 or the filaments observed by Arzoumanian et al. (2011). We assume an isothermal profile with Plummer exponent $p = 2$ and add density perturbations with a relative standard deviation at the center $s_{rc} = 10^{-2}$. The parameters defining these initial conditions are summarized in Table 3.1. The RAMSES simulation code includes different models for cooling, heating, metal enrichment or even star formation. This first attempt was carried out with default values for the parameters ruling these processes, so a more careful tuning would be necessary to obtain truly physically meaningful results. Varying these parameters would also help testing our model and better understanding the formation of pre-stellar cores within the filaments of the interstellar medium.

Central density	ρ_c	10^4 cm^{-3}
Characteristic radius	R_0	0.1 pc
Plummer exponent	p	2
Adiabatic index	γ	5/3
Central relative standard deviation	s_{rc}	0.01

Table 3.1 – *Parameters setting the initial conditions for an idealized interstellar filament.*

[2] The sound speed being defined for an ideal gas as $c = \left(\gamma p/\rho\right)^{1/2} = \left(\gamma kT/m\right)^{1/2}$, where m is the mean mass per particle and γ the adiabatic index,

$$\lambda_{\rm J} \geq 4\Delta x \iff \frac{\pi c^2}{G\rho} \geq 16\Delta x^2 \iff \frac{\pi}{G\rho}\left(\frac{\gamma p}{\rho}\right) \geq 16\Delta x^2 \iff p \geq \frac{16\Delta x^2 G \rho^2}{\pi\gamma} \tag{3.64}$$

and alternatively,

$$\lambda_{\rm J} \geq 4\Delta x \iff \frac{\pi}{G\rho}\left(\frac{kT}{m}\right) \geq 16\Delta x^2 \iff T \geq \frac{16\Delta x^2 G m \rho}{\pi\gamma k}. \tag{3.65}$$

Fig. 3.9 displays the evolution with time of the fiducial filament. After having been relatively stable during 5 Myr, it fragments into high-density spherical structures. The time during which the filament remains stable probably depends on the level of the fluctuations, s_{rc}, but the subsequent collapse happens within a few dynamical timescales, which is comparable to what simulations of core formation in the interstellar medium usually yield (e.g., Kudoh & Basu, 2008; Basu et al., 2009a,b; André et al., 2009; Gong & Ostriker, 2015). Although the cylindrical symmetry of the system initially favors elongated perturbations, the resulting pre-stellar cores are spherical. The fact that the overall cylindrical geometry is not fundamentally disturbed might be explained by the low level of the perturbations that were introduced, or possibly also by the gravitational influence of the virtual filament replicates. The latter possibility would require to increase the box size or change the boundary conditions. In any case, a more detailed and quantitative study would be necessary to better understand the relation between the properties of the pre-stellar cores and their parent filament. In particular, their size, shape and the separation between them could result from some of the filament's properties. The results would also be compared with the dispersion relation obtained analytically in section

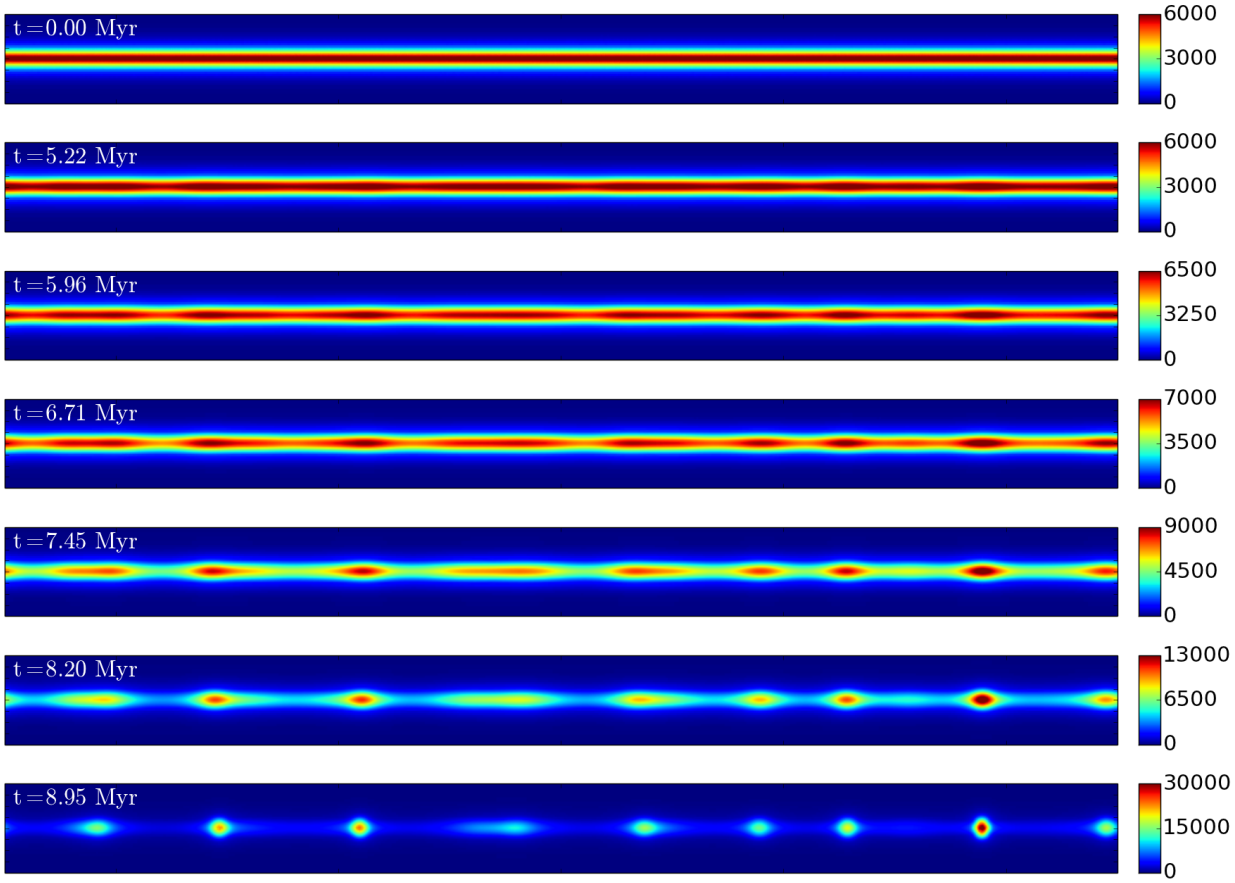

Figure 3.9 – *Evolution of the projected density of an idealized interstellar filament defined as in Table 3.1. The plotted quantity is the volume-density-weighted gas density of the filament along a direction perpendicular to its axis. The axes of the figure span 10 pc in length and 0.8 pc in width.*

3.3. Physically-motivated parameters should be introduced to account for the different baryonic processes, taking advantage of the numerous options offered by the RAMSES code. Amongst them, those supervising cooling, heating, metal enrichment or even star formation and magnetic fields. Our simulations are yet only very preliminary, and should be further investigated.

Galaxy-scale simulations

We are also potentially planning to carry out simulations at larger scales in relation with the observational study presented in Chapter 2. Indeed, the first PHIBSS program has uncovered large molecular gas reservoirs in high redshift galaxies, and simulating such galaxies enables to better understand the cosmic evolution of the star formation rate and the quenching of star formation. As in the ALMA project briefly presented in section 2.4.4, we would concentrate in particular on the relations characterizing star formation at sub-galactic scales, and on the fate of the star-forming regions. Such simulations would also use the RAMSES simulation code and could benefit from the DICE software (Perret et al., 2014), which generates idealized initial conditions for disk galaxies.

Part Three

The influence of baryonic processes on dark matter haloes

CHAPTER 4

From cusps to cores: a stochastic model

Galaxy and star formation in the ΛCDM cosmological model result from a cosmic evolution primarily driven by dark matter dynamics, as baryons only represent a small fraction of the mass and are assumed to condense within dark matter haloes. But star formation and dissipative baryonic processes can in turn affect the dark matter distribution at galactic scales, notably through the different feedback mechanisms. Stars and active galactic nuclei (AGN) indeed give rise to powerful outflows and shock waves which can perturb the gravitational potential of a galaxy and hence the trajectories of the dark matter particles. Such interactions between the baryonic and dark matter components could help solve the remaining discrepancies between the ΛCDM model and observations.

Despite its huge success at explaining the large scale structure of the Universe, the standard ΛCDM model indeed faces severe challenges when confronted with observations at galactic and galaxy cluster scales. The core-cusp problem is one of these apparent discrepancies: early simulations based on the ΛCDM paradigm overpredicted the dark matter density at the center of dark matter haloes. Whereas observations show core-like behaviours in the inner parts of such systems, simulations yielded much steeper, cuspy profiles. Different options can be considered for resolving these challenges. Amongst them, introducing lighter dark matter particles instead of the weakly interacting massive particles usually assumed; rejecting the dark matter scenario itself and explaining the discrepancies between theory and observations by modifying the gravitational laws; and finally, better taking into account the interactions between the baryonic and dark matter components. The effects of the different feedback processes originating from star formation and AGNs at the center of dark matter haloes could indeed significantly change the dark matter distribution and lead to cored density profiles.

In this chapter we study the effects of density fluctuations arising from the different feedback processes on the dark matter distribution through analytical calculations and collisionless numerical simulations. While cosmological simulations of galaxies are already able to reproduce the cored profiles by introducing various feedback mechanisms, we do not detail these complex phenomena and rather model their possible effect as Gaussian random processes, particularly with power-law spectra. The aim is to develop and test

a general theoretical model, and to understand the effects associated with the density fluctuations as inferred from the simulations and their dependence on the physical input and numerical implementation. We notably derive the velocity variance resulting from the perturbations, as well as the characteristic relaxation time of the dark matter particles. We show that these perturbations can indeed transform the cuspy density profile into a cored one, and could thus help resolve the core-cusp discrepancy.

This chapter first presents some of the challenges faced by the ΛCDM model at galactic scales, before focusing on the core-cusp discrepancy and on the processes through which baryons could affect the dark matter distribution and resolve the problem. Sections 4.1 and 4.2 introduce the subject, section 4.3 presents our analytical calculations, while sections 4.4 and 4.5 discuss our numerical setup and its results. This work was carried out in collaboration with Amr El-Zant at the British University of Cairo, Egypt, as part of an Imhotep Franco-Egyptian *Partenariat Hubert Curien*.

Contents

Related publication

- El-Zant, A., **Freundlich, J.**, Combes, F., 2015, *From cusps to cores: a stochastic model*, in preparation

4.1 The core-cusp discrepancy

4.1.1 Challenges of the ΛCDM model at galactic scales

The current ΛCDM cosmological model is very successful at describing the evolution of the Universe, from a very homogeneous state as shown by the cosmic microwave background (CMB), to the present day clustered distribution of matter with galaxies, clusters of galaxies and voids between them. The same cosmological parameters that fit so well the CMB power spectrum indeed also predict the mass distribution that is observed today at all scales (Hlozek et al., 2012). Moreover, numerical simulations within the ΛCDM paradigm are now able to produce realistic galaxies and clusters of galaxies whose properties fit well with the observations (e.g., Ocvirk et al., 2008; Primack, 2012; Schaller et al., 2015; Chan et al., 2015). However, while the ΛCDM model agrees so well with observations of the large-scale structure of the Universe, it has faced and still faces challenges on smaller scales. Here is a brief summary of some of these challenges.

"Downsizing"

The ΛCDM model is hierarchical in the sense that small structures form first and progressively merge and accrete to form bigger structures. If all galaxies were forming stars at similar rates, we would not expect bigger ones to have specifically older stellar populations. However, the oldest stellar populations were observed to reside in the most massive galaxies (e.g., Cowie et al., 1996). As it seemed to indicate that massive galaxies formed earlier than less massive ones, in contradiction with the hierarchical scenario, it was considered as one of the first drawbacks of the ΛCDM model. This apparently problematic inversion of the bottom-up hierarchical scenario became known as "downsizing".

But star formation is not equally efficient, and is actually more efficient in haloes whose masses are between 10^{10} and 10^{12} $M_\odot$. Supernova feedback indeed impedes star formation for halo masses below 10^{10} $M_\odot$ (Dekel & Silk, 1986) while AGN activity heats and blows away the gas above 10^{12} $M_\odot$ (Cattaneo et al., 2009). Additionally, cold accretion along filaments of the cosmic web onto the center of galaxies is a characteristic feature of low-mass haloes, but heating dominates above 10^{12} $M_\odot$, where the gas ceases to accrete (Dekel & Birnboim, 2006; Dekel et al., 2009a). Because of the resulting star-forming band between 10^{10} and 10^{12} $M_\odot$, today's massive galaxies are embedded in haloes which crossed the 10^{10} $M_\odot$ threshold earlier and their progenitors thus started to form stars at earlier epochs. Downsizing can consequently be explained within the ΛCDM model.

The "angular momentum catastrophe"

Early ΛCDM simulations formed disks that had much less angular momentum and were thus much smaller than the disks of observed galaxies (Navarro et al., 1995; Steinmetz &

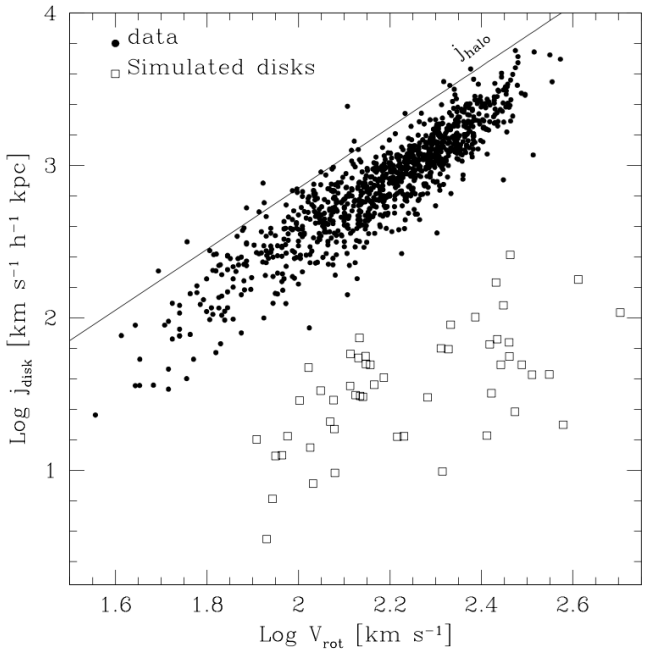

Figure 4.1 – *Comparison of the specific angular momentum of simulated and observed disk galaxies as a function of their rotation velocity, from Steinmetz & Navarro (1999). At any rotation velocity, the angular momentum of simulated galaxies is lower by about an order of magnitude as compared to observations. The solid line shows the typical specific angular momentum of dark matter haloes for comparison.*

Navarro, 1999; Navarro & Steinmetz, 2000). Fig. 4.1 from Steinmetz & Navarro (1999) illustrates this discrepancy, which was not due to numerical effects. A significant fraction of the angular momentum of the baryons had been transferred to the dark matter, leading simulated disks to be an order of magnitude too small.

In addition to gravity, these simulations included gas hydrodynamics, radiative and Compton cooling, simple recipes for transforming gas into stars, and minimal feedback models to account for the energy released by supernovae to their surroundings. But without sufficient feedback, the gas cools excessively, contracts at the center of the haloes and transfers its angular momentum to the dark matter, notably through dynamical friction and tidal stripping (Navarro & Benz, 1991; Navarro et al., 1997; Maller & Dekel, 2002). Higher resolution simulations with stronger feedback yield more realistic disks (e.g., Guedes et al., 2011), which contributes to solve the "angular momentum catastrophe".

Bulgeless giant galaxies

In the hierarchical ΛCDM model, galaxies assemble through more or less violent merger events. Major mergers should perturb galactic disks and transform them into classical bulges. However, observations show that bulgeless galaxies and tiny pseudo-bulges prevail in the local Universe, and the existence of giant, pure-disk galaxies without bulge challenges our picture of galaxy formation (Kormendy & Fisher, 2008; Kormendy et al.,

2010; Kormendy, 2015). Indeed, about two thirds of observed galaxies have little or no bulge, including the Milky Way and other nearby galaxies, whose apparent bulges are rotationally-supported: they are part of the disk, and not independent components resulting from mergers (Shen et al., 2010; Kormendy & Barentine, 2010). These observational constraints impose that most galaxies did not experience major merger events since $z = 4$ and that most existing bulges were built by a combination of minor mergers and secular processes (Weinzirl et al., 2009).

Small galaxies are consistently expected to accrete gas through cold streams of the cosmic web or minor mergers and to experience fewer major mergers (Dekel & Birnboim, 2006; Dekel et al., 2009a). However, the existence of giant bulgeless galaxies is more difficult to explain within the ΛCDM paradigm, especially as such galaxies are not unusual at all (Kormendy et al., 2010). Even if major mergers are rarer than initially thought (Naab, 2013), the secular evolution of observed high redshift clumps should indeed produce bulges or pseudo-bulges. These clumps are expected to interact, lose angular momentum through dynamical friction, and to migrate towards the center of the galaxies to form bulges (Genzel et al., 2008; Elmegreen et al., 2008; Dekel et al., 2009b; Dekel & Krumholz, 2013; Bournaud et al., 2014).

As for other challenges of the ΛCDM model, feedback processes from stars and AGN are often invoked to resolve the problem. Feedback could indeed contribute to disrupt the clumps before they reach the central part of the galaxies. But it is probably insufficient as the galaxy evolution that makes disks instead of bulges does not only depend on the galaxy mass, but also crucially on the environment. Indeed, while most field galaxies such as those of the Local Group are pure disks, the proportion of bulges is much higher in denser environments such as the Virgo cluster (Kormendy et al., 2010). It could also be tempting to invoke feedback to delay star formation until the final halo is assembled: mergers would have already happened, and stars would form in an undisturbed disk. But such a scenario is notably impossible in the case of the Milky Way, as the oldest stars in its disk are 9-10 Gyr old: much of the galaxy growth happened when the disk was already in place (Kormendy et al., 2010). The reason why ΛCDM produces too many bulges is still open.

The 'too big to fail' problem

The "too big to fail" problem is one of the most serious remaining issues of the ΛCDM model. Not only do numerical simulations predict too many subhaloes than are observed for galaxies like our Milky Way (Moore et al., 1999; Klypin et al., 1999), but the simulated subhaloes are too big to fail to form stars and to be observable (Boylan-Kolchin et al., 2012). Fig. 4.2 from the seminal Moore et al. (1999) article compares the abundance of substructures between the Milky Way, the Virgo cluster and simulations of similar masses: while the cluster data fits well with the corresponding simulation, the observed Milky Way satellites are more than an order of magnitude less numerous than expected.

In the hierarchical model of galaxy formation, haloes are formed by successive mergers of smaller haloes, some of them surviving the formation of the galaxy. Such subhaloes are

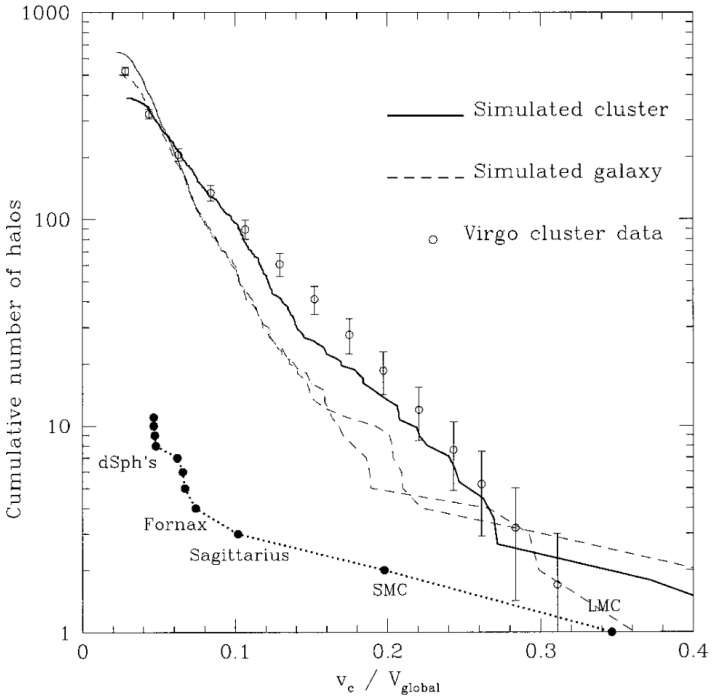

Figure 4.2 – *Comparison of the number of substructures in the Milky Way and the Virgo cluster with numerical simulations of comparable masses from Moore et al. (1999). The black filled circles correspond to the satellites of the Milky Way while the open circles to the Virgo cluster. The cumulative number of substructures is plotted as a function of their circular velocity, which is a proxy for the mass of the substructure.*

formed independently and are thus all potential sites of star formation. One of the first hypothesis to explain the robust discrepancy between the number of subhaloes in dark-matter-only simulations and the observed satellites of the Milky Way is to assume that most of the subhaloes do not contain enough baryons to be observed (Moore et al., 1999; Klypin et al., 1999). Processes such as feedback from supernovae or ultraviolet background heating due to the reionization of the Universe can indeed account for removing the baryons from low mass haloes or suppressing the accretion onto them, hence inhibiting their star formation. Another mechanism to remove gas from low-mass haloes could also involve the cosmic web, as suggested by Benítez-Llambay et al. (2013): because haloes are moving with respect to the cosmic web, ram pressure stripping could remove some of the gas - an effect which would be more signicant in low-mass haloes as their binding energy is lower.

If the only subhaloes to form stars are the most massive, the number of observable satellites decreases from thousands to tens, in agreement with observations. But this implies that Milky Way satellites correspond to the most massive subhaloes expected from simulations, and there seem to be a mismatch between the two. While the best-fitting dark matter haloes of Milky Way satellites all have characteristic circular velocities V_{max} between 12 and 24 km s^{-1}, ΛCDM simulations predict at least ten subhaloes with $V_{max} > 25$ km.s^{-1}: simulated subhaloes have much higher densities than the observed ones (Springel et al., 2008; Boylan-Kolchin et al., 2011, 2012; Garrison-Kimmel et al., 2014).

Strong feedback from supernovae could have lowered the core densities to explain these observations, but seems to be insufficient to resolve this 'too big to fail' problem (Garrison-Kimmel et al., 2013): massive subhaloes are not expected to have had their star formation drastically suppressed, and should be observable. Moreover, the many substructures predicted by ΛCDM simulations might impede the formation and the survival of spiral disks in galaxies such as the Milky Way by inducing strong fluctuations in the gravitational potential (Moore et al., 1999).

The "too big to fail" problem might hint at the necessity to modify the ΛCDM model, notably by adding a warm dark matter (WDM) or self-interacting dark matter instead of the standard cold dark matter. Indeed, the Milky Way does not seem to be an anomalous galaxy and the 'too big to fail' problem is also relevant for other galaxies (e.g., Papastergis et al., 2015). Lovell et al. (2012) notably carry out a high-resolution simulation of a galaxy analogous to that studied by Boylan-Kolchin et al. (2012), but within a WDM paradigm. They show that WDM is able to reduce the number of subhaloes and to reconcile their dynamics with the data. Although the WDM paradigm has its own flaws, it might be part of the solution to the 'too big to fail' problem. But as for most other ΛCDM issues, the solution preferred by proponents of the standard cosmological model involves baryonic physics and feedback mechanisms. The introduction of baryonic physics into simulations, and notably of processes such as supernova feedback and tidal stripping, actually seems to reduce significantly the dark matter mass of observable subhaloes and to better match observations (Zolotov et al., 2012; Brooks et al., 2013; Brooks & Zolotov, 2014). Lowering the halo mass of the Milky Way below 10^{12} $M_\odot$ could also help alleviate the 'too big to fail' problem: such a lowering of the mass is allowed by observations, and the absence of massive subhaloes might thus just indicate that the Milky Way is less massive than expected (Wang et al., 2012).

The core-cusp discrepancy

That dark-matter-only simulations predict cuspy density profiles for dark matter haloes while observations show cored central densities for small galaxies dominated by dark matter was perhaps the first discrepancy to be pointed out within the ΛCDM model (Flores & Primack, 1994; Moore, 1994). Pure dark matter simulations indeed predict that the central density of dark matter haloes scales approximately as $\rho \sim r^{-1}$, where r the radius, and that the density more generally follows a cuspy distribution (Navarro et al., 1996b). On the contrary, observations of the rotation velocity in dwarf galaxies show that most galaxies do not seem to have cuspy dark matter profiles and fit better with constant density cores of size between 1 and 10 kpc (de Blok et al., 2008; Oh et al., 2011). This core-cusp discrepancy will be presented in more detail in the following paragraphs.

Although we mainly focus here on the core-cusp discrepancy, the issue is related to most other challenges of the ΛCDM model. Indeed, cores are more easily stripped of their gas by feedback mechanisms or tidal disruption than cusps because of their shallower gravitational potential. Such profiles would thus make galaxies more vulnerable to feedback processes and more easily quenched. Cored subhalo density profiles could also

help reduce the number of observable star-forming subhaloes and alleviate the 'too big to fail' problem (e.g., Ogiya & Burkert, 2015). Moreover, the transformation of a dark matter cusp into a core is very much tied to the issue of angular momentum transfer from the gas to the dark matter halo. One of the main explanations for the cored dark matter density profiles indeed involves baryonic physics and its influence on the dark matter, and simulations show that there is an important transfer of angular momentum between the two components (e.g., Navarro & Benz, 1991). The precise mechanisms through which angular momentum and energy are transfered from the gas to the dark matter are yet to be specified, but they may involve the clumpiness of the baryonic distribution and thus be related to the fate of the star-forming clumps observed at high redshift and to bulgeless galaxy formation.

4.1.2 Dark matter dynamics predicts cuspy density profiles

In the ΛCDM model, dark matter represents about 84% of the total matter content of the Universe (Planck Collaboration et al., 2014, 2015), so the large scale evolution of the Universe is essentially driven by dark matter dissipationless dynamics. Dark matter haloes are assumed to form through gravitational instabilities stemming from small density perturbations in the very young Universe (e.g., Mo et al., 2010; Loeb, 2011), and galaxies to assemble within the potential wells of these haloes, when the gas cools and starts to form stars (White & Rees, 1978; Davis et al., 1985). While the clustering process is mostly governed by the dark matter component, baryons interfere only at later stages. Hence, dark-matter-only simulations reproduce the large scale structure of the Universe and should describe the first stages of galaxy formation to a good approximation.

The NFW density profile

To a first approximation, dark matter haloes can be modeled as spherical objects whose mass distribution is described by a spherically averaged density profile $\rho(r)$. Dark-matter-only cosmological simulations enable to describe the formation and evolution of dark matter haloes, and halo density profiles within such simulations are shown to be singular at their center (e.g., Dubinski & Carlberg, 1991; Warren et al., 1992). Using N-body simulations of structure formation in the ΛCDM paradigm, Navarro et al. (1996b) notably showed that the density profiles of dark matter haloes were shallower at small radii and steeper at large radii than the isothermal profile $\rho_{\rm isothermal} \propto r^{-2}$, and could be well described by what is now known as the Navarro, Frenk & White (NFW) profile:

$$\rho(r) = \frac{\rho_0}{r/\mathrm{R_s}\,(1 + r/\mathrm{R_s})^2}, \tag{4.1}$$

where $\mathrm{R_s}$ is the scale radius and ρ_0 a characteristic density. Such a profile scales approximately as $\rho \propto r^{-1}$ near the center and as $\rho \propto r^{-3}$ at larger radii. As the density increases sharply near the center, the NFW profile is referred as 'cuspy'.

A profile independent of the halo formation history

Navarro et al. (1996b) considered objects whose masses ranged from those of dwarf galaxies to those of rich galaxy clusters, and Navarro et al. (1997) further showed that the NFW profile could describe haloes of all masses, independently of the chosen cosmological parameters. The universal behavior holds despite the different formation histories of the haloes and although such structures are formed by hierarchical clustering and mergers.

The total mass associated with an NFW density profile formally diverges, as the mass enclosed within a radius r is given by

$$\mathrm{M}(r) = 4\pi\rho_0 \mathrm{R_s^3} \left(\ln\left(1 + \frac{r}{\mathrm{R_s}}\right) - \frac{r/\mathrm{R_s}}{1 + r/\mathrm{R_s}} \right). \tag{4.2}$$

It is therefore necessary to introduce a cutoff radius to define the halo mass, usually taken as the virial radius $\mathrm{R_{vir}}$ [1]. The total halo mass is then defined as its virial mass $\mathrm{M_{vir}}$, which can be expressed as a function of $\mathrm{R_{vir}}$ given the cosmological parameters [2]. Consequently, the NFW profile is entirely determined by the total halo mass $\mathrm{M_{vir}}$ and its concentration parameter $C = \mathrm{R_{vir}}/\mathrm{R_s}$. This parameter depends crucially on the halo formation history, as haloes which have experienced recent major mergers have low concentration parameters while those which underwent a long phase of quiescent growth have larger concentration parameters (Zhao et al., 2003, 2009). Navarro et al. (1997) also showed

[1] The virial radius is defined as the radius within which virial equilibrium holds, i.e., within which the potential energy of the system is equal to twice its kinetic energy in absolute value. The mean overdensity within $\mathrm{R_{vir}}$ relatively to the mean density of the Universe depends on the matter density of the Universe Ω_m, and can be approximated in the ΛCDM model as

$$\Delta_{\mathrm{vir}} \approx \left(18\pi^2 + 82(\Omega_m - 1) - 39(\Omega_m - 1)^2\right)/\Omega_m \tag{4.3}$$

(Bryan & Norman, 1998; Mo et al., 2010). But as the virial radius is difficult to measure observationally, it is often approximated as the radius within which the average density is greater by a certain factor than the mean density of the Universe or than its critical density $\rho_{\mathrm{crit}} = 3H^2/8\pi G$, where H is the Hubble parameter. Although the ΛCDM cosmological parameters with $\Omega_{m,0} = 0.3089$ (Planck Collaboration et al., 2015) yields $\Delta_{\mathrm{vir}} \approx 330$, a widely used choice is to define the virial radius as the radius within which the average density is 200 times the critical density of the Universe,

$$\rho_{\mathrm{mean}}(\mathrm{R_{vir}}) = 200\ \rho_{\mathrm{crit}}. \tag{4.4}$$

Along this work, we use this latter definition of the virial radius, which is still a good approximate estimate of the radius for virial equilibrium.

[2] When the virial radius $\mathrm{R_{vir}}$ is defined as the radius within which the average density equals $\rho_{\mathrm{mean}} = 200\rho_{crit}$, the virial mass is simply

$$\mathrm{M_{vir}} = \frac{4\pi}{3}\mathrm{R_{vir}^3}\ \rho_{\mathrm{mean}}. \tag{4.5}$$

It is also possible to define a virial velocity corresponding to the orbital velocity at $\mathrm{M_{vir}}$,

$$\mathrm{V_{vir}} = \sqrt{\frac{G\mathrm{M_{vir}}}{\mathrm{R_{vir}}}}, \tag{4.6}$$

which can also be unequivocally expressed as a function of the other virial parameters, given that $\mathrm{V_{vir}} \propto \mathrm{R_{vir}} \propto \mathrm{M_{vir}^{1/3}}$.

that the characteristic density ρ_0 was closely related to the mean cosmic density at the time of formation of the galaxy, so that haloes that formed earlier are more concentrated. This is coherent with the mass dependence of the concentration parameter: more massive haloes, which assembled later on average, are less concentrated (Macciò et al., 2007). But despite the different formation histories, the different masses and the different concentration parameters, the density profiles of dark matter haloes always seem to be well fit by NFW profiles. Although various explanations have been proposed, the origin of this universality is still not fully understood (Mo et al., 2010).

The Einasto profile

More recent, higher-resolution dark matter simulations (Navarro et al., 2004; Merritt et al., 2005; Hayashi & White, 2008; Gao et al., 2008; Springel et al., 2008) have showed that the density profiles bore small deviations from the NFW profile and could be better fitted by an Einasto (1965) profile

$$\rho(r) = \rho_{-2} \exp\left[-\frac{2}{\alpha}\left(\left(\frac{r}{r_{-2}}\right)^{\alpha} - 1\right)\right] \tag{4.7}$$

where r_{-2} is the radius at which the logarithmic slope of the density profile corresponds to the isothermal sphere value, $d\ln\rho/d\ln r = -2$, $\rho_{-2} = \rho(r_{-2})$ is the corresponding density, and α a parameter whose best fit is situated between 0.12 and 0.25 (Hayashi & White, 2008; Gao et al., 2008). Although this profile has three free parameters *per se*, imposing $\alpha = 0.17$ still results in a relatively better fit than the NFW profile. Unlike the NFW profile, the Einasto profile does not formally diverge when $r \to 0$, but as its logarithmic slope

$$\frac{d\ln\rho}{d\ln r} = -2\left(\frac{r}{r_{-2}}\right)^{\alpha} \tag{4.8}$$

only gets above -0.5 for radii smaller than about $10^{-3}\ r_{-2}$, it can still be considered cuspy in most cases. Fig 4.3 compares the NFW and Einasto density profiles as well as their logarithmic slope, and show that they mainly differ very close to the center of the halo while the cuspy behavior holds for all radii above $\sim 10^{-3}\ r_{-2}$. In practice, the observed innermost radii are above this value.

4.1.3 Cores versus cusps

Cores in dwarf galaxies

Although simulations produced dark matter haloes with cuspy density profiles, observed rotation curves of dwarf galaxies and low surface brightness galaxies from the 1990s seemed to show that dark matter haloes had central cores instead of cusps. Moore (1994) notably obtained rotation curves for a set of dwarf spiral galaxies and showed that they were

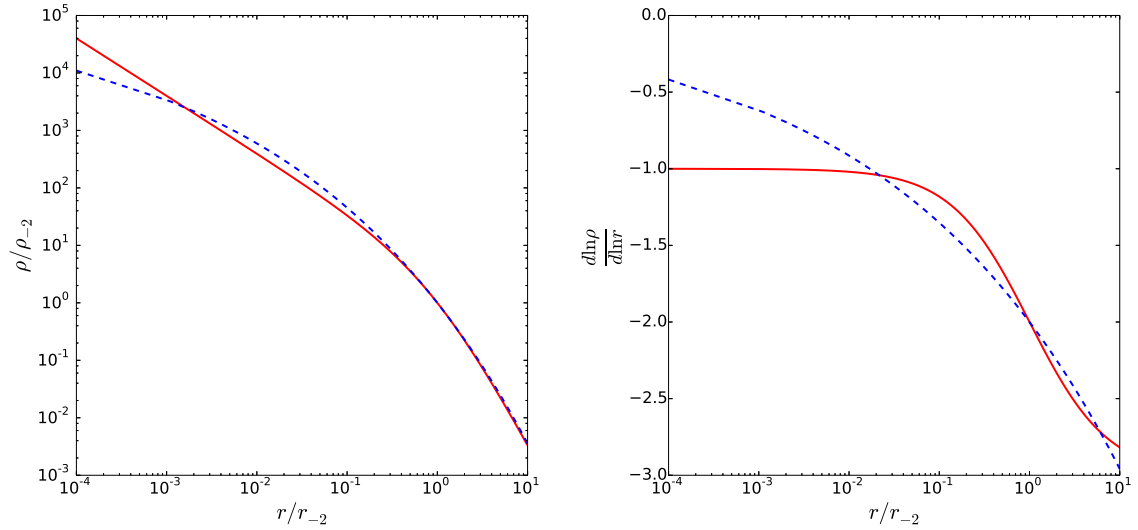

Figure 4.3 – *Comparison between the NFW density profile (red solid line) and an Einasto profile with parameter* $\alpha = 0.17$ *(dashed blue line). The left panel displays the density profile, while the right panel shows the associated logarithmic slope. For the NFW profile, the radius* r_{-2} *where the logarithmic slope equals -2 corresponds to the characteristic radius* $\mathrm{R_s} = \mathrm{R_{vir}}/C$*. The flattening of the Einasto profile only becomes significant for* $r/r_{-2} \lesssim 10^{-3}$*, so the profile can be considered cuspy in most observational cases.*

incompatible with a cuspy density profile. Dwarf galaxies are indeed particularly good probes of the internal structure of their dark matter haloes as their baryonic content is very low beyond the central region (e.g., Carignan & Beaulieu, 1989; Jobin & Carignan, 1990), and as most of their baryonic mass is in the form of neutral hydrogen. Neutral hydrogen can be observed through its 21-cm emission, which enables to determine unambiguously the baryonic contribution to the halo mass. Moore (1994) interpreted his result as a severe drawback for the cold dark matter paradigm, although his approach assumed a specific relation between the size of a disc galaxy and the size of its dark matter halo. Other observations of dwarf galaxies and low surface brightness galaxies, as well as measurements inside galaxy clusters through gravitational lensing, seemed to confirm the fundamental incompatibility between the simulated cuspy profiles and observations (Flores & Primack, 1994; McGaugh & de Blok, 1998a).

Early observations did not always have the spatial resolution needed to unambiguously discriminate between cores and cusps (van den Bosch & Swaters, 2001). Using high-resolution observations from the THINGS survey, Oh et al. (2011) are able to derive more accurate dark matter density profiles for a set of seven dwarf galaxies, and again find a discrepancy between the observed rotation curves and the ΛCDM simulations. As in the previous measurements, they first subtract the disk component to obtain rotation curves specifically reflecting the dark matter distribution, and then deduce the mass and density profiles of the halo. Figure 4.4 compares the resulting density profiles with the NFW profile and with an observationally motivated halo model dominated by a central core. This latter model corresponds approximately to an isothermal sphere, with a density

profile

$$\rho(r) = \rho_{\rm C} \frac{1}{1 + (r{\rm R_C})^2}, \tag{4.9}$$

and has been shown to describe fairly accurately the rotation curves of galaxies (Begeman et al., 1991); $\rho_{\rm C}$ represents the core density and $\rm R_C$ the core radius. Oh et al. (2011) also consider the inner logarithmic slope of the density profile, defined from the three innermost data points, and plot it alongside the slopes corresponding to the NFW and pseudo-isothermal models. The data points have a significant scatter, but the cored density profile with inner slope $\alpha \sim 0$ clearly seems to be favored as compared to the cuspy NFW profile of slope $\alpha = -1$. Oh et al. (2011) indeed obtain a mean inner slope $\alpha = -0.29$, which is comparable to similar measurements in low brightness galaxies (de Blok et al., 2001). Fitting the THINGS rotation curves with Einasto profiles similarly leads to characteristic exponents that are not in agreement with ΛCDM simulations (Chemin et al., 2011). The THINGS sample was recently complemented by the LITTLE THINGS sample (Oh et al., 2015), which again shows that the density profiles of dwarf galaxies deviate significantly from the cuspy dark matter distributions predicted by dark-matter-only ΛCDM simulations.

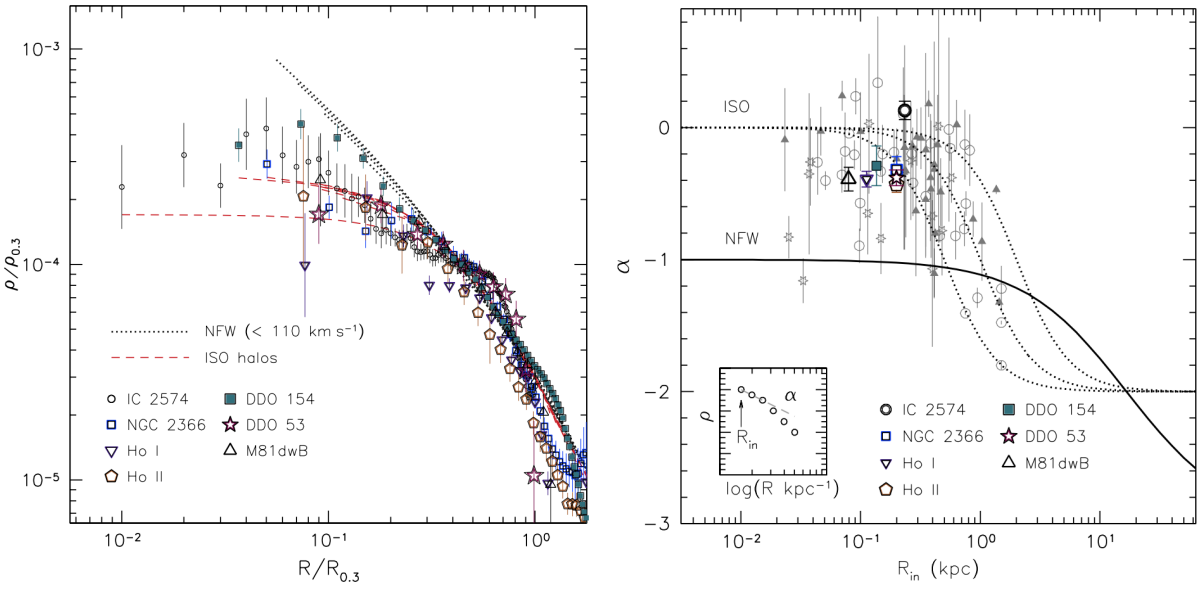

Figure 4.4 – *Dark matter density profiles for the seven dwarf galaxies from the THINGS survey (left) and their corresponding inner slope as a function of R_{in} the innermost point of the measurements (right), from Oh et al. (2011). The data is compared to NFW density profiles of inner slope $\alpha \sim -1$, and to best-fit pseudo-isothermal halo models with inner slope $\alpha \sim 0$. An Einasto profile would approximately follow the NFW models, as its deviation from them would only be significant for radii $R_{in} \lesssim 10^{-2}$kpc given that the characteristic NFW radii used here range from about 1 to 20 kpc (cf. Fig. 4.3).*

Cores in Milky Way satellites

Dwarf satellite galaxies of the Milky Way could provide another probe of the density distribution of dark matter haloes. These small spheroidal galaxies have indeed large mass-to-light ratios and are thus dominated by dark matter (Mateo, 1998). In numerical simulations, these objects correspond to subhaloes which formed independently and only later accreted onto the Milky Way halo (e.g., Klypin et al., 1999). Goerdt et al. (2006) show that the presence of five globular clusters at about 1 kpc of the center of the Fornax Milky Way satellite is incompatible with a cuspy dark matter subhalo while it is consistent with a cored density profile. Similarly, Walker & Peñarrubia (2011) determine the mass profiles of dwarf spheroidals from stellar spectroscopic data and favor cores instead of cusps. Nevertheless, satellite galaxies are prone to strong tidal forces and deviate from spherical symmetry, so determining their mass profiles is not easy and it is not always possible to fully discern cusps from cores (Breddels & Helmi, 2013). Moreover, these objects highlight by themselves one of the challenges of the ΛCDM model, namely the 'too big to fail' problem, and their most basic properties are already a puzzle: given their mass, they should have formed much more stars, and supernova feedback seems to be insufficient to explain their low stellar content (Boylan-Kolchin et al., 2012).

Cores in larger galaxies

For larger galaxies, the gravitational potential is more affected by the baryonic component so it is harder to probe the inner density profile of the dark matter. Nevertheless, about half of the general galaxy population consists in low brightness galaxies which are still dark matter dominated (McGaugh et al., 1995; de Blok & McGaugh, 1997), and the dark matter density distribution is again more consistent with cored density profiles than with cusps (Kuzio de Naray & Spekkens, 2011). At higher masses, rotation curves of disk galaxies also tend to favor cored density profiles (McGaugh et al., 2007) and the persistence of galactic bars over long timescales could indicate that the dark matter distribution is not cuspy. Numerical simulations indeed show that bars are drastically slowed down by dynamical friction in high dark matter density haloes so that the central dark matter density must be lower than expected in barred galaxies such as the Milky Way (Debattista & Sellwood, 1998).

4.1.4 Attempts at solving the problem

Proposed solutions to the core-cusp discrepancy and the related challenges of the ΛCDM model such as the 'too big to fail' problem can be broadly divided into those considering fundamental changes in the physics of the model and those concerned with the baryonic processes at stake during galaxy formation and evolution. The first category of solutions comprises alternatives to the cold, collisionless dark matter such as warm dark matter (WDM) theories, self-interacting dark matter models, and models that fundamentally change the gravitational law like Mordechai Milgrom's MOND theory.

Warm dark matter

As cusps arise as a consequence of cold gravitational collapse, considering warm dark matter particles whose initial velocity distribution is higher than that of cold dark matter may alleviate the problem. Although the cold dark matter scenario has won wider acceptance in the last decades, dark matter has never been directly detected, so its nature remains open to different types of particles. Warm dark matter particles lighter than their cold dark matter counterparts would remain relativistic longer and diffuse out of early density perturbations of size smaller than the streaming length, thus damping structure formation at small scales (e.g., Bond et al., 1980). This effect could theoretically facilitate the obtention of cored dark matter density profiles. However, although numerical simulations within the WDM paradigm produce galaxies in accordance with the number of satellites orbiting the Milky Way, their dark matter density profiles are still cuspy (Colín et al., 2000; Bode et al., 2001; Schneider et al., 2012; Lovell et al., 2014). Indeed, Colín et al. (2000) carry out N-body simulations of Milky Way sized haloes and obtain less cuspy satellites that are more easily destroyed by dynamical friction and tidal disruption than in the cold dark matter simulations. The number of satellites is consequently more consistent with observations, but the host halo still follows a cuspy density profile. Higher-resolution simulations such as those by Schneider et al. (2012) or Lovell et al. (2014) yield similar results. Although the central density of WDM haloes depends on the WDM particle mass and although the obtained density profiles are shallower than their CDM counterparts, pure WDM cosmology does not seem to provide a fully convincing solution to the core-cusp discrepancy by itself (Strigari et al., 2006; Kuzio de Naray et al., 2010; Macciò et al., 2012; Shao et al., 2013). Mixed cold plus warm dark matter models similarly yield mitigated results (Macciò et al., 2013; Anderhalden et al., 2013), and it seems that taking into account baryonic physics and feedback mechanisms might be unavoidable in WDM models to understanding the core-cusp discrepancy while simultaneously resolving the 'too big to fail' problem. Moreover, the power spectrum inferred from WDM models conflicts with that derived from observations of the Lyα forest. The numerous Lyα absorption lines and their depth indeed enable to reconstruct the mass distribution of absorbing structures along the line of sight of distant quasars, and impose a WDM particle mass higher than requested by the presence of cores (Croft et al., 1999; Viel et al., 2013; Kennedy et al., 2014).

Self-interacting dark matter

Given the successes of the cold dark matter paradigm on large scales, modifying the cold dark matter properties might appear as a good approach to solve the problems on small scales. There are strong observational constraints on the interactions between dark matter and ordinary matter, but it is also possible to consider a dark matter that is cold, non-dissipative, but self-interacting. Introducing such a dark matter enables to lower the central densities of galaxies without hampering the successes of the CDM scenario at large scales. Spergel & Steinhardt (2000) notably consider a dark matter whose mean free path is intermediate between $\sim$ 1 kpc and 1 Mpc so it becomes collisional in the inner

halo of galaxies and consequently heats up and produces a shallower density profile. The intermediate mean free path is imposed by the fact that if it were higher than 1 Mpc, the dark matter particles would not experience any interactions, while if it were below 1 kpc, it would behave as a collisional gas and affects much more dramatically the halo evolution. With such a mean free path, a dark matter particle is expected to have less than one collision per Hubble time within the virial radius of the halo. By producing shallower density profiles, this hypothesis could solve the core-cusp discrepancy as well as the 'too big to fail' problem regarding the number of satellites in Milky Way sized haloes. Burkert (2000) carried out numerical simulations to describe the evolution of haloes consisting of weakly self-interacting dark matter particles as suggested by Spergel & Steinhardt (2000), and noted how the central velocity dispersion increases with time to lead to a shallower density distribution in excellent agreement with the observations of dwarf galaxies, as shown in Fig. 4.5. Similarly, Rocha et al. (2013) obtained constant density cores in simulated haloes with self-interacting dark matter. However, such models might require a fine-tuning of the dark matter cross section to avoid core collapse after the expansion phase of the core (Kochanek & White, 2000) and still requires accounting for the influence of baryons on the halo evolution. More problematically, self-interacting dark matter implies spherical cluster shapes which seem to be inconsistent with observations or to constrain too strongly the possible values of the dark matter cross-section (Miralda-Escudé, 2002; Peter et al., 2013; Zavala et al., 2013).

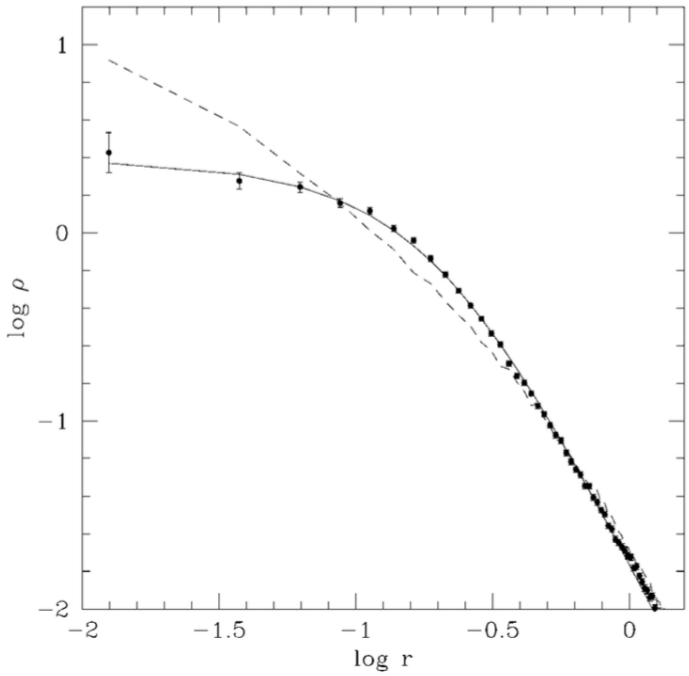

Figure 4.5 – *Dark matter density profile inferred from the rotation curves of dwarf galaxies (solid line) compared with the halo simulated by Burkert (2000) in the case of a cold weakly self-interacting dark matter (points with error bars). The dashed line represents the initial cuspy density profile of the halo.*

Exotic cut-offs in the matter power spectrum

Introducing a minimum scale length below which structure formation is hampered might resolve the missing satellite problem and the core-cusp discrepancy (e.g., Schneider, 2015). Thermal WDM models introduce such a cut-off in the power spectrum due to free-streaming out of small early density perturbations (Bond et al., 1980), but seem to form galaxies too late (Macciò et al., 2012). Allowing CDM to interact with other constituents of the Universe or with itself also suppresses small-scale density perturbations (Spergel & Steinhardt, 2000; Bœhm et al., 2001; Boehm & Schaeffer, 2005). But other solutions to justify such a cut-off have been suggested. Amongst them, Hu et al. (2000) and Marsh & Silk (2014) consider models in which dark matter consists of 'fuzzy' ultra-light axion-like particles or mixtures of these particles predicted by string theory and CDM, and obtain density profiles that include cores without suffering from the late galaxy formation times of WDM models. Asymmetric dark matter theories, in which the current abundance of dark matter stems from an asymmetry of particles and anti-particles, could also lead to a damping of the amplitudes of small-scale perturbations (Petraki & Volkas, 2013). These models obtain a power spectrum cut-off by modifying the nature of dark matter. Other exotic dark matter models proposed to solve the core-cusp discrepancy include models of repulsive dark matter (Goodman, 2000), fermionic dark matter (Destri et al., 2013), or quantum, wave-like dark matter (Schive et al., 2014). In a different way, alternative inflation models could gradually reduce or introduce a sharp drop in the power spectrum at small scales and thus provide a different framework to resolve the 'too big to fail' problem and the core-cusp discrepancy (e.g., Kamionkowski & Liddle, 2000).

MOND

Dark matter was initially introduced to explain the rotation curves of galaxies, as visible matter and Newtonian dynamics could not account for the high velocity plateau observed at large radii (e.g., Zwicky, 1933; Smith, 1936; Faber & Gallagher, 1979; Rubin et al., 1980, 1982). Indeed, the observed baryon distribution would have predicted declining rotation velocities after a certain radius. Adding invisible massive haloes in which galaxies would be embedded enabled to explain the observations, and gave rise to the ΛCDM model. However, instead of adding an additional form of matter, the discrepancy in the rotation curves can also be resolved by modifying the gravitational law itself. Despite the successes of the ΛCDM model, such an approach is not yet ruled out, notably given the elusiveness of dark matter and its recurring non-detection. MOND is an empirically motivated modification of the gravitational law suggested by Mordechai Milgrom as an alternative to dark matter (Milgrom, 1983a,b,c; Sanders & McGaugh, 2002; Famaey & McGaugh, 2012). MOND introduces a characteristic acceleration scale a_0 below which the gravitational attraction approaches $g_{\mathrm{MOND}} = \sqrt{g_N a_0}$, where g_N is the usual Newtonian acceleration, and above which it is Newtonian. This parametrization was originally introduced to account for the flat rotation curves of galaxies and to enforce the empirical Tully-Fisher relation between their mass and their rotation velocity. It was not designed to fit in detail the rotation curves. Nevertheless, the agreement with the observations

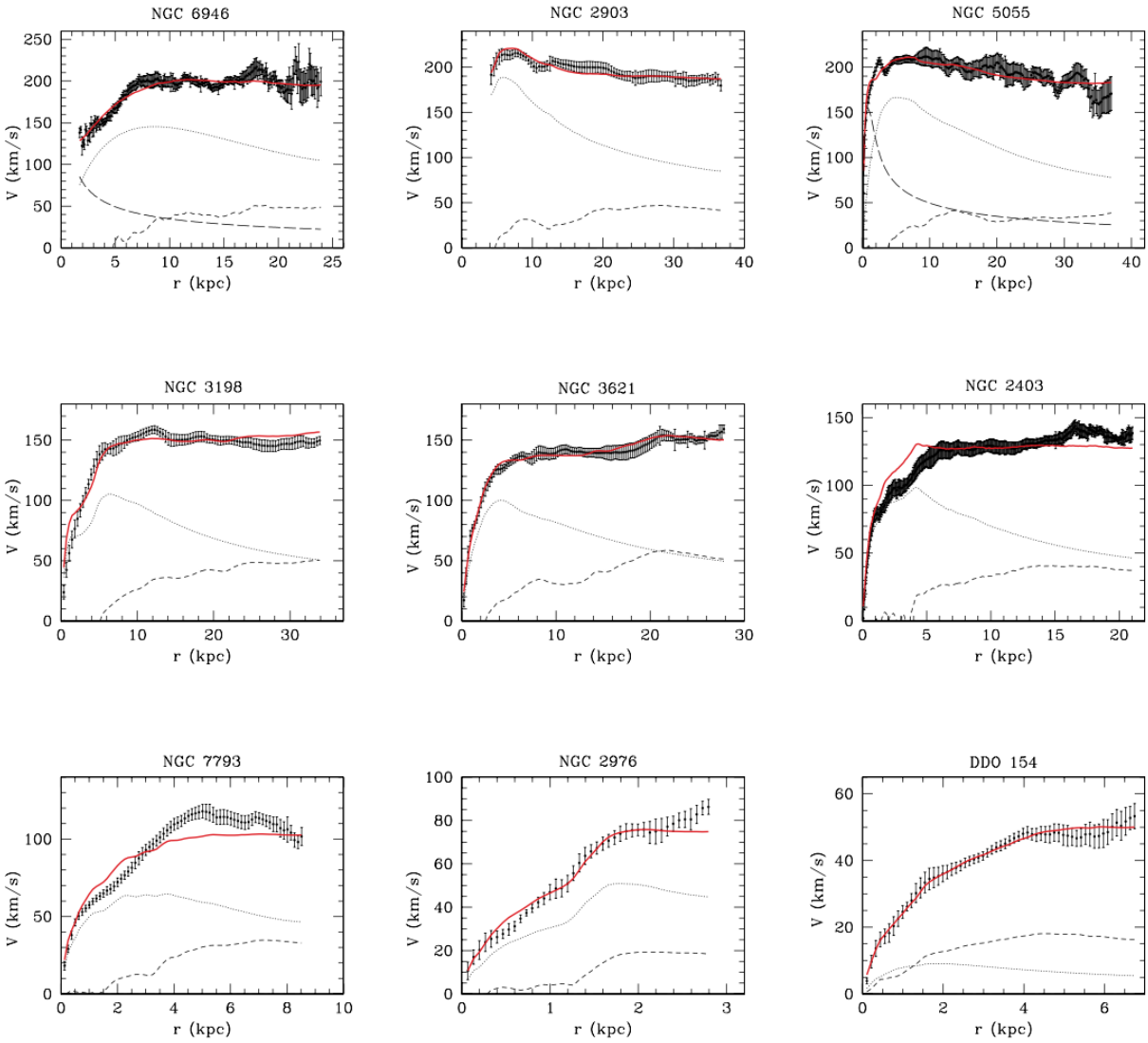

Figure 4.6 – *Examples of MOND rotation curve fits for dwarf galaxies from the THINGS survey Gentile et al. (2011). The MOND best-fit model is in red, while the dashed, dotted, and long-dashed lines respectively represent the Newtonian contributions of the gaseous disk, the stellar disk, and the bulge.*

is striking: there is no cusp problem within MOND. Fig. 4.6 from Gentile et al. (2011) shows the rotation curves of some dwarf galaxies from the THINGS sample with their MOND best-fit model, which is a single parameter fit given a_0. In the absence of dark matter, the observed distribution of stars and gas is indeed assumed to trace mass and to determine the distribution of matter. From this, it is possible to derive the Newtonian gravitational field g_N and the associated effective MOND field g_{MOND}, which depends on a_0, hence the expected orbital velocities. The only free parameters of the fit are a_0 and the mass-to-light ratio M/L, so that only one parameter remains when a_0 is fixed. The value of a_0 is a priori unknown and has to be determined from observations. The M/L ratios derived from the fit are in good agreement with the predictions from stellar population synthesis models, and the obtained rotation curves agree very well with observations for

most galaxies, from low-surface-brightness and dwarf galaxies to normal spirals and more massive high-surface brightness galaxies (Begeman et al., 1991; Sanders, 1996; Sanders & Verheijen, 1998; McGaugh & de Blok, 1998b; de Blok & McGaugh, 1998; Sanders & Noordermeer, 2007; Swaters et al., 2010; Gentile et al., 2011; Famaey & McGaugh, 2012). Despite the fact that MOND was not designed to fit rotation curves (de Blok & McGaugh, 1998), it is able to predict them: MOND at least seems to yield the correct effective force, and dark matter theories should have to account for this success. The MOND framework is also able to reproduce the properties of isolated or interacting galaxies (Tiret & Combes, 2007, 2008), explains the formation of warps in apparently isolated galaxies (Brada & Milgrom, 2000b) and implies that dwarf galaxies are more vulnerable to tidal disruption, which would alleviate the "too big to fail" problem (Brada & Milgrom, 2000a). MOND is generally very successful from dwarf galaxies to superclusters, but lacks an underlying relativistic theory so can't be unambiguously extended to cosmological problems for the moment (Sanders & McGaugh, 2002). Mass discrepancies in clusters also seem to require a form of dark matter within the MOND paradigm, proponents of the theory favoring unseen baryonic matter (e.g., Sanders, 1999) and opponents seeing it as a major drawback for the theory (e.g., Gerbal et al., 1992; Clowe et al., 2006). Interestingly, the value of a_0 is of the same order of magnitude as cH_0, which suggests that MOND reflects the effects of cosmology on local dynamics, as the Hubble constant H_0 describes the expansion of the Universe.

Baryons

The core-cusp discrepancy arose from dark-matter-only ΛCDM simulations, which produced cuspy density distributions instead of the observed cores. These dissipationless simulations did not take baryons into account. But despite constituting only about 16% of the total mass of the Universe in the ΛCDM model (Planck Collaboration et al., 2014, 2015), dissipative baryonic physics could play an important role in the dynamics at galactic scales. Baryons are indeed expected to represent a more significant part of the mass at the centers of dark matter haloes (e.g., Bell & de Jong, 2001), as they dissipate energy through cooling, and collapse to smaller scales than the diffuse dark matter. Although the formation and evolution of the large scale structure of the Universe is mostly determined by the dominant dark matter component in the ΛCDM model, baryons could in turn impact the dark matter distribution on smaller scales. Hence, better accounting for baryonic physics could potentially solve the challenges of the ΛCDM model without changing the paradigm.

Although baryonic physics within the ΛCDM framework is not the only possible solution to the core-cusp discrepancy and to the other challenges of the dark matter model, the following work focuses on this latter possibility. Mechanisms that could heat the dark matter halo would notably help forming cores in simulations. Indeed, an energy supply at the center of the halo could result in the dark matter particles migrating outwards and hence reduce the central density of the halo, as required by observations. However, as dark matter is assumed to interact only gravitationally, it is through their gravitational potential that baryons should affect it. The next section presents different mechanisms through which baryons could influence the dark matter distribution.

4.2 How baryons can affect the dark matter halo

The ΛCDM model is challenged in different ways, and notably through the core-cusp discrepancy. But because this problem precisely affects scales at which baryonic physics is expected to play an important role, it might be a consequence of the interaction between the baryonic and dark matter components. The precise details of these interactions are still relatively poorly understood, and should thus be investigated before making any decisive conclusion about the ΛCDM paradigm. Improving sub-grid models to better describe the complex baryonic processes at stake in numerical simulations is one way to address the issue, as in Governato et al. (2010). Modern hydrodynamical simulations are indeed able to reproduce cored density profiles by implementing realistic recipes for the different feedback processes. But the complexity of such an approach can hide the physical mechanisms at stake. Here we present different ways to solve the core-cusp discrepancy and focus on the direct physical mechanisms in which baryons could influence the dark matter distribution.

4.2.1 Adiabatic contraction

Dark matter particles only interact gravitationally and through weak interactions so baryons can mostly affect the dark matter distribution through their own gravity and by modifying the global gravitational potential. The simplest mechanism with which baryons can affect the dark matter is called adiabatic contraction: when baryonic gas cools and contracts, it accumulates at the center of the dark matter halo, which steepens the potential well and causes the dark matter to contract as well (Blumenthal et al., 1986). Even though dark matter exceeds baryonic matter by a factor $\Omega_{\text{dark matter}}/\Omega_{\text{baryons}} \sim 5$ on average (Planck Collaboration et al., 2014, 2015), baryons indeed dominate the gravitational field in the central regions of galaxies. The additional mass at the center of the halo pulls the dark matter inwards and create cores that are smaller and denser than they would have been without baryonic dissipation. But contrary to the baryons, dark matter evolves without dissipation, and its contraction is thus adiabatic. Together with tidal stripping, reionization and feedback processes from stars and AGN, adiabatic contraction is one of the main processes through which baryons can shape the dark matter distribution of haloes and subhaloes (Zhu et al., 2015).

Fig. 4.7 illustrates the effect of adiabatic contraction in a galaxy formation simulation by Gnedin et al. (2004). While the original adiabatic contraction model by Blumenthal et al. (1986) assumed spherical symmetry and homologous contraction, this simulation takes into account the cosmological context and the series of mergers through which galaxies are formed. When baryons are allowed to cool and to contract at the center of the halo, the central dark matter density increases as well. Interestingly, baryons dominate the total density at $r/\mathrm{R_{vir}} \lesssim 0.03$, $\mathrm{R_{vir}}$ being the virial radius. This is notably due to the very high gas fraction, which reaches 80% in this $z = 4$ simulation run. Gustafsson et al. (2006) similarly show that the central slope of the dark matter density profile of simulated, Milky Way sized galaxies steepens significantly in the presence of baryons. But they also

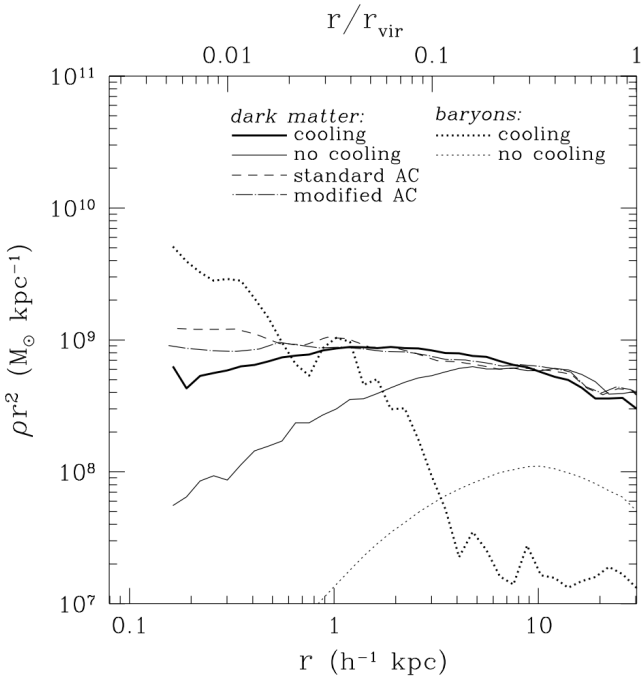

Figure 4.7 – *Density profiles of the dark matter and baryonic components in a galaxy simulation from Gnedin et al. (2004) highlighting adiabatic contraction. When the baryons are allowed to cool, they contract towards the center of the halo, and so does the dark matter. The dashed lines enable to compare the simulation results with analytical adiabatic contraction models.*

note that although the adiabatic contraction model developed by Gnedin et al. (2004) is much more successful at reproducing the density profile than the original spherical model developed by (Blumenthal et al., 1986), it is not perfect. This might indicate that the interactions between baryons and dark matter can't be explained by adiabatic contraction alone.

4.2.2 Dynamical friction

When a massive object such as a satellite galaxy or a clump of gas moves with respect to a background of smaller massive particles, it looses part of its energy through dynamical friction (Chandrasekhar, 1943; White, 1976). Gravity indeed tends to pull the smaller particles towards the bigger object, but as the latter continues to move relatively to the background, the concentration of particles increases in its wake. The backwards gravitational force due to this overdensity of smaller particles slows the massive object down as a drag or frictional force. In the case of a galaxy, big moving clumps of gas as those constituting galaxies at high redshift or those resulting from supernova explosions or AGN activity could thus transfer part of their energy to the dark matter background and indirectly heat the non-baryonic particles. Contrarily to radiative or thermal dissipation though, the mechanical energy is conserved so the energy lost by the gas is fully deposited in the dark matter halo. Dynamical friction also plays an important role in the migration

of giant clumps to the center of galaxies at high redshift and subsequent formation of a bulge (Bournaud et al., 2008; Genzel et al., 2008; Dekel et al., 2009b).

As dynamical friction results in heating the dark matter background of a galaxy, it could help resolve the core-cusp discrepancy. Assuming galaxies in which the gas is clumpy and the clumps bound enough to survive for a few dynamical times without colliding or being disrupted, El-Zant et al. (2001) showed through Monte Carlo simulations that dynamical friction could account for a significant flattening of the dark matter density profile. The orbital energy of the clumps is sufficient to turn the cuspy initial density distribution into a core, and so despite the competing effect of adiabatic contraction. Fig. 4.8 shows the resulting evolution of the density profile for a 10^{12} $M_\odot$ halo, with and without dynamical friction. When there is no dynamical friction, adiabatic contraction leads to an even more peaked density distribution at the center. But when the process is added to the model, the density decreases significantly at the center of the halo.

El-Zant et al. (2004) further carried out N-body simulations in which particles are divided into dark matter particles on one side and massive gaseous clumps on the other to model dynamical friction, and showed that the inner dark matter distribution flattens as expected from the previous study after a few dynamical times. Cosmological simulations by Romano-Díaz et al. (2008) in turn show that the presence of baryons progressively levels the initial cuspy density profile after a phase of adiabatic contraction, and associate it with the clumpy accretion onto the galaxy and the resulting dynamical friction with the dark matter background. Using a different, analytical approach, Tonini et al. (2006) show that an injection of angular momentum to the dark matter suffices to turn a cuspy

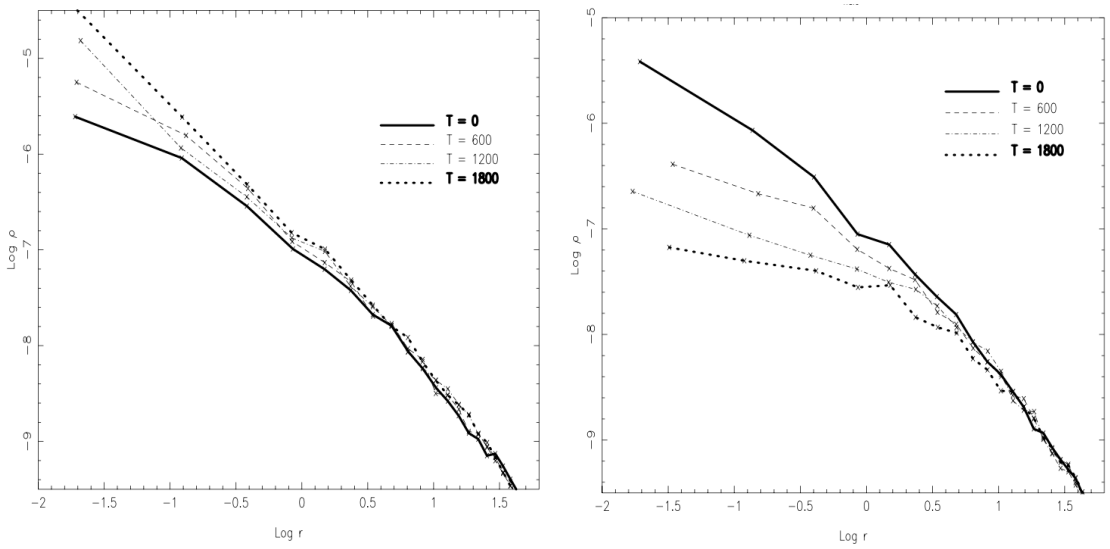

Figure 4.8 – *Evolution of the density profile of a* 10^{12} $M_\odot$ *halo with and without a dynamical friction model from El-Zant et al. (2001). When there is no dynamical friction (left), adiabatic contraction condenses the central part of the halo, while the cuspy initial density profile is turned into a flattened core with dynamical friction (right). The simulation spans about 2 Gyr up to T=1800, corresponding to about 18 central dynamical times, and the radius is in units of 2 kpc.*

NFW dark matter density profile into a core, and that dynamical friction can account for it, as it enables to transfer angular momentum from the baryons to the dark matter. Goerdt et al. (2010) further carry out N-body simulations in which galaxies are perturbed by infalling massive objects and find that such perturbations can indeed contribute to forming a core.

4.2.3 Density fluctuations from feedback processes

Feedback mechanisms and outflows

Young stars and active galactic nuclei (AGN) release energy in their surrounding medium and generate powerful outflows. The corresponding processes, which include supernova winds, radiation from young stars and energy release from black hole accretion (cf. section 1.3.3), are crucial to regulate star formation. In dark matter theories, there is indeed a need for feedback processes that would prevent all the gas to cool down and to form too many stars (White & Rees, 1978; Blanchard et al., 1992).

Observations of nearby and more distant galaxies reveal that most star-forming galaxies generate powerful outflows associated to velocities of a few hundreds of km s^{-1} (Shapley et al., 2003; Wilman et al., 2005; Weiner et al., 2009; Rubin et al., 2010; Kornei et al., 2012; Erb et al., 2012; Geach et al., 2014; Cicone et al., 2014), which are likely driven by supernova explosions, stellar winds, and radiation pressure from massive stars. On sub-galactic scales, high-resolution observations have detected AGN-driven outflows from the central regions of galaxies (e.g., Förster Schreiber et al., 2014; Genzel et al., 2014) as well as outflows induced by stellar feedback at the scale of individual star-forming clumps (e.g., Genzel et al., 2011). Such outflows heat or remove part of the gas from the star-forming regions, prevent further collapse of the gas, and thus decrease the star formation activity of the galaxies. Nevertheless, most of the material ejected by these outflows is expected to re-accrete onto the galaxy as metal-enriched gas (Rubin et al., 2012; Davé et al., 2011b).

But feedback processes do not just affect subsequent star formation. They can also affect the dark matter scaffolding of the halo. Indeed, by generating powerful and significant movements of gas, these processes modify the gravitational potential, which in turn affect the dark matter distribution. The energy released by AGNs or stars can heat the dark matter, and thus potentially puff out the dark matter cusp into a core.

Modelling the effects of outflows on the dark matter density profile

Numerical simulations have played an important role in better understanding the potential causes of the core-cusp discrepancy. As a first attempt to model the influence of supernova outflows on the dark matter potential, Navarro et al. (1996a) just assumed a brutal removal of the gaseous disc from the halo, as if supernovae had expelled all of the gas

from the galaxy. This sudden loss of mass was enough to form a core from the initially cuspy density profile in their simulations. But this model may not be sufficient to explain the formation of cores, as later higher-resolution simulations by Gnedin & Zhao (2002) failed to obtain cores with a similar setup. They observed a steepening of the cusp due to adiabatic contraction in the presence of the gaseous disk, and the dark matter halo did expand when the disk was removed, but it remained cuspy and did not settle as a core. Nevertheless, Read & Gilmore (2005) were able to transform cuspy haloes into cored ones by combining several violent mass loss phases and slow accretion without taking into account gas hydrodynamics. The repetition of such events seems to be of crucial importance to flatten the dark matter distribution.

Starting from cuspy NFW haloes, Mashchenko et al. (2006) assumed that most of the gas was localized in three large clumps oscillating harmonically near the center of the galaxies, and observed the flattening of the dark matter density profile to progressively form a core. The effect is expected to be more efficient for dwarf galaxies, as stellar feedback leads to much more significant large scale gaseous motions (Mac Low & Ferrara, 1999). To validate this semi-analytical model, Mashchenko et al. (2008) further carried out cosmological hydrodynamical simulations modeling star formation and supernova feedback. They confirmed that the heating of the dark matter and its transformation into a core from such baryonic processes was very efficient. Interestingly, when cored galaxies merge together, the resulting galaxy preserves a cored dark matter density profile (Kazantzidis et al., 2006).

Hydrodynamical simulations

Hydrodynamical simulations taking baryonic processes into account are able to reproduce realistic cored galaxies in a cosmological context. Governato et al. (2010) notably carried out a simulation of a dwarf galaxy including baryonic processes such as gas cooling, UV heating, star formation, and supernova heating. They showed that supernova feedback generates holes in the gas distribution due to bubbles of expanding hot gas. These outflows remove part of the gas as in Navarro et al. (1996a) or Read & Gilmore (2005) and enable the dark matter halo to expand to form a core. The expansion of the collisionless dark matter component is indeed correlated with the strongest outflow events. Governato et al. (2012) extend this work by focusing on field galaxies in order to avoid the effects of potential tidal interactions and to concentrate on the consequences of outflows. Their simulations are tuned to reproduce the expected number of stars and the correct ratio between stellar mass and halo mass, not to obtain cores. Strikingly, the addition of baryonic processes is able to reproduce the observed cored density profiles, as shown in Fig. 4.9. Different types of simulations and implementations of stellar feedback give similar results (Macciò et al., 2012; Teyssier et al., 2013; Madau et al., 2014; Di Cintio et al., 2014; Chan et al., 2015) and thus show the crucial role of outflows from supernovae to transform cusps into cores. However, it seems that cusps can reform themselves after destruction (Laporte & Peñarrubia, 2015; Oñorbe et al., 2015), implying that the processes transforming them into cores have to repeat themselves perpetually.

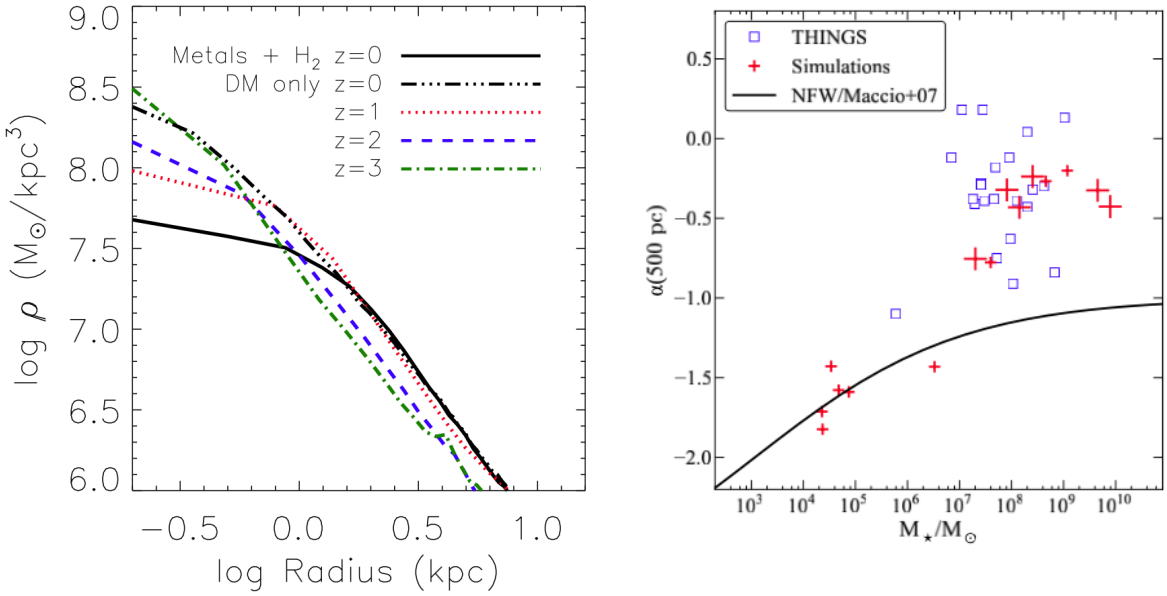

Figure 4.9 – *Evolution of the dark matter density profile of a simulated dwarf galaxy (left) and comparison between the inner slopes of such profiles with observations (right), from Governato et al. (2012). In the left panel, while the dark-matter-only simulation retains its cusp at all redshifts, the simulation with baryonic processes progressively flatten to form a core. The right panel compares the inner slopes from the simulations with the observed data from the THINGS and LITTLE THINGS surveys (Oh et al., 2011, 2015) as well as with the expected cuspy NFW values. While very small haloes of stellar masses below* 10^7 $M_\odot$ *do not seem to flatten to form a core, higher mass simulated galaxies have inner slopes comparable to those observed.*

AGN activity can similarly affect the dark matter distribution. Using idealized hydrodynamical simulations, Martizzi et al. (2012, 2013) indeed showed that the repeated cycles of accretion and expulsion in the vicinity of the central black hole of galaxies lead to the irreversible transformation of the dark matter profile into a core. As in Read & Gilmore (2005), the repetition of the cycles seems to be an important feature of the phenomenon, as it triggers the gravitational potential fluctuations which modify the dark matter distribution.

Repeated potential fluctuations

Although hydrodynamical simulations are able to reproduce the observed cored density profiles of dark matter haloes by adding prescriptions for the various baryonic processes, they do not describe nor quantify the exact mechanisms through which baryons affect the dark matter distribution. Pontzen & Governato (2012, 2014) provided an analytical model to understand such mechanisms, in which repeated, rapid oscillations of the gravitational potential progressively transfer energy from the gas to the dark matter component.

In this model, supernova explosions create pockets of rapidly expanding gas in the central region of the halo, leading to strong fluctuations of the local potential. These

pockets of underdense hot gas can have sizes up to several kpc, and give rise to strong outflows and large movements of gas. The left panel of Fig. 4.10 shows the evolution of the baryonic mass enclosed in spherical shells near the center of the halo, which fluctuates significantly with time. The repetition of the feedback processes progressively transfer energy from the gaseous component to the dark matter, as shown in the right panel of Fig. 4.10: dark matter test particles progressively migrate outwards following the fluctuations of the gravitational potential. Additionally, modeling the process with an adiabatic model does not lead to the formation of a core. It is thus the cumulative effect of violent potential fluctuations that leads to the heating of the dark matter halo and of its transformation into a core.

Pontzen & Governato (2012) developed an analytical model to estimate the energy gain of the halo from the potential fluctuations and test it on their simulations. As shown in Fig. 4.11, the model agrees very well with the simulations, which thus show that the repetitive potential fluctuations stemming from the feedback processes are the main cause of the flattening of the dark matter density profiles. Fig 4.11 indeed shows that when supernova feedback give rise to bulk gas motions and outflows, the initially cuspy dark matter density profile transforms into a core and that its evolution follows that predicted by the model. Although developed to explain stellar feedback, this model could be extended to AGN feedback, as the cycles of accretion and expulsion should also give rise to repetitive oscillations of the gravitational potential.

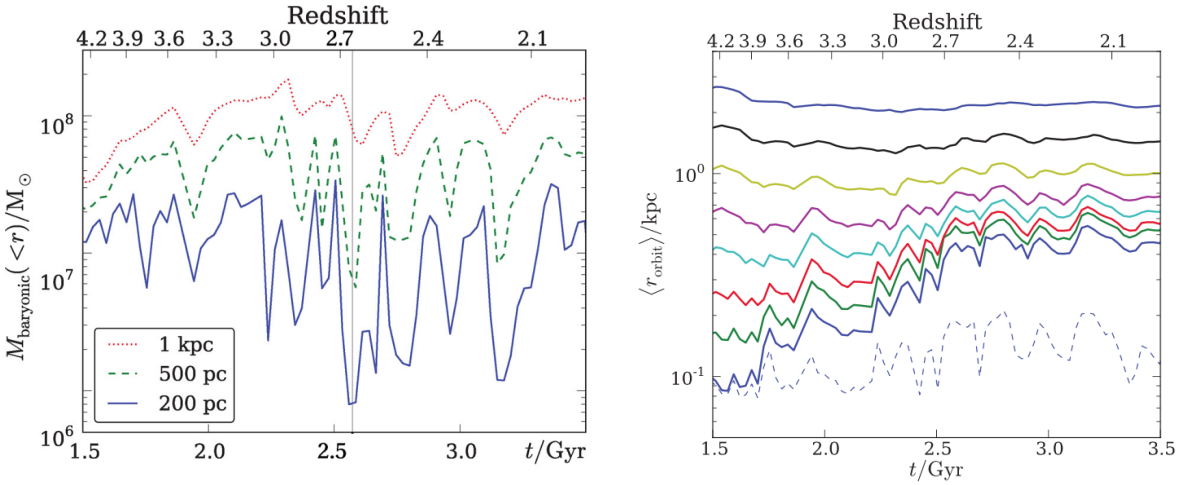

Figure 4.10 – *Left: evolution with time of the baryonic mass enclosed within 1 kpc, 500 pc and 200 pc of the halo center from a simulation with strong supernova feedback by Pontzen & Governato (2012). The outflows generated by the feedback processes yield rapid oscillations of the gravitational potential. Right: evolution of the orbits of test particles given the evolution of the potential. The test particles progressively migrate outwards, which explains the flattening of the central density cusp. The dashed line corresponds to a reversible, adiabatic model which is unable to properly describe the heating of the dark matter halo.*

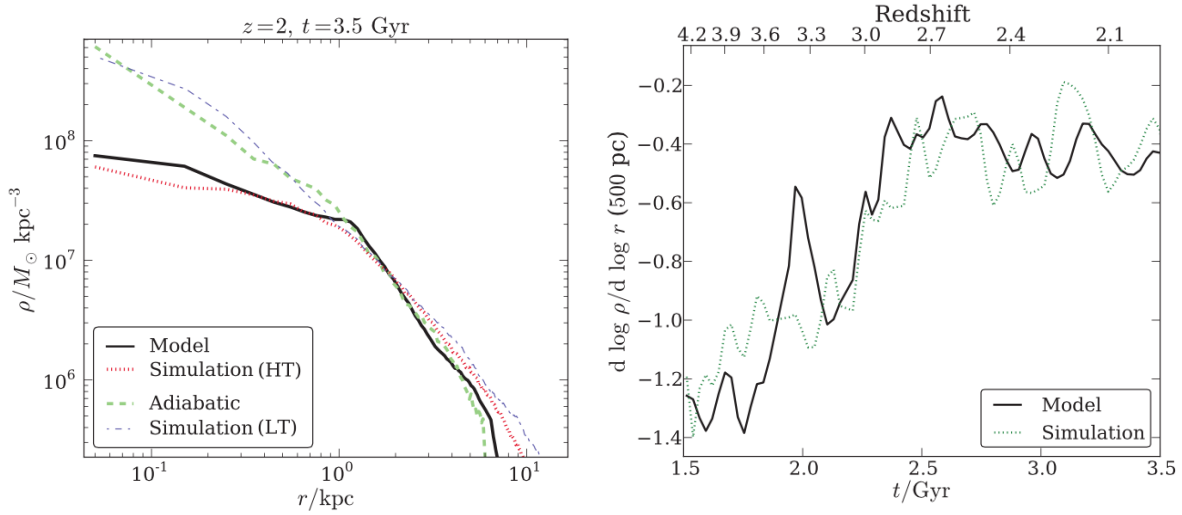

Figure 4.11 – *Left: evolution of the density profile of the simulations from Pontzen & Governato (2012). In the high-threshold (HT) simulation, stars are only allowed to form when the density is above 100 cm^{-3}, thus allowing a better coupling with the feedback mechanisms, while the low-threshold (LT) simulation allows stars to form at densities exceeding 0.1 cm^{-3}. It is only in the HT simulation that supernova feedback will give rise to bulk gas motions and outflows (e.g., Ceverino & Klypin, 2009). The adiabatic model displayed as a dashed line is unable to reproduce the cusp flattening. Right: evolution of the inner logarithmic slope of the density profile corresponding to the strong feedback simulation. This latter evolution confirms the transition from a cuspy profile to a cored one with a slope close to zero.*

4.3 Analytical calculations

We aim at characterizing the effects of gravitational potential fluctuations stemming from large scale movements of gas induced by various feedback mechanisms within dark matter haloes. Such perturbations are expected to heat the dark matter particles and to make them diffuse further away from the center to transform the cusp profile into a cored distribution. Pontzen & Governato (2012) analytically derived the energy gain of a dark matter particle in response to a fluctuating potential. Their calculations rely on the assumptions that the potential is spherically symmetric, that the tracer particles are massless, and that the potential can always be written as a power-law. They validate their approach by comparing the analytical results with numerical simulations. We would like to isolate further the physical mechanism through which dark matter gains energy, assuming a stochastic process. To assess more quantitatively the influence of potential fluctuations on the dark matter halo, we derive the force correlation function and the mean force felt by the dark matter particles, the corresponding velocity variance, which quantify the heating process, and the characteristic relaxation time associated to it.

Unlike Pontzen & Governato (2012) who describe the fluctuations in terms of gravitational potential, we consider the effects of density perturbations in a gaseous medium of average density ρ_0. Our approach is more fundamental in that we derive the potential

fluctuations from the density power spectrum instead of assuming the former. Such an approach is more directly related to the actual feedback processes that move the gas, and on their potential scale dependence. The unperturbed gas distribution ρ_0 is assumed to be homogeneous for simplicity. As AGNs and star formation are likely to influence preferentially the central part of the dark matter halo, we also assume that the perturbations occur within a sphere of radius d inferior to the halo virial radius. The fluctuations are assumed to cascade into smaller scales as in a turbulent or fractal medium, and to have a minimum and a maximum scale length. For turbulence-driven fluctuations, the maximum scale would be the energy driving scale while the minimum scale would be the dissipation scale. The dark matter is not sensitive to the precise fate of the expelled gas, and only dependent on the induced fluctuations of the gravitational potential. The detailed calculations can be found in Appendix F (p. 227).

4.3.1 Force induced by the density fluctuations

Fourier decomposition of the perturbations

The relative density contrast of the perturbations δ, the associated potential Φ and the corresponding force per unit mass $\vec{F}$ can be Fourier decomposed as

$$\delta(\vec{r}) = \frac{V}{(2\pi)^3} \int \delta_{\vec{k}}\ e^{i\vec{k}.\vec{r}}\ d^3\vec{k}. \tag{4.10}$$

$$\Phi(\vec{r}) = \frac{V}{(2\pi)^3} \int \Phi_{\vec{k}}\ e^{i\vec{k}.\vec{r}}\ d^3\vec{k}, \tag{4.11}$$

$$\vec{F}(\vec{r}) = \frac{V}{(2\pi)^3} \int \vec{F}_{\vec{k}}\ e^{i\vec{k}.\vec{r}}\ d^3\vec{k} \tag{4.12}$$

where V is the volume over which the perturbations exist. The components $\phi_{\vec{k}}$ and $\delta_{\vec{k}}$ are related via the Poisson equation $\nabla^2\Phi = 4\pi G\rho_0\delta$ as

$$\phi_{\vec{k}} = -4\pi G\rho_0\ k^{-2}\ \delta_{\vec{k}}, \tag{4.13}$$

while the definition of the force $\vec{F} = -\vec{\nabla}\Phi$ yields

$$\vec{F}_{\vec{k}} = 4\pi i\ G\rho_0\ \vec{k}\ k^{-2}\ \delta_{\vec{k}} \tag{4.14}$$

and

$$|\vec{F}_{\vec{k}}|^2 = (4\pi G\rho_0)^2\ \ k^{-2}\ |\delta_{\vec{k}}|^2. \tag{4.15}$$

This expression of the force per unit mass is valid in the domain where the perturbations occur, i.e., within radius d. We assume that there are no inflows or outflows from this region, so that the gravitational potential remains unperturbed beyond d. Radius d is also much larger than the NFW characteristic radius $\mathrm{R_s}$, than any core radius that may transpire and than the largest fluctuation scale.

Power-law fluctuations

We assume power-law density fluctuations whose power spectrum is defined as

$$\mathcal{P}(k) = V \ \langle |\delta_{\vec{k}}|^2 \rangle = VCk^{-n} \tag{4.16}$$

where C is a constant and n the characteristic exponent of the power-law. In such a power spectrum with $n > 0$, the amplitude of the perturbations increases with their scale, which could account for turbulent processes. A Kolmogorov-like density power-spectrum would notably correspond to $n = 5/3$.

The physical meaning of the power spectrum can be understood in terms of mass variance when the density field is smoothed at different scales. More precisely, the density field $\delta(\vec{r})$ can be filtered at a scale R with a spherically symmetric window function W_R in order to get a smoothed field

$$\delta_R(\vec{r}) = \int \delta(\vec{r'}) W_R(\vec{r} - \vec{r'}) d^3\vec{r'} \tag{4.17}$$

with $\int W_R(\vec{r}) d^3\vec{r} = 1$. The window function has a characteristic scale R and can be for example chosen to be Gaussian, such that

$$W_R(\vec{r}) = \frac{1}{(2\pi)^{3/2} R^3} \exp\left(-\frac{|\tilde{\mathrm{r}}|^2}{2\mathrm{R}^2}\right). \tag{4.18}$$

The variance associated to the smoothed density distribution is

$$s^2(R) = \langle \delta_R^2(\vec{r}) \rangle = \frac{1}{2\pi^2} \int_0^\infty \mathcal{P}(k) k^3 \ \widetilde{W}^2(kR) \frac{dk}{k}, \tag{4.19}$$

where $\widetilde{W}(kR)$ is the Fourier transform of the window function (e.g., Martínez & Saar, 2002; Mo et al., 2010, p. 266). In the case of a Gaussian window function as in Eq. 4.18,

$$\widetilde{W}(kR) = \exp\left(-\frac{(\mathrm{kR})^2}{2}\right). \tag{4.20}$$

For a power-law power-spectrum as in Eq. 4.16 and a Gaussian window function, Eq. 4.19 yields

$$s^2(R) = \frac{VC}{2\pi^2} \ \frac{1}{R^{3-n}} \ \int_0^\infty x^{3-n} \ e^{-x^2/2} \ \frac{dx}{x} \propto R^{n-3}. \tag{4.21}$$

For a top-hat window function, the proportionality holds for $-1 < n < 3$ (e.g., Mo et al., 2010, p. 268). The condition $n < 3$ is required because otherwise the variance would grow indefinitely when the scale of the perturbations increases. The quantity s^2 actually corresponds to the variance associated to the mass distribution smoothed at scale R, which is precisely what is shown in the left panel of Fig. 4.10 from Pontzen & Governato (2012) if we assume stationary and ergodic random processes as the origin of the density fluctuations. For an exponent $n = 2.4$, we thus expect $s \propto R^{-0.3}$ so that the standard deviation in mass increases by a factor 1.3 from $R = 200$ pc to $R = 500$ pc and by a factor 1.6 from $R = 200$ pc to $R = 1$ kpc. Such values are not incompatible with the figure. Numerical simulations with feedback mechanisms providing similar curves, such as that by Teyssier et al. (2013), or even observations, could thus provide a physically-motivated value for the exponent n and for the normalization of the power-spectrum. In our numerical applications, we will more simply assume $n = 2.4$.

The force auto-correlation function

In order to characterize the effects of the density fluctuations on the dark matter particles, we derive the force auto-correlation function $\langle F(0)F(\vec{r})\rangle$, which is the inverse Fourier transform the force power-spectrum (cf. F.1.2):

$$\langle F(0)F(\vec{r})\rangle = \frac{V}{(2\pi)^3}\int |\vec{F_k}|^2\ e^{i\vec{k}.\vec{r}}\ d^3\vec{k}. \tag{4.22}$$

For isotropic power-law fluctuations of wave numbers between k_{min} and k_{max}, Eq. 4.15 and 4.16 yield (cf. Appendix F.2.2)

$$\langle F(0)F(r)\rangle = \frac{D}{r}\int_{k_{min}}^{k_{max}} \frac{\sin\ kr}{k^{n+1}}\ dk, \tag{4.23}$$

with $D = 8CV\left(G\rho_0\right)^2$. The integral can be evaluated in terms of incomplete Gamma functions[3] to obtain

$$\langle F(0)F(r)\rangle = \frac{D}{2}\left(ir\right)^{n-1}\left[\Gamma(-n, ik_{max}r) - \Gamma(-n, ik_{min}r)\right] + C.C. \tag{4.24}$$

where $C.C.$ refers to the complex conjugate of the first term. We further assume that $k_{min} \ll k_{max}$ and $n > 0$, so we can neglect the terms depending on k_{max}. In the diffusion limit where $k_{min}r \gg 1$, i.e., for points separated by distances much larger than the largest fluctuation scale $1/k_{min}$, the asymptotic behavior of the force auto-correlation function is[4]

$$\langle F(0)F(r)\rangle \sim \frac{D}{r^2}\ \frac{1}{k_{min}^{n+1}}\ \cos(k_{min}r). \tag{4.25}$$

Eq. 4.24 can also be used to estimate the average force per unit mass felt by the dark matter particles when $n > 1$, namely as

$$\langle F(0)^2\rangle = \frac{8\left(G\rho_0\right)^2\langle|\delta_{k_{min}}|^2\rangle\ d^3}{n-1}\ k_{min}\ \left(1 - \left(\frac{k_{min}}{k_{max}}\right)^{n-1}\right). \tag{4.26}$$

When $k_{max} \gg k_{min}$ and $n > 1$, this expression yields

$$\langle F(0)^2\rangle \approx \frac{8\left(G\rho_0\right)^2\langle|\delta_{k_{min}}|^2\rangle\ d^3}{n-1}\ k_{min}. \tag{4.27}$$

In this regime, the force is proportional to $k_{min}^{1/2}$ so inversely proportional to the square root of the largest fluctuation scale.

---

[3] $\Gamma(s,x) = \int_x^\infty t^{s-1}e^{-t}dt$

[4] $\Gamma(s,x) \underset{|x|\to+\infty}{\sim} x^{s-1}e^{-x}$

4.3.2 Velocity variance

$\langle \Delta v^2 \rangle$ as a function of the force time-correlation function

We are interested in the effects of the force fluctuations born out of the density perturbations in the gaseous field on the motions of the dark matter particles composing the surrounding halo. These fluctuations are expected to heat the halo, and their influence can thus be described by the resulting velocity variance of the dark matter particles. Integrating the equation of motion of a dark matter particle and averaging over the different particles enable to write the velocity variance after a time T in terms of the force time-correlation function (cf. F.3.1):

$$\langle \Delta v^2 \rangle = 2 \int_0^T (T - t) \langle F(0) F(t) \rangle \, dt. \tag{4.28}$$

This expression assumes that the force is a random function with stationary statistical properties, hence corresponding to feedback processes that are random but persistent.

$\langle \Delta v^2 \rangle$ as a function of the spatial force correlation function

Eq. 4.28 expresses the velocity variance as a function of the force time-correlation function, whereas our previous calculations involved the spatial correlation function. The two descriptions can be bridged by considering a test dark matter particle moving with respect to the fluctuating gaseous field. The main contributions to the relative velocity of the dark matter particle with respect to the fluctuating field will come from large-scale flows such as the orbital velocity $\langle v \rangle$ and from the temporal variations in the field on the largest fluctuations scales, which will correspond to a characteristic velocity $\langle u^2 \rangle^{1/2}$. The perturbations on large scales will indeed sweep out the movements induced at smaller scales. The correspondence between the spatial statistical properties of a random field and its temporal properties has been extensively studied in the case of turbulent geophysical and atmospheric flows, notably to understand whether the spatial field properties were transported frozen in the bulk flow of average velocity $\langle v \rangle$ or randomly swept with velocity $\langle u^2 \rangle^{1/2}$ (Taylor, 1938; Kraichnan, 1964; Tennekes, 1975). Various theoretical, numerical and experimental studies suggest that the statistical properties of the field in the temporal domain can be translated to the spatial domain through a velocity $v_r = \sqrt{\langle v \rangle^2 + \langle u^2 \rangle}$, such that the temporal statistical properties at a given point are the spatial properties of the fluid transported at velocity v_r through that point (e.g., L'vov et al., 2001; He & Zhang, 2006; Zhao et al., 2009; He & Tong, 2011; Wilczek & Narita, 2012; Wilczek et al., 2014). Given v_r, we define $r = v_r t$ the distance a test dark matter particle travels with respect to the fluctuating gas field during time t, and similarly $R = v_r T$, the corresponding distance traveled during the duration T. With these assumptions, Eq. 4.28 can be rewritten as

$$\langle \Delta v^2 \rangle = \frac{2}{v_r^2} \int_0^R (R - r) \langle F(0) F(r) \rangle \, dr. \tag{4.29}$$

In our case, both the mean flow $\langle v \rangle$ and the large scale random gaseous motions at velocity $\langle u^2 \rangle^{1/2}$ have timescales comparable to the dynamical time. Indeed, the orbital motions of the dark matter particles are directly driven by the gravitational field, while the large scale fluctuations are in energy equilibrium with it, as we assume that there are no inflows or outflows from or out of the central region within radius d in which the fluctuations occur. For a characteristic scale length $l \leq d$ associated with the density fluctuations, we thus expect to have $v_r \sim l/t_D(l)$ where $t_D(l)$ is the dynamical time at radius l. Given that the large scale perturbations are likely to sweep out the smaller scale ones, the characteristic length scale l would relate to the size of the largest perturbations $2\pi/k_{min}$ or even to the extension radius of the perturbations d.

Explicit expression of $\langle \Delta v^2 \rangle$

Injecting the expression of the spatial force correlation function (Eq. 4.24) into Eq. 4.29 while assuming $k_{min} \ll k_{max}$ yields (cf. F.3.2)

$$\langle \Delta v^2 \rangle = \frac{DR}{v_r^2} k_{min}^{-n} \left(\frac{2}{n} \mathrm{Si}\left(k_{min}R\right) + T_1(k_{min}R) + T_2(k_{min}R) \right) \tag{4.30}$$

where Si refers to the sine integral function[5] and

$$T_1(k_{min}R) = \left(\frac{1}{n} - \frac{1}{n+1} \right) i(ik_{min}R)^n \Gamma(-n, ik_{min}R) + C.C., \tag{4.31}$$

$$T_2(k_{min}R) = \frac{2}{n+1} \frac{1}{k_{min}R} \left(\cos\left(k_{min}R\right) - 1 \right) \tag{4.32}$$

are transient terms much smaller than the sine integral term as soon as $k_{min}R \gg 1$. The sine integral function itself converges to $\pi/2$ when $k_{min}R \gg 1$ so that

$$\langle \Delta v^2 \rangle \sim \frac{\pi D}{n v_r} \frac{T}{k_{min}^n} \tag{4.33}$$

for large enough values of $R = v_r T$. This expression assumes isotropic fluctuations which span scales between $2\pi/k_{max}$ and $2\pi/k_{min}$ with $k_{min} \ll k_{max}$, and that during time T the test dark matter particles move distances much larger than the maximum wavelength of the perturbations, $R \gg 1/k_{min}$. Such a regime corresponds to the diffusion limit, in which the dark matter particles are not ballistically displaced by the bulk motion of the flow but instead undergo random walks initiated by the persistent density fluctuations. Given $v_r \sim l/t_D(l)$, the diffusion condition $Rk_{min} \gg 1$ is attained on a dynamical time scale provided $l \gg 1/k_{min}$, i.e., for dark matter orbits above the largest fluctuation scale $1/k_{min}$.

[5] $\mathrm{Si}(x) = \int_0^x \frac{\sin x}{x} dx$

4.3.3 Relaxation time

In stellar dynamics, stars get deflected by their two-body interactions with one another. When a star travels across a galaxy, its perturbed velocity Δv grows progressively and eventually reaches its original unperturbed velocity $\langle v \rangle$. The relaxation time $t_{\rm relax}$ is defined as the time at which $\Delta v = v$, and corresponds to the time required for the star to lose the memory of its original orbit. Similarly, we can introduce here the relaxation time of the dark matter particles perturbed by the potential fluctuations. If $\langle v \rangle$ is the mean unperturbed velocity of dark matter particles, the relaxation time would be defined in the diffusion limit as

$$t_{\rm relax} = \frac{n v_r \langle v \rangle^2 k_{min}^n}{\pi D} \tag{4.34}$$

given Eq. 4.33. Recalling $D = 8CV(G\rho_0)^2$ and expressing the normalization of the power spectrum in terms of the level of fluctuations at the maximum scale, such that $C = k_{min}^n \langle |\delta_{k_{min}}|^2 \rangle$, yield

$$t_{\rm relax} = \frac{n v_r \langle v \rangle^2}{8\pi (G\rho_0)^2 V \langle |\delta_{k_{min}}|^2 \rangle}. \tag{4.35}$$

While $\langle v \rangle$ is the mean unperturbed orbital velocity of dark matter particles, v_r is their mean velocity with respect to the fluctuating gas field. Both velocities are determined by the gravitational field. The orbital velocity at a scale l can be estimated as $\langle v \rangle \sim l/t_D(l) \sim l\sqrt{G\rho(l)}$, where $t_D(l) = 1/\sqrt{G\rho(l)}$ is the dynamical time at radius l. We further assume that the main contribution due to the fluctuating gaseous field comes from the largest scale fluctuations so that $v_r \sim d\sqrt{G\rho(d)}$. With these approximations and identifying $V \approx d^3$, the relaxation time becomes (cf. F.4)

$$t_{\rm relax} \approx \frac{n}{8\pi \langle |\delta_{k_{min}}|^2 \rangle} f^{-2} \left(\frac{l}{d}\right)^2 \frac{\rho(d)}{\rho(l)}\, t_D(d) \tag{4.36}$$

where $f = \rho_0/\rho(l)$ is the total gas fraction initially at radius l. Note that while ρ_0 corresponds to the gaseous component, $\rho(l)$ and $\rho(d)$ correspond to the total baryonic plus dark matter density of the halo, for example defined as a cuspy NFW halo. Assuming that the unperturbed gas density ρ_0 is constant with radius, this expression yields a constant relaxation time for an isothermal halo whose density $\rho(l) \propto l^{-2}$ while it reaches a maximum at the characteristic radius R_s for an NFW halo.

The expression of the relaxation time obtained here is relatively analogous to that obtained for two-body relaxation in N-body systems, for example in the case of stars or dark matter particles deflected by their successive interactions with one another (e.g., Binney & Tremaine, 1987; Huang et al., 1993; El-Zant, 2006). Two-body relaxation is indeed often modeled as a diffusion process due to random encounters between particles, and the associated relaxation time in the case of a system constituted by N identical stars or dark matter particles can be expressed as

$$t_{\rm relax} \sim 0.1\, \frac{N}{\ln\Lambda} t_D, \tag{4.37}$$

where $\Lambda = b_{max}/b_{min}$ is the ratio between the maximum and minimum impact parameters while t_D is the dynamical time (e.g., Binney & Tremaine, 1987, p. 34). In such a system, the mass variance is expected to be proportional to N so the variance associated to the relative density contrast $\langle\delta^2\rangle \propto 1/N$. Both expressions of the relaxation time thus have similar dependences in $\langle\delta^2\rangle$ and t_D. However, Λ does also depend on N in the case of a two-body relaxation, notably as the minimal impact parameter b_{min} decreases when the number of particles rises.

Estimating grossly the relaxation time at radius d from Eq. 4.36 with $f = 10\%$ at the virial radius and fluctuation levels of order one at the top of the power spectrum, i.e., for $\delta_{k_{min}} \sim 1$, we find that it only takes a few dynamical times $t_D(d)$ for the trajectories of the dark matter particles to be significantly affected by the density fluctuations of the gas. Alternatively, one needs $\langle|\delta_{k_{min}}|^2\rangle \sim 100$ in order to have a significant effect over a hundred dynamical times. More precisely, Fig. 4.12 shows the evolution with radius of the relaxation time calculated from Eq. 4.36 for an NFW halo perturbed by density fluctuations with a power-law power-spectrum of exponent $n = 2.4$, $\delta_{k_{min}} = \sqrt{\langle|\delta_{k_{min}}|^2\rangle} = 10$ and a perturbed domain of radius $d = 5$ kpc. The NFW halo has a total mass $\mathrm{M_{tot}} = 2.26\ 10^{11}\ \mathrm{M_\odot}$ within $\mathrm{R_{vir}} = 30$ kpc, a characteristic radius $\mathrm{R_s} = 0.9$ kpc and $f = 10\%$. The curve displays a maximum at $\mathrm{R_s}$, but the relaxation time does not exceed 75 times the dynamical time $t_D(d)$ at the edge of the domain in which the perturbations occur. This corresponds to 560 Myr, so we expect to observe an effect of the density variations on the dark matter halo within about 500 Myr. Moreover, the relaxation time becomes smaller when the radius decreases below $r \sim 1$ kpc, which suggests a stronger effect at the smallest radii, hinting at a flattening of the density profile. Such a prediction can be tested against numerical simulations.

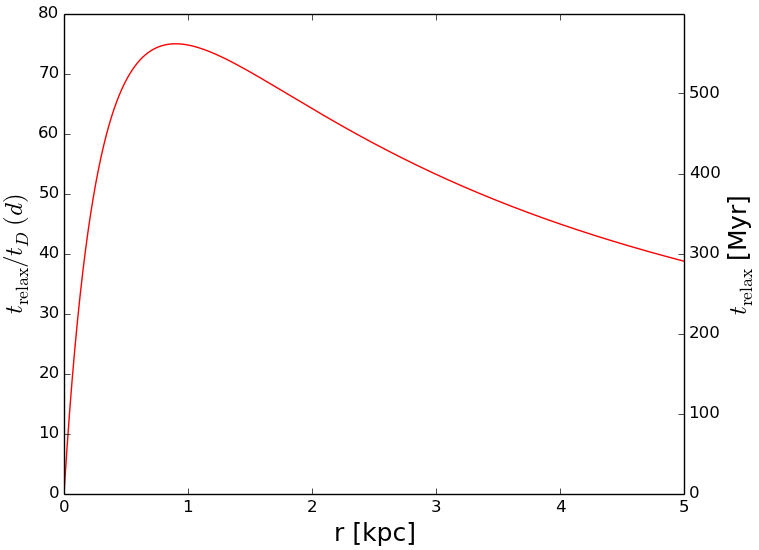

Figure 4.12 – *Evolution of the relaxation time as calculated from Eq. 4.36 in the case of an NFW halo submitted to perturbations as in the fiducial case of our simulations (Tables 4.1 and 4.2). The relaxation time is expressed in terms of the dynamical time* $t_D(d)$ *at* $d = 5$ kpc.

4.4 Simulating the effects of the pertubations

4.4.1 The SCF code

In order to simulate the effects of power-law density fluctuations on the dark matter distribution of a galactic halo, we use the self-consistent field (SCF) method developped by Hernquist & Ostriker (1992). This Fortran algorithm was designed to describe the evolution of collisionless stellar systems, but instead of directly evaluating the interactions between the particles, it solves Poisson equation to compute the gravitational potential at each time step and advances the trajectories of the particles from the potential one by one. As all particles evolve in the same potential, the method is equivalent to solving N one-body problems, which saves a lot of computational time. At each time step, orbits are computed given the potential and used to determine the evolving density distribution. From this, the potential is recomputed, and the whole process is iterated at the next time step.

The Poisson equation is solved by expanding the density and the potential in a set of basis functions deriving from the spherical harmonics $Y_{lm}(\theta, \phi)$:

$$\rho(\vec{r}) = \sum_{n=0}^{n_{max}} \sum_{l=0}^{l_{max}} \sum_{m=-l}^{l} A_{nlm}\ \rho_{nl}(r)\ Y_{lm}(\theta, \phi) \tag{4.38}$$

$$\Phi(\vec{r}) = \sum_{n=0}^{n_{max}} \sum_{l=0}^{l_{max}} \sum_{m=-l}^{l} B_{nlm}\ \Phi_{nl}(r)\ Y_{lm}(\theta, \phi), \tag{4.39}$$

where n is the radial "quantum" number and l and m the corresponding quantities for the angular variables, namely analogous to the orbital quantum number and to the magnetic quantum number respectively. This expansion separates the radial and angular components, and the individual harmonics satisfy Poisson equation

$$\nabla^2 \left[A_{nlm}\ \Phi_{nl}(r)\ Y_{lm}(\theta, \phi)\right] = 4\pi\ B_{nlm}\ \rho_{nl}(r)\ Y_{lm}(\theta, \phi). \tag{4.40}$$

The choice of basis could have been different, but the one chosen by Hernquist & Ostriker (1992) enables to retrieve a radial density profile at the smallest order that approximates the luminosity distribution of spheroidal galaxies. By cutting the expansion at a relatively low-order couple (n_{max}, l_{max}), the potential is smoothed and loses its dependence in the specific set of test particles that were used to compute it. The effect of this truncation is analogous to the softening carried out in N-body simulations, which is an unavoidable step to compute the potential.

The choice of (n_{max}, l_{max}) is crucial to capture the radial and angular structure of the halo without being dominated by the particle noise: if the harmonic expansion does not use enough terms, there will be a large bias, but if it uses too many, the resulting density distribution will have huge inhomogeneities depending on the positions of the test particles. This suggests that there is an optimal expansion cutoff, which depends on the number of particles (Weinberg, 1996; Meiron et al., 2014), and that increasing the

couple (n_{max}, l_{max}) beyond it might be harmful to the simulation in addition to being unnecessarily costly in terms of CPU time. Vasiliev (2013) tests the choice of (n_{max}, l_{max}) for simulations analogous to the SCF code with N = 10^5 and 10^6 particles and shows that while increasing n_{max} generally leads to smaller errors, increasing l_{max} only improves the expansion up to $l_{max} = 4$ for N = 10^5 and yields noise-dominated terms beyond $l_{max} = 8$. In our simulations, we test different values of (n_{max}, l_{max}) and use the typical (n_{max}, l_{max}) = (10, 4) for our N= 240 000 fiducial simulations, as advocated by Vasiliev (2013).

4.4.2 Initial conditions

We aim at understanding the flattening of the density profiles of dark matter haloes and their transformation into cored distributions, so we start our simulations with initial conditions corresponding to standard, cuspy NFW profiles as described by Eq. 4.1. We restrict ourselves to low-mass galaxies and consider the case of a small galaxy with a total halo mass of $M_{tot} = 2.26\ 10^{11}\ M_\odot$ as a fiducial illustration. The core-cusp discrepancy is indeed more visible in dwarf or low mass galaxies as the dark matter distribution is more difficult to ascertain in Milky-Way like galaxies (Pontzen & Governato, 2014). The initial conditions were computed for 240 000 dark matter particles, with a mass cut-off radius R_{vir} = 30 kpc and an NFW characteristic radius R_s = 0.9 kpc, so the concentration parameter $C = R_{vir}/R_s$ is about 30. The total mass M_{tot} being defined as the mass enclosed within R_{vir}, it can be expressed as

$$M_{tot} = 4\pi\rho_0 R_s^3 \left(\ln(1+C) - \frac{C}{1+C}\right) \tag{4.41}$$

so the central density of the halo yields $\ln(\rho_0) = 0.63$ with ρ_0 in units of $2.26\ 10^9\ M_\odot/kpc^2$. Fig. 4.13 shows the column density map of the initial dark matter halo, and its NFW profile with inner slope -1, while Table 4.1 summarizes the halo parameters used for the

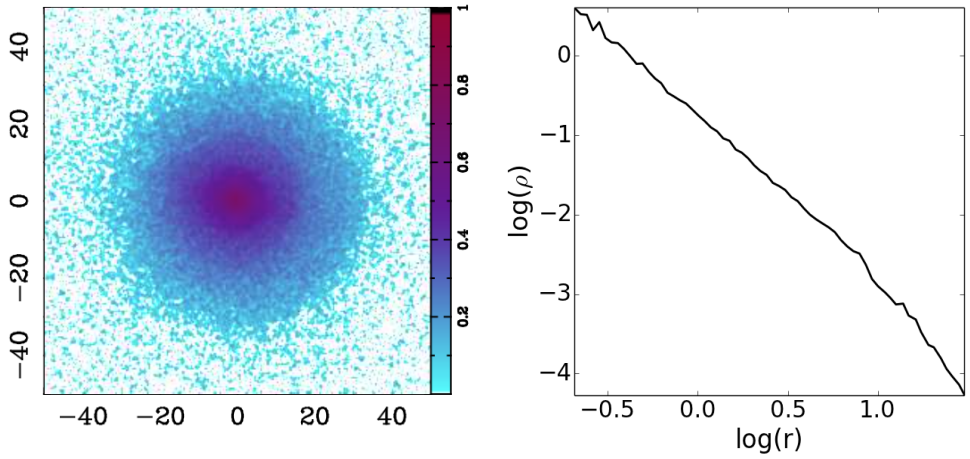

Figure 4.13 – *Map and density profile of the NFW initial conditions taken for the SCF simulations. The distances are indicated in kpc while the density is in units of* $2.26\ 10^9\ M_\odot/kpc^3$.

fiducial simulations. The gas mass fraction $f_{gas} = M_{gas}/(M_{gas} + M_{star})$ is defined relatively to the total baryonic mass, and only intervenes in the dynamics of the dark matter system through the gas density perturbations.

Mass of the dark matter halo	M_{tot}	$2.26\ 10^{11}\ M_{\odot}$
NFW cut-off radius	R_{vir}	30 kpc
NFW characteristic radius	R_s	0.9 kpc
Gas fraction	f_{gas}	0.5

Table 4.1 – *Parameters describing the halo initial conditions for the fiducial simulations.*

4.4.3 Adding the perturbations

Gaseous density fluctuations

The density perturbations are practically added in the code through their effect on the force and on the gravitational potential felt by the test dark matter particles. We assume a galactic halo in which baryons account for 20% of the total mass, which is slightly above but of the same order of magnitude as the universal baryon fraction $\Omega_b/(\Omega_b+\Omega_{dm}) = 0.16$ (Planck Collaboration et al., 2014, 2015). The perturbations on the gravitational potential are assumed to arise from density fluctuations within a homogeneous gaseous component of density

$$\rho_{gas} = f_{gas}\ 0.2\ \rho_{mean}, \tag{4.42}$$

where $f_{gas} = M_{gas}/\left(M_{gas} + M_{stars}\right)$ is the gas fraction relatively to all the baryons and ρ_{mean} the mean total density of the halo,

$$\rho_{mean} = \frac{M_{tot}}{4\pi R_{vir}^3/3}. \tag{4.43}$$

The choice of $f_{gas} = 0.5$ in the fiducial simulations is motivated by the high-gas fractions observed at high redshift (e.g., Daddi et al., 2010a; Tacconi et al., 2010; Förster Schreiber et al., 2011) and yields an overall gas fraction relative to the mean total baryonic and dark matter mass $f_{mean} = \rho_{gas}/\rho_{mean} = 10\%$.

A power-law power spectrum

The density fluctuations follow the same assumptions as in the analytical calculations of section 4.3. Namely, they are assumed to constitute a stochastic process with a power-law power spectrum

$$\langle|\delta_{\vec{k}}|^2\rangle \propto k^{-n}. \tag{4.44}$$

The wave numbers $k = |\vec{k}|$ are comprised between two thresholds, k_{min} and k_{max}. These thresholds correspond to the maximum and minimum scales at which the perturbations

occur, namely $\lambda_{max} = 2\pi/k_{min}$ and $\lambda_{min} = 2\pi/k_{max}$. In the fiducial simulations, we take $\lambda_{min} = 10$ pc and $\lambda_{max} = 1$ kpc, so that $\lambda_{min} \ll \lambda_{max}$ as in the analytical calculations. These scales encompass typical scales at which feedback processes affect the gas density distribution (e.g., Governato et al., 2010). We normalize the density perturbation $\delta_{\vec{k}}$ by its rms value at k_{min}, $\delta_{k_{min}} = \sqrt{\langle|\delta_{\vec{k_{min}}}|^2\rangle}$, so that

$$|\delta_{\vec{k}}| = \delta_{k_{min}} \left(\frac{k}{k_{min}}\right)^{-n/2}. \tag{4.45}$$

The force deriving from the power-law fluctuations

As in section 4.3, the contribution of a perturbation $\delta_{\vec{k}}$ to the stochastic force felt by a dark matter particle is

$$\vec{F_{\vec{k}}} = -i\vec{k}\Phi_{\vec{k}} = 4\pi i G\rho_{\rm gas}\vec{k}k^{-2}\delta_{\vec{k}}. \tag{4.46}$$

As the force depends on the direction of $\vec{k}$, we consider a random direction (θ_k, ϕ_k) for each value of k, with $\theta_k \in [0, \pi]$ and $\phi_k \in [0, 2\pi]$:

$$\vec{k} = k\left(\sin(\theta_k)\cos(\phi_k)\vec{u_x} + \sin(\theta_k)\sin(\phi_k)\vec{u_y} + \cos(\theta_k)\vec{u_z}\right). \tag{4.47}$$

We also introduce a random phase ψ_k and a pulsation frequency $\omega(k)$ in order to write the force corresponding to mode k felt by a dark matter particle situated in $\vec{r}$ at time t as:

$$\vec{F_{\vec{k}}}(\vec{r}, t) = 4\pi G\rho_{\rm gas}\delta_{k_{min}}\ k_{min}^{n/2}\ \vec{k}\ k^{-n/2-2}\ \sin\left(\omega(k)t - \vec{k}.\vec{r} + \psi_k\right). \tag{4.48}$$

We further assume that only the particles whose radius $r = |\vec{r}|$ is below a certain radius d are affected by the perturbations, so the force $\vec{F_{\vec{k}}}$ is only added when computing the trajectories of these particles. By doing so, we only consider density fluctuations happening in the central region of the galaxy - which is where most of the star formation occurs and where the AGN is located. The force is rescaled to match the assumed power-spectrum normalization, such that its rms value averaged over all the dark matter particles is equal to the theoretical value whose square was calculated in section 4.3:

$$\langle F(0)^2\rangle = \frac{8\left(G\rho_{\rm gas}\right)^2\delta_{k_{min}}^2\ d^3}{n-1}\ k_{min}\ \left(1 - \left(\frac{k_{min}}{k_{max}}\right)^{n-1}\right), \tag{4.49}$$

The different parameters needed to describe the perturbations to the NFW dark matter halo are summarized in Table 4.2, as well as their values in the fiducial simulations. The same rms value of the force can be attained by different sets of parameters, as it notably depends on the perturbation level $\delta_{k_{min}}$ and on the extension of the central fluctuating zone d. For a given value of k_{min}, the force is indeed proportional to $f_{mean}\delta_{k_{min}}d^{3/2}$, where $f_{mean} = \rho_0/\rho_{mean}$ is the mean gas fraction relative to the total density of the halo. Fig. 4.14 shows different sets of parameters (f_{mean}, $\delta_{k_{min}}$, d) leading to the same value of the mean force as in the fiducial parameters.

Minimum scale of the perturbations	$\lambda_{min} = 2\pi/k_{max}$	10 pc
Maximum scale of the perturbations	$\lambda_{max} = 2\pi/k_{min}$	1 kpc
Cutoff radius for the perturbations	d	5 kpc
Power-law exponent	n	2.4
Perturbation overdensity at k_{min}	$\delta_{k_{min}}$	10

Table 4.2 – *Parameters describing the perturbations for the fiducial simulations.*

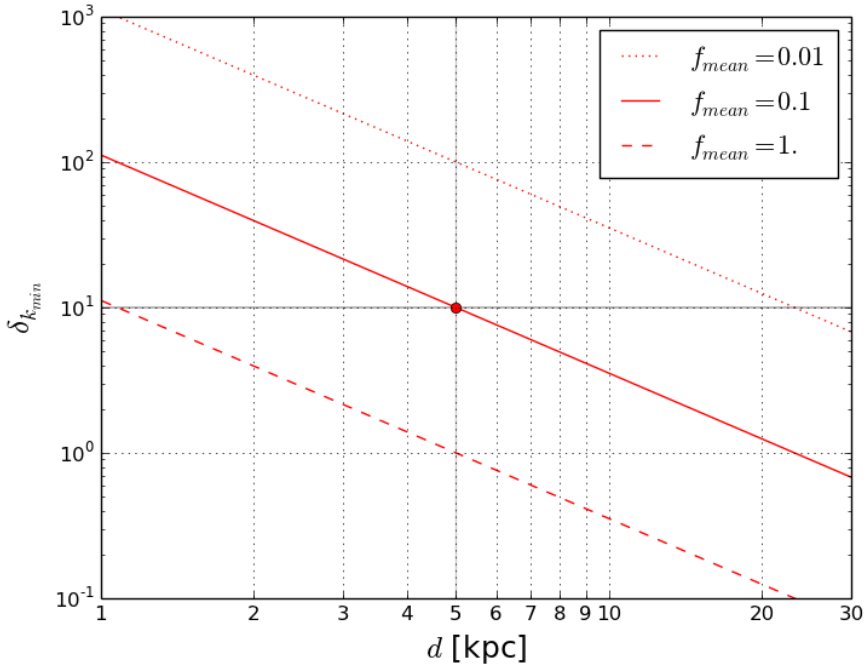

Figure 4.14 – *Ensemble of parameters leading to the same mean force* $\langle F(0)^2 \rangle^{1/2}$ *as in the fiducial case of the simulations.* f_{mean} *is the mean gas density within the halo,* $\delta_{k_{min}}$ *the amplitude associated to the largest scale fluctuations, and d the radius within which the perturbations occur.*

Pulsation frequency associated to the perturbations

We carry out simulations with two different definitions of the pulsation frequency of the density perturbations. This frequency $\omega(k)$ depends on the mode k of the perturbation and is related to its propagation velocity v_g. Physically, each mode k corresponds to a gaseous structure of size $\lambda = 2\pi/k$ perturbing the gravitational potential.

In the first set of simulations, we assume a constant propagation velocity defined from the dynamical time scale associated to the volume affected by the perturbations. This dynamical time scale is estimated as

$$t_{D,mean}(d) = \frac{1}{\sqrt{G\rho_{\rm mean}(d)}}, \tag{4.50}$$

with $\rho_{\rm mean}(d)$ the mean total density within the sphere of radius d, as calculated in Appendix F.1.4. The corresponding velocity is thus

$$v_g = \frac{d}{t_{D,mean}(d)}, \tag{4.51}$$

which is taken as propagation velocity so that

$$\omega(k) = v_g k \tag{4.52}$$

Given the initial conditions and $d = 5$ kpc, we have $v_g = 134$ km s^{-1} for our fiducial simulations. This value lies in the velocity range observed for molecular outflows in nearby galaxies. Indeed, Cicone et al. (2014) report average outflow velocities ranging from 50 to 800 km.s^{-1} in local ULIRGs and quasar-hosts with a median of about 200 km s^{-1}. While outflow velocities can sometimes reach values close and above 1000 km s^{-1} (Fischer et al., 2010; Sturm et al., 2011; Dasyra & Combes, 2012), values of a few hundreds of km s^{-1} seem to be common (Sakamoto et al., 2009; Combes et al., 2013).

In the second set of simulations, we define $\omega(k)$ from Larson's relation, which relates the velocity dispersion of a gaseous structure to its size (Larson, 1981; Solomon et al., 1987, cf. section 1.3.1). We can indeed expect the propagation velocity associated to a density perturbation mode of size λ to scale as its velocity dispersion $\sigma(\lambda)$. This latter quantity can be derived from Larson's relation (Solomon et al., 1987),

$$\left(\frac{\sigma}{\text{km s}^{-1}}\right) \simeq 1.0 \left(\frac{\lambda}{\text{pc}}\right)^{0.5}. \tag{4.53}$$

Assuming that the propagation velocity $v_g = d\omega/dk$ equals σ, this empirical relation yields $\omega(k) \simeq 1.6\sqrt{k}$, with ω in (10 Myr)$^{-1}$ and k in kpc^{-1}. We actually take

$$\omega(k) = 2\sqrt{k} \tag{4.54}$$

for simplicity, which also corresponds approximately to a characteristic time scale $\tau = 2\pi/\omega$ of 10 Myr for a kpc-sized structure. This time scale corresponds to the dynamical time within the gaseous structures and is comparable to the lifetimes of large star-forming molecular clouds, which are evaluated at a few tens of Myr (Blitz & Shu, 1980; Larson, 1981; Elmegreen, 1991). It is also of the same order of magnitude as the time needed for massive molecular outflows to expel the cold gas reservoir from a galaxy, as notably evaluated for Mrk 231 from IRAM Plateau-de-Bure CO(1-0) observations by Feruglio et al. (2010) or for a set of different galaxies by Sturm et al. (2011).

4.4.4 Choice of the time step

Time scales associated to the perturbation modes

We implement perturbation modes whose wave numbers are comprised between k_{min} and k_{max}. This corresponds to perturbations of spatial size between $\lambda_{min} = 2\pi/k_{max}$ and $\lambda_{max} = 2\pi/k_{min}$, and in the fiducial simulations we took $\lambda_{min} = 10$ pc and $\lambda_{max} = 1$ kpc. To each perturbation mode corresponds a timescale, which depends on the definition of the pulsation $\omega(k)$.

- When $\omega(k)$ is defined as $\omega(k) = v_g\, k$ (Eq. 4.52) in order to have a constant propagation velocity v_g, the corresponding timescales are $T(k_{min}) = \lambda_{max}/v_g = 7.5$ Myr and $T(k_{max}) = \lambda_{min}/v_g = 0.075$ Myr. In the fiducial case, we indeed have $v_g = 134$ km/s and $d = 5$ kpc.

- When $\omega(k)$ is defined from Larson's relation as in Eq. 4.54, the periods corresponding to the maximum and minimum time scales of the perturbations are respectively $T(k_{min}) = 2\pi/\omega(k_{min}) = 12.53$ Myr and $T(k_{max}) = 2\pi/\omega(k_{max}) = 1.25$ Myr.

Sampling method

In order to understand the influence of the time step δt on a random force simulation, we consider a one-dimensional force whose form at each timestep $t_i = i\delta t$ is

$$F(t_i) = F_i \cos\left(2\pi \frac{t_i}{T}\right), \tag{4.55}$$

where F_i is a random number between $[-1, 1]$ and T is the caracteristic time scale associated to it. This force is analogous to the perturbation term added to the force in the halo simulations. We study the influence of the time step δt on the mean value of the cumulative force

$$\langle F \rangle(t) = \sum_{t_i=0}^{t} F_i \tag{4.56}$$

and on the corresponding standard deviation σ_F. As shown in Fig. 4.15, whereas the mean value of the force always tends to zero with time, the behavior of the standard deviation is very different depending on δt and T: when $\delta t < 0.5T$ the force is well sampled, which is not the case when $\delta t > 0.5T$. This corresponds to the Nyquist-Shannon sampling theorem, and we thus always have to choose a time step for our simulations smaller than half the smallest timescale of the force perturbation. As the smallest time scale for the fiducial simulations is 0.075 Myr, we should a priori select a time step inferior to 0.03 Myr, for example 0.01 Myr.

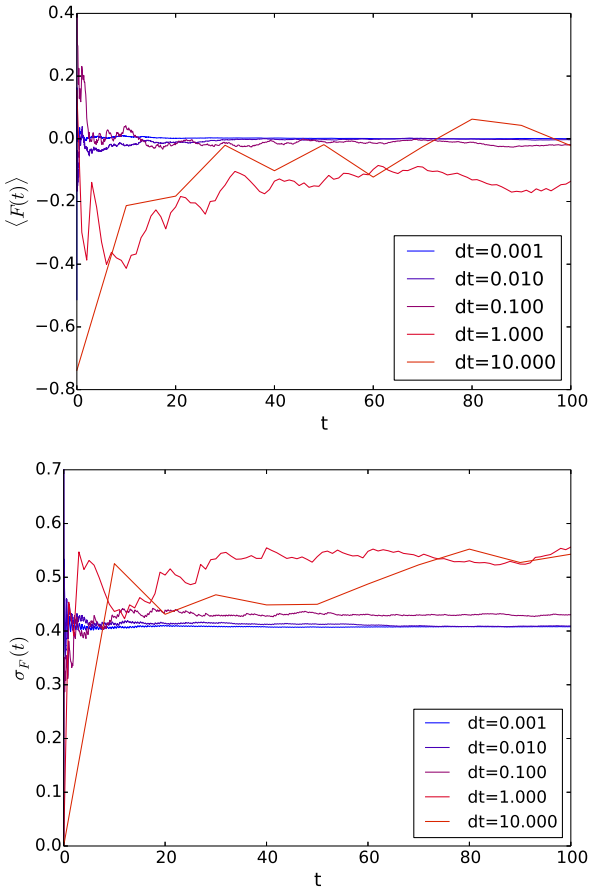

Figure 4.15 – *Evolution of the cumulative mean value of the force* $F = F_i \cos\left(2\pi \frac{t_i}{T}\right)$ *(upper panel) and of its standard deviation (lower panel) as a function of time, with* $T = 1$. *Whereas* $\sigma_F(t_f) \simeq 0.4$ *when* $\delta t < 0.5T$, $\sigma_F(t_f) > 0.5$ *when* $\delta t > 0.5T$. F_i *is a uniformly distributed random variable between* -1 *and* 1, *so the theoretical value of the standard deviation a time* $t \gg T$ *is* $\sigma_F = 0.5 <F_i^2> = 0.5\sqrt{2/3} \approx 0.41$.

Effect of the timescale on the simulations

However, the simulations converge for timesteps bigger than 0.01 Myr, so such a small timestep is not required. Fig. 4.16 shows the evolution of the final density profile after a 500 Myr evolution for different timesteps in the case of density fluctuations with constant propagations velocity $v_g = 134$ km.s^{-1} corresponding to the fiducial case described in Tables 4.1 and 4.2. The simulations already converges for time steps of about 1 Myr, i.e., for time steps which only resolve the highest perturbation scales: because the amplitude of the density power spectrum decreases from k_{min} to k_{max} and because the small scale perturbations are swept out by the larger ones, the fluctuations are dominated by those near k_{min}. The time scales associated to the largest fluctuation scales are indeed close to 10 Myr. As simulations with $\delta t = 0.01$ Myr and $\delta t = 0.1$ Myr yield similar results, we carry out most of our simulations with the less time-consuming timestep $\delta t = 0.1$ Myr. This timestep is a compromise between the necessity to sample properly the simulations and the fact that the smallest fluctuations are swept out by the largest ones.

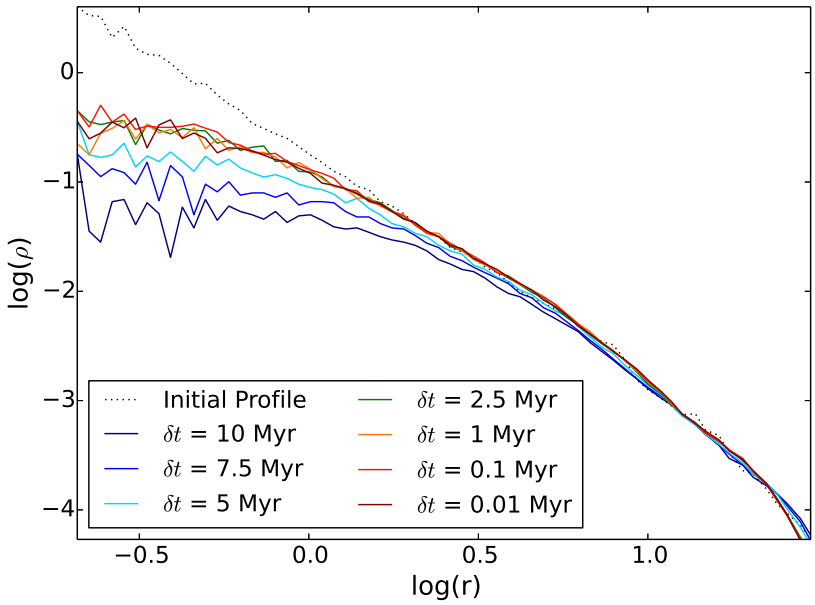

Figure 4.16 – *Evolution of the dark matter density profile after 500 Myr for different values of the time step dt, in the case of density fluctuations with constant propagations velocity* v_g.

4.5 Simulation results

4.5.1 Cusp flattening due to stochastic fluctuations

Our fiducial simulations start with an NFW halo as specified in section 4.4.2 and perturbations as indicated in Table 4.2. We use a timestep $\delta t = 0.1$ Myr and choose maximum SCF extension numbers $(n_{max},\ l_{max}) = (10,\ 4)$, as advocated by Vasiliev (2013) given the number of dark matter particles of the simulation. We compare the two different implementations of the pulsation frequency considered section 4.4.3, namely $\omega(k) = v_g k$ on one side and $\omega(k) = 2\sqrt{k}$ on the other. The constant propagation velocity is estimated from the dynamical time at radius $d = 5$ kpc, and equals $v_g = 134$ km.s^{-1}. We also carry a simulation with constant propagation velocity with a Kolmogorov power spectrum with exponent $n = 5/3$ instead of our fiducial $n = 2.4$. Fig. 4.17 shows the evolution of the density profile of a fiducial halo under the influence of a stochastic force born out of density fluctuations as described earlier, assuming a constant propagation velocity for the fluctuations. The total timescale of the simulation, 500 Myr, corresponds to about 70 dynamical times at $d = 5$ kpc, which is the timescale on which one would expect the imposed fluctuating force to have a significant effect on the trajectories of the dark matter particles, as discussed in section 4.3.3. The figure shows that the force does have an effect on such a timescale, which is to erase the central cusp and to transform it into a nearly constant density core. The flattening is progressive but converges after a few hundreds of Myr, and the shape of the density profile at larger radii remains largely unaltered. Fig.

4.18 compares the evolution of the density profile of the same initial halo for the different implementations of the pulsation frequency, i.e., either with a constant propagation velocity v_g or with $\omega = 2\sqrt{k}$ from Larson's relation, and for a Kolmogorov power-spectrum. In this figure, each curve corresponds to an average over ten realizations of the simulation in order to highlight the global trends and be less dependent on the fluctuations within each realization. Compared to the previous figure, this decreases the standard deviation associated to each curve by about a factor three. In all cases, the density perturbations are sufficient to flatten the density profile and to transform the cusp into a core. The two implementations of the pulsation frequency imply slightly different time scales for the fluctuations, but yield very similar results. A Kolmogorov power-spectrum for the density fluctuations leads to a slightly more enhanced flattening, which is quite understandable given that the Kolmogorov exponent yields a more gradual decrease of the amplitude of the perturbations after k_{min}. It is also coherent with the linear dependence of the relation time with the power-law exponent n, as expressed in Eq. 4.36.

As may be expected, the normalization of the imposed force plays an important role in the magnitude of the ensuing effect. This is illustrated in Fig. 4.19, where we show the effect of varying the values of $\delta_{k_{min}}$ and in which the curves are averaged over ten realizations for each value of the amplitude of the fluctuations at k_{min}. Larger levels of fluctuations logically lead to more flattening, but the stochasticity of the process yields more and more scatter with increasing $\delta_{k_{min}}$, as highlighted by the shaded areas on the figure.

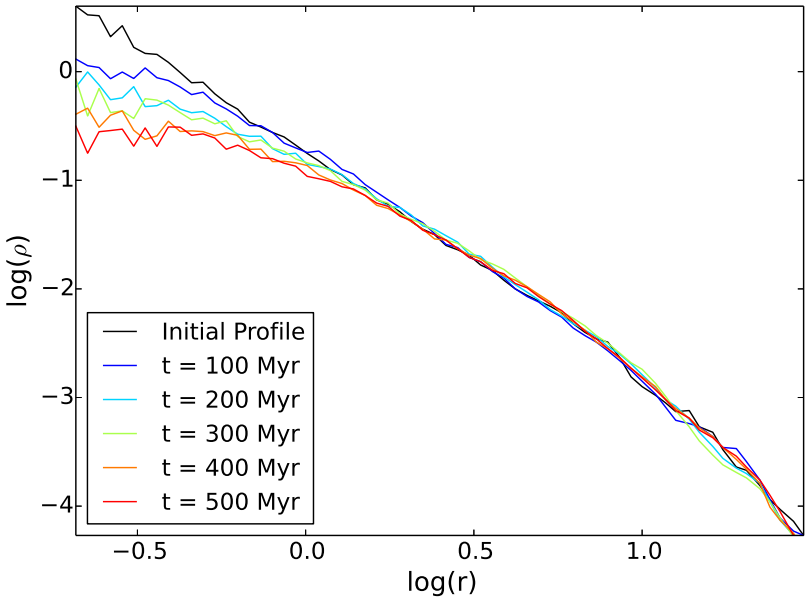

Figure 4.17 – *Fiducial evolution of the dark matter density profile for an NFW halo submitted to a fluctuating gravitational potential stemming from power-law density fluctuations. This simulation was carried out with a constant propagation velocity* $v_g = 134$ km.s^{-1}. *The radius is indicated in kpc while the density is in units of* 2.26 10^9 $M_\odot$/kpc^3.

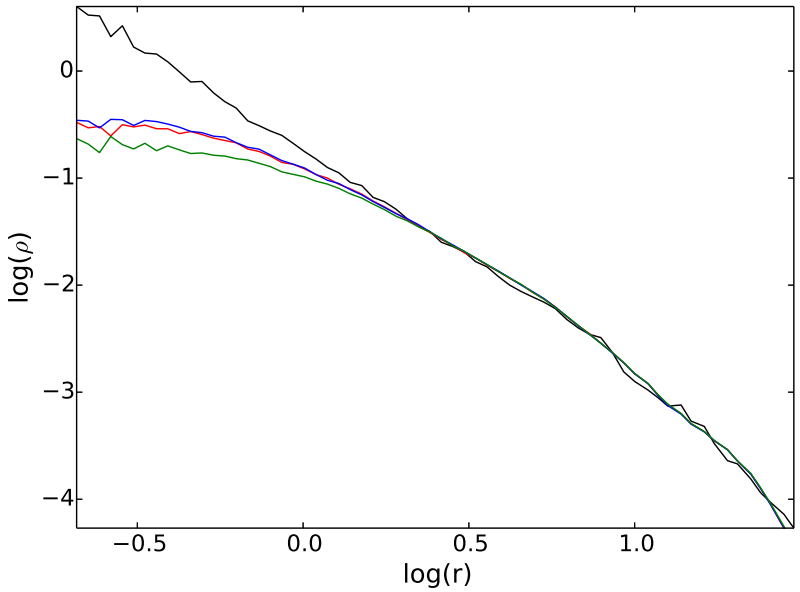

Figure 4.18 – *Comparison of the dark matter density profile after 500 Myr for different perturbations setups: (i) with a constant propagation velocity* $v_g = 134\ \mathrm{km.s^{-1}}$ *(in red), (ii) with* $\omega(k) = 2\sqrt{k}$ *from Larson's relation (in blue), and (iii) with a constant propagation velocity* v_g *but a Kolmogorov power-law exponent* $n = 5/3$ *(in green). The initial NFW density profile is shown as a solid black line, and each other profile corresponds to an average over ten realizations of the simulation. The units are as in Fig. 4.17.*

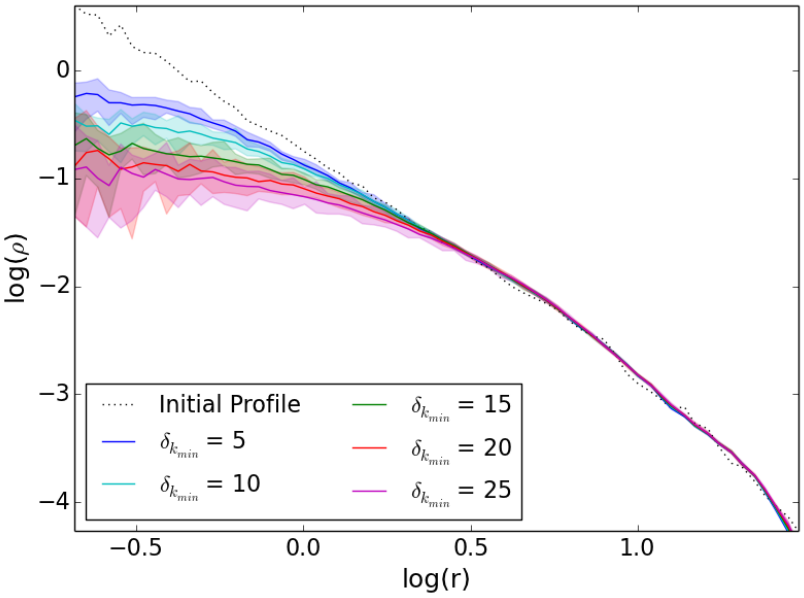

Figure 4.19 – *Evolution of the dark matter density profile after 500 Myr for different values of* $\delta_{k_{min}}$ *in the case of density fluctuations with constant propagation velocity. Each profile has been averaged over ten random realizations of the simulation; the shaded areas correspond to the span of these ten realizations. The units are as in the previous figures.*

4.5.2 Influence of the minimum and maximum fluctuation scales

The normalization of the fluctuating force by the analytical value of $\langle F(0)^2 \rangle$ (Eq. 4.49) only weakly depends on the minimum fluctuation scale $\lambda_{min} = 2\pi/k_{max}$ as $k_{min} \ll k_{max}$ but does depend on the maximum fluctuation scale determined by k_{min}. Nevertheless, the actual effect of the perturbations on the trajectories of the dark matter particles as determined by the velocity dispersion and the relaxation time is not expected to depend on k_{min} in the diffusion limit $k_{min}R \gg 1$. Indeed, Eqs. 4.33 and 4.35 do not depend on the minimum and maximum scales of the perturbations. Accordingly, Fig. 4.20 shows that the flattening of the dark matter density profile does not significantly depend on λ_{min} and λ_{max}. The scatter between the different curves indeed fall within the scatter expected from one simulation realization to another, as notably shown by the shaded areas of Fig. 4.19. Variations in the largest fluctuation scale however lead to slightly more scatter than fluctuations in λ_{min}, as the evolution of the dark matter density profile is mostly lead by the fluctuations at the largest scales.

The fact that the perturbations on the trajectories of the dark matter particles do not depend on the minimum and maximum scales of the density fluctuations can be explained using the following heuristic argument. In a diffusion process, particle trajectories are affected by small successive kicks, each of them being associated to a velocity change $\Delta v \sim F\Delta t$, where Δt is the characteristic duration of the kick. As we assume a pulsation frequency $\omega = v_g k$, Δt varies as $1/k$. After a given time interval in which a dark matter particle is subjected to N kicks, the resulting velocity variance is $\langle \Delta v^2 \rangle = N \Delta v^2$. However, since $\Delta t \propto 1/k$, the number of kicks during this time interval is proportional to k. Consequently,

$$\langle \Delta v^2 \rangle \propto N \; F^2 \; \Delta t^2 \propto F^2/k \tag{4.57}$$

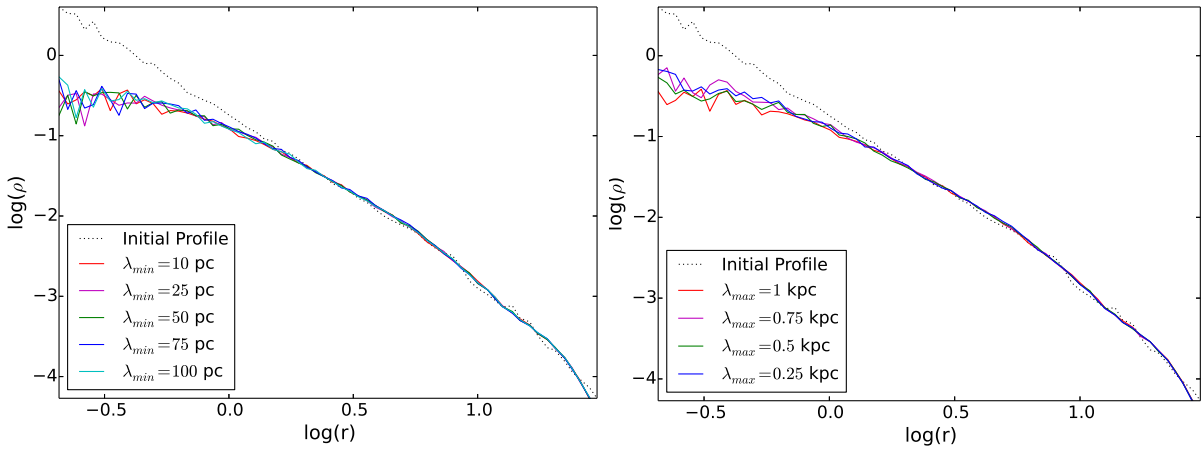

Figure 4.20 – *Dark matter density profiles after 500 Myr of perturbations for different values of the minimum (left) and maximum (right) scales of the perturbations. The simulations correspond to fiducial simulations with constant propagation velocity* v_g*. The maximum scale of perturbations is* $\lambda_{max} = 1$ kpc *when varying* λ_{min} *(left panel), and* $\lambda_{min} = 10$ pc *when varying* λ_{max} *(right panel).*

and as $\langle F(0)^2 \rangle \propto k_{min}$ (Eq. 4.27), the resulting velocity variance should be independent of $k_{min} = 2\pi/\lambda_{max}$ even though this wavenumber determines the dominant scale of the perturbations.

4.5.3 Importance of the harmonic decomposition

At each time step during the simulation, the density and the gravitational potential are approximated by a series of basis functions deriving from spherical harmonics as presented in section 4.4.1. This expansion separates the radial component $\rho_{nl}(r)$, depending on the "quantum" numbers n and l, and the angular component Y_{lm}, m being an integer between $-l$ and $+l$. The maximum value of the principal quantum number, n_{max}, thus characterizes the radial expansion of the fields, while l_{max} determines its angular extension. Indeed, $n_{max} = 0$ corresponds to fixed radial density and potential profiles,

$$\rho_{0l}(r) = \frac{1}{2\pi} \frac{(2l+1)(l+1)}{r} \frac{r^l}{(1+r)^{2l+3}} \tag{4.58}$$

$$\Phi_{0l}(r) = -\frac{r^l}{(1+r)^{2l+1}}, \tag{4.59}$$

while $l_{max} = 0$ yields spherically symmetric fields. The basis designed by Hernquist & Ostriker (1992) for the SCF code was indeed chosen so that the first term with $(n, l) = (0, 0)$ corresponds to an observationally motivated model describing spheroidal galaxies.

Radial decomposition.

The evolution of the dark matter density profile after 500 Myr with n_{max} at fixed $l_{max} = 4$ is shown in Fig. 4.21. While $n_{max} = 0$ freezes the density profile and stops its evolution from the beginning, increasing values of n_{max} converge rapidly after $n_{max} = 2$. However, Vasiliev (2013) indicates that $n_{max} = 10$ would be the optimal choice for a simulation with $N = 10^5$ particles, so we select this higher value of n_{max} for our simulations. This choice is also motivated by our focus on the radial profile of the dark matter halo, which we would not want to undersample.

Orbital decomposition.

The evolution of the dark matter density profile after 500 Myr with l_{max} for a given value $n_{max} = 10$ is shown in Fig. 4.22. When $l_{max} = 0$, the flattening of the dark matter density profile is almost imperceptible, but not non-existing. Running the simulation for a longer time indeed yields a significant flattening, as shown in the next subsection. For $l_{max} = 8$, the discreteness of the simulation is clearly visible, with a sharp drop near the center,

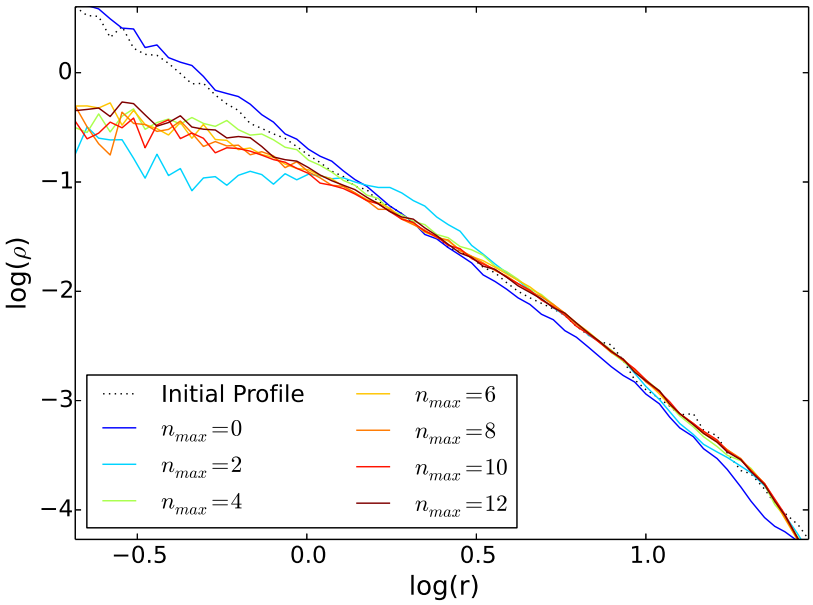

Figure 4.21 – *Evolution of the dark matter density profile after 500 Myr for different values of the maximum principal radial "quantum" number n_{max}. The simulation corresponds to a fiducial run with a constant propagation velocity v_g. The maximum orbital "quantum" number is $l_{max} = 4$.*

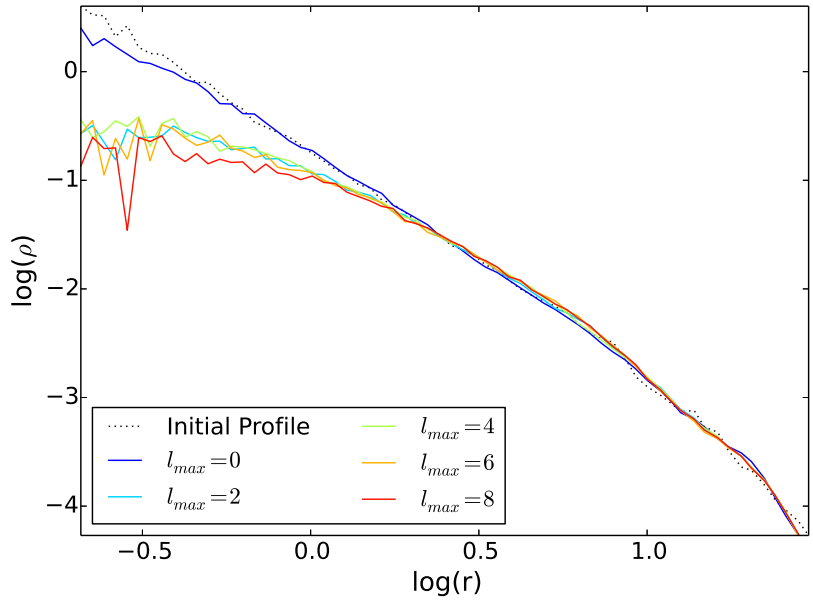

Figure 4.22 – *Evolution of the dark matter density profile after 500 Myr for different values of the maximum orbital "quantum" number l_{max}. The simulation corresponds to a fiducial run with a constant propagation velocity v_g. The maximum radial "quantum" number is $n_{max} = 10$.*

but the effect already exists for $l_{max} = 6$, with small oscillations towards the center. This effect is expected to become more and more prevalent with increasing l_{max}. Our choice of $l_{max} = 4$ for the fiducial simulations is motivated by a balance between sufficient angular resolution and avoiding the effects of the inherent discreetness of the simulation. This choice is also advocated through a more detailed study of the influence of the harmonic decomposition by Vasiliev (2013).

Long-term evolution with $l_{max} = 0$

When the simulation with $l_{max} = 0$ is allowed to run for more than 500 Myr, the flattening of the cusp becomes more significant. Indeed, as shown in Fig. 4.23, the dark matter density profile converges to that obtained in 500 Myr with $l_{max} = 4$. Imposing $l_{max} = 0$ yields a spherically-symmetric gravitational potential at each time step of the simulation, which smooths out the effects of the perturbations as they are averaged over the angular variables θ and ϕ. Although the norm of the force is assumed to be isotropic in the analytical calculations and in its implementation in the numerical code, its effect on the discrete dark matter particles may not be isotropic because of the individual orbits of the particles and because of the random directions of the force kicks. In this simulation with $l_{max} = 0$, each dark matter particle might be affected by the potential fluctuations over a relaxation time, but the averaging prevents the energy to be redistributed properly inside the whole system. Consequently, the collective response of the halo takes much more time.

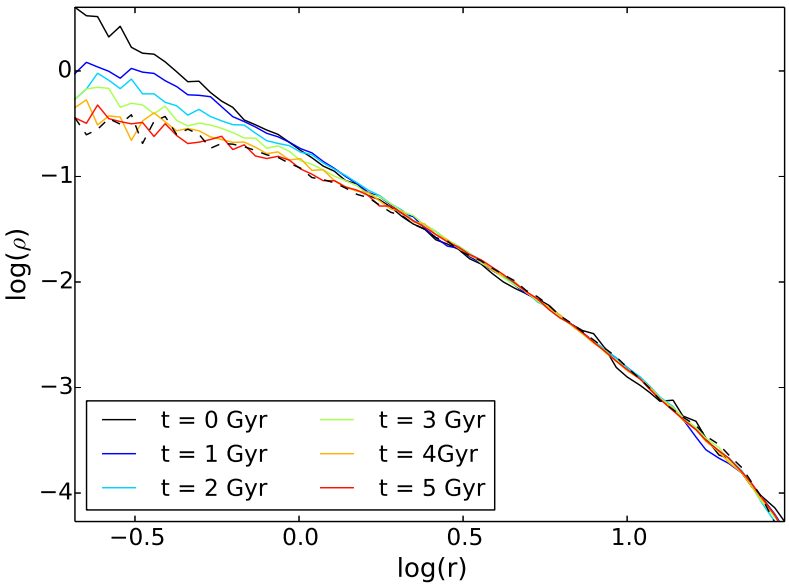

Figure 4.23 – *Evolution of the dark matter density profile with (n_{max}, l_{max}) = (10, 0) up to 5 Gyr. The profile converges with that obtained in 500 Myr with (n_{max}, l_{max}) = (10, 6), shown as a black dashed line.*

4.6 Conclusion and perspectives

4.6.1 Summary

In this study, we presented a theoretical model in which gravitational potential fluctuations leading to core formation in dark matter haloes arise from stochastic density variations in the gas distribution. Different stellar and AGN feedback mechanisms could account for these density variations. Our purpose was to understand the dynamics of core formation in terms of the statistical properties of the fluctuations in the gaseous density field.

Assuming stationarity, we derived analytically the velocity dispersion and the relaxation time characterizing the effects of the density variations on the trajectories of the dark matter particles. The calculations were made in the diffusion limit, where the particles undergo random walks initiated by the persistent density fluctuations. The situation is relatively analogous to a two-body relaxation, in which the random walks arise from a myriad of two-body encounters. We assumed a power-law power-spectrum of exponent n for the density fluctuations, as well as maximum and minimum cutoff scales. The relaxation time does not depend on these, and only weakly on the exponent n. For a given dark matter configuration, the important parameters determining the relaxation time are the gas mass fraction and the normalization of the power-spectrum.

The relaxation time gives us a timescale at which the density variations are expected to affect the trajectories of the dark matter particles, but does not specify the global response of the system. We thus carried out numerical simulations with the SCF code (Hernquist & Ostriker, 1992) for a small fiducial galaxy halo submitted to random density fluctuations as in the analytical calculations. The simulations showed that the stochastic processes we assumed could indeed lead to the formation of a core in an initially cuspy configuration within a timescale comparable to the relaxation time derived from the theoretical calculations. We assumed a gas-rich galaxy with a baryonic gas fraction $\mathrm{f_{gas}} = 50\%$, as can be observed at high redshift, and relatively large density fluctuations. The relative density contrast at the largest fluctuation scale was indeed assumed to have a standard deviation $\delta_{k_{min}} = 10$. The numerical setup included the self-gravity of the dark matter halo and any potential non-linear coupling between the unperturbed dark matter particle trajectories and the imposed force. It did not assume the diffusion limit a priori, but confirmed the independence of the flattening of the dark matter density profile on the maximum and minimum fluctuation scales, as well as its weak dependence on the exponent n.

Our results thus suggest that the fluctuations leading to core formation in dark matter haloes may be modeled as stochastic processes determined by a power-law power-spectrum and their dynamical effects as a diffusion process. If the pure power-law approximation is indeed valid, the whole process should depend mainly on the normalization of the power-spectrum and could hence be parametrized from hydrodynamical simulations.

4.6.2 On the normalization of the power-spectrum

In our analytical calculations and in the numerical simulations, we parametrized the density fluctuations through their standard deviation at the largest fluctuation scale, $\delta_{k_{min}} = \sqrt{\langle|\delta_{k_{min}}|^2\rangle}$. However, this parametrization does not depend on the volume within which the perturbations occur, or on their maximum radius d, although these quantities are crucial to describe the perturbations. Instead, it could be possible to normalize the power-spectrum $\mathcal{P}(k) = V\langle|\delta_{\vec{k}}|^2\rangle$ through its dimensionless counterpart

$$\Delta^2(k) = \frac{k^3}{2\pi^2}\mathcal{P}(k), \tag{4.60}$$

which expresses its contribution to the variance in density contrast per unit $\ln(k)$. Indeed, the variance at scale R associated to a smoothed density distribution with a window function as in section 4.3.1 is

$$s^2(R) = \int \Delta^2(k)\widetilde{W}^2(kR)d\ln k \tag{4.61}$$

where $\widetilde{W}(kR)$ is the Fourier transform of the window function. The variance s^2 can be inferred from hydrodynamical simulations such at that of a dwarf galaxy by Teyssier et al. (2013). This simulation corresponds to an isolated dwarf galaxy of virial mass $M_{tot} = 1.4\ 10^{10}\ M_\odot$, virial radius $R_{vir} = 50$ kpc and baryonic gas fraction $f_{gas} = 75\%$ (or alternatively, gas fraction over the total baryonic and dark matter mass $f = 15\%$). It uses the RAMSES simulation code (Teyssier, 2002), and includes a strong supernova feedback model. Consistently with Pontzen & Governato (2012), it yields a flattening of the dark matter density profile to form a core of radius 800 pc. The time evolution of the gas mass within spheres of different radii as in the left panel of Fig. 4.10 is computed, which would give access to the mass variance s^2, and hence to the parameters of the power-spectrum associated to the density fluctuations. More generally, simulations including different types of feedback could be used to infer the normalization of the power-spectrum and its exponent n. These quantities probably depend on which feedback mechanisms are simulated and on their numerical implementation. Such inputs could further validate our model, and also give a means to compare the different feedback processes in terms of their effects on the dark matter distribution and of their associated relaxation time.

4.6.3 Miscellaneous

We tested our numerical setup with a power-law exponent $n = 2.4$ and with a Kolmogorov exponent $n = 5/3$. If inputs from hydrodynamical simulations with different forms of feedback would be the ideal way to further test and quantify our model, we could also more simply test different values of n. As already mentioned, we expect a weak dependence of the behavior of the system with n, as it appears linearly in the expression of the relaxation time.

In section 4.5.3, we considered the evolution of the dark matter halo with $l_{max} = 0$, i.e., with spherically-symmetric density and potential fields. In this case, although each dark matter particle is probably affected by the density fluctuations within a relaxation time, the global response of the halo is delayed. This is related to the processes through which the local energy stemming from the fluctuations is redistributed within the halo, and these processes are consequently largely non-isotropic. They could notably involve collective modes enabled by self-gravity. The observed behavior of the halo when $l_{max} = 0$ is comparable to that obtained by Pontzen et al. (2015), whose triaxial halo submitted to time-dependent potential fluctuations flattens into a core within 1 Gyr while a similar spherical halo remains cuspy on such a timescale. Asphericity seems to be necessary for an efficient cusp-core transition, and a more detailed study of the redistribution of energy within the halo could be interesting.

Our study also suggests that numerical simulations should properly resolve the timescale of the feedback processes so as not to overestimate the flattening of the dark matter halo and core formation. Fig. 4.16 indeed shows that when the timestep is not sufficient, the flattening is enhanced. In this case, the fluctuations are sampled randomly as white noise and the dark matter particles feel a flat power-spectrum instead of the proper one arising from the actual physical processes which are modeled. This leads to a significant enhancement of core formation, which could be misleading and should be avoided in numerical simulations.

Conclusion

CHAPTER 5

Conclusion and perspectives

This work addresses the issue of star formation in the Universe from three different perspectives and hence approaches various aspects of galaxy formation and evolution, through different techniques. In the first part, we try to characterize star formation and its efficiency at scales close to the size of the star-forming regions in distant, high redshift galaxies. We develop a method to beat the resolution limit and obtain a Kennicutt-Schmidt relation at sub-galactic scales by taking advantage of the rotating disk kinematics. Observations may generally hint towards an increased star formation efficiency earlier in the history of the Universe, but a more meaningful sample of galaxies at high redshift would be necessary to confirm the trend. In the second part, we try to better understand the first stages of core and star formation in the interstellar medium through analytical calculations. We derive a dispersion relation describing the growth of gravitational instabilities within interstellar filaments, first assuming local perturbations, and then considering fluctuations of arbitrary size but within static filaments. The first dispersion relation indeed reduces to the standard spherical case when there is no rotation, as the local assumption prevents the system feeling the larger-scale cylindrical geometry. Without this assumption, the dispersion relation retains its complex terms and all modes are thus potentially unstable. Prolate condensations seem to be favored, but a numerical approach seems necessary to complement our analytical calculations. In the third part, we focus on the effects of the feedback mechanisms stemming from star formation and active galactic nuclei on the dark matter distribution itself. Indeed, if structure formation in the standard ΛCDM cosmological model is primarily driven by dark matter dynamics, baryons can in turn affect the dark matter distribution at galactic scales. We assume that feedback processes result in stochastic fluctuations in the density field, with a power-law power-spectrum, and show through analytical calculations and numerical simulations that such a model is able to reproduce cored dark matter density profiles as inferred from observations.

In the first part, we obtain a Kennicutt-Schmidt relation for ensembles of clumps in a sample of four galaxies observed as part of the IRAM PHIBSS program. This pilot study should be complemented by more observations at high redshift, and notably within the IRAM PHIBSS2 legacy program, which will more than triple the number of molecular gas observations available at $z = 0.5 - 2.5$. The PHIBSS2 program will enable us to better

characterize the star formation efficiency averaged at galactic scales, but also to apply our kinematic method to a wider subsample of galaxies and thus to obtain a more precise resolved Kennicutt-Schmidt relation at high redshift. Motivated by the same desire to understand star formation at sub-galactic scales, we also proposed an ALMA cycle 3 program aiming at obtaining high-resolution molecular gas images of six galaxies after the peak epoch of star formation. In addition to obtaining resolved Kennicutt-Schmidt relations, this program would allow us to better understand the fate of the clumpy star-forming regions, the quenching of star formation, and the formation of bulges. We are notably planning to try to detect outflows from the star-forming clumps by stacking different measurements. This study could be further complemented with hydrodynamical simulations of gas-rich galaxies at high redshift, which would provide a comparison in which the physical processes are unambiguously constrained.

The second part could be enriched by further analytical developments regarding gravitational instabilities in interstellar filaments, such as taking into account more complex velocity distributions, magnetic fields, or non-axisymmetric perturbations. More complex velocity distributions could notably arise from turbulence or velocity gradients and torques due to the environment. But we should also better understand the correspondence between observations and the global dispersion relation we finally obtained. Numerical simulations such as those we have started could help, notably as they provide an idealized setup in which all parameters are controlled. A description in terms of small linear perturbations is also necessarily incomplete, as it only describes the first linear stage of the perturbations' growth. Numerical simulations would hence enable to bridge the gap between the initial linear growth and observed pre-stellar cores.

Finally, the third part would notably benefit from inputs from hydrodynamical simulations of galaxies in order to test our assumption of a stochastic process with power-law power-spectrum, and to implement more 'realistic' statistical properties for the density fluctuations resulting from the different feedback processes. This would allow us to have more quantitative results, and to compare different feedback mechanisms and their implementation in numerical simulations directly through their effects on the dark matter distribution.

Appendices

APPENDIX A

Journal articles

A&A 553, A130 (2013)
DOI: 10.1051/0004-6361/201220981

Astronomy & Astrophysics

Towards a resolved Kennicutt-Schmidt law at high redshift

J. Freundlich[1], F. Combes[1], L. J. Tacconi[2], M. C. Cooper[3], R. Genzel[2,4,5], R. Neri[6], A. Bolatto[7], F. Bournaud[8], A. Burkert[9,⋆], P. Cox[6], M. Davis[5], N. M. Förster Schreiber[2], S. Garcia-Burillo[10], J. Gracia-Carpio[2], D. Lutz[2], T. Naab[11], S. Newman[5], A. Sternberg[12], and B. Weiner[13]

[1] LERMA, Observatoire de Paris, CNRS, 61 Av. de l'Observatoire, 75014 Paris, France
e-mail: jonathan.freundlich@obspm.fr
[2] Max–Planck–Institute für extraterrestrische Physik (MPE), Giessenbachstrasse 1, 85748 Garching, Germany
[3] Dept. of Physics & Astronomy, Frederick Reines Hall, University of California, Irvine, CA 92697, USA
[4] Dept. of Physics, Le Conte Hall, University of California, CA 94720 Berkeley, USA
[5] Dept. of Astronomy, Campbell Hall, University of California, CA 94720 Berkeley, USA
[6] IRAM, 300 rue de la Piscine, 38406 St. Martin d'Hères, Grenoble, France
[7] Dept. of Astronomy, University of Maryland, College Park, MD 20742-2421, USA
[8] CEA, IRFU, SAp, 91191 Gif-sur-Yvette, France
[9] Universitätsternwarte der Ludwig–Maximiliansuniversität, Scheinerstrasse 1, 81679 München, Germany
[10] Observatorio Astronómico Nacional – OAN, Apartado 1143, 28800 Alcalá de Henares, Madrid, Spain
[11] Max Planck Institut für Astrophysik, Karl Schwarzshildstrasse 1, 85748 Garching, Germany
[12] School of Physics and Astronomy, Tel Aviv University, 69978 Tel Aviv, Israel
[13] Steward Observatory, 933 N. Cherry Ave., University of Arizona, Tucson, AZ 85721-0065, USA

Received 21 December 2012 / Accepted 24 March 2013

ABSTRACT

Massive galaxies in the distant Universe form stars at much higher rates than today. Although direct resolution of the star forming regions of these galaxies is still a challenge, recent molecular gas observations at the IRAM Plateau de Bure interferometer enable us to study the star formation efficiency on subgalactic scales around redshift $z = 1.2$. We present a method for obtaining the gas and star formation rate (SFR) surface densities of ensembles of clumps composing galaxies at this redshift, even though the corresponding scales are not resolved. This method is based on identifying these structures in position-velocity diagrams corresponding to slices within the galaxies. We use unique IRAM observations of the CO(3–2) rotational line and DEEP2 spectra of four massive star forming distant galaxies – EGS13003805, EGS13004291, EGS12007881, and EGS13019128 in the AEGIS terminology – to determine the gas and SFR surface densities of the identifiable ensembles of clumps that constitute them. The integrated CO line luminosity is assumed to be directly proportional to the total gas mass, and the SFR is deduced from the [OII] line. We identify the ensembles of clumps with the angular resolution available in both CO and [OII] spectroscopy; i.e., 1–1.5″. SFR and gas surface densities are averaged in areas of this size, which is also the thickness of the DEEP2 slits and of the extracted IRAM slices, and we derive a spatially resolved Kennicutt-Schmidt (KS) relation on a scale of ∼8 kpc. The data generally indicates an average depletion time of 1.9 Gyr, but with significant variations from point to point within the galaxies.

Key words. galaxies: evolution – galaxies: high-redshift – galaxies: structure – stars: formation – galaxies: ISM – galaxies: starburst

The Astrophysical Journal, 773:68 (12pp), 2013 August 10 doi:10.1088/0004-637X/773/1/68

PHIBSS: MOLECULAR GAS, EXTINCTION, STAR FORMATION, AND KINEMATICS IN THE $z = 1.5$ STAR-FORMING GALAXY EGS13011166*

R. Genzel[1,2,3], L. J. Tacconi[1], J. Kurk[1], S. Wuyts[1], F. Combes[4], J. Freundlich[4], A. Bolatto[5], M. C. Cooper[6], R. Neri[7], R. Nordon[8], F. Bournaud[9], A. Burkert[10,17], J. Comerford[11], P. Cox[2], M. Davis[3], N. M. Förster Schreiber[1], S. García-Burillo[12], J. Gracia-Carpio[1], D. Lutz, T. Naab[13], S. Newman[3], A. Saintonge, K. Shapiro Griffin[14], A. Shapley[15], A. Sternberg[8], and B. Weiner[16]

[1] Max-Planck-Institut für extraterrestrische Physik (MPE), Giessenbachstr., D-85748 Garching, Germany; genzel@mpe.mpg.de, linda@mpe.mpg.de
[2] Department of Physics, Le Conte Hall, University of California, 94720 Berkeley, CA, USA
[3] Department of Astronomy, Campbell Hall, University of California, Berkeley, CA 94720, USA
[4] Observatoire de Paris, LERMA, CNRS, 61 Av. de l'Observatoire, F-75014 Paris, France
[5] Department of Astronomy, University of Maryland, College Park, MD 20742-2421, USA
[6] Department of Physics & Astronomy, Frederick Reines Hall, University of California, Irvine, CA 92697, USA
[7] IRAM, 300 Rue de la Piscine, F-38406 St. Martin d'Heres, Grenoble, France
[8] Sackler School of Physics and Astronomy, Tel Aviv University, Tel Aviv 69978, Israel
[9] Service d'Astrophysique, DAPNIA, CEA/Saclay, F-91191 Gif-sur-Yvette Cedex, France
[10] Universitätssternwarte der Ludwig-Maximiliansuniversität, Scheinerstr. 1, D-81679 München, Germany
[11] Department of Astronomy & McDonald Observatory, 1 University Station, C1402 Austin, TX 78712-0259, USA
[12] Observatorio Astronómico Nacional-OAN, Observatorio de Madrid, Alfonso XII, 3, E-28014 Madrid, Spain
[13] Max-Planck Institut für Astrophysik, Karl Schwarzschildstrasse 1, D-85748 Garching, Germany
[14] Space Sciences Research Group, Northrop Grumman Aerospace Systems, Redondo Beach, CA 90278, USA
[15] Department of Physics & Astronomy, University of California, Los Angeles, CA 90095-1547, USA
[16] Steward Observatory, 933 North Cherry Avenue, University of Arizona, Tucson, AZ 85721-0065, USA
Received 2013 March 27; accepted 2013 May 30; published 2013 July 26

ABSTRACT

We report matched resolution imaging spectroscopy of the CO 3–2 line (with the IRAM Plateau de Bure millimeter interferometer) and of the Hα line (with LUCI at the Large Binocular Telescope) in the massive $z = 1.53$ main-sequence galaxy EGS 13011166, as part of the "Plateau de Bure high-z, blue-sequence survey" (PHIBSS: Tacconi et al.). We combine these data with *Hubble Space Telescope V–I–J–H*-band maps to derive spatially resolved distributions of stellar surface density, star formation rate, molecular gas surface density, optical extinction, and gas kinematics. The spatial distribution and kinematics of the ionized and molecular gas are remarkably similar and are well modeled by a turbulent, globally Toomre unstable, rotating disk. The stellar surface density distribution is smoother than the clumpy rest-frame UV/optical light distribution and peaks in an obscured, star-forming massive bulge near the dynamical center. The molecular gas surface density and the effective optical screen extinction track each other and are well modeled by a "mixed" extinction model. The inferred slope of the spatially resolved molecular gas to star formation rate relation, $N = d\log\Sigma_{\rm star\,form}/d\log\Sigma_{\rm mol\,gas}$, depends strongly on the adopted extinction model, and can vary from 0.8 to 1.7. For the preferred mixed dust–gas model, we find $N = 1.14 \pm 0.1$.

Key words: galaxies: evolution – galaxies: high-redshift – galaxies: ISM – ISM: molecules – stars: formation

Online-only material: color figure

A&A 564, A7 (2014)
DOI: 10.1051/0004-6361/201323325

Astronomy & Astrophysics

Local stability of a gravitating filament: a dispersion relation⋆

J. Freundlich[1], C. J. Jog[2], and F. Combes[1]

[1] LERMA, Observatoire de Paris, CNRS, 61 av. de l'Observatoire, 75014 Paris, France
e-mail: jonathan.freundlich@obspm.fr
[2] Department of Physics, Indian Institute of Science, Bangalore 560012, India

Received 23 December 2013 / Accepted 4 February 2014

ABSTRACT

Filamentary structures are ubiquitous in astrophysics and are observed at various scales. On a cosmological scale, matter is usually distributed along filaments, and filaments are also typical features of the interstellar medium. Within a cosmic filament, matter can contract and form galaxies, whereas an interstellar gas filament can clump into a series of bead-like structures that can then turn into stars. To investigate the growth of such instabilities, we derive a local dispersion relation for an idealized self-gravitating filament and study some of its properties. Our idealized picture consists of an infinite self-gravitating and rotating cylinder with pressure and density related by a polytropic equation of state. We assume no specific density distribution, treat matter as a fluid, and use hydrodynamics to derive the linearized equations that govern the local perturbations. We obtain a dispersion relation for axisymmetric perturbations and study its properties in the (k_R, k_z) phase space, where k_R and k_z are the radial and longitudinal wavenumbers, respectively. While the boundary between the stable and unstable regimes is symmetrical in k_R and k_z and analogous to the Jeans criterion, the most unstable mode displays an asymmetry that could constrain the shape of the structures that form within the filament. Here the results are applied to a fiducial interstellar filament, but could be extended for other astrophysical systems, such as cosmological filaments and tidal tails.

Key words. gravitation – hydrodynamics – instabilities – large-scale structure of Universe – ISM: structure

The Astrophysical Journal, 800:20 (25pp), 2015 February 10 doi:10.1088/0004-637X/800/1/20

COMBINED CO AND DUST SCALING RELATIONS OF DEPLETION TIME AND MOLECULAR GAS FRACTIONS WITH COSMIC TIME, SPECIFIC STAR-FORMATION RATE, AND STELLAR MASS*

R. Genzel[1,2,3], L. J. Tacconi[1], D. Lutz[1], A. Saintonge[4], S. Berta[1], B. Magnelli[5], F. Combes[6], S. García-Burillo[7], R. Neri[8], A. Bolatto[9], T. Contini[10], S. Lilly[11], J. Boissier[8], F. Boone[10], N. Bouché[10], F. Bournaud[12], A. Burkert[1,13], M. Carollo[11], L. Colina[14], M. C. Cooper[15], P. Cox[16], C. Feruglio[8], N. M. Förster Schreiber[1], J. Freundlich[6], J. Gracia-Carpio[1], S. Juneau[12], K. Kovac[11], M. Lippa[1], T. Naab[17], P. Salome[6], A. Renzini[18], A. Sternberg[19], F. Walter[20], B. Weiner[21], A. Weiss[22], and S. Wuyts[1]

[1] Max-Planck-Institut für Extraterrestrische Physik (MPE), Giessenbachstr., D-85748 Garching, Germany; linda@mpe.mpg.de, genzel@mpe.mpg.de
[2] Department of Physics, Le Conte Hall, University of California, Berkeley, CA 94720, USA
[3] Department of Astronomy, Campbell Hall, University of California, Berkeley, CA 94720, USA
[4] Department of Physics and Astronomy, University College London, Gower Place, London WC1E 6BT, UK
[5] Argelander-Institut für Astronomie, Universität Bonn, Auf dem Hügel 71, D-53121 Bonn, Germany
[6] Observatoire de Paris, LERMA, CNRS, 61 Av. de l'Observatoire, F-75014 Paris, France
[7] Observatorio Astronómico Nacional-OAN, Observatorio de Madrid, Alfonso XII, 3, 28014 Madrid, Spain
[8] IRAM, 300 Rue de la Piscine, F-38406 St. Martin d'Heres, Grenoble, France
[9] Department of Astronomy, University of Maryland, College Park, MD 20742-2421, USA
[10] Institut d'Astrophysique et de Planétologie, Universite de Toulouse, 9 Avenue du Colonel Roche BP 44346, F-31028 Toulouse Cedex 4, France
[11] Institute of Astronomy, Department of Physics, Eidgenössische Technische Hochschule, CH-8093 ETH Zürich, Switzerland
[12] Service d'Astrophysique, DAPNIA, CEA/Saclay, F-91191 Gif-sur-Yvette Cedex, France
[13] Universitätssternwarte der Ludwig-Maximiliansuniversität, Scheinerstr. 1, D-81679 München, Germany
[14] CSIC Instituto Estructura Materia, C/Serrano 121, E-28006 Madrid, Spain
[15] Department of Physics and Astronomy, Frederick Reines Hall, University of California, Irvine, CA 92697, USA
[16] ALMA Santiago Central Office, Alonso de Córdova 3107, Vitacura, Santiago, Chile
[17] Max-Planck Institut für Astrophysik, Karl Schwarzschildstrasse 1, D-85748 Garching, Germany
[18] Osservatorio Astronomico di Padova, Vicolo dell'Osservatorio 5, I-35122, Padova, Italy
[19] School of Physics and Astronomy, Tel Aviv University, Tel Aviv 69978, Israel
[20] Max Planck Institut für Astronomie (MPIA), Königstuhl 17, D-69117 Heidelberg, Germany
[21] Steward Observatory, 933 North Cherry Avenue, University of Arizona, Tucson, AZ 85721-0065, USA
[22] Max Planck Institut für Radioastronomie (MPIfR), Auf dem Hügel 69, D-53121 Bonn, Germany
Received 2014 September 2; accepted 2014 December 4; published 2015 February 5

ABSTRACT

We combine molecular gas masses inferred from CO emission in 500 star-forming galaxies (SFGs) between $z = 0$ and 3, from the IRAM-COLDGASS, PHIBSS1/2, and other surveys, with gas masses derived from *Herschel* far-IR dust measurements in 512 galaxy stacks over the same stellar mass/redshift range. We constrain the scaling relations of molecular gas depletion timescale ($t_{\rm depl}$) and gas to stellar mass ratio ($M_{\rm mol\ gas}/M_*$) of SFGs near the star formation "main-sequence" with redshift, specific star-formation rate (sSFR), and stellar mass (M_*). The CO- and dust-based scaling relations agree remarkably well. This suggests that the CO $\rightarrow$ H_2 mass conversion factor varies little within ± 0.6 dex of the main sequence (sSFR(ms, z, M_*)), and less than 0.3 dex throughout this redshift range. This study builds on and strengthens the results of earlier work. We find that $t_{\rm depl}$ scales as $(1+z)^{-0.3} \times ({\rm sSFR/sSFR(ms}, z, M_*))^{-0.5}$, with little dependence on M_*. The resulting steep redshift dependence of $M_{\rm mol\ gas}/M_* \approx (1+z)^3$ mirrors that of the sSFR and probably reflects the gas supply rate. The decreasing gas fractions at high M_* are driven by the flattening of the SFR–M_* relation. Throughout the probed redshift range a combination of an increasing gas fraction and a decreasing depletion timescale causes a larger sSFR at constant M_*. As a result, galaxy integrated samples of the $M_{\rm mol\ gas}$–SFR rate relation exhibit a super-linear slope, which increases with the range of sSFR. With these new relations it is now possible to determine $M_{\rm mol\ gas}$ with an accuracy of ± 0.1 dex in relative terms, and ± 0.2 dex including systematic uncertainties.

Key words: galaxies: evolution – galaxies: high-redshift – galaxies: kinematics and dynamics – infrared: galaxies

APPENDIX B

Conference proceedings

SF2A 2013
L. Cambrésy, F. Martins, E. Nuss and A. Palacios (eds)

STAR FORMATION EFFICIENCY AT HIGH Z AND SUBGALACTIC SCALES

J. Freundlich[1], F. Combes[1], L. J. Tacconi[2], M. C. Cooper[3], R. Genzel[2,4,5], R. Neri[6] and the PHIBSS consortium

Abstract. Massive galaxies in the distant Universe form stars at much higher rates than their local counterparts. Although direct resolution of the star forming regions of these galaxies is still a challenge, recent molecular gas observations at the IRAM Plateau de Bure interferometer enable us to study the star formation efficiency at sub-galactic scales around z = 1.2. We present a method to obtain the gas and star formation rate (SFR) surface densities of ensembles of clumps within galaxies at this redshift, and derive a spatially resolved Kennicutt-Schmidt (KS) relation at a scale of about 8.5 kpc. This method is based on the identification of these structures in position-velocity diagrams corresponding to slices within the galaxies, even though the corresponding scales are not resolved. The data globally indicates an average depletion time of 1.9 Gyr, but with significant variations from point to point within the galaxies.

Keywords: galaxies: evolution, galaxies: high redshift, galaxies: ISM, galaxies: starburst

SF2A 2014
J. Ballet, F. Bournaud, F. Martins, R. Monier and C. Reylé (eds)

ON THE STABILITY OF SELF-GRAVITATING FILAMENTS

J. Freundlich[1], C. J. Jog[2], F. Combes[1] and S. Anathpindika[2]

Abstract. Filamentary structures are very common in astrophysical environments and are observed at various scales. On a cosmological scale, matter is usually distributed along filaments, and filaments are also typical features of the interstellar medium. Within a cosmic filament, matter can possibly contract and form galaxies, whereas an interstellar gas filament can clump into a series of bead-like structures which can then turn into stars. To investigate the growth of such instabilities and the properties of the resulting substructures, we consider idealized self-gravitating filaments and derive the dispersion relation for perturbations within them. We assume no specific density distribution, treat matter as a fluid, and use hydrodynamics to derive the linearized equations that govern the growth of perturbations. Assuming small local perturbations leads to a dispersion relation analogous to the spherical Jeans case: perturbations of size higher than the Jeans length collapse and asymmetries regarding their growth rates arise only because of rotation. For perturbations of arbitrary size, the dispersion relation retains its complex terms: all modes are potentially unstable, but elongated perturbations near the axis of the cylinder grow faster. Prolate substructures and global collapse are favored, which is corroborated by most observations of interstellar filaments.

Keywords: gravitation, hydrodynamics, instabilities, large-scale structure of the Universe, ISM: structure

SF2A 2014
J. Ballet, F. Bournaud, F. Martins, R. Monier and C. Reylé (eds)

HIGH-REDSHIFT STAR FORMATION EFFICIENCY AS UNCOVERED BY THE IRAM PHIBSS PROGRAMS

J. Freundlich[1], P. Salomé[1], F. Combes[1], L. Tacconi[2], R. Neri[3], S. Garcia-Burillo[4], R. Genzel[2,5,6], T. Contini[7,8], S. Lilly[9] and the PHIBSS Consortium

Abstract. The evolution of the cosmic star formation rate (SFR) is characterized by a peak around redshift z=2-3 and a subsequent drop by an order of magnitude. High levels of star formation are sustained by a continuous supply of fresh gas and high molecular gas fractions. But once galaxies exceed a certain mass or enter a harsh environment, star formation is quenched, and different phenomena could explain the resulting evolution of the cosmic SFR. Is it mostly driven by the available molecular gas, or because star formation processes are more efficient at high redshift? Here we present the results and the perspectives of the PHIBSS programs, which aim at understanding early galaxy evolution and the winding-down of star formation from the perspective of the galaxies' molecular gas reservoirs. These programs use statistically meaningful samples of galaxies belonging to the massive end of the star formation main-sequence at different redshifts. The previous IRAM PHIBSS program has already uncovered large molecular gas reservoirs at redshifts z∼1-2, with gas fractions 4 to 10 times higher than in the local Universe, and the ongoing IRAM and ALMA programs extend the sample to a wider range of redshifts and to a more complete sampling of the stellar mass-SFR plane. The IRAM PHIBSS2 legacy program is designed to make full use of the upcoming NOEMA capabilities.

Keywords: galaxies: evolution, galaxies: high-redshift, galaxies: structure, stars: formation, galaxies: ISM

Title of your IAU Symposium
Proceedings IAU Symposium No. xxx, 2015
A.C. Editor, B.D. Editor & C.E. Editor, eds.

DOI: 00.0000/X000000000000000X

Perturbation growth within self-gravitating interstellar filaments

Jonathan Freundlich[1,2], Chanda J. Jog[3], and Françoise Combes[1,4]

[1]LERMA, Observatoire de Paris, PSL Research University, CNRS, Sorbonne Universités, UPMC Univ. Paris 06, F-75014, Paris, France; [2]IFCPAR/CEFIPRA Raman-Charpak fellow; [3]Indian Institute of Science, Bangalore, India; [4]Collège de France, PSL Research University, F-75005, Paris, France

Abstract. Observations show that the interstellar medium hosts complex networks of filamentary structures. The formation of turbulence-driven filaments and their subsequent gravitational fragmentation could represent an important step towards core and star formation. Gravitational instabilities could indeed lead these filaments to clump into a series of bead-like structures which would then turn into stars. To investigate the growth of such instabilities and the properties of the resulting substructures, we consider idealized self-gravitating filaments and derive the dispersion relation for perturbations within them. We assume no specific density distribution and use hydrodynamics to derive the linearized equations that govern the perturbations' growth. Assuming local perturbations leads to a dispersion relation analogous to the spherical Jeans case, but all modes are potentially unstable for perturbations of arbitrary size. Elongated perturbations near the axis of the filament should grow faster so prolate substructures and global collapse are favored, which is corroborated by most observations.

Keywords. gravitation, hydrodynamics, instabilities, large-scale structure of the Universe, ISM: structure

Title of your IAU Symposium
Proceedings IAU Symposium No. xxx, 2015
A.C. Editor, B.D. Editor & C.E. Editor, eds.

DOI: 00.0000/X000000000000000X

Resolved star formation relations at high redshift from the IRAM PHIBSS program

Jonathan Freundlich[1], Françoise Combes[1,2], Linda Tacconi[3], Michael Cooper[4], Reinhard Genzel[3,5], Roberto Neri[6] and the PHIBSS consortium

[1]LERMA, Observatoire de Paris, PSL Research University, CNRS, Sorbonne Universités, UPMC Univ. Paris 06, F-75014, Paris, France; [2]Collège de France, PSL Research University, F-75005, Paris, France; [3]Max-Planck-Institut für extraterrestrische Physik (MPE), Garching, Germany; [4]Dept. of Physics & Astronomy, Frederick Reines Hall, University of California, Irvine, CA, United States; [5]University of California, Berkeley, CA, United States; [6]IRAM, Grenoble, France

Abstract. Observed massive galaxies in the distant Universe form stars at much higher rates than today. High levels of star formation are sustained by a continuous supply of fresh gas and high molecular gas fractions. But after a peak around redshift z=2-3, the star formation rate decreases by an order of magnitude. Is this evolution mostly driven by the available cold gas reservoir, or are the star formation processes qualitatively different near the star formation peak? The Kennicutt-Schmidt relation enables to characterize the star formation efficiency at low and high redshift, but resolved measurements at the scale of the star-forming regions themselves are still challenging at high redshift. Molecular gas observations carried out at the IRAM Plateau de Bure interferometer within the PHIBSS program (Tacconi, Combes et al.) permit us to study the star formation efficiency at sub-galactic scales around z=1.2 and 1.5 for a limited sample of galaxies, and thus help characterize the star formation processes at this epoch. Our results lay in the continuation of the resolved low-redshift measurements, but further studies would be necessary to complement our sample and validate our conclusions.

Keywords. galaxies: evolution, galaxies: high-redshift, galaxies: structure, stars: formation

APPENDIX C

Posters

SF2A 2013, Montpellier

TOWARDS A RESOLVED KENNICUTT-SCHMIDT LAW AT HIGH REDSHIFT

JONATHAN FREUNDLICH (jonathan.freundlich@obspm.fr)

F. COMBES, L. J. TACCONI, M. C. COOPER, R. GENZEL, R. NERI, A. BOLATTO, F. BOURNAUD, A. BURKERT, P. COX, M. DAVIS, N. M. FÖRSTER SCHREIBER, S. GARCIA-BURILLO, J. GRACIA-CARPIO, D. LUTZ, T. NAAB, S. NEWMAN, A. STERNBERG, B. WEINER

INTRODUCTION

Massive galaxies in the distant Universe form stars at much higher rates than today. Was star formation qualitatively different at high redshifts ?

The Kennicutt-Schmidt (KS) relation between total molecular gas and star formation rate (SFR) surface densities describes the star formation efficiency and is nearly linear at all redshifts, implying that the star formation processes seem to be largely independent of the cosmic epoch.

But most studies only consider averaged quantities for distant galaxies, as direct observations of the star forming regions of high redshift galaxies are challenging.

GOAL

We present a method for obtaining the gas and SFR surface densities of ensembles of clumps composing galaxies around redshift z=1.2, even though the corresponding scales are not resolved. This method is based on identifying these structures in position-velocity diagrams corresponding to slices within the galaxies.

A SET OF FOUR GALAXIES AT Z=1.2

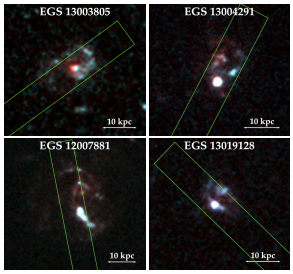

Composite HST images combining I and V bands.

METHOD

The total mass of gas of a galaxy is assumed to be directly proportional to the integrated CO(3-2) line luminosity, obtained from high resolution observations carried at the IRAM Plateau de Bure interferometer.

The SFR is deduced from the [OII] line displayed in spectra provided by the Keck DEEP2 survey. The global dust extinction is estimated from a SED reconstruction using CFHT photometric data.

SEPARATING SUBSTRUCTURES

Smoothed 1"-sized ensembles of clumps can be separated along the velocity axis of the position-velocity diagrams. The [OII] line luminosity is displayed on the left and the CO luminosity on the right.

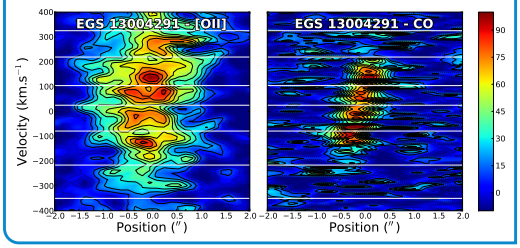

RESULTS

We derive a spatially resolved KS relation on a scale of $\sim$ 8 kpc. The data generally indicates an average depletion time of 1.9 Gyr, but with significant variations from point to point within the galaxies.

Our results, as well as most other observations, indicate that the KS relation is not significantly different at high redshift than in the local Universe : the star formation processes ten billion years ago were similar to the ones that are observed in the local Universe.

The method developed here could be applied to a more significant sample of high redshift galaxies (notably within the upcoming PHIBSS2 IRAM Legacy Program).

A RESOLVED KS RELATION

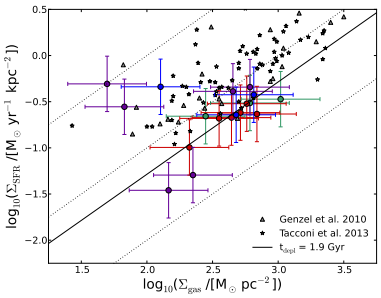

Kennicutt-Schmidt diagram for 1" ensembles of clumps of EGS13003805 (green), EGS13004291 (red), EGS12007881 (blue), and EGS13019128 (purple). The dotted diagonal lines correspond to constant gas depletion times of 0.1, 1, and 10 Gyr from top to bottom, and the solid black line to a constant depletion time equal to the mean depletion time of the clumps, t_{depl}=1.9 Gyr.

REFERENCES

- Freundlich et al., 2013, accepted by A&A, arXiv:1301.0628
- Genzel et al., 2010, MNRAS, 407, 2091
- Genzel et al., 2013, submitted to ApJ, arXiv:1304.0668
- Tacconi et al., 2010, Nature, 463, 781T
- Tacconi et al., 2013, submitted to ApJ, arXiv:1211.5743

SF2A 2014, Paris

On the stability of self-gravitating filaments

Jonathan Freundlich[1,2] (jonathan.freundlich@obspm.fr), Chanda J. Jog[3], Françoise Combes[1], & Sumedh Anathpindika[3]

[1]LERMA, Observatoire de Paris, France; [2]IFCPAR/CEFIPRA Raman-Charpak fellow; [3]Indian Institute of Science, Bangalore, India

ABSTRACT

Filamentary structures are very common in astrophysics and are observed at various scales. On a cosmological scale, matter is usually distributed along filaments, and filaments are also typical features of the interstellar medium. Within a cosmic filament, matter can possibly contract and form galaxies, whereas an interstellar gas filament can clump into a series of bead-like structures which can then turn into stars. To investigate the growth of such instabilities and the properties of the resulting substructures, we consider idealized self-gravitating filaments and derive the dispersion relation for perturbations within them. We assume no specific density distribution, treat matter as a fluid, and use hydrodynamics to derive the linearized equations that govern the perturbations. Assuming small local perturbations leads to a dispersion relation analogous to the spherical Jeans case: perturbations of size higher than the Jeans length collapse and asymmetries arise only regarding their growth rates, because of rotation. For perturbations of arbitrary size, the dispersion relation retains its complex terms: all modes are potentially unstable, but elongated perturbations near the axis of the cylinder grow faster. Prolate substructures and global collapse are favored, which is corroborated by most observations of interstellar filaments.

Background — filamentary structures are ubiquitous

Filamentary structures are very common in astrophysics and are observed at various scales.

• **On a cosmological scale**, matter is usually distributed along filaments, forming a cosmic web that connects galaxies to one another. Cosmological simulations confirm the existence of such features, and this cosmic web should provide the gas reservoir from which galaxies grow and accrete. The inner core of many of these filaments may be predominantly made of gas (Harford & Hamilton 2011).

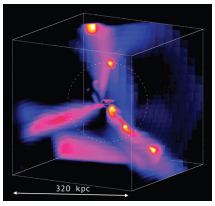

Figure 1. Cold gas streams feeding a typical 10^{12} $M_\odot$ galaxy at z=2.5, from a cosmological simulation (Dekel et al. 2009).

• **In the interstellar medium**, observations show filamentary structures on much smaller scales. The formation of turbulence-driven filaments in the interstellar medium may indeed represents the first step towards core and star formation (André et al. 2010).

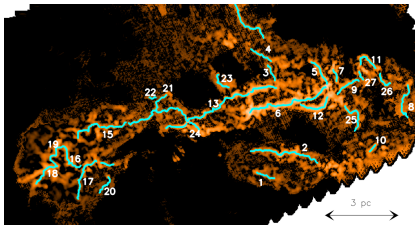

Figure 2. Column density map from the Herschel Gould Belt survey revealing interstellar filaments in the IC5146 molecular cloud (Arzoumanian et al. 2011).

Within a cosmic filament, matter can possibly **contract** and form galaxies, whereas an interstellar gas filament can clump into a series of bead-like structures which can then turn into stars.

Goal — studying the growth of instabilities in gas filaments

Our goal is to obtain a **dispersion relation** for perturbations arising in an idealized filament and to compare its properties with available observations and simulations. The standard Jeans instability describes the collapse of a spherical gas cloud, but the cylindrical case is less straightforward and has not been fully investigated yet.

Model — an idealized and infinite barotropic cylinder

Our idealized picture consists of an **infinite** self-gravitating **cylinder** with pressure and density related by a **barotropic** equation of state. We neglect the role of magnetic fields for simplicity, treat matter as an inviscid fluid and use hydrodynamics to obtain the **linearized equations** that govern the local perturbations (e.g., Mikhailovskii & Fridman 1973). We assume that there is no radial velocity in the undisturbed system and that all fluid particles share the same initial axial velocity, and further introduce **axisymmetric perturbations** of the generic form $e^{-i\omega t}e^{ik_R R}e^{ik_z z}$.

Local perturbations in a rotating filament

We first assume **local perturbations**: the typical scale of the perturbation is small compared to that of the unperturbed quantities, i.e., $k_R R_0 >> 1$, where R_0 is the typical radius for the unperturbed distribution. This assumption is analogous to the Wentzel-Kramers-Brillouin approximation (WKB) used in quantum physics and leads to the following local dispersion relation (Freundlich et al. 2014):

$$\omega^4 + \omega^2\left(4\pi G\rho_0 - c_0^2k^2 - \kappa^2\right) + \kappa^2k_z^2\left(c_0^2 - \frac{4\pi G\rho_0}{k^2}\right) = 0$$

where $k = \sqrt{{k_R}^2 + {k_z}^2}$ corresponds to the total wavenumber and κ is the epicyclic frequency, $\rho_0(R)$ and $c_0(R)$ being respectively the initial density distribution and the effective sound speed. Rotation induces asymmetries but the boundary between the stable and unstable regimes is symmetrical in the phase plane (k_R, k_z): the system is stable when $k^2 \geqslant k_{\rm crit}$ with $k_{\rm crit} = 4\pi G\rho_0/c_0^2$, and unstable below, which corresponds to the standard **Jeans criterion**. When there is no rotation, the dispersion relation further reduces to the standard dispersion relation for collapsing spherical systems.

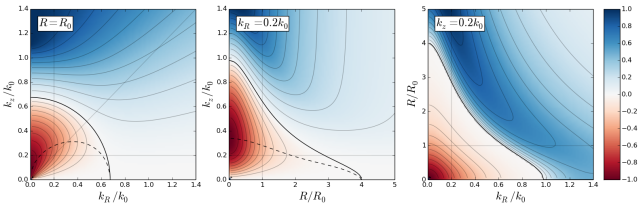

Figure 3. As an illustrative example, we model a filament from the Taurus molecular cloud, TMC-1 (also known as "The Bull's Tail"), with a Plummer-like density profile (Malinen et al. 2012) and plot the resulting distribution of the square of the minimal angular frequency in the planes $R = R_0$, $k_R = 0.2k_0$, and $k_z = 0.2k_0$, where $k_0 = \sqrt{4\pi G\rho_c}/c_0$ is a characteristic wavenumber depending on the central density ρ_c. Negative values of this quantity correspond to an unstable filament, and the solid black curve separates the stable and unstable regimes ($k = k_{\rm crit}$). The dashed line corresponds to the minimum value of the frequency, i.e., to the most unstable mode.

Global perturbations in a non-rotating filament

The local WKB assumption prevents the perturbations feeling the large-scale geometry of the system and thus leads to the standard spherical Jeans case when there is no rotation. **Without this assumption** and for **non-rotating** cylinders, the dispersion relation retains its complex terms and all modes are thus potentially unstable:

$$\omega^2 = -4\pi G\rho_0\frac{k^2}{k^2 - i\frac{k_R}{R}}\left[1 - i\frac{k_R}{k^2}\left(\frac{1}{R} + \frac{1}{\rho_0}\frac{\partial\rho_0}{\partial R}\right)\right] + c_0^2k^2 - ik_R\left[\frac{c_0^2}{R} + \frac{\partial c_0^2}{\partial R}\right] - \left[\frac{1}{R} + \frac{1}{\rho_0}\frac{\partial\rho_0}{\partial R}\right]\left[\frac{\partial c_0^2}{\partial R} - c_0^2\frac{1}{\rho_0}\frac{\partial\rho_0}{\partial R}\right].$$

This dispersion relation shows that **elongated perturbations** near the axis of the filament grow faster, thus favoring elongated substructures. This is corroborated by observations, as most observations in the Taurus molecular cloud or in other molecular clouds favor prolate structures within interstellar filaments and tend to show that cores are elongated along the direction of the filaments (e.g., Curry 2002, Hartmann 2002).

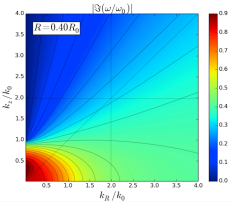

Figure 4. Imaginary part of the angular frequency for an idealized filament inspired by TMC-1 in the phase plane (k_R, k_z). Whereas we assumed local perturbations in Fig. 3, here we consider the dispersion relation obtained without WKB assumption and without rotation, which is more relevant to describe interstellar filaments. The plotted quantity is a measure of the growth rate of the perturbations, thus prolate structures with $k_z < k_R$ are likely to be favored.

Perspectives

Our model assumes an infinite and isolated filament, but we could generalize our calculations to a cylinder of **finite size** and to take into account the effects of the **environment** and of more complex velocity distributions.

This work should be complemented by **numerical studies** of the formation and subsequent collapse of idealized filaments (e.g., Anathpindika et al. 2014, in preparation).

References

Anathpindika, S., Freundlich, & J., Jog, C. J., 2014, in preparation • André, P., Menshchikov, A., Bontemps, S., et al., 2010, A&A, 518, L102 • Arzoumanian D., André, P., Didelon P., et al., 2011, A&A, 529, L6 • Curry, C. L., 2002, ApJ, 576, 849C • Dekel, A., Birnboim, Y., Engel, G., et al., 2009, Nature, 457, 451D • **Freundlich, J., Jog, C. J., & Combes, F., 2014, A&A, 564, 7** • Harford A. G. & Hamilton A. J. S., 2011, MNRAS, 416, 2678 • Hartmann, L., 2002, ApJ, 578, 914H • Malinen, J., Juvela, M., Rawlings, M. G., et al., 2012, A&A, 544A, 50 • Mikhailovskii A. B. & Fridman A. M., 1973, Soviet Physics - JETP, 17, 57

French embassy in Cairo, Egypt, 2015

THE EFFECT OF POWER LAW FLUCTUATIONS ON DARK MATTER HALOES

AMR EL-ZANT[1], JONATHAN FREUNDLICH[2] & FRANÇOISE COMBES[2,3]

[1]Centre for Theoretical Physics, The British University in Egypt, Cairo, Egypt [2]LERMA, Observatoire de Paris, CNRS, Sorbonne Universités, UPMC Université Paris 6, France [3]College de France, Paris, France

SUMMARY

Despite its huge success at explaining the large scale structure of the Universe, the standard **ΛCDM cosmological model**, which assumes the existence of a cold dark matter component, faces **severe challenges** when confronted to observations at galactic and galaxy cluster scales. Possible solutions to these challenges include: **a)** taking into account the **interactions between baryonic and dark matter components**, including star formation and feedback mechanisms from stars and active galactic nuclei; **b)** introducing **lighter dark matter particles**, warmer than the standard weakly interacting massive particles normally assumed to constitute the dark matter; and **c)** rejecting the dark matter scenario and explaining the discrepancies between theory and observations by **modifying the gravitational laws**. The **core-cusp problem** is one of these apparent discrepancies: early simulations based on the ΛCDM paradigm, where most of the mass of the Universe consists of collisionless cold dark matter particles, seemed to **overpredict the dark matter density** at the center of dark matter haloes. Whereas observations show core-like behaviours in the inner parts of such systems, simulations yielded much steeper, cuspy profiles. Here we consider the **gravitational interactions between the baryonic and dark matter components** as a possible means to change significantly the dark matter distribution. Energy can be transferred between these two components in two different ways: through **dynamical friction** from the kinetic energy of material coming into the dark matter halo, or from baryonic processes related to the different **feedback mechanisms**. These two types of interaction are expected to heat the dark matter halo, and thus to flatten its density profile. Star formation and active galactic nuclei give rise to powerful outflows of gas and stars, which perturb the gravitational potential of the dark matter halo. We study the effects of such perturbations, assuming **density fluctuations with a self-similar power spectrum**. We derive the expressions of the force auto-correlation function and of the velocity dispersion, and notably study their dependance on the scales of the fluctuations. We also carry out **collisionless numerical simulations** in order to quantify the conditions of the flattening of the cusp, and our preliminary results indeed show that the perturbations flatten the dark matter density profile. This seems to indicate that such interactions between the baryonic and dark matter components would help resolve the core-cusp problem.

BACKGROUND THE ΛCDM MODEL

The current standard ΛCDM cosmological model assumes the existence of a **cold, non baryonic dark matter** that only interacts gravitationnally, and of a non-zero cosmological constant Λ associated to dark energy. In the ΛCDM model, dark matter represents 84.5% of the total matter content of the Universe (Planck Collaboration, 2013).

Structure formation in the ΛCDM model. The ΛCDM model is very successful at describing the evolution of the Universe, from a very homogeneous state as shown by the Cosmic Microwave Background, to the present day clustered distribution of matter with galaxies, clusters of galaxies and voids between them. As dark matter is much more abundant than baryonic matter, the large scale evolution of the Universe is essentially driven by dark matter collisionless dynamics. Dark matter haloes form through gravitational instabilities from small linear perturbations. Galaxies then form within the potential wells of the dark matter haloes, when the gas cools and starts to form stars (White & Rees 1978).

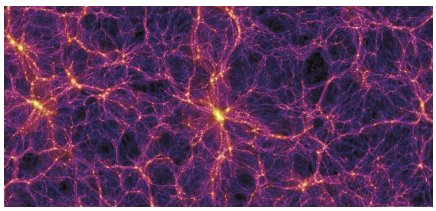

Figure 1. The large scale structure of the Universe from the Millenium dark matter cosmological simulation (Springel et al. 2005).

CORES VERSUS CUSPS

Dark matter only simulations within the ΛCDM paradigm predict dark matter haloes with steep, **"cuspy"** inner density profiles (e.g., Moore et al. 1998). Observations of dwarf galaxies, however, show that the central dark matter profiles are shallower, or **"cored"** (e.g., de Blok et al. 2008).

Introducing baryonic physics in the simulations is essential to resolve this core-cusp discrepancy. Gravitational interactions between the baryonic and dark matter components can notably occur through **dynamical friction** from the material coming into the dark matter halo (El-Zant et al. 2001), or from **feedback processes** related to star formation or active galactic nuclei (Mashchenko et al. 2006, Pontzen & Governato 2014). Young stellar populations and active galactic nuclei indeed release energy in their surrounding medium, notably through powerful outflows, which prevent further collapse, heat the dark matter halo and perturb its gravitational potential and density distribution.

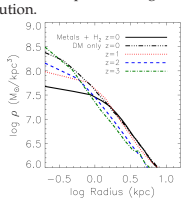

Figure 2. Empirical recipes for baryonic physics and feedback mechanisms enable to remove cusps and to reproduce cored density distributions in simulations (Governato et al. 2012).

OUR GOAL STUDYING THE EFFECT OF POWER LAW FLUCTUATIONS ON DARK MATTER HALOES

The effects of the different feedback processes originating from star formation or active galactic nuclei at the center of dark matter haloes should essentially be felt by the dark matter as **density fluctuations**. These fluctuations perturb the gravitational potential, and hence the trajectories of the dark matter particles.

Our goal is to characterize the effects of these density fluctuations on the dark matter, and their contribution to its heating and the flattening of the density profile. We assume density perturbations with a **self-similar power spectrum**, and fluctuations that cascade into smaller scales with a minimal scale $\lambda_{min} = 2\pi/k_{max}$ and a maximal one $\lambda_{max} = 2\pi/k_{min}$. The perturbations occur in a finite volume within the dark matter halo, namely within a radius d from the center of the halo. We carry out **analytical calculations** to derive the expressions of the force auto-correlation function and of the velocity dispersion, and define a characteristic relaxation time scale for these processes. We further run **collisionless dark matter simulations** with potential fluctuations in order to corroborate our calculations.

ANALYTICAL CALCULATIONS

We consider large scale density fluctuations $\delta(\vec{r})$ over the volume $V = d^3$ within a fluid of average density ρ_0. Assuming density perturbations with a self-similar power spectrum $\langle|\delta_{\vec{k}}|^2\rangle = Ck^{-n}$, we estimate the **force auto-correlation function** $\langle F(0)F(r)\rangle$ and the **velocity dispersion** $\langle\Delta v^2\rangle$ when $\lambda_{max} \gg \lambda_{min}$, which yields:

$$\langle F(0)^2\rangle \sim \frac{8\,(G\rho_0)^2\,\langle|\delta_{k_{min}}|^2\rangle\,d^3}{n-1}\,k_{min}. \qquad \text{and} \qquad \langle\Delta v^2\rangle \sim \frac{\pi D}{v_r}\frac{T}{k_{min}^n}.$$

where T is the duration of the perturbations and $D = 8Cd^3\,(G\rho_0)^2$. This enable us to obtain a characteristic **relaxation time scale**, which is the time at which the velocity dispersion resulting from the perturbations reaches the original velocity of dark matter particles. This time scale can be compared to the dynamical time in order to characterize the effects of the perturbations on the dark matter.

NUMERICAL SIMULATIONS

We use the "self-consistend field" (SCF) N-body code developed by Hernquist & Ostriker (1992) to study the effects of potential fluctuations stemming from density perturbations with a self-similar power spectrum on a collisionless dark matter system. At each time step, the potential is reevaluated from the trajectories of a number of test particles taking into account the perturbations. We start with a cuspy NFW dark matter profile (Navarro et al. 1996), and study the evolution of the dark matter distribution with time.

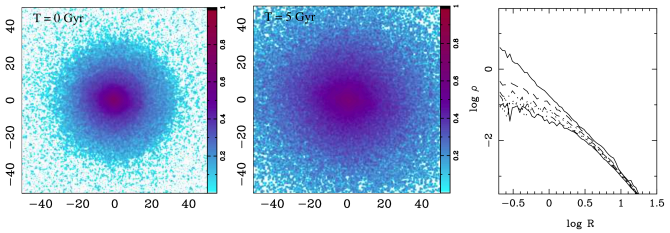

Figure 3. Density contrast at the initial and final time steps as well as the evolution of the density profile with time for one of our preliminary simulations. The transformation of the cusp into a core is clearly visible, but we still have to refine our methods and decrease the time steps.

CONCLUSION

We derive analytically some of the characteristics of the effects of power law density fluctuations on dark matter haloes, and we develop numerical simulations to validate our approach. The assumed perturbations could stem from a wide range of baryonic processes. The preliminary results are promising, as it seems that such perturbations are able to flatten significantly the inner part of the halo density profiles, leading to cores instead of cusps.

The next stage of this work will consist in using inputs from RAMSES hydrodynamical simulations (Teyssier 2002), that include star formation and feedback mechanisms, in order to constrain better and refine our model.

REFERENCES

de Blok, W. J. G., Walter, F., Brinks, E., et al., 2008, AJ, 136, 2648 • El-Zant, A., Shlosman, I., Hoffman, Y., 2001, ApJ, 560, 636 • Governato, F., Zolotov, A., Pontzen, A., et al., 2012, MNRAS, 422, 1231 • Hernquist, L., & Ostriker, J. P., 1992, ApJ, 386, 375 • Mashchenko, S., Couchman, H. M. P., & Wadsley, J., 2006, Nature, 442, 539 • Moore, B., Governato, F., Quinn, T., et al., 1998, ApJ, 499, 5 • Navarro, J. F., Frenk, C. S., & White, S. D. M., 1996, ApJ, 462, 563 • Planck Collaboration, et al., 2013, A&A, 571, 16 • Pontzen, A., & Governato, F., 2013, MNRAS, 430, 121 • Springel, V., White, S. D. M., Jenkins, A., et al., 2005, Nature, 435, 629 • Teyssier, R., 2002, A&A, 385, 337 • White, S. D. M., & Rees, M. J., 1978, MNRAS, 183, 341

IAU General Assembly, Honolulu, USA, 2015

RESOLVED STAR FORMATION RELATIONS AT HIGH REDSHIFT FROM THE IRAM PHIBSS PROGRAM

JONATHAN FREUNDLICH[1] (jonathan.freundlich@obspm.fr), FRANÇOISE COMBES[1,2], LINDA TACCONI[3], MICHAEL COOPER[4], REINHARD GENZEL[3,5], ROBERTO NERI[6] & THE PHIBSS CONSORTIUM

[1]LERMA, Observatoire de Paris, France; [2]Collège de France, Paris, France; [3]Max Planck Institute fur extraterrestrische Physik (MPE), Garching, Germany; [4]Dept. of Physics & Astronomy, Frederick Reines Hall, University of California, Irvine, CA, United States; [5]University of California, Berkeley, CA, United States; [6]IRAM, Grenoble, France

ABSTRACT

Observed massive galaxies in the distant Universe form stars at much higher rates than today. High levels of star formation are sustained by a continuous supply of fresh gas and high molecular gas fractions. But after a peak around redshift z=2-3, the star formation rate decreases by an order of magnitude. Is this evolution mostly driven by the available cold gas reservoir, or are the star formation processes qualitatively different near the star formation peak? The Kennicutt-Schmidt relation enables to characterize the star formation efficiency at low and high redshift, but resolved measurements at the scale of the star-forming regions themselves are still challenging at high redshift. Molecular gas observations carried out at the IRAM Plateau de Bure interferometer within the PHIBSS program (Tacconi, Combes et al.) permit us to study the star formation efficiency at sub-galactic scales around z=1.2 and 1.5 for a limited sample of galaxies, and thus help characterize the star formation processes at this epoch. Our results lay in the continuation of the resolved low-redshift measurements, but further studies would be necessary to complement our sample and validate our conclusions.

BACKGROUND

Ten billion years ago, between z=2-3, observed galaxies formed their stars at rates up to 20 times higher than now. **What are the causes of the winding down of star formation?**

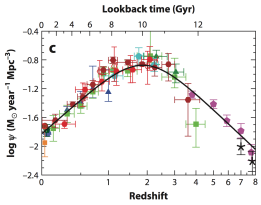

Figure 1. The evolution of the star formation rate with cosmic time (Madau & Dickinson 2014)

Blue star-forming galaxies lie on a tight relationship in the in the stellar mass M_*-SFR plane, the main sequence of star formation (MS). **How do galaxies evolve from blue star-forming disk galaxies to red and dead spheroids?**

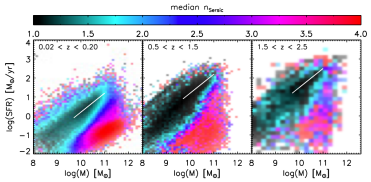

Figure 2. The main sequence of star formation in terms of Sersic index (Wuyts et al. 2011)

As stars are formed from cold molecular gas clouds, a high star formation rate (SFR) means a significant gas content. Galaxies near the star formation peak are indeed much more gas-rich and clumpy than their low-redshift counterparts. **Is the evolution of the cosmic SFR mostly driven by the declining cold gas reservoir, or are the star formation processes qualitatively different at high redshifts?**

THE PHIBSS PROGRAM

The **IRAM Plateau de Bure High-z Blue Sequence CO(3-2) Survey (PHIBSS)** studies the molecular gas properties of star-forming galaxies on the star-forming main sequence near the star formation peak. It notably aims at better understanding the winding down of star formation and the gas quenching processes.

- Observations at the IRAM Plateau de Bure Interferometer
- CO rotational lines to trace the cold molecular gas
- two redshift slices: z = 1.2 and 2.2
- massive tail of the MS: $\log(M_*/M_\odot) \leq 10.4$ & $\log(SFR/M_\odot yr^{-1}) \leq 1.5$
- 52 CO detections (FWHM ∼2-4″)
- 8 high-resolution imaging (FWHM ∼0.3-1″)

We focus here on the results concerning the **star formation efficiency**, first from the galaxy-averaged observations, and then from the resolved observations.

GALAXY-AVERAGED KS RELATION

The **Kennicutt-Schmidt (KS) relation** between the gas and SFR densities characterizes the star formation efficiency, and is shown to be near linear at low redshift. The same trend is observed at z=1-3 for the galaxies of the PHIBSS sample (Genzel et al. 2010; Tacconi et al. 2010, 2013). Nevertheless, the global mean depletion time (tdepl = Mgas/SFR) of 0.7 Gyr is slightly lower than at present time, which could imply a faster star formation duty cycle, more efficient star formation, and a need for gas replenishment at the peak of the star formation activity.

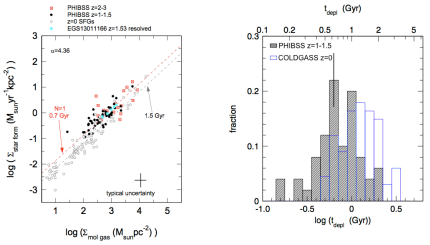

Figure 3. Near-linear KS relation from the PHIBSS program and distribution of the depletion times as compared to the COLDGASS low-redshift sample (Tacconi et al. 2013).

RESOLVED KS RELATIONS AT SUB-GALACTIC SCALES

The PHIBSS high-resolution observations of the molecular gas reach an angular resolution of 0.3″-1″, 1″ corresponding to about 8 kpc at z = 1.2.

- Resolved kinematics enables to separate **smoothed ensembles of clumps** due to their different velocities, and to obtain a resolved KS relation averaged at a scale below 8 kpc for four z = 1 galaxies of the PHIBSS sample (Freundlich et al. 2013).
- Obtention of a **pixel by pixel KS relation** for one typical z=1.53 massive star-forming galaxy from the PHIBSS sample (Genzel et al. 2013)

These results are compatible with a linear relation and a constant depletion time of about 1.9 Gyr, and fit well with the corresponding low-redshift observations.

This seems to point towards similar star formation processes at high and low redshifts, but a bigger statistical sample would be necessary to obtain more meaningful mean depletion times for the substructures.

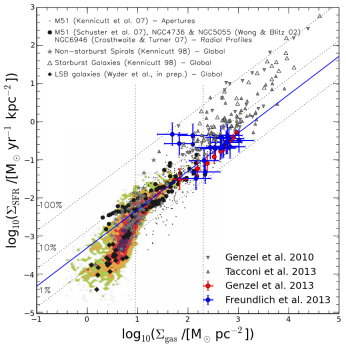

Figure 4. Spatially resolved molecular KS relation for ensembles of clumps of four galaxies from the PHIBSS sample (Freundlich et al. 2013) and for binned groups of pixels in EGS13011166 (Genzel et al. 2013), superimposed on the sub-galactic KS diagram obtained at low redshift by Bigiel et al. (2008). The solid blue line corresponds to a constant depletion time tdepl = 1.9 Gyr, and the grey data points to galaxy-averaged measurements.

PERSPECTIVES

The ongoing **IRAM PHIBSS2 Legacy Program** (Combes, Garcia-Burillo, Neri, Tacconi, et al.) will more than triple the number of high-redshift normal star-forming galaxies with CO measurements, extend their redshift range, and include galaxies below the MS.

Complementary **ALMA programs** will further contribute to extend the sample (Genzel et al.), probe higher CO transitions (Weiss et al.), and possibly obtain high-resolution images and kinematics of the molecular gas in galaxies at intermediate redshifts (Freundlich et al.).

REFERENCES

Bigiel, F., Leroy, A., Walter, F., et al. 2008, AJ, 136, 2846 • Freundlich, J., Combes, F., Tacconi, L. J., et al. 2013, A&A, 553, A130 • Genzel, R., Tacconi, L. J., Gracia-Carpio, J., et al. 2010, MNRAS, 407, 2091 • Genzel, R., Tacconi, L. J., Kurk, J., et al. 2013, ApJ, 773, 68 • Madau, P., & Dickinson, M. 2014, ARA&A, 52, 415 • Tacconi, L. J., Genzel, R., Neri, R., et al. 2010, Nature, 463, 781 • Tacconi, L. J., Neri, R., Genzel, R., et al. 2013, ApJ, 768, 74 • Wuyts, S., Förster Schreiber, N. M., van der Wel, A., et al. 2011, ApJ, 742, 96

APPENDIX D

Popular science articles for The Hindu - In School

I have always been interested in science popularization and teaching, and my stay at the Indian Institute of Science during the course of my PhD provided me with the opportunity to start writing for the 'In School' edition of The Hindu, targetting young students. The Hindu is one of the main English-language newspapers in India, and its In School edition is distributed through schools as part of The Hindu's 'Newspaper in Education' program. It daily features the important news as well as sports, sciences, and regional news.

My astrophysical series for The Hindu - In School takes up various aspects of my PhD work, notably with articles about distant galaxies or the formation of stars, but also extends to other domains of astrophysics and cosmology. It starts with three introduction articles imagined as a journey from our Solar System (*A travel guide to Mars*, 22 September 2014) to extrasolar planets (*Faraway, so close*, 29 September 2014) and distant galaxies (*Island worlds in the vastness of the Universe*, 6 October 2014). The series continues with three articles about cosmology and our Universe as a whole, evoking the Cosmic Microwave Background (*The earliest light*, 17 November 2014), the expansion of the Universe (*Drifting away from us*, 1 December 2014) and dark matter (*The dark side of the Universe*). It then focuses on star formation (*A nursery for stars*) and stellar evolution (*Life and fate of a star*, 5 January 2015, *The grand finale of a giant star*, 2 February 2015), to finish with black holes (*An irresistible attraction*, 9 March 2015) and the formation of our Solar System (*A glimpse at the formation of our Solar System*, 13 April 2015, *Meteorites: witnesses of the solar system's birth*, 1 June 2015). The last two articles were written together with Emmanuel Jacquet, from the *Muséum d'Histoire Naturelle* in Paris.

A travel guide to Mars

India's Mars Orbiter Mission is due to reach its final orbit around Mars on September 24. Here is a quick look into the red planet

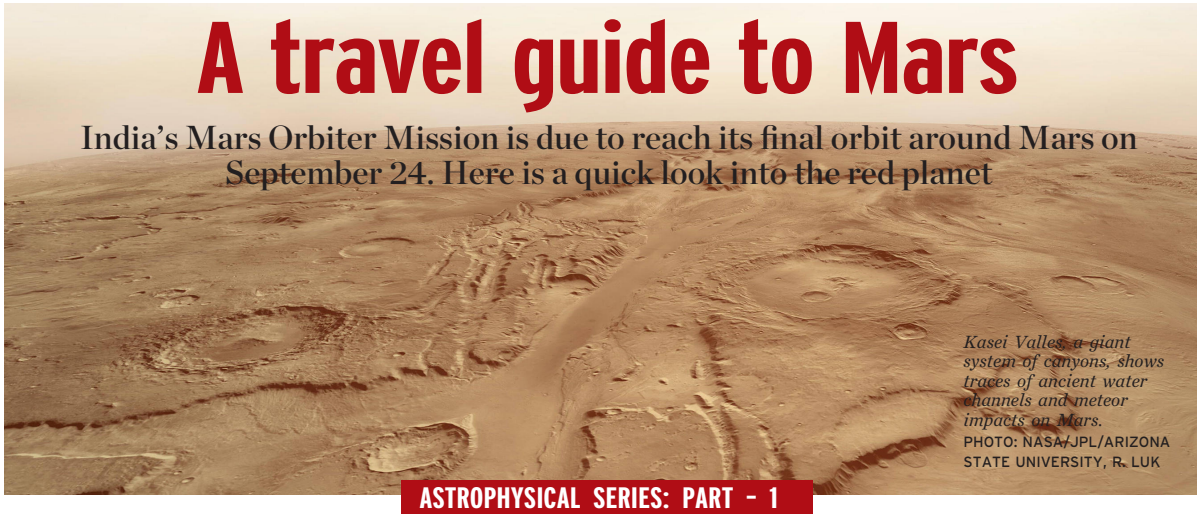

Kasei Valles, a giant system of canyons, shows traces of ancient water channels and meteor impacts on Mars.
PHOTO: NASA/JPL/ARIZONA STATE UNIVERSITY, R. LUK

ASTROPHYSICAL SERIES: PART - 1

Jonathan Freundlich

- Mars is home to the tallest mountain of the Solar System, Olympus Mons, and to a 7km deep canyon named Valles Marineris, which is more than 4, 000 km long.
- Water on Mars and Earth probably comes from asteroids made of ice travelling from the edge of the Solar System.
- In Hindu astrology, Mars is named Mangala and also associated with war. It is often identified with Kartikeya.
- Mangalyaan, launched on 5 November 2013, will observe the surface of Mars and study its atmosphere.

Imagine a vast barren desert of red dust and rocks, sand dunes swept by the winds, incredible canyons and the tallest mountain of the Solar System. Imagine a world where you could effortlessly jump 3 meters high, climb down steep craters, and set foot on everlasting carbon dioxide ice, that turns into vapour instead of melting. Welcome to planet Mars, one of our nearest neighbours!

Like Earth, Mars orbits around the Sun. But Mars is further away from it, so the Sun appears smaller in the Martian sky. It would take around nine months to reach Mars from Earth, and communications with Earth would be delayed because of the distance, as it is impossible to send messages at a speed higher than the speed of light. It takes 8 minutes for the light from the Sun to cross the distance between Sun and Earth, and it would take up to 20 minutes for a message from Earth to reach Mars. Can you imagine a conversation where you have to wait that long to hear your interlocutor's answers?

Rust and volcanic rocks

Mars was named after the Roman god of war because of its blood red colour in the sky. It is due to a thin layer of rust that formed on the iron-rich soil of the planet. But if you walk on Mars your footprints would remove the rust and reveal underlying black volcanic rocks. Mars is home to the tallest mountain of the Solar System, Olympus Mons, which is a gently sloped volcano. This gigantic mountain is 21,229 m high, more than twice as high as Mount Everest. But the climb wouldn't be as tiring as in the Himalayas: the gravity on Mars is only one third of Earth's, so you would jump three times higher than usual!

It wouldn't be wise to step out without a proper space suit though. Mars atmosphere is indeed very thin, and almost entirely made of carbon dioxide. Earth atmosphere was probably similar very long ago, but the first living organisms on Earth consumed the carbon dioxide to produce the oxygen we now breathe. On Mars, even some clouds are made of carbon dioxide!

Warm clothes are also advisable, as the temperatures on Mars are low and can vary dramatically between day and night. They can reach a pleasant 20° C at noon during summer, fall to -70° C the next night, and be as low as -150° C in winter. A thin layer of frost usually forms during the night, and there are everlasting carbon dioxide ice caps in the polar regions. The sharp differences of temperature can generate big dust storms. Dust storms on Mars can cover the entire planet and last for months.

Mars once had rivers, lakes, and maybe even oceans like the Earth does. But water did not remain liquid very long, and is now trapped as ice mixed with dust at the poles and inside the rocks. Today we can only see traces of the ancient dried-up water channels, which constitute an amazing sight! Mars shows an example of a planet that once looked very much like Earth before the apparition of life, but then evolved differently to become a harsh and hostile environment. Would you like to visit it if it were possible?

(Jonathan Freundlich is a PhD student at the Paris Observatory, in France, working on star formation and galaxy evolution.)

Faraway, so close

Jonathan Freundlich

An artist's impression of a sunset on Gliese 667 Cc. The planet orbits around the brightest star, but two other suns are visible in the sky. CREDIT: ESO/L. CALCADA

ASTROPHYSICAL SERIES: PART- 2

Have you ever tried to count the stars in the night sky? Have you ever wondered how many worlds like our Solar System could exist in the vastness of the Universe?

Most shining dots you see in the night sky are stars like our Sun. Some are bigger, some are smaller. But they are all part of our Galaxy, the Milky Way. A galaxy is a group of many stars, dust and gas held together by the gravitational force. The same force that holds you to the ground and prevent Earth to escape from the vicinity of the Sun. There are more than hundred billion stars in the Milky Way!

Earth and the other planets of our Solar System, like Mars or Jupiter, orbit around the Sun. Similarly, there could also be planets around other stars. A planet orbiting around a star which is not our Sun is called an exoplanet, and the first one was discovered in 1995 from a telescope in the South of France. We have now detected over 1800 exoplanets, and we are yet only looking at nearby stars. As there are billions and billions of stars in the Milky Way, there could also be billions and billions of exoplanets.

Detections are indirect

But detecting exoplanets is not easy. Planets don't emit visible light on their own, and we are blinded by the extreme brightness of the stars around which they orbit. Observing an exoplanet is like spotting a firefly in the direction of the sun during a bright sunny day.

This is why most detections of exoplanets are indirect. For example, when a planet passes in front of its parent star, the luminosity of the star slightly decreases, and as the planet continues its orbit, this is due to happen at regular intervals. Detecting periodical drops of the star luminosity thus indicates the presence of a planet, and also enables to calculate its size. Moreover, the parent star is attracted to the planet in the same way that the planet is attracted to the star. So, as the planet turns around the star, the star also moves a little. As the star is much more massive than the planet, the movement is very faint, but still detectable, and it even permits to determine the mass of the planet.

Gaseous 51 Pegasi B

51 Pegasi B is the first exoplanet that was ever detected. It is a gaseous planet like Jupiter, but it is much closer to its parent star. Since it therefore receives more light from the star, it is very hot and the temperature reaches around 1000°C. But like Jupiter, you wouldn't be able to set foot on this planet, as it is entirely made of gas!

Gliese 667 Cc is a rocky exoplanet that is much more similar to Earth. It is just slightly smaller than our planet, and its surface temperature might be very close to Earth's. There could even be liquid water on the surface! But there are also major differences: the full round of seasons only last 28 days instead of a year, and three suns should be visible in the day sky. This definitively changes the vista!

We will surely discover more exoplanets in the future, and one of the key questions is whether life happened in other planets than Earth. As we expect to find many more exoplanets, that is quite possible! Besides, we are yet only probing a small area of our Milky Way. What about other galaxies? There are many more galaxies in the Universe, and thus even more stars. So many that the thought makes me dizzy!

(Jonathan Freundlich is a PhD student at the Paris Observatory, in France, working on star formation and galaxy evolution)

Did you know?

- Ancient Greeks named our Galaxy the Milky Way because it appears as a milky white glowing band across the night sky, and "galaxy" actually means "milky" in ancient Greek.
- Seen from outside, our Milky Way looks like a flat disk made of stars, whose diameter is about 100,000 light-years: light itself takes 100,000 years to travel from one side to the other!
- As most other stars, our Sun rotates around the center of the Milky Way. The nearest star to our Sun is named Proxima Centauri and is already 4 light-years away from us.
- 51 Pegasi B is named after its host constellation, Pegasus, while Gliese 667 Cc bears the name of the German astronomer Wilhelm Gliese, who catalogued the planet's parent stars in 1957.
- While Earth takes a full year to complete its revolution around the Sun, 51 Pegasi B circles around its star in just a few days

Island worlds
in the vastness of the Universe

ASTROPHYSICAL SERIES: PART - 3

Jonathan Freundlich

All the stars you see in the sky belong to our Galaxy, the Milky Way. But our naked eyes can't see everything: if you point a powerful telescope to any seemingly empty region of the sky, it will uncover hundreds and hundreds of other galaxies! Each of these galaxies is a world in itself, containing billions of stars and planets. Our Milky Way may be huge, but it is only one galaxy amongst hundreds of billions!

The Andromeda Galaxy is one of the nearest galaxies to the Milky Way. But it is already two million light-years away, which means it took two million years for its light to reach us: we see it as it was when there were still no humans on Earth! Because light takes time to travel from one place to another, we see distant galaxies not as they are right now, but as they were long ago in the past. The farther we look in space, the farther we see back in time.

Some of the faintest galaxies telescopes can see are ten billion light-years away, and we can thus probe the Universe as it was ten billion years ago. Galaxies at that time looked quite different than now. Whereas our Milky Way and the Andromeda Galaxy have beautifully smooth spiral shapes, galaxies were less regular and much lumpier ten billion years ago. Besides, they were forming much more stars.

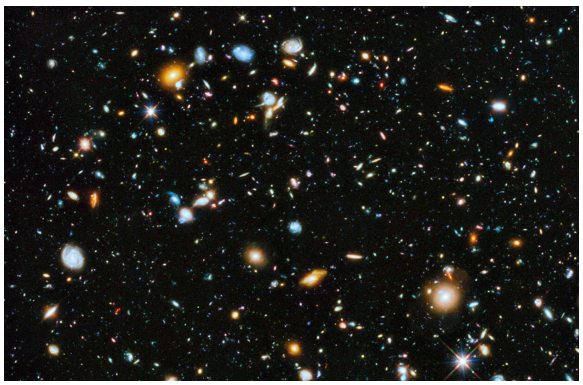

The Hubble Ultra Deep Field image uncovers a multitude of galaxies in a tiny region of the sky. CREDIT: NASA, ESA, H. TEPLITZ AND M. RAFELSKI (IPAC/CALTECH), A. KOEKEMOER (STSCI), R. WINDHORST (ASU), Z. LEVAY (STSCI)

How do stars form?

Stars originate from cold gas clouds that are mainly composed of hydrogen, as hydrogen is the most abundant element in the Universe. Gravity pulls the gas particles together, up to a point where pressure and temperature are so high that nuclear fusion reactions start: atoms merge and form heavier elements, like helium, carbon, and even iron. These powerful nuclear reactions generate the incredible amount of energy that makes stars shine, and produce most chemical elements in the Universe, including the atoms of your own body. We are all made of stardust!

Galaxies progressively consume their gas reservoir to form stars. Also, giant stars often explode at the end of their lives, which eject some of the remaining gas out of their galaxy. The gas content of a galaxy consequently decreases with time, and this is the main reason why galaxies formed much more stars ten billion years ago. Nevertheless, our Milky Way still gives birth to a couple of stars each year!

The Universe is not static

We often imagine the Universe as an unchanging ocean in which our Galaxy would be fixed for all times. But our Universe is not static. As stars form and die, galaxies evolve and change. The life of a galaxy is far from quiet, and can even be violent! Galaxies can indeed collide and merge with each other. For example, the Andromeda Galaxy will merge with our Milky Way in four billion years. But be reassured, although it will definitively change the night sky, it shouldn't disturb Earth and our Solar System that much!

For the moment, we are only able to observe other galaxies from the distance. Each galaxy is unique and they all have different shapes and colours. But these worlds may seem too far away to be ever reachable. Do you think mankind will be able to explore them one day?

Jonathan Freundlich is a PhD student at the Paris Observatory, in France, working on star formation and galaxy evolution.

- Giant stars usually explode at the end of their lives. The explosion is called a supernova, and can be as luminous as a whole galaxy. It generates huge winds that can expel some of the gas from the galaxy in which it happens.
- Andromeda Galaxy is about the same size as our Milky Way, and it is actually visible with the naked eye during dark moonless nights. It appears as a dim, hazy dot in the sky.
- Andromeda Galaxy and our Milky Way are both part of a group of galaxies named the Local Group.
- The Hubble Ultra Deep Field image taken by the Hubble Space Telescope reveals thousands of galaxies in an area which is hundred times smaller than the apparent surface of the moon.

The earliest light

What the universe was like in its earliest stages

Jonathan Freundlich

When we look at the universe with our telescopes today, we can see stars, galaxies, clusters of galaxies and huge voids between them. As matter gathers around galaxies and leaves big empty regions, the universe is highly inhomogeneous. Have you ever wondered what the universe looked like in its earliest stages?

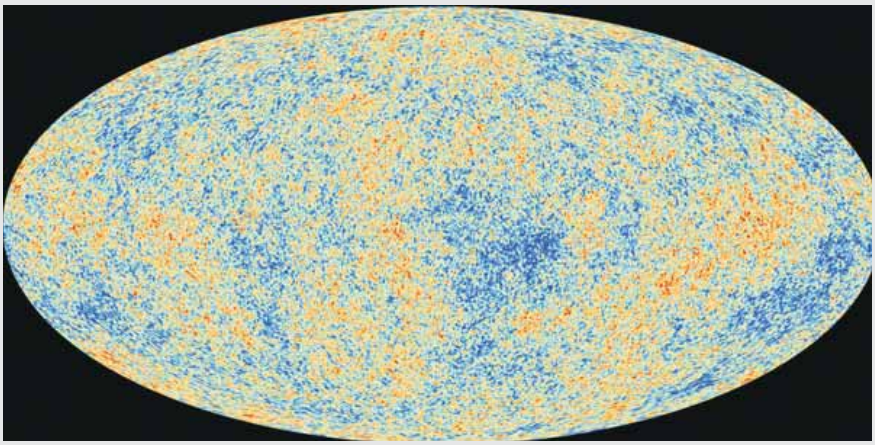

SHORTLY AFTER THE BIG BANG *The Cosmic Microwave Background as observed by the Planck satellite.* PHOTO: ESA AND THE PLANCK COLLABORATION

ASTROPHYSICAL SERIES

- Planck is a mission of the European Space Agency (ESA) designed to make the most precise measurements of the Cosmic Microwave Background. It was launched in May 2009 and started releasing its scientific conclusions in 2013.
- Planck's predecessors include NASA missions COBE (launched in 1989) and WMAP (2001).
- Light emitted before the epoch of the Cosmic Microwave Background doesn't reach us because the Universe then was too dense and opaque.
- The glow of the Cosmic Microwave Background is strongest in the microwave region of the electromagnetic spectrum, hence its name.

A homogeneous universe

What we call the Cosmic Microwave Background is the closest we can get to an image of the universe as it was right after the Big Bang, more than 14 billion years ago. It is a light which is not associated to any star or to any other astrophysical object, but rather bathes the entire universe in a background glow. It is the oldest light we can see, emitted when the universe was only 380,000 years old. At that time, the universe was much hotter and much more condensed than it is today.

In the same way that heated metals emit light and change colour with temperature, the Cosmic Microwave Background is a measure of the temperature of the universe. To each fluctuation of temperature corresponds a change in the matter distribution, so the Cosmic Microwave Background also traces the matter distribution of the Universe long before Earth and our Milky Way came into existence. And contrary to what we can observe today, it reveals an incredibly homogeneous universe!

The amount of matter is almost exactly the same everywhere in the universe at the epoch of the Cosmic Microwave Background: between the blue and red areas on the map, the difference in matter density is comparable to the difference a sand grain would make on your own weight. But although small, there are tiny fluctuations and they are the seeds of all future galaxies!

The formation of galaxies

Gravitation is an attractive force, so each excess of matter tends to attract more matter and to grow. This is how the tiny density fluctuations seen in the Cosmic Microwave Background lead to matter structures as large as galaxies and clusters of galaxies.

The temperature of the universe decreases with time, which helps forming stable structures. Lower temperatures indeed imply smaller velocities for the matter particles, and a particle with a small velocity is more likely to feel the gravitational attraction of the other particles and to aggregate with them, as it is less carried away by its own momentum. But while gravitation pulls particles together, the expansion of the universe tends to dilute and scatter them, as more space becomes progressively available to the same amount of matter. The formation of structures is a constant fight between the gravitational force and the expansion of the universe!

Nevertheless, a huge network of matter structures slowly starts to assemble. In the densest regions, gas cools and starts to form stars. Galaxies are born.

The Cosmic Microwave Background is a snapshot of the universe as it was shortly after the Big Bang, before the first galaxies were created.

But it is also much more than this. The detailed properties of its temperature fluctuations tell us about the very nature of our universe, and help us answer fundamental questions such as: What is the composition of our universe? How old is it? Is it going to expand forever? Is it finite? Is it infinite?

(Jonathan Freundlich is a PhD student at the Paris Observatory, in France, working on star formation and galaxy evolution. The author can be reached at jonathan.freundlich@obspm.fr)

Drifting away from us

Jonathan Freundlich

The milky white glow you can see across the sky during dark moonless nights is our Galaxy, the Milky Way. It is made of a myriad of stars held together by the gravitational force, our Sun being only one of them. Although philosophers and scientists had imagined the possibility of a multitude of island worlds like our Milky Way far away from us, it is only in the beginning of the 20th century that this possibility became a scientific fact. All at once, the Universe appeared much wider than initially thought.

An expanding Universe

Galaxies outside of the Milky Way have in common the fact that the farther they are, the redder they appear. This is because they are all drifting away from us.

Have you ever noticed the shift in the sound of a motorcycle or in the siren of a fire-fighter truck as it passes you? If you pay attention, you would notice that the pitch of these sounds is higher when they come towards you, and lower when they go away from you. This is called the Doppler Effect. In a similar way, galaxies that come towards us would appear bluer than if they were standing still, while galaxies that are moving away from us would appear redder. Distant galaxies appear redder than they should, so they are moving away from us. And the farther they are, the faster they are moving away!

Space itself is expanding

This phenomenon concerns all galaxies and they are all moving away from each other. There is a global expansion of the Universe. As strange as it may seem, space itself is expanding! Imagine the Universe as a dotted balloon where each dot represents a galaxy: when the balloon is blown up, the distance between the dots increase in the same way as the distance between galaxies. Current models state that such distances have increased by a factor higher than thousand since the epoch of the Cosmic Microwave Background! However, galaxies themselves are held by gravity and are thus able to retain their shapes.

The galaxy group HCG 87 with more distant background galaxies. CREDIT: GMOS-S COMMISSIONING TEAM, GEMINI OBSERVATORY

Observable galaxies are slowly disappearing

Recent observations have shown that the expansion of the Universe is actually accelerating: galaxies are moving away from each other faster and faster!

If the receding velocity of a galaxy keeps increasing, there will be a time when it will reach the speed of light. After that, light from this galaxy will never be able to reach us and the galaxy will totally disappear from our sight. Indeed, you can imagine the light coming from this galaxy as a runner on an expanding track whose finishing line is our galaxy: if the track expands faster than the runner can run, the runner will never reach the end of the track! Consequently, in an accelerated expanding Universe and according to our current models, we are doomed to see less and less galaxies.

In hundred billion years, there would ultimately be only one single visible galaxy: ours. Not exactly the Milky Way, because it would have merged with Andromeda Galaxy, but the galaxy resulting from the merger. If there are still humans around, they won't be able to see as much of the Universe as we can see now. Do you think they would trust our observations and theories about the Universe and galaxies they wouldn't be able to see?

(Jonathan Freundlich is a PhD student at the Paris Observatory, in France, working on star formation and galaxy evolution. The author can be reached at jonathan.freundlich@obspm.fr)

ASTROPHYSICAL SERIES

Did you know?

*** The earliest known observation of a galaxy outside of the Milky Way was made by the Persian astronomer Abd al-Rahman al-Sufi in the 10th century A.D., when he noted the fuzzy appearance of the Andromeda Galaxy.**

*** Hubble's law states that the receding velocity of a galaxy is proportional to its distance from Earth. It is named after the American astronomer Edwin Hubble, who published it in 1929.**

*** The velocity associated with the expansion of the Universe can be higher than the speed of light. However, this does not mean that objects can move through space faster than light, since the expansion of the Universe is an expansion of space itself.**

*** Since farther galaxies are redder than they should because of the expansion of the Universe, their "redshift" is a measure of their distance from us.**

The dark side of the Universe

Dark matter: the known and the unknown

Jonathan Freundlich

We are all made of the same building blocks: particles such as protons, neutrons and electrons. All the matter we can see is made of these particles. But what if they were only a small portion of all the matter in the Universe? What if there were other forms of matter? As strange as it may seem, the current model describing the Universe assumes the existence of an unseen type of matter.

Cosmic whirling dances

Gravity is the invisible bound that makes apples fall towards the ground and satellites like the Moon orbit around the Earth instead of flying away. The Moon is indeed always falling towards us, but its velocity makes it drift sideways and circle instead of falling straight down. It will always continue to circle and its velocity is set by the mass of the Earth and by the distance between the two celestial bodies. If the Earth was more massive, the Moon would spin faster around us!

On bigger scales, galaxies are also held by gravity. Galaxies often look like magnificent whirlpools, in which billions of stars and huge amounts of gas orbit around a central black hole. As for the Moon, the speed at which these stars rotate should be set by the mass of the galaxy and by the distance from its center. The more massive a galaxy is, the faster its stars rotate.

Some mass is missing!

But stars actually orbit faster than they should, as if galaxies were much more massive than observations suggest. Could there be some matter we can't see? Is our theory of gravitation wrong? The easiest answer is to assume that there is some additional invisible matter in all galaxies: dark matter. This assumption is not necessarily strange, as our perception of the Universe is always limited: for example, our eyes can't see ultraviolet or infrared light, although we know it exists.

The current model describing the Universe used by most astrophysicists assumes the existence of a dark matter that is fundamentally different from all other types of matter. It wouldn't be made of protons, neutrons and electrons as we are. Indeed, the amount of ordinary matter was set once and for all at the beginning of our Universe, and it can't account for the large amount of dark matter that is needed to explain the velocities of stars in galaxies. There should be more than five times more dark matter than ordinary matter!

STILL IN THE DARK *The Whirlpool Galaxy is a typical spiral galaxy with stars and gas rotating around its center.* CREDITS: NASA/HUBBLE

Did you know?

- The Swiss astronomer Fritz Zwicky first used the term "dark matter" in the 1930s to explain the velocities inside a cluster of galaxies and the apparent missing mass, but the idea became much more popular in the 1970s with U.S. astronomer Vera Rubin and her observations of the velocities of stars in galaxies.
- The Israeli physicist Mordehai Milgrom proposed a serious alternative theory to dark matter in 1983, which modifies Newton's law of gravitation.
- Collisions of highly energetic particles can sometimes produce new types of particles. The Large Hadron Collider (LHC) at CERN is the largest and most powerful particle collider in the world.

ASTROPHYSICAL SERIES

In search for dark matter

Uncovering dark matter is one of the big challenges of physics today. But as dark matter shouldn't emit or absorb any light, nor interact much with ordinary matter, it should be totally invisible and almost impossible to detect directly. Hundreds of dark matter particles may be just crossing your body right now, without you noticing anything! We can just observe its gravitational influence on the visible matter at large scales, or hope to detect compatible new particles in colliders such as the ones at CERN, in Switzerland. Much is expected from particle colliders in the next few years.

It might also be possible to explain the velocities of stars in galaxies without dark matter. That would require to change our models drastically! Notably, we would have to change our conception of gravitation itself. Dark matter is still one of the great mysteries of the Universe, but the next few years might be crucial for our understanding of it. Stay tuned!

(Jonathan Freundlich is a PhD student at the Paris Observatory, in France, working on star formation and galaxy evolution. The author can be reached at jonathan.freundlich@obspm.fr)

A nursery for stars

The Orion Nebula is the nearest region of massive star formation to Earth: just 1,300 light-years away

Jonathan Freundlich

The Orion Constellation is one of the easiest constellations to identify in the winter night sky, because of three aligned stars that constitute Orion's belt. It represents a giant hunter with broad chest and strong feet from Ancient Greek mythology, whom the gods placed amongst the stars at his death.

The Orion Nebula as seen by the Hubble Space Telescope. PHOTO: NASA,ESA, M. ROBBERTO (SPACE TELESCOPE SCIENCE INSTITUTE/ESA) AND THE HUBBLE SPACE TELESCOPE ORION TREASURY PROJECT TEAM. *(Left) The Orion Constellation.* CREDIT: JOHAN MEURIS/STELLARIUM

A colourful cloud

Below Orion's belt is an alignment of stars that could represent his sword sheath. This is where one of the most magnificent astronomical objects lies: the Orion Nebula. It can be visible to the naked eye or with binoculars as a faint red glow, but one need a powerful telescope such as the Hubble Space Telescope to uncover its inner structure and beauty.

Yet beware that astrophysical images usually use false colours and do not necessarily show what our eyes would see! Such images are indeed obtained from combinations of black and white pictures taken with different filters. For example, ultraviolet light is often displayed in blue, so we can visualize its distribution in space, which is something we wouldn't be able to see directly with our limited sight.

Each filter and each colour tells us something about the contents of the objects we observe, in the same way that you can guess the composition of a fruit juice from its colour. In the Orion Nebula, young stars emit ultraviolet light, while the surrounding gas glows red. The combination of both colours can result in purple strokes in the images, while denser regions occasionally obscure this background and appear as dark foreground clouds. Green shades indicate the presence of oxygen atoms.

Born in turmoil

The Orion Nebula is the nearest region of massive star formation to Earth: it is only about 1,300 light-years away from us, which is a very small distance when compared to the total size of the Milky Way. Thousands of stars of various sizes and ages are visible in the sharpest images of this nebula. These stars are embedded in a giant cloud of gas and dust, from which even more stars are being born.

New stars form in the densest regions, where gravity pulls gas particles together. There, density and temperature can be so high that atoms start to merge through powerful and incredibly luminous nuclear fusion reactions. These reactions are the ones that make stars shine, and young stars are particularly vigorous. They emit highly energetic ultraviolet light and generate strong winds that blow away their surroundings. At the center of the Orion Nebula lies a group of four very bright young stars, named the Trapezium. Each of these stars is thousands of times brighter than our Sun and the winds they generate carve a huge oval cavity in the nebula and thus disturb the growth of hundreds of smaller stars!

The Orion Nebula is a very active and turbulent region, with flows of gas in different directions, sometimes colliding, areas denser than others, and streams of particles and light unleashed by the numerous stars. It hosts all stages of star formation, from the dense gas clouds where new stars are forming to the massive young stars at its center.

ASTROPHYSICAL SERIES

Try spotting

Would you be able to spot Orion in the sky during the next winter months and to see the faint red glow of the Orion Nebula?

(Jonathan Freundlich is a PhD student at the Paris Observatory, in France, working on star formation and galaxy evolution)

- The names of many Western constellations are inspired by Ancient Greek mythology.
- In Hindu Vedic astronomy, the Orion Constellation is seen as a deer (Mriga).
- The word nebula comes from Latin, so its plural is nebulae. It originally means a small cloud, because this is how it looks like at first sight.
- Our Solar System and the Orion Nebula are located on the same spiral arm of the Milky Way, which was appropriately named the Orion Arm.

Life and fate of a star

Jonathan Freundlich

The warm light of the Sun that basks the Earth has enabled life to bloom on our planet. Our fate is inevitably tied to the fate of our star.

A gaseous structure

The Sun is an incredibly hot sphere of gas, mainly made of hydrogen, and the temperature in its core can reach millions of degrees. In this unbearable furnace, hundreds of millions of tons of hydrogen atoms fuse together each second to form heavier elements like helium through powerful nuclear reactions. These fusion reactions are very energetic and emit the intense light that would blind you if you were to stare at the Sun for too long.

Unlike the Earth, a star is made of gas and has no definite boundary: a falling object would never hit any ground! Gravity pulls the gas particles together, until the gas is too dense to contract anymore. The closer to the center, the higher the pressure and the denser it gets. The nuclear fusion reactions, that make the Sun shine, take place in its very center, where density and temperature are the highest.

The evolution of the Sun

Our Sun was born about five billion years ago from a giant gaseous cloud mostly made of hydrogen. The cloud contracted because of its gravitational pull, and temperature and pressure became so high that the nuclear fusion reactions started. But these reactions slowly drain the available hydrogen reservoir. In another five billion years, the core of our Sun will run out of fuel as its hydrogen will have been consumed to form helium atoms. The nuclear reactions will stop.

There will still be some hydrogen around the core though. So when pressure and temperature increase again, this hydrogen will start to fuse, and the Sun will become even more luminous than before! Such a star is called a red giant star because its outer layers expand dramatically. At that stage, the Sun will be so big it will engulf the Earth's orbit!

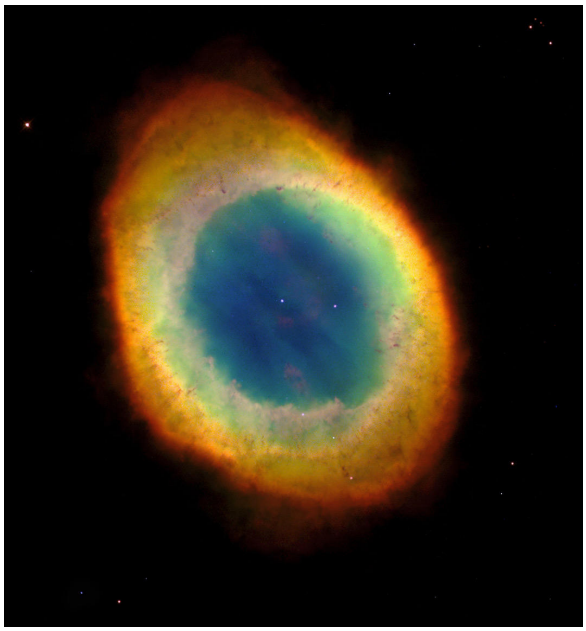

The Ring Nebula as seen by the Hubble Space Telescope. CREDIT: THE HUBBLE HERITAGE TEAM (AURA/STSCL/NASA)

Eventually, the outer layers of the Sun will be ejected away from the dense core and all nuclear fusion reactions will stop. The exposed core will slowly cool down without the power supply of the nuclear reactions. Such a remnant is called a white dwarf, and there is notably a faint white dwarf in the middle of the Ring Nebula. The Ring Nebula is the glowing remain of a star like our Sun. The outer layers of the star were ejected four thousand years ago, and their fading red glow is now slowly moving away from the white dwarf. The stellar remnant still emits some ultraviolet light, which bathes the central area of the nebula. This is how the future of our Sun may look like.

Life on Earth will become impossible during the last stages of our Sun's lifetime. But there is still a lot of time before that and humanity will hopefully have moved away from the vicinity of the Sun by then!

(Jonathan Freundlich is a PhD student at the Paris Observatory, in France, working on star formation and galaxy evolution.

He can be reached at jonathan.freundlich@obspm.fr)

ASTROPHYSICAL SERIES

- Thermonuclear weapons use uncontrolled but powerful hydrogen fusion reactions like in the stars
- The international ITER project currently being built in the South of France aims at achieving controlled nuclear fusion for the first time. Its completion is expected around 2027
- At the end of the red giant phase of the Sun, nuclear fusion reactions should produce carbon and oxygen atoms from the helium of the core. Heavier elements only form in more massive stars
- Stars much more massive than the Sun may explode as supernovae at the end of their lives and result in neutron stars and black holes instead of white dwarfs

The grand finale of a giant star

Jonathan Freundlich

During the summer of the year 1054, Chinese and Japanese chroniclers recorded the apparition of a new object in the sky. It looked like a very bright star, so bright it was even visible during daytime for a couple of weeks. Its luminosity then slowly faded, although the new object remained visible to the naked eye during the night for about two years. Some American Indians carved the event in stone, while a doctor from Baghdad saw it as bad omen and related it to the plague epidemics that had burst in Constantinople and Cairo. In this epoch, people often tried to interpret astronomical events in the light of their own history.

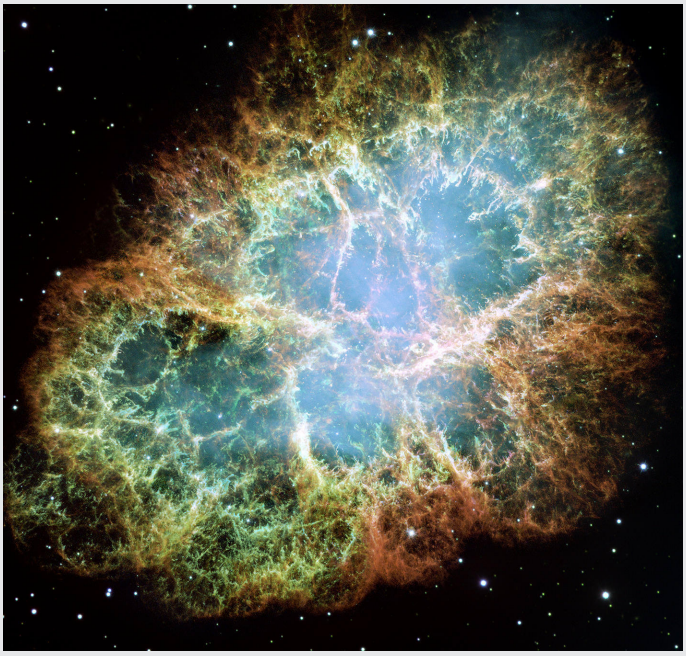

BLAST FROM THE PAST *The Crab Nebula as seen by the Hubble Space Telescope (false colours).* CREDIT: NASA, ESA, J. HESTER AND A. LOLL (ARIZONA STATE UNIVERSITY)

A cosmic explosion

If we follow the indications left by the Chinese chroniclers and point our telescopes where this object appeared to them in the sky, there is an amazing thing to see: the Crab Nebula. It looks like a huge bomb blast with an intricate inner structure, and it is indeed a blast. This is what remains of the 1054 supernova.

A supernova is when a giant star explodes toward the end of its life. The explosion is so luminous it can be as bright as a whole galaxy! The violent blast ejects most of the star's material at incredible speed and diffuses the gas in the surrounding medium. Although you won't see the expansion of the nebula in a single observation session because of the distance, you could clearly perceive it when comparing pictures separated by a few years.

The blast of a supernova disperses the chemical elements formed in the star all around it, which makes them available when new stars and planets form. Elements like carbon or iron can be formed during the lifetime of the star through nuclear fusion reactions in its core, but the formation of heavier elements requires more extreme conditions like those of a supernova explosion. For example, the lead, the gold and the uranium found on Earth might all have been formed during supernovae.

A lighthouse beyond comparison

While most of its gas was pushed away during the 1054 supernova, the core of the giant star that lead to the Crab Nebula compressed dramatically. What remains now is almost entirely composed of neutrons, which makes it incredibly dense. Such a stellar remnant is called a neutron star. At the center of the Crab Nebula, the neutron star has approximately the same mass as our Sun, but just the size of a middle-sized city! The gravitational force at its surface is billions of times greater than on Earth and we would thus be totally crushed if we were to approach it too closely.

Besides, this neutron star rotates extremely rapidly, with about thirty revolutions per second, and its magnetic field is just colossal. Two narrow beams of radiation are emitted from its magnetic poles and rotate with the stellar remnant, like beams of a lighthouse sweeping the vastness of the Universe. One of these beams hit the Earth at each revolution, so the neutron star appears to pulse thirty times per second. Such an object is also called a pulsar.

Various supernovae have been recorded in the course of human history, either belonging to our Milky Way like the Crab Nebula, or belonging to other galaxies. But no supernova has ever been observed in our Milky Way since the invention of the telescope. Astrophysicists are eagerly waiting for such an astounding event to happen, and I hope that we will be able to witness one during our lifetime!

(Jonathan Freundlich is a PhD student at the Paris Observatory, in France, working on star formation and galaxy evolution. He can be reached at **jonathan.freundlich@obspm.fr**)

ASTROPHYSICAL SERIES

- No clear records of the 1054 supernova have been found in Indian and European medieval sources so far, although it must have been visible from all the northern hemisphere.
- Supernovae were initially referred as *stella nova*, or new stars in Latin.
- Typical neutron stars have radiuses of about 10 km.
- The cores of the most massive stars can become black holes instead of neutron stars when they explode as a supernovae.

An irresistible attraction

There is something fascinating about Black holes. Perhaps it is their strong gravitational pull and elusiveness

Jonathan Freundlich

ASTROPHYSICAL SERIES

Black holes are among the most fascinating objects in the Universe. How would a journey towards a black hole look like?

The escape velocity

When you throw a ball up in the air, it always falls back down to the ground because of the Earth's gravitational attraction. If you throw the ball harder, it will get higher but will still fall down afterwards. The ball can't easily escape the Earth's gravity!

If you could throw the ball at an extremely high speed though, it would escape the Earth's gravitational attraction and continue its journey into outer space. The velocity required for that is called the escape velocity, and it is about 11 kilometers per second at the surface of the Earth. This is the speed space rockets have to reach in order to **liberate** themselves from the Earth's gravitational influence, and it requires a lot of energy. Have you ever seen how impressive rocket launches look?

If the Earth was more massive, its gravitational attraction would be stronger, your ball wouldn't go as high as usual, and it would require more energy to send something into outer space: the escape velocity would be higher and hence more difficult to reach. For extremely massive objects, the escape velocity could even be impossible to reach!

A black hole is an object which is so massive and so compact that its escape velocity is greater than the speed of light: as nothing can move faster than the speed of light, nothing can get out of a black hole. Even light. Any light emitted inside the black hole is dragged back by its strong gravitational attraction and thus never reaches observers situated outside. A black hole looks black because there is simply no light coming out of it.

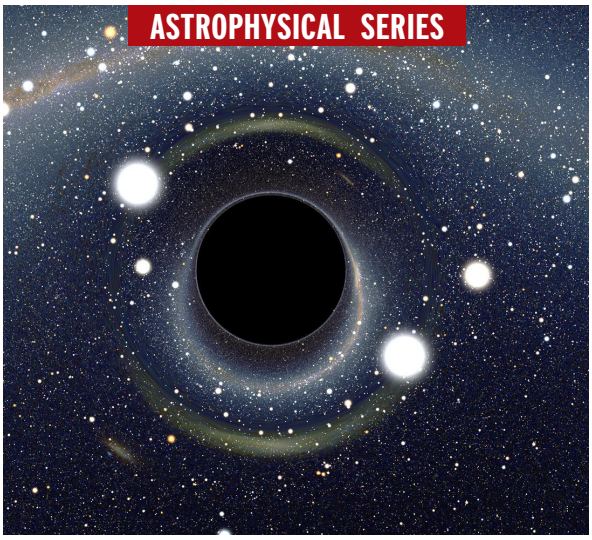

IN THE DARK *A computer generated image of a black hole showing the visual distortions it would cause if you were to approach it.* CREDIT: ALAIN RIAZUELO, IAP/UPMC/CNRS.

- The contracting core of a very big star can become a black hole during its explosion as a supernova, but our Sun will never turn into a black hole because it is far from massive enough.
- Gravity around a black hole is so strong it would stretch you and tear you apart as you get closer.
- A black hole disrupts the structure of space-time itself, which would cause unusual visual distortions when you approach it.
- Time flows differently near the event horizon of a black hole: you would age much slower there than on Earth, and a few minutes spent there could mean years on Earth if you come back.

A journey into a black hole

A black hole is like a huge maelstrom that attracts the surrounding matter, so moving towards it would be a bit like swimming towards a huge waterfall. Gravity would pull you towards the black hole as the water flow would towards the fall. If you are far away, you can still swim back and get away. But as you get nearer, the current gets faster and faster, up to a point where there is no turning back anymore: you are **doomed** to fall with the flow. For a black hole, this point of no return is called the event horizon and this is where the escape velocity is equal to the speed of light. But although crossing the event horizon of a black hole would mark a turning point in your life, as you wouldn't be able to travel back anymore nor communicate with the outside world, you wouldn't necessarily notice anything special on the moment as you would still seem to fall towards an endless black pit.

But what is exactly inside a black hole? There are many **speculations** about it, but no decisive answers yet: as no light ever comes out, we can't see anything beyond the event horizon. Are black holes gateways to different places or even different universes? Is all their mass concentrated in a single point in space? Or are they just extreme astrophysical objects denser than neutron stars? All of these are open questions, as we still lack a unified model to describe the inside of black holes.

Nevertheless, it is possible to observe how gravity affects stars and gas around them, and this is how we know they do exist. There is notably a supermassive black hole at the center of our Milky Way, as in most other galaxies. It is named Sagittarius A* (to be pronounced *"Sagittarius A-star"*) and should weigh as much as four million suns. As in a whirlpool, stars orbit extremely fast around it, in an **irresistible** cosmic dance!

(Jonathan Freundlich is a PhD student at the Paris Observatory, in France, working on star formation and galaxy evolution. He can be reached at jonathan.freundlich@obspm.fr)

A glimpse at the formation of our Solar System

The remarkable story of how the Sun, the planets and other celestial objects that make up the solar system came to be

Emmanuel Jacquet &
Jonathan Freundlich

ASTROPHYSICAL SERIES

The history of our Solar System probably started 4.57 billion years ago when a fragment of a huge cloud of gas and dust started to contract because of its own gravity, somewhere in **interstellar** space. While contracting, it became denser and denser, until its core became a star – our Sun. But not all the matter went straight to the Sun...

A rotating disk

Rotation plays an important role in the formation of a planetary system like our Solar System. In all likelihood, our parent cloud fragment had some rotation, and this rotation accelerated upon contraction. Have you ever tried spinning on a rotating chair? If you do so (but be careful!), you could notice that you would spin faster when you pull your arms in close to your chest than when you stretch them out wide. It would work even better if you held something heavy in your hands, but in all cases, the more you would curl up, the faster you would spin. In the same way, when our parent cloud fragment curled up, it started to spin faster. As a result, the increased rotation flattened it into a disk, centered on the Sun. Such a disk made of gas and dust is known as a protoplanetary disk, as this is where planets can form. All planets and most other celestial bodies in the Solar System indeed orbit approximately in the same plane, which corresponds to the plane of the former protoplanetary disk.

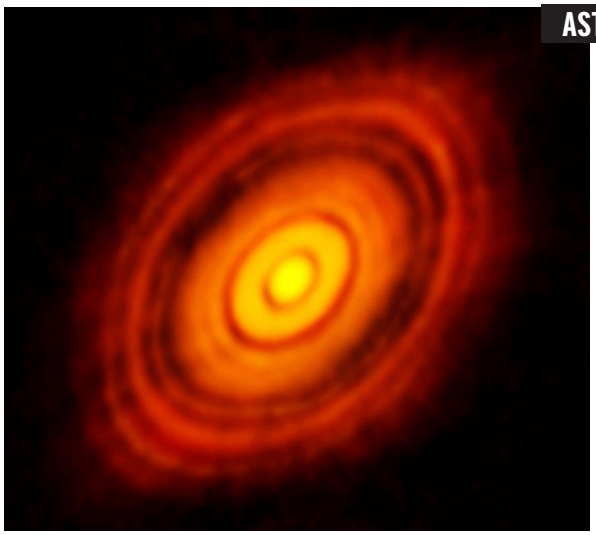

IT ALL STARTED HERE *Solar system in formation: the HL Tauri protoplanetary disk as seen by the ALMA telescope.*
PHOTO: ALMA (ESO/NAOJ/NRAO)

From dust grains to planets

Our protoplanetary disk probably lasted "only" a few million years before being absorbed or blown away by the Sun, but most of the planet formation could be completed during that time. Our parent cloud was mostly made of gaseous hydrogen and helium, which are the main constituents of the Universe, but also included small dust grains. These grains are made of elements originating from stars and are ten to hundred times smaller than the dust particles you can find in your home. As these solids collided with each other, they grew until millimeter sizes and settled at the midplane of the disk. There, they could **coagulate** further to form asteroids (a kilometre to hundreds of kilometres in size), which in turn could merge in planet-sized objects, helped by their own gravitational attraction.

Temperatures varied across the disk, being higher closer to the Sun than further out. While water was gaseous in the inner regions, it was solid ice beyond a certain radius called the "snow line". Beyond this radius, the presence of ice with the stony material enhanced the growth of planets: planets formed below the snow line never exceeded the mass of the Earth, whereas outer planets reached ten times more, at which stage they even started to retain the **ambient** gas. This led to the formation of giant gas planets, among which Jupiter is the largest.

Although we still observe a clean separation between stone-dominated planets close to the Sun (Mercury, Venus, Earth, Mars) and giant planets further out (Jupiter, Saturn, Uranus, Neptune), some astrophysicists have hypothesized that the orbits of the giant planets changed significantly at different **epochs** in the history of the Solar System.

This would have had dramatic consequences, notably on the **flux** of asteroids near the inner planets. But nowadays, the planets are fortunately on rather stable orbits!

Emmanuel Jacquet is assistant professor at the French National Museum of Natural History in Paris, working on meteorites and the formation of the Solar System. Jonathan Freundlich is a PhD student at the Paris Observatory, in France, working on star formation and galaxy evolution. The authors can be reached at jonathan.freundlich@obspm.fr.

ALL ABOUT ALMA

- HL Tauri is 450 light-years from Earth and the star is less than a million years old, which makes it pretty young by astronomical standards. The dark rings on the ALMA image may indicate the positions of planets under formation.
- ALMA is an array of telescopes located in the Atacama desert of Chile at 5000 metres altitude which observes the radio waves emitted by astrophysical objects such as stars and gas clouds. Each of its telescopes looks like a big satellite dish.
- The bigger a telescope is, the sharper its images are. ALMA dishes can be moved over distances up to 16 kilometres, making it one of the sharpest telescopes ever built.

Meteorites: witnesses of the solar system's birth

Emmanuel Jacquet & Jonathan Freundlich

Have you ever seen shooting stars **streaking** across a clear night sky? These flashes of light often disappear as fast as they appeared, in the blink of an eye... But they actually have nothing to do with stars! Shooting stars, or meteors, are small solid grains entering our atmosphere at high speeds. They are going so fast that the air around them heats up, makes them shine, and usually burns them up.

Fragments of asteroids

During its orbit around the Sun, the Earth is constantly bombarded by particles of all sizes, and **extraterrestrial** stones that make it to the ground are called meteorites. Videos of meteorite falls have allowed scientists to reconstruct the **trajectories** of these objects and to track their **provenance**: meteorites almost invariably come from a region between Mars and Jupiter named the "Main Asteroid Belt". Most of them are indeed fragments of asteroids.

Asteroids are like small planets, although often of irregular shapes. They are the left-overs of the formation of the bigger planets at the beginning of the Solar System.

The link between meteorites and asteroids was recently spectacularly confirmed by a Japanese probe which returned dust samples from a 600 meter-sized asteroid named Itokawa: these samples were found to be identical with one of the major groups of meteorites, thus proving that the meteorites belonging to this group and Itokawa derived from the fragmentation of the same asteroid.

A glimpse of the past

Most meteorites have undergone little change since their parent asteroid assembled. They thus give us a glimpse at the composition of the Solar System in its first million years. In fact, it is through primitive meteorites that scientists were able to determine the age of the Solar System with great precision: they obtained 4.568 billion years. Our Sun deserves a cheerful "happy birthday", right?

As they represent the original matter from which planets were built, **primitive** meteorites are made of the same chemical elements as the Earth (iron, magnesium, silicon, oxygen, etc.). Yet, they contain distinctive inclusions, the most conspicuous among them being millimeter-sized round grains called chondrules. The origin of chondrules is still a mystery, although it seems they were formed as molten droplets which solidified before being incorporated in the asteroid. The temperature must have been very high to melt the minerals they contain, but the nature of the heating events that lead to their formation is still controversial.

Asteroids have not always been cold **inert** bodies. Like the Earth, they were originally heated up by **spontaneous** radioactive **disintegration** of atoms within them, as occurs in a nuclear power plant. Some of them were heated so intensely that they experienced a large degree of melting, which erased the primitive structures such as the chondrules. In these asteroids, the dense metals separated from the stony material to form a metallic core overlaid by a stony mantle and crust. Some meteorites are fragments of these "differentiated" asteroids.

Meteorites originating from their cores are fully metallic, whereas fragments from the mantle are metal-free and quite similar to terrestrial igneous rocks. In fact, the Earth underwent the very same differentiation between a metallic core and a rocky crust. So, when you hold an iron meteorite, which is a piece from a shattered celestial body, it is almost as though you were touching the deepest regions of our planet!

Emmanuel Jacquet is assistant professor at the French National Museum of Natural History in Paris, working on meteorites and the formation of the Solar System. Jonathan Freundlich is a PhD student at the Paris Observatory, in France, working on star formation and galaxy evolution. The authors can be reached at jonathan.freundlich@obspm.fr.

SHOOTING STAR *A spectacular meteor fall painted by Frederic Edwin Church in 1860.* COLLECTION OF JUDITH FILENBAUM HERNSTADT.

- To determine the age of the Solar System, scientists can use radioactive elements in meteorites. The amount of such an element decreases with time, so measuring its abundance yields the age of the meteorite.
- The name "chondrule" comes from the Greek "chondros", which means "small grain". A meteorite with chondrules is called a chondrite.
- Igneous rocks are rocks formed from solidified magma or lava, such as basalt or granite.
- An impressive meteor fall such took place recently in Chelyabinsk, Russia. You can easily find videos of the event on the Internet.

Analytical calculations

APPENDIX E

Detailed calculations for Chapter 3

E.1 Expressions of the enthalpy

E.1.1 For a polytropic equation of state

We initially assumed a polytropic equation of state $p_0 = C\rho_0^\gamma$, where C is a positive constant and γ the adiabatic index. The speed of sound is defined by $c_0^2 = \partial p_0/\partial\rho_0 = \gamma C\rho_0^{\gamma-1} = \gamma p_0/\rho_0$, so that when $\gamma \neq 1$, the enthalpy can be written as:

$$h_0 = \frac{\gamma}{\gamma-1} C\rho_0^{\gamma-1} = \frac{c_0^2}{\gamma-1}. \tag{E.1}$$

In the case of an isothermal equation of state ($\gamma = 1$), the speed of sound is constant and entirely fixed by temperature. The isothermal equation of state can be written $p_0 = c_0^2\ \rho_0$ and the enthalpy yields:

$$h_0 = c_0^2\ \ln\rho_0. \tag{E.2}$$

In both cases, the first order perturbation of the enthalpy can be written as:

$$h_1 = c_0^2\ \frac{\rho_1}{\rho_0}. \tag{E.3}$$

Indeed, the perturbed fluid remains polytropic, so up to the first order in ρ_1/ρ_0, when $\gamma \neq 1$,

$$h_0 + h_1 = \frac{\gamma C}{\gamma-1}\ (\rho_0+\rho_1)^{\gamma-1} = h_0 + \gamma C\ \rho_0^{\gamma-2}\rho_1 = h_0 + c_0^2\frac{\rho_1}{\rho_0}$$

and when $\gamma = 1$,

$$h_0 + h_1 = c_0^2\ \ln(\rho_0+\rho_1) = h_0 + c_0^2\frac{\rho_1}{\rho_0}.$$

E.1.2 For a barotropic equation of state

The above relation for the first order enthalpy perturbation is actually more general. For a barotropic fluid in which the pressure is only a function of the density, with $p = p(\rho)$ and $h = h(\rho)$, the enthalpy is defined by

$$dh = \frac{1}{\rho} dp. \tag{E.4}$$

The perturbed enthalpy can thus be written up to the first order

$$h_0 + h_1 = h(\rho_0 + \rho_1) = h(\rho_0) + \left(\frac{dh}{d\rho}\right)_{\rho_0} \rho_1 \tag{E.5}$$

Consequently,

$$\begin{aligned} h_1 &= \left(\frac{dh}{d\rho}\right)_{\rho_0} \rho_1 \\ &= \left(\frac{dh}{dp}\right)_{p(\rho_0)} \left(\frac{dp}{d\rho}\right)_{\rho_0} \rho_1 \\ &= \frac{1}{\rho_0} \left(\frac{dp}{d\rho}\right)_{\rho_0} \rho_1 \\ h_1 &= \frac{1}{\rho_0} c_0^2 \, \rho_1. \end{aligned} \tag{E.6}$$

E.2 Discriminant of the dispersion relation

E.2.1 The discriminant is always positive

The dimensionless dispersion relation introduced in section 3.2.2 (Eq. (3.29)) involves two dimensionless quantities, α and β. Considering that

$$\alpha = -\left(\frac{\omega_0^2 k^2}{\kappa^2 k_z^2}\beta + \frac{\kappa^2}{\omega_0^2}\right) \tag{E.7}$$

the discriminant can be written as a second order polynomial expression in β:

$$\Delta = \alpha^2 - 4\beta = \frac{\omega_0^4 k^4}{\kappa^4 k_z^4}\beta^2 + 2\frac{k_R^2 - k_z^2}{k_z^2}\beta + \frac{\kappa^4}{\omega_0^4}. \tag{E.8}$$

In turn, the discriminant Δ' of this latter polynomial expression is always negative:

$$\Delta' = \left(\frac{k_R^2 - k_z^2}{k_z^2}\right)^2 - \frac{k^4}{k_z^4} = -4\left(\frac{k_R}{k_z}\right)^2. \tag{E.9}$$

Consequently, as β is a real quantity, the discriminant Δ is always positive and

$$x_\pm^2 = \frac{-\alpha \pm \sqrt{\Delta}}{2} \tag{E.10}$$

always real.

E.2.2 Two roots are real

There are four solutions for x, which can be either real or with a non-zero imaginary part, depending on the sign of $-\alpha \pm \sqrt{\Delta}$. But out of these four solutions, two are always real. Indeed, $-\alpha + \sqrt{\Delta}$ is always positive:

- If $\alpha \leqslant 0$, $-\alpha + \sqrt{\Delta} \geqslant 0$.

- If $\alpha > 0$, β has to be negative because of Eq. (E.7), so $\Delta = \alpha^2 - 4\beta > \alpha^2$ and $-\alpha + \sqrt{\Delta} > 0$.

E.2.3 A condition for stability

All roots are real and the system is stable when and only when $-\alpha - \sqrt{\Delta}$ is also positive, i.e., when $\alpha \leqslant 0$ and $|\alpha| \geqslant \sqrt{\Delta}$. These two conditions can be expressed as conditions on the total wavenumber k:

$$\begin{aligned} \alpha \leqslant 0 \quad &\Leftrightarrow \quad \frac{\rho_0}{\rho_c} - \frac{c_0^2 k^2}{\omega_0^2} - \frac{\kappa^2}{\omega_0^2} \leqslant 0 \\ &\Leftrightarrow \quad k^2 \geqslant \frac{4\pi G\rho_0 - \kappa^2}{c_0^2} \end{aligned} \tag{E.11}$$

$$\begin{aligned} |\alpha| \geqslant \sqrt{\Delta} \quad &\Leftrightarrow \quad \alpha^2 \geqslant \alpha^2 - 4\beta \\ &\Leftrightarrow \quad \beta \geqslant 0 \\ &\Leftrightarrow \quad \frac{c_0^2}{\omega_0^2} - \frac{1}{k^2}\frac{\rho_0}{\rho_c} \geqslant 0 \\ &\Leftrightarrow \quad k^2 \geqslant \frac{4\pi G\rho_0}{c_0^2}. \end{aligned} \tag{E.12}$$

The second condition encompasses the first one, and is analogous to the Jeans criterion. All roots are thus real and the system is stable for $k \geqslant k_{\rm crit}$, with $k_{\rm crit}^2 = 4\pi G\rho_0/c_0^2$.

E.3 About the fastest growing mode

E.3.1 A parametric expression for the fastest growing mode

At a given radius R and for a given k_R, the quantity $x_-^2 = -(\alpha + \sqrt{\Delta})/2$ introduced in section 3.2.2 is minimal when

$$\begin{aligned}
\frac{\partial x_-^2}{\partial k_z} = 0 \quad &\Leftrightarrow \quad \frac{\partial}{\partial k_z}\left(\alpha + \sqrt{\Delta}\right) = 0 \\
&\Leftrightarrow \quad \left(1 + \frac{\alpha}{\sqrt{\Delta}}\right)\frac{\partial \alpha}{\partial k_z} - \frac{2}{\sqrt{\Delta}}\frac{\partial \beta}{\partial k_z} = 0 \\
&\Leftrightarrow \quad k_z\left(1 + \frac{\alpha}{\sqrt{\Delta}} + \frac{2\kappa^2}{c_0^2\sqrt{\Delta}}\left(\frac{c_0^2}{\omega_0^2} - \frac{\rho_0}{\rho_c}\frac{k_R^2}{k^4}\right)\right) = 0 \\
&\Leftrightarrow \quad k_z = 0 \text{ or } \sqrt{\Delta} = -\alpha - 2\frac{\kappa^2}{c_0^2}\left(\frac{c_0^2}{\omega_0^2} - \frac{\rho_0}{\rho_c}\frac{k_R^2}{k^4}\right).
\end{aligned} \tag{E.13}$$

When $k_z \neq 0$, the latter condition yields

$$\begin{cases}
\alpha + 2\dfrac{\kappa^2}{c_0^2}\left(\dfrac{c_0^2}{\omega_0^2} - \dfrac{\rho_0}{\rho_c}\dfrac{k_R^2}{k^4}\right) \leqslant 0 \\
\text{and} \\
\Delta = \alpha^2 - 4\beta = \left(\alpha + 2\dfrac{\kappa^2}{c_0^2}\left(\dfrac{c_0^2}{\omega_0^2} - \dfrac{\rho_0}{\rho_c}\dfrac{k_R^2}{k^4}\right)\right)^2.
\end{cases} \tag{E.14}$$

Using the expressions of α and β and developing the intermediate expressions, the second equation leads to the following parametric equation describing the fastest growing mode:

$$\left(\frac{\rho_0}{\rho_c}\right)^2 \frac{k_R^2}{k^2} = \frac{c_0^2}{\kappa^2}k^2\left[\left(\frac{c_0^2}{\omega_0^2}k^2 - \frac{\rho_0}{\rho_c}\right)^2 + \frac{\rho_0}{\rho_c}\frac{\kappa^2}{\omega_0^2}\right]. \tag{E.15}$$

E.3.2 Intersection with the line $k_z = k_R$

In order to characterize the shape of the perturbations, it would be of interest to determine the intersection of the curve describing the fastest growing mode with the line $k_z = k_R$. At the intersection, $k^2 = 2k_R^2$ and k_R satisfies

$$\frac{1}{2}\left(\frac{\rho_0}{\rho_c}\right)^2 = \frac{c_0^2}{\kappa^2}2k_R^2\left[\left(\frac{c_0^2}{\omega_0^2}2k_R^2 - \frac{\rho_0}{\rho_c}\right)^2 + \frac{\rho_0}{\rho_c}\frac{\kappa^2}{\omega_0^2}\right]. \tag{E.16}$$

It reduces to the following polynomial expression, which can be solved numerically:

$$\left(\frac{k_R}{k_0}\right)^6 - \frac{\rho_0}{\rho_c}\left(\frac{k_R}{k_0}\right)^4 + \frac{1}{4}\frac{\rho_0}{\rho_c}\left(\frac{\rho_0}{\rho_c} + \frac{\kappa^2}{\omega_0^2}\right)\left(\frac{k_R}{k_0}\right)^2 - \frac{1}{16}\left(\frac{\rho_0}{\rho_c}\right)^2\frac{\kappa^2}{\omega_0^2} = 0 \tag{E.17}$$

where $k_0 = \omega_0/c_0$ is a characteristic wavenumber depending on the position R through c_0.

E.4 Dispersion relation without WKB assumption

E.4.1 Full dispersion relation

Without the local WKB assumption $k_R R \gg 1$, additional terms have to be considered in the different equations (in bold blue) :

$$\begin{cases} \omega v_{1R} - 2i\Omega_0 v_{1\theta} = k_R \dfrac{c_0^2}{\rho_0}\rho_1 \boldsymbol{-i\rho_1 \dfrac{\partial}{\partial R}\left(\dfrac{c_0^2}{\rho_0}\right)} + k_R\Phi_1 \\ \omega v_{1\theta} - 2iBv_{1R} = 0 \\ \omega v_{1z} = k_z \dfrac{c_0^2}{\rho_0}\rho_1 + k_z\Phi_1 \\ \omega\rho_1 - \rho_0 k_r v_{1R} \boldsymbol{+iv_{1R}\dfrac{1}{R}\dfrac{\partial}{\partial R}(R\rho_0)} - k_z\rho_0 v_{1z} = 0 \\ -k_R^2\Phi_1 \boldsymbol{+i\dfrac{k_R}{R}\Phi_1} - k_z^2\Phi_1 = 4\pi G\rho_1. \end{cases} \tag{E.18}$$

Combining these equations as in section 3.2.1, we obtain:

$$v_{1R} = \frac{\omega}{\omega^2-\kappa^2}\left(k_R\Phi_1 + \left(k_R\frac{c_0^2}{\rho_0} \boldsymbol{-i\frac{\partial}{\partial R}\left(\frac{c_0^2}{\rho_0}\right)}\right)\rho_1\right) \tag{E.19}$$

$$\begin{aligned} \omega\rho_1 + \left(-\rho_0 k_R \boldsymbol{+i\frac{1}{R}\frac{\partial}{\partial R}(R\rho_0)}\right)\frac{\omega}{\omega^2-\kappa^2}\left(k_R\Phi_1 + \left(k_R\frac{c_0^2}{\rho_0} \boldsymbol{-i\frac{\partial}{\partial R}\left(\frac{c_0^2}{\rho_0}\right)}\right)\rho_1\right) \\ -\frac{\rho_0 k_z^2}{\omega}\left(\frac{c_0^2}{\rho_0}\rho_1 + \Phi_1\right) = 0 \end{aligned} \tag{E.20}$$

$$\begin{aligned} \left(1 - \frac{c_0^2k_R^2}{\omega^2-\kappa^2} - \frac{c_0^2k_z^2}{\omega^2} \boldsymbol{+\frac{1}{\omega^2-\kappa^2}\left(i\frac{k_R}{R}\frac{\partial}{\partial R}\left(Rc_0^2\right) + \frac{1}{R}\frac{\partial}{\partial R}(R\rho_0)\frac{\partial}{\partial R}\left(\frac{c_0^2}{\rho_0}\right)\right)}\right)\rho_1 \\ = \left(\frac{k_R^2}{\omega^2-\kappa^2} + \frac{k_z^2}{\omega^2} \boldsymbol{-i\frac{k_R}{\omega^2-\kappa^2}\frac{1}{R\rho_0}\frac{\partial}{\partial R}(R\rho_0)}\right)\rho_0\Phi_1, \end{aligned} \tag{E.21}$$

which yields when introducing Poisson's equation and $k^2 = k_R^2 + k_z^2$

$$\begin{aligned} 1 - \frac{c_0^2k_R^2}{\omega^2-\kappa^2} - \frac{c_0^2k_z^2}{\omega^2} \boldsymbol{+\frac{1}{\omega^2-\kappa^2}\left(i\frac{k_R}{R}\frac{\partial}{\partial R}\left(Rc_0^2\right) + \frac{1}{R}\frac{\partial}{\partial R}(R\rho_0)\frac{\partial}{\partial R}\left(\frac{c_0^2}{\rho_0}\right)\right)} \\ = -\frac{4\pi G\rho_0}{k^2 \boldsymbol{-i\frac{k_R}{R}}}\left(\frac{k_R^2}{\omega^2-\kappa^2} + \frac{k_z^2}{\omega^2} \boldsymbol{-i\frac{k_R}{\omega^2-\kappa^2}\frac{1}{R\rho_0}\frac{\partial}{\partial R}(R\rho_0)}\right) \end{aligned} \tag{E.22}$$

$$\begin{aligned} \omega^2\left(\omega^2-\kappa^2\right) - \omega^2c_0^2k_R^2 - \left(\omega^2-\kappa^2\right)c_0^2k_z^2 \boldsymbol{+\omega^2\left(i\frac{k_R}{R}\frac{\partial}{\partial R}\left(rc_0^2\right) + \frac{1}{R}\frac{\partial}{\partial R}(R\rho_0)\frac{\partial}{\partial R}\left(\frac{c_0^2}{\rho_0}\right)\right)} \\ = -\frac{4\pi G\rho_0}{k^2 \boldsymbol{-i\frac{k_R}{R}}}\left(k_R^2\omega^2 + k_z^2\left(\omega^2-\kappa^2\right) \boldsymbol{-ik_R\omega^2\frac{1}{R\rho_0}\frac{\partial}{\partial R}(R\rho_0)}\right) \end{aligned} \tag{E.23}$$

$$\omega^4+\omega^2\left(-\kappa^2-c_0^2k_R^2-c_0^2k_z^2+i\frac{k_R}{R}\frac{\partial}{\partial R}\left(Rc_0^2\right)+\frac{1}{R}\frac{\partial}{\partial R}\left(R\rho_0\right)\frac{\partial}{\partial R}\left(\frac{c_0^2}{\rho_0}\right)\right.$$
$$\left.+\frac{4\pi G\rho_0}{k^2-i\frac{k_R}{R}}\left(k^2-ik_R\frac{1}{R\rho_0}\frac{\partial}{\partial R}\left(R\rho_0\right)\right)\right)+k_z^2\kappa^2\left(c_0^2-\frac{4\pi G\rho_0}{k^2-i\frac{k_R}{R}}\right)=0. \tag{E.24}$$

Noticing that

$$\frac{1}{k^2-i\frac{k_R}{R}}=\frac{1}{k^2}\left(1+i\frac{\frac{k_R}{R}}{k^2-i\frac{k_R}{R}}\right), \tag{E.25}$$

we finally obtain the most general expression for the dispersion relation:

$$\omega^4+\omega^2\left[4\pi G\rho_0\left(1-i\frac{k_R}{k^2}\frac{1}{R\rho_0}\frac{\partial}{\partial R}\left(R\rho_0\right)\right)\left(1+i\frac{\frac{k_R}{R}}{k^2-i\frac{k_R}{R}}\right)\right.$$
$$\left.-c_0^2k^2-\kappa^2+i\frac{k_R}{R}\frac{\partial}{\partial R}\left(Rc_0^2\right)+\frac{1}{R}\frac{\partial}{\partial R}\left(R\rho_0\right)\frac{\partial}{\partial R}\left(\frac{c_0^2}{\rho_0}\right)\right]$$
$$+k_z^2\kappa^2\left(c_0^2-\frac{4\pi G\rho_0}{k^2}\left(1+i\frac{\frac{k_R}{R}}{k^2-i\frac{k_R}{R}}\right)\right)=0. \tag{E.26}$$

E.4.2 Dispersion relation without rotation

When there is no rotation, i.e., when $\kappa^2=0$, Eq. E.26 becomes

$$\omega^2=-4\pi G\rho_0\frac{k^2}{k^2-i\frac{k_R}{R}}\left[1-i\frac{k_R}{k^2}\left(\frac{1}{R}+\frac{1}{\rho_0}\frac{\partial\rho_0}{\partial R}\right)\right]+c_0^2k^2$$
$$-ik_R\left[\frac{c_0^2}{R}+\frac{\partial c_0^2}{\partial R}\right]-\left[\frac{1}{R}+\frac{1}{\rho_0}\frac{\partial\rho_0}{\partial R}\right]\left[\frac{\partial c_0^2}{\partial R}-c_0^2\frac{1}{\rho_0}\frac{\partial\rho_0}{\partial R}\right]. \tag{E.27}$$

E.5 Hydrostatic equilibrium of Plummer-like filaments

E.5.1 The isothermal case

The case of an isothermal self-gravitating cylinder has been considered by Ostriker (1964b). Its density profile yields

$$\rho_0(R)=\rho_c\frac{1}{\left(1+\left(\frac{R}{R_0}\right)^2\right)^2} \tag{E.28}$$

with ρ_c the central density and $R_0 = c_0\sqrt{8}/\sqrt{4\pi G\rho_c}$. The expression of the gravitational potential can be recovered from Poisson's equation as follow:

$$\Delta\Phi_0 = 4\pi G\rho_0 \tag{E.29}$$

$$\frac{1}{R}\frac{d}{dR}\left(R\frac{d\Phi_0}{dR}\right) = 4\pi G\rho_c \frac{1}{\left(1+\left(\frac{R}{R_0}\right)^2\right)^2} \tag{E.30}$$

$$R\frac{d\Phi_0}{dR} = -2\pi G\rho_c R_0^2\left(\frac{1}{1+\left(\frac{R}{R_0}\right)^2} + C\right) \tag{E.31}$$

$$\frac{d\Phi_0}{dR} = -2\pi G\rho_c R_0^2\left(\frac{1}{R} - \frac{\frac{R}{R_0^2}}{1+\left(\frac{R}{R_0}\right)^2} + \frac{C}{R}\right) \tag{E.32}$$

$$\Phi_0 = \pi G\rho_c R_0^2\left(\ln\left(1+\left(\frac{R}{R_0}\right)^2\right) - 2\,(1+C)\ln\left(\frac{R}{R_0}\right) + C'\right). \tag{E.33}$$

C and C' are real integration constants. In order to guarantee a finite potential at $R = 0$, we have to set $1 + C = 0$, and we can arbitrarily choose $C' = 0$. The expression of the potential thus finally yields

$$\Phi_0 = \pi G\rho_c r_0^2\,\ln\left(1+\left(\frac{R}{R_0}\right)^2\right). \tag{E.34}$$

E.5.2 Plummer-like profile with $p \neq 1$

For a more general Plummer-like density profile

$$\rho_0(R) = \rho_c \frac{1}{\left(1+\left(\frac{R}{R_0}\right)^2\right)^p} \tag{E.35}$$

with $p \neq 1$, Poisson's equation yields

$$\frac{1}{R}\frac{d}{dR}\left(R\frac{d\Phi_0}{dR}\right) = 4\pi G\rho_c \frac{1}{\left(1+\left(\frac{R}{R_0}\right)^2\right)^p} \tag{E.36}$$

$$R\frac{d\Phi_0}{dR} = -2\pi G\rho_c R_0^2 \, \frac{1}{p-1}\left(\frac{1}{\left(1+\left(\frac{R}{R_0}\right)^2\right)^{p-1}} + C\right) \tag{E.37}$$

$$\frac{d\Phi_0}{dR} = -\frac{2\pi G\rho_c R_0^2}{p-1}\left(\frac{1}{R\left(1+\left(\frac{R}{R_0}\right)^2\right)^{p-1}} + \frac{C}{R}\right). \tag{E.38}$$

As the force shouldn't diverge in $R = 0$, the integration constant is $C = -1$ and the gravitational force is finally

$$\frac{d\Phi_0}{dR} = \frac{2\pi G\rho_c R_0^2}{p-1}\frac{1}{R}\left(1 - \frac{1}{\left(1+\left(\frac{R}{R_0}\right)^2\right)^{p-1}}\right). \tag{E.39}$$

E.5.3 Plummer-like profile with $p = 1$

When $p = 1$, Poisson's equation similarly yields

$$\frac{1}{R}\frac{d}{dR}\left(R\frac{d\Phi_0}{dR}\right) = 4\pi G\rho_c \frac{1}{1+\left(\frac{R}{R_0}\right)^2} \tag{E.40}$$

$$R\frac{d\Phi_0}{dR} = 2\pi G\rho_c R_0^2 \, \left(\ln\left(1+\left(\frac{R}{R_0}\right)^2\right) + C\right) \tag{E.41}$$

$$\frac{d\Phi_0}{dR} = 2\pi G\rho_c R_0^2 \, \left(\frac{1}{R}\ln\left(1+\left(\frac{R}{R_0}\right)^2\right) + \frac{C}{R}\right). \tag{E.42}$$

A finite force in $R = 0$ requires $C = 0$, so that

$$\frac{d\Phi_0}{dR} = 2\pi G\rho_c R_0^2 \, \frac{1}{R}\ln\left(1+\left(\frac{R}{R_0}\right)^2\right). \tag{E.43}$$

APPENDIX F

Detailed calculations for Chapter 4

F.1 Analytical prerequisites

F.1.1 Radial Fourier transform

The Fourier transform of a radial function $F(\vec{r}) = F(r)$, with $r = |\vec{r}|$, is also radial and can be written $\hat{F}(\vec{k}) = \hat{F}(k)$ with $k = |\vec{k}|$. More precisely,

$$\hat{F}(k) \equiv \mathcal{TF}\left[F(r)\right] = \frac{1}{V}\int e^{-i\vec{k}.\vec{r}}\ F(r)\ d^3\vec{r} \tag{F.1}$$

and

$$F(r) \equiv \mathcal{TF}^{-1}\left[F(k)\right] = \frac{V}{(2\pi)^3}\int e^{i\vec{k}.\vec{r}}\ \hat{F}(k)\ d^3\vec{k}, \tag{F.2}$$

where the characteristic volume V guarantees that $F(r)$ and $\hat{F}(k)$ have the same dimension. Introducing $\vec{u}_z = \vec{k}/k$ and $\vec{k}.\vec{r} = k\ r\ cos\theta$, the three dimensional integral can be expressed as:

$$\begin{aligned}
\hat{F}(k) &= \frac{1}{V}\int_{r=0}^{+\infty}\int_{\theta=0}^{\pi}\int_{\phi=0}^{2\pi} e^{-ikrcos\theta}\ F(r)\ r^2\ \sin\theta\ d\theta\ dr\ d\phi \\
&= \frac{2\pi}{V}\int_{r=0}^{+\infty} F(r)\ r^2\ \left(\int_{\theta=0}^{\pi} e^{-ikrcos\theta}\ \sin\theta\ d\theta\right)\ dr \\
&= \frac{2\pi}{V}\int_{r=0}^{+\infty} F(r)\ r^2\ \left(\int_{-1}^{1} e^{ikrx}\ dx\right)\ dr \quad \text{with } x = -cos\theta \\
&= \frac{2\pi}{V}\int_{r=0}^{+\infty} F(r)\ r^2\ \left[\frac{e^{ikrx}}{ikr}\right]_{-1}^{1}\ dr \\
&= \frac{2\pi}{V}\int_{r=0}^{+\infty} F(r)\ r^2\ \left(\frac{e^{ikr}}{ikr} - \frac{e^{-ikr}}{ikr}\right)\ dr \\
&= \frac{2\pi}{V}\int_{r=0}^{+\infty} F(r)\ r^2\ \left(2\frac{\sin\ kr}{kr}\right)\ dr \\
\hat{F}(k) &= \frac{1}{V}\int_{r=0}^{+\infty} F(r)\ 4\pi\ r^2\frac{\sin\ kr}{kr}\ dr
\end{aligned} \tag{F.3}$$

F.1.2 Wiener-Khinchin theorem

The power spectrum of a stationary random process is the inverse Fourier transform of the autocorrelation function of this process. Using the fact that the Dirac delta function is the inverse Fourier transform of the unity distribution[1], this can be demonstrated as follow:

$$\begin{aligned}
\langle F(0)F(\vec{r})\rangle &= \frac{1}{V}\int F(\vec{x})^{\star}\ F(\vec{x}+\vec{r})\ d^3\vec{x} \\
&= \frac{1}{V}\int \left[\frac{V}{(2\pi)^3}\int \hat{F}(\vec{k})^{\star} e^{-i\vec{k}.\vec{r}}\ d^3\vec{k}\right]\left[\frac{V}{(2\pi)^3}\int \hat{F}(\vec{k'}) e^{i\vec{k'}.(\vec{x}+\vec{r})}\ d^3\vec{k'}\right] d^3\vec{x} \\
&= \frac{V}{(2\pi)^6}\iiint \hat{F}(\vec{k})^{\star}\ \hat{F}(\vec{k'})\ e^{i(\vec{k'}-\vec{k}).\vec{x}}\ e^{i\vec{k'}.\vec{r}}\ d^3\vec{k}\ d^3\vec{k'}\ d^3\vec{x} \\
&= \frac{V}{(2\pi)^3}\iint \hat{F}(\vec{k})^{\star}\ \hat{F}(\vec{k'})\left[\frac{1}{(2\pi)^3}\int e^{i(\vec{k'}-\vec{k}).\vec{x}}\ d^3\vec{x}\right] e^{i\vec{k'}.\vec{r}}\ d^3\vec{k}\ d^3\vec{k'} \\
&= \frac{V}{(2\pi)^3}\iint \hat{F}(\vec{k})^{\star}\ \hat{F}(\vec{k'})\ \delta_{\text{Dirac}}(\vec{k'}-\vec{k})\ e^{i\vec{k'}.\vec{r}}\ d^3\vec{k}\ d^3\vec{k'} \\
&= \frac{V}{(2\pi)^3}\int |\hat{F}(\vec{k})|^2\ e^{i\vec{k}.\vec{r}}\ d^3\vec{k} \\
\langle F(0)F(\vec{r})\rangle &= \mathcal{TF}^{-1}\left[|F(\vec{k})|^2\right].
\end{aligned} \tag{F.4}$$

F.1.3 Incomplete Gamma functions

The upper and lower incomplete Gamma functions are respectively defined as

$$\Gamma(s,x) = \int_x^{\infty} t^{s-1}e^{-t}dt \tag{F.5}$$

and

$$\gamma(s,x) = \int_0^{x} t^{s-1}e^{-t}dt. \tag{F.6}$$

These functions can be expressed as power series, and as such, developed into holomorphic functions of complex variables with the same properties. Their sum yields

$$\Gamma(s,x) + \gamma(s,x) = \int_0^{\infty} t^{s-1}e^{-t}dt \equiv \Gamma(s) \tag{F.7}$$

and the asymptotic behavior of the upper Gamma functions follows

$$\Gamma(s,x) \underset{|x|\to+\infty}{\sim} x^{s-1}e^{-x}. \tag{F.8}$$

Integrating by parts enables to express the following integrals in terms of other Gamma functions:

$$\int x^{b-1}\ \gamma(s,x)\ dx = \frac{1}{b}\left[x^b\gamma(s,x) + \Gamma(s+b,x)\right], \tag{F.9}$$

$$\int x^{b-1}\ \Gamma(s,x)\ dx = \frac{1}{b}\left[x^b\Gamma(s,x) - \Gamma(s+b,x)\right]. \tag{F.10}$$

[1] $\delta_{\text{Dirac}}(\vec{k}) = \dfrac{1}{(2\pi)^3}\displaystyle\int e^{i\vec{k}.\vec{x}}\ d^3\vec{x}$

F.1.4 Mean density of a NFW halo

The density profile of a NFW halo (Navarro et al., 1996b) is defined as

$$\rho(r) = \frac{\rho_0}{\frac{r}{R_s}\left(1+\frac{r}{R_s}\right)^2}, \tag{F.11}$$

where R_s is a characteristic radius and ρ_0 the characteristic density. In order to define a finite halo mass mathematically, it is necessary to introduce a cut-off radius R_{cut}, which is usually chosen to be the virial radius R_{vir} (cf. section 4.1.2, p. 133). The mass within a sphere of radius $R < R_{cut}$ for a NFW halo can be expressed from the density profile:

$$\begin{aligned}
M(R) &= \int_0^R \rho(r)\ 4\pi r^2\ dr \\
&= 4\pi\rho_c \int_0^R \frac{1}{\frac{r}{R_s}\left(1+\frac{r}{R_s}\right)^2}\ r^2\ dr \\
&= 4\pi\rho_c R_s^3 \int_0^{R/R_s} \frac{x}{(1+x)^2}\ dx \\
&= 4\pi\rho_c R_s^3 \int_0^{R/R_s} \left[\frac{1}{1+x} - \frac{1}{(1+x)^2}\right] dx \\
&= 4\pi\rho_c R_s^3 \left[\ln(1+x) + \frac{1}{1+x}\right]_0^{R/R_s} \\
&= 4\pi\rho_c R_s^3 \left(\ln\left(1+\frac{R}{R_s}\right) + \frac{1}{1+\frac{R}{R_s}} - 1\right) \\
M(R) &= 4\pi\rho_c R_s^3 \left(\ln\left(1+\frac{R}{R_s}\right) - \frac{\frac{R}{R_s}}{1+\frac{R}{R_s}}\right).
\end{aligned} \tag{F.12}$$

Introducing the concentration parameter $C = R_{vir}/R_s$, the total mass of the NFW halo within R_{vir} is thus

$$\mathrm{M_{tot}} = 4\pi\rho_c R_s^3 \left(\ln(1+C) - \frac{C}{1+C}\right), \tag{F.13}$$

and the associated mean density,

$$\rho_{mean} = \frac{\mathrm{M_{tot}}}{\frac{4\pi}{3}\mathrm{R_{vir}^3}} = 3\rho_c \frac{1}{C^3} \left(\ln(1+C) - \frac{C}{1+C}\right). \tag{F.14}$$

The mean density within a sphere of radius $R < R_{cut}$ is similarly

$$\begin{aligned}
\overline{\rho(R)} &= \frac{M(R)}{\frac{4\pi}{3}R^3} \\
&= 3\rho_c \left(\frac{R_s}{R}\right)^3 \left(\ln\left(1+\frac{R}{R_s}\right) - \frac{\frac{R}{R_s}}{1+\frac{R}{R_s}}\right) \\
&= \rho_{mean}\ C^3 \left(\frac{R_s}{R}\right)^3 \frac{\ln\left(1+\frac{R}{R_s}\right) - \frac{\frac{R}{R_s}}{1+\frac{R}{R_s}}}{\ln(1+C) - \frac{C}{1+C}} \\
\overline{\rho(R)} &= \rho_{mean} \left(\frac{R_{vir}}{R}\right)^3 \frac{\ln\left(1+\frac{R}{R_s}\right) - \frac{\frac{R}{R_s}}{1+\frac{R}{R_s}}}{\ln(1+C) - \frac{C}{1+C}}.
\end{aligned} \tag{F.15}$$

F.2 Force correlation function

F.2.1 Force deriving from the density perturbations

As indicated in section 4.3, we consider large scale fluctuations over a volume $V = d^3$ in a gaseous medium of average density ρ_0. The relative density contrast of the perturbations δ, the associated potential Φ and the force per unit mass $\vec{F}$ can be Fourier decomposed as

$$\delta(\vec{r}) = \frac{V}{(2\pi)^3} \int \delta_{\vec{k}}\ e^{i\vec{k}.\vec{r}}\ d^3\vec{k}. \tag{F.16}$$

$$\Phi(\vec{r}) = \frac{V}{(2\pi)^3} \int \Phi_{\vec{k}}\ e^{i\vec{k}.\vec{r}}\ d^3\vec{k}, \tag{F.17}$$

$$\vec{F}(\vec{r}) = \frac{V}{(2\pi)^3} \int \vec{F}_{\vec{k}}\ e^{i\vec{k}.\vec{r}}\ d^3\vec{k} \tag{F.18}$$

where V is the volume over which the perturbations exist. We assume power-law density fluctuations whose power spectrum is defined as

$$\mathcal{P}(k) = V\ \langle|\delta_{\vec{k}}|^2\rangle = VCk^{-n} \tag{F.19}$$

where C is a constant and n the characteristic exponent of the power-law. The components $\phi_{\vec{k}}$ and $\delta_{\vec{k}}$ are related via the Poisson equation $\nabla^2\Phi = 4\pi G\rho_0\delta$ as

$$\phi_{\vec{k}} = -4\pi G\rho_0\ k^{-2}\ \delta_{\vec{k}}, \tag{F.20}$$

while the definition of the force $\vec{F} = -\vec{\nabla}\Phi$ yields

$$\vec{F}_{\vec{k}} = 4\pi i\ G\rho_0\ \vec{k}\ k^{-2}\ \delta_{\vec{k}} \tag{F.21}$$

and

$$|\vec{F}_{\vec{k}}|^2 = (4\pi G\rho_0)^2\ \ k^{-2}\ |\delta_{\vec{k}}|^2. \tag{F.22}$$

F.2.2 Expressions of the force correlation function

Expression as an integral

The Wiener-Khinchin theorem (Eq. F.4) enables to write the force auto-correlation function $\langle F(0)F(\vec{r})\rangle$ as the inverse Fourier transform of the force power spectrum $|\vec{F}_{\vec{k}}|^2$:

$$\langle F(0)F(\vec{r})\rangle = \frac{V}{(2\pi)^3} \int |\vec{F}_{\vec{k}}|^2\ e^{i\vec{k}.\vec{r}}\ d^3\vec{k}. \tag{F.23}$$

Assuming mean isotropic fluctuations, this expression reduces to a radial Fourier transform as in Eq. F.3:

$$\langle F(0)F(r)\rangle = \frac{V}{(2\pi)^3}\int_0^\infty \langle|\vec{F}_{\vec{k}}|^2\rangle\ 4\pi k^2 \frac{\sin\ kr}{kr}\ dk. \tag{F.24}$$

The power-law power spectrum (Eq. F.19) and the expression of $|\vec{F}_{\vec{k}}|^2$ (Eq. F.22) now enable to determine the force auto-correlation function as an integral over k:

$$\begin{aligned}
\langle F(0)F(r)\rangle &= \frac{V}{(2\pi)^3}\int_0^\infty \left((4\pi G\rho_0)^2\ k^{-2}\ \langle|\delta_{\vec{k}}|^2\rangle\right)\ 4\pi k^2\frac{\sin\ kr}{kr}\ dk \\
&= 8V\left(G\rho_0\right)^2\int_0^\infty Ck^{-n}\frac{\sin\ kr}{kr}\ dk \\
&= \frac{8Cd^3\left(G\rho_0\right)^2}{r}\int_0^\infty \frac{\sin\ kr}{k^{n+1}}\ dk \\
\langle F(0)F(r)\rangle &= \frac{D}{r}\int_0^\infty \frac{\sin\ kr}{k^{n+1}}\ dk
\end{aligned}$$

with $D = 8Cd^3\left(G\rho_0\right)^2$. Assuming perturbations of scale between $\lambda_{min} = 2\pi/k_{max}$ and $\lambda_{max} = 2\pi/k_{min}$, this expression reduces to

$$\langle F(0)F(r)\rangle = \frac{D}{r}\int_{k_{min}}^{k_{max}} \frac{\sin\ kr}{k^{n+1}}\ dk. \tag{F.25}$$

Expression in terms of incomplete Gamma functions

The force auto-correlation function can be expressed in terms of incomplete gamma functions extended for complex variables:

$$\begin{aligned}
\langle F(0)F(r)\rangle &= \frac{D}{r}\frac{1}{2i}\int_{k_{min}}^{k_{max}}\frac{e^{ikr}-e^{-ikr}}{k^{n+1}}\ dk \\
&= \frac{D}{r}\frac{1}{2i}(ir)^n\int_{ik_{min}r}^{ik_{max}r}\frac{e^x-e^{-x}}{x^{n+1}}\ dx \\
&= \frac{D}{2}(ir)^{n-1}\left[\int_0^{ik_{max}r}\frac{e^x}{x^{n+1}}dx - \int_0^{ik_{max}r}\frac{e^{-x}}{x^{n+1}}dx\right. \\
&\qquad \left. - \int_0^{ik_{min}r}\frac{e^x}{x^{n+1}}dx + \int_0^{ik_{min}r}\frac{e^{-x}}{x^{n+1}}dx\right] \\
&= \frac{D}{2}(ir)^{n-1}\left[(-1)^n\int_0^{-ik_{max}r}\frac{e^{-x}}{x^{n+1}}dx - \int_0^{ik_{max}r}\frac{e^{-x}}{x^{n+1}}dx\right. \\
&\qquad \left. -(-1)^n\int_0^{-ik_{min}r}\frac{e^{-x}}{x^{n+1}}dx + \int_0^{ik_{min}r}\frac{e^{-x}}{x^{n+1}}dx\right] \\
&= \frac{D}{2}(ir)^{n-1}\left[(-1)^n\gamma(-n,-ik_{max}r) - \gamma(-n,ik_{max}r)\right. \\
&\qquad \left. -(-1)^n\gamma(-n,-ik_{min}r) + \gamma(-n,ik_{min}r)\right] \\
\langle F(0)F(r)\rangle &= \frac{D}{2}(ir)^{n-1}\left[\gamma(-n,ik_{min}r) - \gamma(-n,ik_{max}r)\right] \\
&\qquad + \frac{D}{2}(-ir)^{n-1}\left[\gamma(-n,-ik_{min}r) - \gamma(-n,-ik_{max}r)\right],
\end{aligned}$$

which can be rewritten more simply as

$$\langle F(0)F(r)\rangle = \frac{D}{2}(ir)^{n-1}\left[\gamma(-n, ik_{min}r) - \gamma(-n, ik_{max}r)\right] + C.C. \tag{F.26}$$

or

$$\langle F(0)F(r)\rangle = \frac{D}{2}(ir)^{n-1}\left[\Gamma(-n, ik_{max}r) - \Gamma(-n, ik_{min}r)\right] + C.C. \tag{F.27}$$

given that $\Gamma(s,x) + \gamma(s,x) = \Gamma(s)$ (Eq. F.7).

Asymptotic behavior

As $\Gamma(s,x) \underset{|x|\to+\infty}{\sim} x^{s-1}e^{-x}$ (Eq. F.8), the asymptotic behavior of the force correlation function when $\langle F(0)F(r)\rangle$ when $k_{max}r \gg k_{min}r \gg 1$ and assuming $n+1>0$ is

$$\begin{aligned}
\langle F(0)F(r)\rangle &\sim \frac{D}{2}(ir)^{n-1}\left[(ik_{max}r)^{-n-1}e^{-ik_{max}r} - (ik_{min}r)^{-n-1}e^{-ik_{min}r}\right] + C.C. \\
&\sim -\frac{D}{2r^2}\left[k_{max}^{-n-1}e^{-ik_{max}r} - k_{min}^{-n-1}e^{-ik_{min}r}\right] + C.C. \\
&\sim \frac{D}{r^2}\left[k_{min}^{-n-1}\cos(k_{min}r) - k_{max}^{-n-1}\cos(k_{max}r)\right] \\
\langle F(0)F(r)\rangle &\sim \frac{D}{r^2}\frac{1}{k_{min}^{n+1}}\cos(k_{min}r).
\end{aligned} \tag{F.28}$$

An estimate of the force

The value of $\langle F(0)^2\rangle$ can be used as an estimate of the square of the force, and can be determined from Eq. F.25:

$$\begin{aligned}
\langle F(0)^2\rangle &= D\int_{k_{min}}^{k_{max}} \frac{1}{k^n}\lim_{r\to 0}\left(\frac{\sin\ kr}{kr}\right)\ dk \\
&= D\int_{k_{min}}^{k_{max}} \frac{1}{k^n}\ dk \\
&= D\left[\frac{k^{-n+1}}{-n+1}\right]_{k_{min}}^{k_{max}} \\
\langle F(0)^2\rangle &= \frac{D}{n-1}\left[k_{min}^{-n+1} - k_{max}^{-n+1}\right].
\end{aligned}$$

Recalling $D = 8CV(G\rho_0)^2$ and expressing $C = k_{min}^n\delta_{k_{min}}^2$, with $\delta_{k_{min}}^2 = \langle|\delta_{k_{min}}|^2\rangle$, yield

$$\langle F(0)^2\rangle = \frac{8\left(G\rho_0\right)^2\delta_{k_{min}}^2\ d^3}{n-1}\ k_{min}\ \left(1 - \left(\frac{k_{min}}{k_{max}}\right)^{n-1}\right), \tag{F.29}$$

so that when $k_{max} \gg k_{min}$ and $n > 1$,

$$\langle F(0)^2\rangle \approx \frac{8\left(G\rho_0\right)^2\delta_{k_{min}}^2\ d^3}{n-1}\ k_{min}. \tag{F.30}$$

F.3 Velocity variance

F.3.1 Expression from the equation of motion

Considering the effect of the random perturbation force in the direction i during a time T, the equation of motion

$$\frac{d^2x_i}{dt^2} = F_i \tag{F.31}$$

leads to

$$\frac{dx_i}{dt} = v_{0i} + \int_0^T F_i(\tau)d\tau, \tag{F.32}$$

where v_{0i} is the initial velocity in direction i. The velocity variance is obtained by averaging the latter equation:

$$\begin{aligned}
\langle \Delta v_i^2 \rangle &= \langle \left(\frac{dx_i}{dt} - v_{0i} \right)^2 \rangle \\
&= \langle \left(\int_0^T F_i(\tau)d\tau \right)^2 \rangle \\
&= \langle \int_0^T \int_0^T F_i(\tau)F_i(\tau')\ d\tau d\tau' \rangle \\
\langle \Delta v_i^2 \rangle &= \int_0^T \int_0^T \langle F_i(\tau)F_i(\tau') \rangle\ d\tau d\tau'
\end{aligned}$$

The integrand is symmetrical in τ, τ' and the integration domain correspond to a square of radius t in the plane (τ, τ'). We can thus replace the integral over the square by twice the integral over the triangle defined by $0 < \tau < t$ and $\tau < \tau' < t$:

$$\langle \Delta v_i^2 \rangle = 2 \int_0^T d\tau \int_\tau^T d\tau'\ \langle F_i(\tau)F_i(\tau') \rangle.$$

Introducing the time difference $t = \tau' - \tau$ we have

$$\langle \Delta v_i^2 \rangle = 2 \int_0^T d\tau \int_0^{T-\tau} dt\ \langle F_i(\tau)F_i(\tau + t) \rangle.$$

The integration domain corresponds to the triangle defined by $0 < \tau < T$ and $0 < t < T - \tau$ in the plane (τ, t), which can also be defined as $0 < t < T$ and $0 < \tau < T - t$. Consequently, the integral can be rewritten as

$$\langle \Delta v_i^2 \rangle = 2 \int_0^T dt \int_0^{T-t} d\tau\ \langle F_i(\tau)F_i(\tau + t) \rangle.$$

The perturbations being stationary, $\langle F_i(\tau)F_i(\tau + t) \rangle = \langle F_i(0)F_i(t) \rangle$ and the expression of the velocity variance simplifies to

$$\langle \Delta v_i^2 \rangle = 2 \int_0^T dt \int_0^{T-t} d\tau\ \langle F_i(0)F_i(t) \rangle.$$

$$\langle \Delta v_i^2 \rangle = 2 \int_0^T (T-t) \langle F_i(0) F_i(t) \rangle \, dt. \tag{F.33}$$

And the total velocity variance is given by

$$\langle \Delta v^2 \rangle = 2 \int_0^T (T-t) \langle F(0) F(t) \rangle \, dt. \tag{F.34}$$

As indicated in section 4.3.2, the velocity variance can be expressed in terms of the spatial correlation function instead of the temporal time-correlation function by introducing a velocity v_r corresponding to the movement of the fluctuating gaseous field. Introducing $R = v_r T$ the distance traveled during time T by a test dark matter particles with respect to the fluctuating gaseous field, Eq. F.34 can be rewritten as

$$\langle \Delta v^2 \rangle = \frac{2}{v_r^2} \int_0^R (R-r) \langle F(0) F(r) \rangle \, dr. \tag{F.35}$$

F.3.2 Explicit expression of the velocity variance

Preliminary calculations

Eq. F.35 expresses the velocity variance $\langle \Delta v^2 \rangle$ as a function of the force correlation function $\langle F(0)F(r) \rangle$, which we developed in terms of incomplete Gamma functions in Eq. F.27. Deriving the full expression of the velocity variance is not trivial, and notably necessitates some preliminary calculations. Firstly, assuming that Eq. F.7 remains valid when $s \to 0$ so that $\Gamma(0,x) - \Gamma(0,-x) = -\gamma(0,x) + \gamma(0,-x)$ even if $\Gamma(0)$ is not defined,

$$\begin{aligned}
\Gamma(0, ik_{min}R) - \Gamma(0, -ik_{min}R) &= -\gamma(0, ik_{min}R) + \gamma(0, -ik_{min}R) \\
&= -\int_0^{ik_{min}R} \frac{e^{-t}}{t} \, dt + \int_0^{-ik_{min}R} \frac{e^{-t}}{t} \, dt \\
&= -\int_0^{k_{min}R} \frac{e^{-ix}}{x} \, dx + \int_0^{k_{min}R} \frac{e^{ix}}{x} \, dt \\
&= 2i \int_0^{k_{min}R} \frac{\sin x}{x} \, dx \\
\Gamma(0, ik_{min}R) - \Gamma(0, -ik_{min}R) &= 2i \; Si(k_{min}R)
\end{aligned} \tag{F.36}$$

where $Si(x) \equiv \int_0^x \frac{\sin x}{x} \, dx$ is the sine integral function, whose limit when $w \to +\infty$ is equal to $\pi/2$. Secondly, we notice that

$$\begin{aligned}
2\Gamma(1,0) - \Gamma(1, ik_{min}R) - \Gamma(1, -ik_{min}R) &= \gamma(1, ik_{min}R) + \gamma(1, -ik_{min}R) \\
&= \int_0^{ik_{min}R} e^{-t} \, dt + \int_0^{-ik_{min}R} e^{-t} \, dt \\
&= \int_0^{k_{min}R} e^{-ix} \; i dx + \int_0^{k_{min}R} e^{ix} \; (-i) \, dx \\
&= -i \int_0^{k_{min}R} \left(e^{ix} - e^{-ix} \right) \; dx \\
&= 2 \int_0^{k_{min}R} \sin x \; dx \\
2\Gamma(1,0) - \Gamma(1, ik_{min}R) - \Gamma(1, -ik_{min}R) &= -2 \Big(\cos(k_{min}R) - 1 \Big).
\end{aligned} \tag{F.37}$$

Derivation of the explicit expression

The expression of the force auto-correlation function obtained in terms of incomplete Gamma functions in section F.2.2 (p. 231) can be developed as

$$\begin{aligned}\langle F(0)F(r)\rangle = \; & \frac{D}{2}k_{max}^{-n+1}\left[(ik_{max}r)^{n-1}\,\Gamma(-n,ik_{max}r)+(-ik_{max}r)^{n-1}\,\Gamma(-n,-ik_{max}r)\right]\\ & -\frac{D}{2}k_{min}^{-n+1}\left[(ik_{min}r)^{n-1}\,\Gamma(-n,ik_{min}r)+(-ik_{min}r)^{n-1}\,\Gamma(-n,-ik_{min}r)\right].\end{aligned}$$

Injecting this expression in the expression of the velocity variance (Eq. F.35) yields

$$\langle \Delta v^2\rangle = \frac{D}{v_r^2}k_{max}^{-n+1}\left[I_{max}+I_{max}^*\right]-\frac{D}{v_r^2}k_{min}^{-n+1}\left[I_{min}+I_{min}^*\right] \tag{F.38}$$

with

$$I_{max}=\int_0^R (R-r)\,(ik_{max}r)^{n-1}\,\Gamma(-n,ik_{max}r)\;dr, \tag{F.39}$$

$$I_{min}=\int_0^R (R-r)\,(ik_{min}r)^{n-1}\,\Gamma(-n,ik_{min}r)\;dr, \tag{F.40}$$

and I_{max}^*, I_{min}^* their respective complex conjugates. We determine the terms intervening in this expression of the velocity variance step by step.

First of all, we express the sum $I_{max}+I_{max}^*$ in terms of two integrals I_1 and I_2, which we will calculate separately:

$$\begin{aligned}I_{max}+I_{max}^* &= \int_0^R (R-r)\,(ik_{max}r)^{n-1}\,\Gamma(-n,ik_{max}r)\;dr\\ &\qquad +\int_0^R (R-r)\,(-ik_{max}r)^{n-1}\,\Gamma(-n,-ik_{max}r)\;dr\\ &= \int_0^{ik_{max}R}\left(R-\frac{x}{ik_{max}}\right)x^{n-1}\Gamma(-n,x)\frac{dx}{ik_{max}}\\ &\qquad +\int_0^{-ik_{max}R}\left(R-\frac{x}{-ik_{max}}\right)x^{n-1}\Gamma(-n,x)\frac{dx}{-ik_{max}}\\ I_{max}+I_{max}^* &= -\frac{iR}{k_{max}}I_1+\frac{1}{k_{max}^2}I_2\end{aligned} \tag{F.41}$$

with

$$I_1=\int_0^{ik_{max}R} x^{n-1}\Gamma(-n,x)\;dx-\int_0^{-ik_{max}R} x^{n-1}\Gamma(-n,x)\;dx, \tag{F.42}$$

$$I_2=\int_0^{ik_{max}R} x^{n}\Gamma(-n,x)\;dx+\int_0^{-ik_{max}R} x^{n}\Gamma(-n,x)\;dx. \tag{F.43}$$

We can calculate I_1 and I_2 using Eq. F.10, Eq. F.36 and Eq. F.37, the last two ones introducing a sine integral function and a cosine function:

$$\begin{aligned}
I_1 &= \int_{-ik_{max}R}^{ik_{max}R} x^{n-1}\Gamma(-n,x)\ dx \\
&= \frac{1}{n}\Big[x^n\Gamma(-n,x)-\Gamma(0,x)\Big]_{-ik_{max}R}^{ik_{max}R} \\
&= \frac{1}{n}\Big[(ik_{max}R)^n\,\Gamma(-n,ik_{max}R)-(-ik_{max}R)^n\,\Gamma(-n,-ik_{max}R) \\
&\qquad -\Gamma(0,ik_{max}R)+\Gamma(0,-ik_{max}R)\Big] \\
&= \frac{1}{n}\Big[(ik_{max}R)^n\,\Gamma(-n,ik_{max}R)-(-ik_{max}R)^n\,\Gamma(-n,-ik_{max}R)-2i\ Si(k_{max}R)\Big] \\
I_1 &= \frac{1}{n}\Big[(ik_{max}R)^n\,\Gamma(-n,ik_{max}R)-(-ik_{max}R)^n\,\Gamma(-n,-ik_{max}R)\Big]-\frac{2i}{n}Si(k_{max}R)
\end{aligned} \tag{F.44}$$

and

$$\begin{aligned}
I_2 &= \int_0^{ik_{max}R} x^n\Gamma(-n,x)\ dx+\int_0^{-ik_{max}R} x^n\Gamma(-n,x)\ dx. \\
&= \frac{1}{n+1}\left(\Big[x^{n+1}\Gamma(-n,x)-\Gamma(1,x)\Big]_0^{ik_{max}R}+\Big[x^{n+1}\Gamma(-n,x)-\Gamma(1,x)\Big]_0^{-ik_{max}R}\right) \\
&= \frac{1}{n+1}\Big[(ik_{max}R)^{n+1}\,\Gamma(-n,ik_{max}R)+(-ik_{max}R)^{n+1}\,\Gamma(-n,-ik_{max}R) \\
&\qquad -\Gamma(1,ik_{max}R)-\Gamma(1,-ik_{max}R)+2\Gamma(1,0)\Big] \\
&= \frac{1}{n+1}\Big[(ik_{max}R)^{n+1}\,\Gamma(-n,ik_{max}R)+(-ik_{max}R)^{n+1}\,\Gamma(-n,-ik_{max}R) \\
&\qquad -2\Big(\cos(k_{max}R)-1\Big)\Big] \\
I_2 &= \frac{1}{n+1}\Big[(ik_{max}R)^{n+1}\,\Gamma(-n,ik_{max}R)+(-ik_{max}R)^{n+1}\,\Gamma(-n,-ik_{max}R)\Big] \\
&\qquad -\frac{2}{n+1}\Big[\cos(k_{max}R)-1\Big]
\end{aligned} \tag{F.45}$$

so that

$$\begin{aligned}
I_{max}+I_{max}^* &= \frac{1}{k_{max}^2}\left[\left(\frac{1}{n+1}-\frac{1}{n}\right)\Big((ik_{max}R)^{n+1}\,\Gamma(-n,ik_{max}R)+C.C.\Big)\right. \\
&\qquad \left.-\frac{2k_{max}R}{n}Si(k_{max}R)-\frac{2}{n+1}\Big(\cos(k_{max}R)-1\Big)\right].
\end{aligned} \tag{F.46}$$

The sum $I_{min}+I_{min}^*$ yields a similar expression, which enables to reconstitute the full expression of the velocity variance from Eq. F.38, as specified in section 4.3.2 (p. 155).

Assymptotic behavior

As mentioned in Eq. F.8, $\Gamma(s,x) \underset{|x|\to+\infty}{\sim} x^{s-1}e^{-x}$, so when $k_{max}R >> 1$ and $k_{min}R >> 1$,

$$\begin{aligned}
I_{max} + I^*_{max} &\sim \frac{1}{k_{max}^2}\Bigg[\left(\frac{1}{n+1}-\frac{1}{n}\right)\Big((ik_{max}R)^{n+1}(ik_{max}R)^{-n-1}e^{-ik_{max}R} + C.C.\Big) \\
&\qquad -\frac{2k_{max}R}{n}Si(k_{max}R) - \frac{2}{n+1}\Big(\cos(k_{max}R)-1\Big)\Bigg] \\
&\sim \frac{1}{k_{max}^2}\Bigg[\left(\frac{1}{n+1}-\frac{1}{n}\right)\left(e^{-ik_{max}R}+e^{ik_{max}R}\right) \\
&\qquad -\frac{2k_{max}R}{n}Si(k_{max}R) - \frac{2}{n+1}\Big(\cos(k_{max}R)-1\Big)\Bigg] \\
&\sim -\frac{2R}{n\ k_{max}}Si(k_{max}R) \\
I_{max} + I^*_{max} &\sim -\frac{\pi R}{n\ k_{max}}
\end{aligned} \tag{F.47}$$

and similarly,

$$I_{min} + I^*_{min} \sim -\frac{\pi R}{n\ k_{min}}. \tag{F.48}$$

Consequently,

$$\langle \Delta v^2 \rangle \sim -\frac{\pi RD}{nv_r^2}\frac{1}{k_{max}^n} + \frac{\pi RD}{nv_r^2}\frac{1}{k_{min}^n}, \tag{F.49}$$

and when $k_{max} \gg k_{min}$,

$$\langle \Delta v^2 \rangle \sim \frac{\pi RD}{nv_r^2}\frac{1}{k_{min}^n}, \tag{F.50}$$

or as a function of time T,

$$\langle \Delta v^2 \rangle \sim \frac{\pi D}{nv_r}\frac{T}{k_{min}^n}. \tag{F.51}$$

This study of the asymptotic behavior of the velocity variance justifies the introduction of the transient terms T_1 and T_2 in section 4.3.2 to write the velocity variance in a more compact way emphasizing on its asymptotic behavior.

F.4 Relaxation time

We consider the relaxation time as defined in section 4.3.3 (p. 156) according to Eq. 4.35:

$$t_{\text{relax}} = \frac{nv_r\langle v\rangle^2}{8\pi(G\rho_0)^2 V \delta^2_{k_{min}}}.$$

Introducing $\langle v \rangle \sim l\sqrt{G\rho(l)}$ and $v_r \sim d\sqrt{G\rho(d)}$, $\rho(d)$ yields

$$\begin{aligned} t_{relax} &\sim \frac{n\ d\sqrt{G\rho(d)}\ l^2\ (G\rho(l))}{8\pi\ (G\rho_0)^2\ d^3 \langle|\delta_{kmin}|^2\rangle} \\ &\sim \frac{n}{8\pi}\frac{1}{\langle|\delta_{kmin}|^2\rangle}\left(\frac{\rho(l)}{\rho_0}\right)^2\left(\frac{l}{d}\right)^2\left(\frac{\rho(d)}{\rho(l)}\right)\frac{1}{\sqrt{G\rho(d)}} \\ t_{relax} &\sim \frac{n}{8\pi}\frac{1}{\langle|\delta_{kmin}|^2\rangle}\frac{1}{f^2}\left(\frac{l}{d}\right)^2\left(\frac{\rho(d)}{\rho(l)}\right)\ t_D(d) \end{aligned}$$

where $f = \rho_0/\rho(l)$ and $t_D(d) \sim 1/\sqrt{G\rho(d)}$. While ρ_0 corresponds to the gaseous component, $\rho(l)$ and $\rho(d)$ correspond to the total density of the halo, for example defined as in F.1.4 as a cuspy NFW halo.

References

References

Aalto, S. 2015, IAU General Assembly, 22, 56596

Agertz, O. & Kravtsov, A. V. 2015, ApJ, 804, 18

Agertz, O., Kravtsov, A. V., Leitner, S. N., & Gnedin, N. Y. 2013, ApJ, 770, 25

Agertz, O., Teyssier, R., & Moore, B. 2009, MNRAS, 397, L64

Alves de Oliveira, C., Schneider, N., Merín, B., et al. 2014, A&A, 568, A98

Anderhalden, D., Schneider, A., Macciò, A. V., Diemand, J., & Bertone, G. 2013, J. Cosmology Astropart. Phys., 3, 14

André, P., Basu, S., & Inutsuka, S. 2009, The formation and evolution of prestellar cores, ed. G. Chabrier (Cambridge University Press), 254

André, P., Di Francesco, J., Ward-Thompson, D., et al. 2014, Protostars and Planets VI, 27

André, P., Men'shchikov, A., Bontemps, S., et al. 2010, A&A, 518, L102

Aragón-Calvo, M. A., van de Weygaert, R., & Jones, B. J. T. 2010, MNRAS, 408, 2163

Arcoragi, J.-P., Bonnell, I., Martel, H., Bastien, P., & Benz, W. 1991, ApJ, 380, 476

Arzoumanian, D., André, P., Didelon, P., et al. 2011, A&A, 529, L6

Athanassoula, E. 2005, MNRAS, 358, 1477

Baldry, I. K., Glazebrook, K., Brinkmann, J., et al. 2004, ApJ, 600, 681

Bally, J., Langer, W. D., Stark, A. A., & Wilson, R. W. 1987, ApJ, 312, L45

Barmby, P., Ashby, M. L. N., Bianchi, L., et al. 2006, ApJ, 650, L45

Barnes, J. E. & Hernquist, L. E. 1991, ApJ, 370, L65

Bastien, P. 1983, A&A, 119, 109

Bastien, P., Arcoragi, J.-P., Benz, W., Bonnell, I., & Martel, H. 1991, ApJ, 378, 255

Bastien, P. & Mitalas, R. 1979, MNRAS, 186, 755

Basu, S., Ciolek, G. E., Dapp, W. B., & Wurster, J. 2009a, New A, 14, 483

Basu, S., Ciolek, G. E., & Wurster, J. 2009b, New A, 14, 221

Baugh, C. M., Cole, S., & Frenk, C. S. 1996, MNRAS, 283, 1361

Begeman, K. G., Broeils, A. H., & Sanders, R. H. 1991, MNRAS, 249, 523

Bell, E. F. & de Jong, R. S. 2001, ApJ, 550, 212

Bell, E. F., Papovich, C., Wolf, C., et al. 2005, ApJ, 625, 23

Benítez-Llambay, A., Navarro, J. F., Abadi, M. G., et al. 2013, ApJ, 763, L41

Benson, A. J., Bower, R. G., Frenk, C. S., et al. 2003, ApJ, 599, 38

Bertoldi, F. 1989, ApJ, 346, 735

Beygu, B., Kreckel, K., van de Weygaert, R., van der Hulst, J. M., & van Gorkom, J. H. 2013, AJ, 145, 120

Bieri, R., Dubois, Y., Silk, J., Mamon, G., & Gaibler, V. 2015a, ArXiv: 1507.00730

Bieri, R., Dubois, Y., Silk, J., & Mamon, G. A. 2015b, ArXiv: 1503.05823

Bigiel, F., Leroy, A., Walter, F., et al. 2008, AJ, 136, 2846

Bigiel, F., Leroy, A. K., Walter, F., et al. 2011, ApJ, 730, L13

Binney, J., Gerhard, O. E., Stark, A. A., Bally, J., & Uchida, K. I. 1991, MNRAS, 252, 210

Binney, J. & Tremaine, S. 1987, Galactic dynamics

Birnboim, Y. & Dekel, A. 2003, MNRAS, 345, 349

Birnboim, Y., Dekel, A., & Neistein, E. 2007, MNRAS, 380, 339

Bîrzan, L., Rafferty, D. A., McNamara, B. R., Wise, M. W., & Nulsen, P. E. J. 2004, ApJ, 607, 800

Blanchard, A., Valls-Gabaud, D., & Mamon, G. A. 1992, A&A, 264, 365

Blanton, M. R. & Roweis, S. 2007, AJ, 133, 734

Blitz, L. 1993, in Protostars and Planets III, ed. E. H. Levy & J. I. Lunine, 125–161

Blitz, L., Fukui, Y., Kawamura, A., et al. 2007, Protostars and Planets V, 81

Blitz, L. & Shu, F. H. 1980, ApJ, 238, 148

Blumenthal, G. R., Faber, S. M., Flores, R., & Primack, J. R. 1986, ApJ, 301, 27

Bode, P., Ostriker, J. P., & Turok, N. 2001, ApJ, 556, 93

Bœhm, C., Fayet, P., & Schaeffer, R. 2001, Physics Letters B, 518, 8

Boehm, C. & Schaeffer, R. 2005, A&A, 438, 419

Boissier, S., Prantzos, N., Boselli, A., & Gavazzi, G. 2003, MNRAS, 346, 1215

Bond, J. R., Efstathiou, G., & Silk, J. 1980, Physical Review Letters, 45, 1980

Bond, J. R., Kofman, L., & Pogosyan, D. 1996, Nature, 380, 603

Bonnell, I. A., Dobbs, C. L., Robitaille, T. P., & Pringle, J. E. 2006, MNRAS, 365, 37

Booth, C. M. & Schaye, J. 2009, MNRAS, 398, 53

Bothwell, M. S., Kennicutt, R. C., & Lee, J. C. 2009, MNRAS, 400, 154

Bouché, N., Cresci, G., Davies, R., et al. 2007, ApJ, 671, 303

Bouché, N., Dekel, A., Genzel, R., et al. 2010, ApJ, 718, 1001

Boulanger, F. & Viallefond, F. 1992, A&A, 266, 37

Bournaud, F., Daddi, E., Elmegreen, B. G., et al. 2008, A&A, 486, 741

Bournaud, F., Elmegreen, B. G., & Martig, M. 2009, ApJ, 707, L1

Bournaud, F., Perret, V., Renaud, F., et al. 2014, ApJ, 780, 57

Bouwens, R. J., Illingworth, G. D., Oesch, P. A., et al. 2012a, ApJ, 754, 83

Bouwens, R. J., Illingworth, G. D., Oesch, P. A., et al. 2011, ApJ, 737, 90

Bouwens, R. J., Illingworth, G. D., Oesch, P. A., et al. 2010, ApJ, 709, L133

Bouwens, R. J., Illingworth, G. D., Oesch, P. A., et al. 2012b, ApJ, 752, L5

Bower, R. G., Benson, A. J., Malbon, R., et al. 2006, MNRAS, 370, 645

Boylan-Kolchin, M., Bullock, J. S., & Kaplinghat, M. 2011, MNRAS, 415, L40

Boylan-Kolchin, M., Bullock, J. S., & Kaplinghat, M. 2012, MNRAS, 422, 1203

Boylan-Kolchin, M., Springel, V., White, S. D. M., Jenkins, A., & Lemson, G. 2009, MNRAS, 398, 1150

Brada, R. & Milgrom, M. 2000a, ApJ, 541, 556

Brada, R. & Milgrom, M. 2000b, ApJ, 531, L21

Breddels, M. A. & Helmi, A. 2013, A&A, 558, A35

Breysse, P. C., Kamionkowski, M., & Benson, A. 2014, MNRAS, 437, 2675

Brooks, A. M., Kuhlen, M., Zolotov, A., & Hooper, D. 2013, ApJ, 765, 22

Brooks, A. M. & Zolotov, A. 2014, ApJ, 786, 87

Bryan, G. L. & Norman, M. L. 1998, ApJ, 495, 80

Buat, V. 1992, A&A, 264, 444

Buat, V., Deharveng, J. M., & Donas, J. 1989, A&A, 223, 42

Burkert, A. 2000, ApJ, 534, L143

Burkert, A. & Hartmann, L. 2004, ApJ, 616, 288

Calzetti, D., Armus, L., Bohlin, R. C., et al. 2000, ApJ, 533, 682

Calzetti, D., Kennicutt, R. C., Engelbracht, C. W., et al. 2007, ApJ, 666, 870

Cantalupo, S., Arrigoni-Battaia, F., Prochaska, J. X., Hennawi, J. F., & Madau, P. 2014, Nature, 506, 63

Cantalupo, S., Lilly, S. J., & Haehnelt, M. G. 2012, MNRAS, 425, 1992

Caon, N., Capaccioli, M., & D'Onofrio, M. 1993, MNRAS, 265, 1013

Cappellari, M., Emsellem, E., Krajnović, D., et al. 2011, MNRAS, 416, 1680

Caputi, K. I., Dole, H., Lagache, G., et al. 2006, ApJ, 637, 727

Carignan, C. & Beaulieu, S. 1989, ApJ, 347, 760

Casasola, V., Hunt, L., Combes, F., & García-Burillo, S. 2015, A&A, 577, A135

Cattaneo, A., Dekel, A., Devriendt, J., Guiderdoni, B., & Blaizot, J. 2006, MNRAS, 370, 1651

Cattaneo, A., Faber, S. M., Binney, J., et al. 2009, Nature, 460, 213

Cen, R. & Ostriker, J. P. 1999, ApJ, 514, 1

Ceverino, D., Dekel, A., & Bournaud, F. 2010, MNRAS, 404, 2151

Ceverino, D. & Klypin, A. 2009, ApJ, 695, 292

Ceverino, D., Klypin, A., Klimek, E. S., et al. 2014, MNRAS, 442, 1545

Chabrier, G. 2003, PASP, 115, 763

Chan, T. K., Kereš, D., Oñorbe, J., et al. 2015, ArXiv: 1507.02282

Chandrasekhar, S. 1943, ApJ, 97, 255

Chandrasekhar, S. & Fermi, E. 1953, ApJ, 118, 116

Chemin, L., de Blok, W. J. G., & Mamon, G. A. 2011, AJ, 142, 109

Chien, L.-H., Barnes, J. E., Kewley, L. J., & Chambers, K. C. 2007, ApJ, 660, L105

Cicone, C., Maiolino, R., Sturm, E., et al. 2014, A&A, 562, A21

Clowe, D., Bradač, M., Gonzalez, A. H., et al. 2006, ApJ, 648, L109

Coil, A. L., Newman, J. A., Kaiser, N., et al. 2004, ApJ, 617, 765

Colín, P., Avila-Reese, V., & Valenzuela, O. 2000, ApJ, 542, 622

Colless, M. 1995, in Wide Field Spectroscopy and the Distant Universe, ed. S. J. Maddox & A. Aragon-Salamanca, 263

Combes, F. 1991, ARA&A, 29, 195

Combes, F. 2009, Mysteries of Galaxy Formation

Combes, F., Boissé, P., Mazure, A., & Blanchard, A. 1991, "Galaxies et cosmologie"

Combes, F., Boisse, P., Mazure, A., Blanchard, A., & Seymour, M. 1995, Galaxies and Cosmology

Combes, F., García-Burillo, S., Braine, J., et al. 2011, A&A, 528, A124

Combes, F., García-Burillo, S., Casasola, V., et al. 2013, A&A, 558, A124

Combes, F., Leon, S., & Meylan, G. 1999, A&A, 352, 149

Combes, F. & Sanders, R. H. 1981, A&A, 96, 164

Comparetta, J. & Quillen, A. C. 2011, MNRAS, 414, 810

Connolly, A. J., Szalay, A. S., Dickinson, M., SubbaRao, M. U., & Brunner, R. J. 1997, ApJ, 486, L11

Conselice, C. J., Grogin, N. A., Jogee, S., et al. 2004, ApJ, 600, L139

Cooper, M. C., Aird, J. A., Coil, A. L., et al. 2011, ApJS, 193, 14

Cooper, M. C., Newman, J. A., Davis, M., Finkbeiner, D. P., & Gerke, B. F. 2012, spec2d: DEEP2 DEIMOS Spectral Pipeline, Astrophysics Source Code Library

Cowie, L. L., Hu, E. M., & Songaila, A. 1995, AJ, 110, 1576

Cowie, L. L., Songaila, A., Hu, E. M., & Cohen, J. G. 1996, AJ, 112, 839

Croft, R. A. C., Weinberg, D. H., Pettini, M., Hernquist, L., & Katz, N. 1999, ApJ, 520, 1

Crosthwaite, L. P. & Turner, J. L. 2007, AJ, 134, 1827

Croton, D. J., Springel, V., White, S. D. M., et al. 2006, MNRAS, 365, 11

Curry, C. L. 2002, ApJ, 576, 849

Curtis, H. D. 1917, PASP, 29, 206

Daddi, E., Bournaud, F., Walter, F., et al. 2010a, ApJ, 713, 686

Daddi, E., Cimatti, A., Renzini, A., et al. 2004, ApJ, 617, 746

Daddi, E., Dickinson, M., Morrison, G., et al. 2007, ApJ, 670, 156

Daddi, E., Elbaz, D., Walter, F., et al. 2010b, ApJ, 714, L118

Daddi, E., Renzini, A., Pirzkal, N., et al. 2005, ApJ, 626, 680

Dame, T. M., Hartmann, D., & Thaddeus, P. 2001, ApJ, 547, 792

Damen, M., Labbé, I., Franx, M., et al. 2009, ApJ, 690, 937

Danforth, C. W. & Shull, J. M. 2005, ApJ, 624, 555

Danielson, A. L. R., Swinbank, A. M., Smail, I., et al. 2011, MNRAS, 410, 1687

Dasyra, K. M. & Combes, F. 2012, A&A, 541, L7

Dauphole, B., Geffert, M., Colin, J., et al. 1996, A&A, 313, 119

Davé, R., Cen, R., Ostriker, J. P., et al. 2001, ApJ, 552, 473

Davé, R., Finlator, K., & Oppenheimer, B. D. 2011a, MNRAS, 416, 1354

Davé, R., Oppenheimer, B. D., & Finlator, K. 2011b, MNRAS, 415, 11

Davis, M., Efstathiou, G., Frenk, C. S., & White, S. D. M. 1985, ApJ, 292, 371

Davis, M., Faber, S. M., Newman, J., et al. 2003, in Society of Photo-Optical Instrumentation Engineers (SPIE) Conference Series, Vol. 4834, Discoveries and Research Prospects from 6- to 10-Meter-Class Telescopes II, ed. P. Guhathakurta, 161–172

Davis, M., Guhathakurta, P., Konidaris, N. P., et al. 2007, ApJ, 660, L1

de Blok, W. J. G. & McGaugh, S. S. 1997, MNRAS, 290, 533

de Blok, W. J. G. & McGaugh, S. S. 1998, ApJ, 508, 132

de Blok, W. J. G., McGaugh, S. S., Bosma, A., & Rubin, V. C. 2001, ApJ, 552, L23

de Blok, W. J. G., Walter, F., Brinks, E., et al. 2008, AJ, 136, 2648

de Jong, R. S. 1996, A&A, 313, 45

de Mello, D. F., Smith, L. J., Sabbi, E., et al. 2008, AJ, 135, 548

de Vaucouleurs, G. 1948, Annales d'Astrophysique, 11, 247

de Vaucouleurs, G. 1959, Handbuch der Physik, 53, 275

de Vaucouleurs, G. 1974, in IAU Symposium, Vol. 58, The Formation and Dynamics of Galaxies, ed. J. R. Shakeshaft, 1–52

Debattista, V. P. & Sellwood, J. A. 1998, ApJ, 493, L5

Decarli, R., Walter, F., Neri, R., et al. 2012, ApJ, 752, 2

Deharveng, J.-M., Sasseen, T. P., Buat, V., et al. 1994, A&A, 289, 715

Dekel, A. & Birnboim, Y. 2006, MNRAS, 368, 2

Dekel, A., Birnboim, Y., Engel, G., et al. 2009a, Nature, 457, 451

Dekel, A. & Krumholz, M. R. 2013, MNRAS, 432, 455

Dekel, A. & Mandelker, N. 2014, MNRAS, 444, 2071

Dekel, A., Sari, R., & Ceverino, D. 2009b, ApJ, 703, 785

Dekel, A. & Silk, J. 1986, ApJ, 303, 39

Dekel, A. & Woo, J. 2003, MNRAS, 344, 1131

Destri, C., de Vega, H. J., & Sanchez, N. G. 2013, New A, 22, 39

Di Cintio, A., Brook, C. B., Macciò, A. V., et al. 2014, MNRAS, 437, 415

Di Matteo, P., Bournaud, F., Martig, M., et al. 2008, A&A, 492, 31

Di Matteo, P., Combes, F., Melchior, A.-L., & Semelin, B. 2007, A&A, 468, 61

Di Matteo, P., Gómez, A., Haywood, M., et al. 2015, A&A, 577, A1

Di Matteo, T., Springel, V., & Hernquist, L. 2005, Nature, 433, 604

Dib, S., Bell, E., & Burkert, A. 2006, ApJ, 638, 797

Dickman, R. L., Snell, R. L., & Schloerb, F. P. 1986, ApJ, 309, 326

Dobbs, C. L. & Pringle, J. E. 2013, MNRAS, 432, 653

Dreyer, J. L. E. 1888, MmRAS, 49, 1

Dreyer, J. L. E. 1895, MmRAS, 51, 185

Dreyer, J. L. E. 1908, MmRAS, 59, 105

Dubinski, J. & Carlberg, R. G. 1991, ApJ, 378, 496

Easton, C. 1900, ApJ, 12, 136

Efstathiou, G. 1992, MNRAS, 256, 43P

Efstathiou, G. 2000, MNRAS, 317, 697

Einasto, J. 1965, Trudy Astrofizicheskogo Instituta Alma-Ata, 5, 87

Einstein, A. 1916, Annalen der Physik, 354, 769

Einstein, A. 1917, Sitzungsberichte der Königlich Preußischen Akademie der Wissenschaften (Berlin), Seite 142-152., 142

El-Zant, A., Shlosman, I., & Hoffman, Y. 2001, ApJ, 560, 636

El-Zant, A. A. 2006, MNRAS, 370, 1247

El-Zant, A. A., Hoffman, Y., Primack, J., Combes, F., & Shlosman, I. 2004, ApJ, 607, L75

Elbaz, D. & Cesarsky, C. J. 2003, Science, 300, 270

Elbaz, D., Daddi, E., Le Borgne, D., et al. 2007, A&A, 468, 33

Ellis, R. S., Colless, M., Broadhurst, T., Heyl, J., & Glazebrook, K. 1996, MNRAS, 280, 235

Elmegreen, B. G. 1991, in NATO Advanced Science Institutes (ASI) Series C, Vol. 342, NATO Advanced Science Institutes (ASI) Series C, ed. C. J. Lada & N. D. Kylafis, 35

Elmegreen, B. G. 2011, in EAS Publications Series, Vol. 51, EAS Publications Series, ed. C. Charbonnel & T. Montmerle, 19–30

Elmegreen, B. G., Bournaud, F., & Elmegreen, D. M. 2008, ApJ, 688, 67

Elmegreen, B. G. & Elmegreen, D. M. 1983, MNRAS, 203, 31

Elmegreen, B. G. & Elmegreen, D. M. 2005, ApJ, 627, 632

Elmegreen, B. G., Elmegreen, D. M., Fernandez, M. X., & Lemonias, J. J. 2009, ApJ, 692, 12

Elmegreen, D. M., Elmegreen, B. G., Ravindranath, S., & Coe, D. A. 2007, ApJ, 658, 763

Elmegreen, D. M., Elmegreen, B. G., & Sheets, C. M. 2004, ApJ, 603, 74

Engargiola, G., Plambeck, R. L., Rosolowsky, E., & Blitz, L. 2003, ApJS, 149, 343

Erb, D. K., Quider, A. M., Henry, A. L., & Martin, C. L. 2012, ApJ, 759, 26

Erb, D. K., Steidel, C. C., Shapley, A. E., et al. 2006, ApJ, 646, 107

Espada, D., Komugi, S., Muller, E., et al. 2012, ApJ, 760, L25

Faber, S. M. & Gallagher, J. S. 1979, ARA&A, 17, 135

Faber, S. M., Phillips, A. C., Kibrick, R. I., et al. 2003, in Society of Photo-Optical Instrumentation Engineers (SPIE) Conference Series, Vol. 4841, Instrument Design and Performance for Optical/Infrared Ground-based Telescopes, ed. M. Iye & A. F. M. Moorwood, 1657–1669

Fabian, A. C. 2012, ARA&A, 50, 455

Fabian, A. C., Sanders, J. S., Allen, S. W., et al. 2003, MNRAS, 344, L43

Falgarone, E., Pety, J., & Phillips, T. G. 2001, ApJ, 555, 178

Falgarone, E. & Puget, J. L. 1986, A&A, 162, 235

Famaey, B. & McGaugh, S. S. 2012, Living Reviews in Relativity, 15, 10

Feruglio, C., Maiolino, R., Piconcelli, E., et al. 2010, A&A, 518, L155

Finkelstein, S. L., Papovich, C., Salmon, B., et al. 2012, ApJ, 756, 164

Finley, H., Petitjean, P., Noterdaeme, P., & Pâris, I. 2014, A&A, 572, A31

Fischer, J., Sturm, E., González-Alfonso, E., et al. 2010, A&A, 518, L41

Fischera, J. & Martin, P. G. 2012, A&A, 542, A77

Flores, R. A. & Primack, J. R. 1994, ApJ, 427, L1

Förster Schreiber, N. M., Genzel, R., Bouché, N., et al. 2009, ApJ, 706, 1364

Förster Schreiber, N. M., Genzel, R., Lehnert, M. D., et al. 2006, ApJ, 645, 1062

Förster Schreiber, N. M., Genzel, R., Newman, S. F., et al. 2014, ApJ, 787, 38

Förster Schreiber, N. M., Shapley, A. E., Genzel, R., et al. 2011, ApJ, 739, 45

Freundlich, J., Combes, F., Tacconi, L. J., et al. 2013, A&A, 553, A130

Freundlich, J., Jog, C. J., & Combes, F. 2014a, A&A, 564, A7

Freundlich, J., Salomé, P., Combes, F., et al. 2014b, in SF2A-2014: Proceedings of the Annual meeting of the French Society of Astronomy and Astrophysics, ed. J. Ballet, F. Martins, F. Bournaud, R. Monier, & C. Reylé, 387–390

Fridman, A. M. & Poliachenko, V. L. 1984, Physics of gravitating systems. II - Nonlinear collective processes: Nonlinear waves, solitons, collisionless shocks, turbulence. Astrophysical applications

Fukugita, M., Hogan, C. J., & Peebles, P. J. E. 1998, ApJ, 503, 518

Fukugita, M. & Peebles, P. J. E. 2004, ApJ, 616, 643

Fukui, Y., Mizuno, N., Yamaguchi, R., et al. 1999, PASJ, 51, 745

Fumagalli, M., Prochaska, J. X., Kasen, D., et al. 2011, MNRAS, 418, 1796

Gabor, J. M. & Bournaud, F. 2014, MNRAS, 441, 1615

Gaibler, V., Khochfar, S., Krause, M., & Silk, J. 2012, MNRAS, 425, 438

Gallego, J., Zamorano, J., Aragon-Salamanca, A., & Rego, M. 1995, ApJ, 455, L1

Gao, L., Navarro, J. F., Cole, S., et al. 2008, MNRAS, 387, 536

Garrison-Kimmel, S., Boylan-Kolchin, M., Bullock, J. S., & Kirby, E. N. 2014, MNRAS, 444, 222

Garrison-Kimmel, S., Rocha, M., Boylan-Kolchin, M., Bullock, J. S., & Lally, J. 2013, MNRAS, 433, 3539

Geach, J. E., Hickox, R. C., Diamond-Stanic, A. M., et al. 2014, Nature, 516, 68

Geehan, J. J., Fardal, M. A., Babul, A., & Guhathakurta, P. 2006, MNRAS, 366, 996

Geller, M. J. & Huchra, J. P. 1989, Science, 246, 897

Gentile, G., Famaey, B., & de Blok, W. J. G. 2011, A&A, 527, A76

Genzel, R., Burkert, A., Bouché, N., et al. 2008, ApJ, 687, 59

Genzel, R., Förster Schreiber, N. M., Rosario, D., et al. 2014, ApJ, 796, 7

Genzel, R., Newman, S., Jones, T., et al. 2011, ApJ, 733, 101

Genzel, R., Pichon, C., Eckart, A., Gerhard, O. E., & Ott, T. 2000, MNRAS, 317, 348

Genzel, R., Tacconi, L. J., Eisenhauer, F., et al. 2006, Nature, 442, 786

Genzel, R., Tacconi, L. J., Gracia-Carpio, J., et al. 2010, MNRAS, 407, 2091

Genzel, R., Tacconi, L. J., Kurk, J., et al. 2013, ApJ, 773, 68

Genzel, R., Tacconi, L. J., Lutz, D., et al. 2015, ApJ, 800, 20

Gerbal, D., Durret, F., Lachieze-Rey, M., & Lima-Neto, G. 1992, A&A, 262, 395

Ghez, A. M., Salim, S., Hornstein, S. D., et al. 2005, ApJ, 620, 744

Giavalisco, M., Dickinson, M., Ferguson, H. C., et al. 2004, ApJ, 600, L103

Gnedin, N. Y. & Ostriker, J. P. 1997, ApJ, 486, 581

Gnedin, O. Y., Kravtsov, A. V., Klypin, A. A., & Nagai, D. 2004, ApJ, 616, 16

Gnedin, O. Y. & Zhao, H. 2002, MNRAS, 333, 299

Goerdt, T., Moore, B., Read, J. I., & Stadel, J. 2010, ApJ, 725, 1707

Goerdt, T., Moore, B., Read, J. I., Stadel, J., & Zemp, M. 2006, MNRAS, 368, 1073

Goldsmith, P. F., Heyer, M., Narayanan, G., et al. 2008, ApJ, 680, 428

Gómez, G. C. & Vázquez-Semadeni, E. 2014, ApJ, 791, 124

Gong, M. & Ostriker, E. C. 2015, ApJ, 806, 31

Goodman, J. 2000, New A, 5, 103

Gott, III, J. R., Jurić, M., Schlegel, D., et al. 2005, ApJ, 624, 463

Governato, F., Brook, C., Mayer, L., et al. 2010, Nature, 463, 203

Governato, F., Zolotov, A., Pontzen, A., et al. 2012, MNRAS, 422, 1231

Gray, W. J. & Scannapieco, E. 2013, ApJ, 768, 174

Greif, T. H., Johnson, J. L., Bromm, V., & Klessen, R. S. 2007, ApJ, 670, 1

Guedes, J., Callegari, S., Madau, P., & Mayer, L. 2011, ApJ, 742, 76

Gusev, A. S. & Efremov, Y. N. 2013, MNRAS, 434, 313

Gustafsson, M., Fairbairn, M., & Sommer-Larsen, J. 2006, Phys. Rev. D, 74, 123522

Habart, E., Walmsley, M., Verstraete, L., et al. 2005, Space Sci. Rev., 119, 71

Hacar, A., Tafalla, M., Kauffmann, J., & Kovács, A. 2013, A&A, 554, A55

Haiman, Z., Rees, M. J., & Loeb, A. 1997, ApJ, 476, 458

Hamajima, K. & Tosa, M. 1975, PASJ, 27, 561

Hammer, F., Yang, Y. B., Flores, H., Puech, M., & Fouquet, S. 2015, ApJ, 813, 110

Hansen, C. J., Aizenman, M. L., & Ross, R. L. 1976, ApJ, 207, 736

Harford, A. G. & Hamilton, A. J. S. 2011, MNRAS, 416, 2678

Harford, A. G., Hamilton, A. J. S., & Gnedin, N. Y. 2008, MNRAS, 389, 880

Harris, W. E. 1996, AJ, 112, 1487

Hartmann, L. 2002, ApJ, 578, 914

Hartwick, F. D. A. 1971, ApJ, 163, 431

Hatchell, J., Richer, J. S., Fuller, G. A., et al. 2005, A&A, 440, 151

Hayashi, E. & White, S. D. M. 2008, MNRAS, 388, 2

He, G.-W. & Zhang, J.-B. 2006, Phys. Rev. E, 73, 055303

He, X. & Tong, P. 2011, Phys. Rev. E, 83, 037302

Heckman, T. M., Armus, L., & Miley, G. K. 1990, ApJS, 74, 833

Heiderman, A., Evans, II, N. J., Allen, L. E., Huard, T., & Heyer, M. 2010, ApJ, 723, 1019

Heitsch, F. 2013, ApJ, 769, 115

Henderson, A. P., Jackson, P. D., & Kerr, F. J. 1982, ApJ, 263, 116

Hennebelle, P. 2013, A&A, 556, A153

Hennebelle, P. & André, P. 2013, A&A, 560, A68

Hennebelle, P. & Falgarone, E. 2012, A&A Rev., 20, 55

Hernandez, X., Valls-Gabaud, D., & Gilmore, G. 2000, MNRAS, 316, 605

Hernquist, L. & Ostriker, J. P. 1992, ApJ, 386, 375

Herschel, W. 1785, Royal Society of London Philosophical Transactions Series I, 75, 213

Heyer, M., Krawczyk, C., Duval, J., & Jackson, J. M. 2009, ApJ, 699, 1092

Heyer, M. H. & Brunt, C. M. 2004, ApJ, 615, L45

Heyer, M. H., Corbelli, E., Schneider, S. E., & Young, J. S. 2004, ApJ, 602, 723

Hily-Blant, P. & Falgarone, E. 2007, A&A, 469, 173

Hlozek, R., Dunkley, J., Addison, G., et al. 2012, ApJ, 749, 90

Hodge, J. A., Carilli, C. L., Walter, F., et al. 2012, ApJ, 760, 11

Hodge, J. A., Riechers, D., Decarli, R., et al. 2015, ApJ, 798, L18

Hopkins, P. F., Cox, T. J., Younger, J. D., & Hernquist, L. 2009, ApJ, 691, 1168

Hopkins, P. F., Kereš, D., Oñorbe, J., et al. 2014, MNRAS, 445, 581

Hu, W., Barkana, R., & Gruzinov, A. 2000, Physical Review Letters, 85, 1158

Huang, S., Dubinski, J., & Carlberg, R. G. 1993, ApJ, 404, 73

Hubble, E. 1929, Proceedings of the National Academy of Science, 15, 168

Hubble, E. P. 1925, The Observatory, 48, 139

Hubble, E. P. 1936, Realm of the Nebulae

Iben, Jr., I. 1965, ApJ, 141, 993

Immeli, A., Samland, M., Gerhard, O., & Westera, P. 2004, A&A, 413, 547

Inutsuka, S.-I. & Miyama, S. M. 1992, ApJ, 388, 392

Inutsuka, S.-i. & Miyama, S. M. 1997, ApJ, 480, 681

Jackson, J. M., Finn, S. C., Chambers, E. T., Rathborne, J. M., & Simon, R. 2010, ApJ, 719, L185

Jeans, J. H. 1902, Royal Society of London Philosophical Transactions Series A, 199, 1

Jeans, J. H. 1928, Astronomy and cosmogony

Jobin, M. & Carignan, C. 1990, AJ, 100, 648

Jog, C. J. 2013, MNRAS, 434, L56

Jog, C. J. & Solomon, P. M. 1984, ApJ, 276, 114

Jones, C. E. & Basu, S. 2002, ApJ, 569, 280

Jones, C. E., Basu, S., & Dubinski, J. 2001, ApJ, 551, 387

Jones, T. A., Swinbank, A. M., Ellis, R. S., Richard, J., & Stark, D. P. 2010, MNRAS, 404, 1247

Kainulainen, J., Ragan, S. E., Henning, T., & Stutz, A. 2013, A&A, 557, A120

Kamionkowski, M. & Liddle, A. R. 2000, Physical Review Letters, 84, 4525

Kant, I. 1755, Allgemeine Naturgeschichte und Theorie des Himmels

Karachentsev, I. D., Karachentseva, V. E., Huchtmeier, W. K., & Makarov, D. I. 2004, AJ, 127, 2031

Kassin, S. A., Weiner, B. J., Faber, S. M., et al. 2012, ApJ, 758, 106

Kazantzidis, S., Zentner, A. R., & Kravtsov, A. V. 2006, ApJ, 641, 647

Kennedy, R., Frenk, C., Cole, S., & Benson, A. 2014, MNRAS, 442, 2487

Kennicutt, R. C. & Evans, N. J. 2012, ARA&A, 50, 531

Kennicutt, Jr., R. C. 1992, ApJ, 388, 310

Kennicutt, Jr., R. C. 1998a, ARA&A, 36, 189

Kennicutt, Jr., R. C. 1998b, ApJ, 498, 541

Kennicutt, Jr., R. C., Calzetti, D., Walter, F., et al. 2007, ApJ, 671, 333

Kereš, D., Katz, N., Fardal, M., Davé, R., & Weinberg, D. H. 2009, MNRAS, 395, 160

Kereš, D., Katz, N., Weinberg, D. H., & Davé, R. 2005, MNRAS, 363, 2

Kewley, L. J., Geller, M. J., & Jansen, R. A. 2004, AJ, 127, 2002

Kirk, J. M., Ward-Thompson, D., Palmeirim, P., et al. 2013, MNRAS, 432, 1424

Klessen, R. S., Ballesteros-Paredes, J., Li, Y., & Mac Low, M.-M. 2004, in Astronomical Society of the Pacific Conference Series, Vol. 322, The Formation and Evolution of Massive Young Star Clusters, ed. H. J. G. L. M. Lamers, L. J. Smith, & A. Nota, 299–308

Klessen, R. S. & Hennebelle, P. 2010, A&A, 520, A17

Klypin, A., Kravtsov, A. V., Valenzuela, O., & Prada, F. 1999, ApJ, 522, 82

Klypin, A. A., Trujillo-Gomez, S., & Primack, J. 2011, ApJ, 740, 102

Knapen, J. H. & Beckman, J. E. 1996, MNRAS, 283, 251

Kochanek, C. S. & White, M. 2000, ApJ, 543, 514

Koda, J., Scoville, N., Hasegawa, T., et al. 2012, ApJ, 761, 41

Komatsu, E., Smith, K. M., Dunkley, J., et al. 2011, ApJS, 192, 18

Konyves, V., Andre, P., Men'shchikov, A., et al. 2015, ArXiv: 1507.05926

Könyves, V., André, P., Men'shchikov, A., et al. 2010, A&A, 518, L106

Kormendy, J. 2015, ArXiv: 1504.03330

Kormendy, J. & Barentine, J. C. 2010, ApJ, 715, L176

Kormendy, J. & Bender, R. 2012, ApJS, 198, 2

Kormendy, J., Drory, N., Bender, R., & Cornell, M. E. 2010, ApJ, 723, 54

Kormendy, J. & Fisher, D. B. 2008, in Astronomical Society of the Pacific Conference Series, Vol. 396, Formation and Evolution of Galaxy Disks, ed. J. G. Funes & E. M. Corsini, 297

Kormendy, J. & Kennicutt, Jr., R. C. 2004, ARA&A, 42, 603

Kornei, K. A., Shapley, A. E., Martin, C. L., et al. 2012, ApJ, 758, 135

Kragh, H. S. 2007, "Conceptions of Cosmos. From Myths to the Accelerating Universe: A History of Cosmology" (Oxford University Press)

Kraichnan, R. H. 1964, Physics of Fluids, 7, 1723

Kriek, M., van Dokkum, P. G., Franx, M., Illingworth, G. D., & Magee, D. K. 2009, ApJ, 705, L71

Kroupa, P. 2001, MNRAS, 322, 231

Kroupa, P. 2002, Science, 295, 82

Kroupa, P., Theis, C., & Boily, C. M. 2005, A&A, 431, 517

Krumholz, M. R., Dekel, A., & McKee, C. F. 2012, ApJ, 745, 69

Krumholz, M. R. & Matzner, C. D. 2009, ApJ, 703, 1352

Krumholz, M. R. & McKee, C. F. 2005, ApJ, 630, 250

Krumholz, M. R. & Thompson, T. A. 2012, ApJ, 760, 155

Kudoh, T. & Basu, S. 2008, ApJ, 679, L97

Kuzio de Naray, R., Martinez, G. D., Bullock, J. S., & Kaplinghat, M. 2010, ApJ, 710, L161

Kuzio de Naray, R. & Spekkens, K. 2011, ApJ, 741, L29

Lada, C. J., Lombardi, M., & Alves, J. F. 2010, ApJ, 724, 687

Laporte, C. F. P. & Peñarrubia, J. 2015, MNRAS, 449, L90

Larson, R. B. 1969, MNRAS, 145, 271

Larson, R. B. 1974, MNRAS, 169, 229

Larson, R. B. 1981, MNRAS, 194, 809

Larson, R. B. 1985, MNRAS, 214, 379

Larson, R. B. & Tinsley, B. M. 1978, ApJ, 219, 46

Law, D. R., Steidel, C. C., Erb, D. K., et al. 2009, ApJ, 697, 2057

Lehner, N., Savage, B. D., Richter, P., et al. 2007, ApJ, 658, 680

Lehnert, M. D. & Heckman, T. M. 1996, ApJ, 462, 651

Lehnert, M. D., Le Tiran, L., Nesvadba, N. P. H., et al. 2013, A&A, 555, A72

Leisawitz, D., Bash, F. N., & Thaddeus, P. 1989, ApJS, 70, 731

Leroy, A. K., Bigiel, F., de Blok, W. J. G., et al. 2012, AJ, 144, 3

Leroy, A. K., Walter, F., Brinks, E., et al. 2008, AJ, 136, 2782

Leroy, A. K., Walter, F., Sandstrom, K., et al. 2013, AJ, 146, 19

L'Huillier, B., Combes, F., & Semelin, B. 2012, A&A, 544, A68

Li, Y.-S. & Helmi, A. 2008, MNRAS, 385, 1365

Li, Z.-Y., Wang, P., Abel, T., & Nakamura, F. 2010, ApJ, 720, L26

Licquia, T. C. & Newman, J. A. 2015, ApJ, 806, 96

Lilly, S. J., Carollo, C. M., Pipino, A., Renzini, A., & Peng, Y. 2013, ApJ, 772, 119

Lilly, S. J., Le Fevre, O., Hammer, F., & Crampton, D. 1996, ApJ, 460, L1

Lin, C. C., Mestel, L., & Shu, F. H. 1965, ApJ, 142, 1431

Lin, C. C. & Shu, F. H. 1964, ApJ, 140, 646

Lin, C. C. & Shu, F. H. 1966, Proceedings of the National Academy of Science, 55, 229

Lindblad, B. 1963, Stockholms Observatoriums Annaler, 22, 3

Loeb, A. 2011, J. Cosmology Astropart. Phys., 4, 23

Loeb, A. & Furlanetto, S. R. 2013, "The First Galaxies in the Universe"

Lombardi, M., Alves, J., & Lada, C. J. 2010, A&A, 519, L7

Loren, R. B. 1989, ApJ, 338, 925

Lovell, M. R., Eke, V., Frenk, C. S., et al. 2012, MNRAS, 420, 2318

Lovell, M. R., Eke, V. R., Frenk, C. S., & Jenkins, A. 2011, MNRAS, 413, 3013

Lovell, M. R., Frenk, C. S., Eke, V. R., et al. 2014, MNRAS, 439, 300

L'vov, V. S., Pomyalov, A., & Procaccia, I. 2001, Phys. Rev. E, 63, 056118

Lynden-Bell, D. 1969, Nature, 223, 690

Lynden-Bell, D. 1976, MNRAS, 174, 695

Mac Low, M.-M. & Ferrara, A. 1999, ApJ, 513, 142

Macciò, A. V., Dutton, A. A., van den Bosch, F. C., et al. 2007, MNRAS, 378, 55

Macciò, A. V., Ruchayskiy, O., Boyarsky, A., & Muñoz-Cuartas, J. C. 2013, MNRAS, 428, 882

Macciò, A. V., Stinson, G., Brook, C. B., et al. 2012, ApJ, 744, L9

Madau, P. 1997, in American Institute of Physics Conference Series, Vol. 393, American Institute of Physics Conference Series, ed. S. S. Holt & L. G. Mundy, 481–490

Madau, P. & Dickinson, M. 2014, ARA&A, 52, 415

Madau, P., Ferguson, H. C., Dickinson, M. E., et al. 1996, MNRAS, 283, 1388

Madau, P., Shen, S., & Governato, F. 2014, ApJ, 789, L17

Madore, B. F. 1977, MNRAS, 178, 1

Madore, B. F., van den Bergh, S., & Rogstad, D. H. 1974, ApJ, 191, 317

Magdis, G. E., Daddi, E., Béthermin, M., et al. 2012, ApJ, 760, 6

Maiolino, R., Gallerani, S., Neri, R., et al. 2012, MNRAS, 425, L66

Malinen, J., Juvela, M., Rawlings, M. G., et al. 2012, A&A, 544, A50

Maller, A. H. & Dekel, A. 2002, MNRAS, 335, 487

Mannucci, F., Cresci, G., Maiolino, R., Marconi, A., & Gnerucci, A. 2010, MNRAS, 408, 2115

Marsh, D. J. E. & Silk, J. 2014, MNRAS, 437, 2652

Martig, M. & Bournaud, F. 2008, MNRAS, 385, L38

Martínez, V. J. & Saar, E. 2002, Statistics of the Galaxy Distribution (Chapman)

Martizzi, D., Teyssier, R., & Moore, B. 2013, MNRAS, 432, 1947

Martizzi, D., Teyssier, R., Moore, B., & Wentz, T. 2012, MNRAS, 422, 3081

Mashchenko, S., Couchman, H. M. P., & Wadsley, J. 2006, Nature, 442, 539

Mashchenko, S., Wadsley, J., & Couchman, H. M. P. 2008, Science, 319, 174

Mastrobuono-Battisti, A., Di Matteo, P., Montuori, M., & Haywood, M. 2012, A&A, 546, L7

Mateo, M. L. 1998, ARA&A, 36, 435

Matsumoto, T., Nakamura, F., & Hanawa, T. 1994, PASJ, 46, 243

McClure-Griffiths, N. M., Dickey, J. M., Gaensler, B. M., Green, A. J., & Haverkorn, M. 2006, ApJ, 652, 1339

McGaugh, S. S., Bothun, G. D., & Schombert, J. M. 1995, AJ, 110, 573

McGaugh, S. S. & de Blok, W. J. G. 1998a, ApJ, 499, 41

McGaugh, S. S. & de Blok, W. J. G. 1998b, ApJ, 499, 66

McGaugh, S. S., de Blok, W. J. G., Schombert, J. M., Kuzio de Naray, R., & Kim, J. H. 2007, ApJ, 659, 149

McKee, C. F. & Ostriker, E. C. 2007, ARA&A, 45, 565

McMillan, P. J. 2011, MNRAS, 414, 2446

Meiron, Y., Li, B., Holley-Bockelmann, K., & Spurzem, R. 2014, ApJ, 792, 98

Men'shchikov, A., André, P., Didelon, P., et al. 2010, A&A, 518, L103

Merritt, D., Navarro, J. F., Ludlow, A., & Jenkins, A. 2005, ApJ, 624, L85

Messier, C. 1781, Catalogue des Nébuleuses & des amas d'Étoiles (Catalog of Nebulae and Star Clusters), Tech. rep.

Metz, M., Kroupa, P., & Jerjen, H. 2007, MNRAS, 374, 1125

Mihos, J. C. & Hernquist, L. 1996, ApJ, 464, 641

Mikhailovskii, A. B. & Fridman, A. M. 1972, Soviet Physics - JETP, 34, 243

Mikhailovskii, A. B. & Fridman, A. M. 1973, Soviet Physics - JETP, 17, 57

Milgrom, M. 1983a, ApJ, 270, 365

Milgrom, M. 1983b, ApJ, 270, 371

Milgrom, M. 1983c, ApJ, 270, 384

Miralda-Escudé, J. 2002, ApJ, 564, 60

Misiriotis, A., Xilouris, E. M., Papamastorakis, J., Boumis, P., & Goudis, C. D. 2006, A&A, 459, 113

Miville-Deschênes, M.-A., Martin, P. G., Abergel, A., et al. 2010, A&A, 518, L104

Miyama, S. M., Narita, S., & Hayashi, C. 1987a, Progress of Theoretical Physics, 78, 1051

Miyama, S. M., Narita, S., & Hayashi, C. 1987b, Progress of Theoretical Physics, 78, 1273

Mizuno, A., Onishi, T., Yonekura, Y., et al. 1995, ApJ, 445, L161

Mo, H., van den Bosch, F. C., & White, S. 2010, "Galaxy Formation and Evolution"

Moore, B. 1994, Nature, 370, 629

Moore, B., Ghigna, S., Governato, F., et al. 1999, ApJ, 524, L19

Mortlock, D. J., Warren, S. J., Venemans, B. P., et al. 2011, Nature, 474, 616

Moster, B. P., Somerville, R. S., Maulbetsch, C., et al. 2010, ApJ, 710, 903

Moustakas, J., Kennicutt, Jr., R. C., & Tremonti, C. A. 2006, ApJ, 642, 775

Murray, N., Quataert, E., & Thompson, T. A. 2010, ApJ, 709, 191

Myers, P. C. 2009, ApJ, 700, 1609

Myers, P. C. & Fuller, G. A. 1992, ApJ, 396, 631

Myers, P. C., Fuller, G. A., Goodman, A. A., & Benson, P. J. 1991, ApJ, 376, 561

Naab, T. 2013, in IAU Symposium, Vol. 295, IAU Symposium, ed. D. Thomas, A. Pasquali, & I. Ferreras, 340–349

Nagai, T., Inutsuka, S.-i., & Miyama, S. M. 1998, ApJ, 506, 306

Nagasawa, M. 1987, Progress of Theoretical Physics, 77, 635

Nakamura, F., Hanawa, T., & Nakano, T. 1993, PASJ, 45, 551

Nakamura, F., Hanawa, T., & Nakano, T. 1995, ApJ, 444, 770

Nakamura, F. & Li, Z.-Y. 2008, ApJ, 687, 354

Narayanan, G., Heyer, M. H., Brunt, C., et al. 2008, ApJS, 177, 341

Navarro, J. F. & Benz, W. 1991, ApJ, 380, 320

Navarro, J. F., Eke, V. R., & Frenk, C. S. 1996a, MNRAS, 283, L72

Navarro, J. F., Frenk, C. S., & White, S. D. M. 1995, MNRAS, 275, 56

Navarro, J. F., Frenk, C. S., & White, S. D. M. 1996b, ApJ, 462, 563

Navarro, J. F., Frenk, C. S., & White, S. D. M. 1997, ApJ, 490, 493

Navarro, J. F., Hayashi, E., Power, C., et al. 2004, MNRAS, 349, 1039

Navarro, J. F. & Steinmetz, M. 2000, ApJ, 538, 477

Nayakshin, S. & Zubovas, K. 2012, MNRAS, 427, 372

Ness, M., Freeman, K., Athanassoula, E., et al. 2013, MNRAS, 432, 2092

Newman, J. A., Cooper, M. C., Davis, M., et al. 2013, ApJS, 208, 5

Newman, S. F., Genzel, R., Förster-Schreiber, N. M., et al. 2012a, ApJ, 761, 43

Newman, S. F., Shapiro Griffin, K., Genzel, R., et al. 2012b, ApJ, 752, 111

Newton, K. 1980, MNRAS, 190, 689

Noeske, K. G., Weiner, B. J., Faber, S. M., et al. 2007, ApJ, 660, L43

Nozawa, S., Mizuno, A., Teshima, Y., Ogawa, H., & Fukui, Y. 1991, ApJS, 77, 647

Ntormousi, E., Hennebelle, P., & André, P. 2015, IAU General Assembly, 22, 52264

Nutter, D., Kirk, J. M., Stamatellos, D., & Ward-Thompson, D. 2008, MNRAS, 384, 755

Oñorbe, J., Boylan-Kolchin, M., Bullock, J. S., et al. 2015, ArXiv: 1502.02036

Ocvirk, P., Pichon, C., & Teyssier, R. 2008, MNRAS, 390, 1326

Odenkirchen, M., Grebel, E. K., Dehnen, W., Rix, H.-W., & Cudworth, K. M. 2002, AJ, 124, 1497

O'Donnell, J. E. 1994, ApJ, 422, 158

Oesch, P. A., Bouwens, R. J., Illingworth, G. D., et al. 2014, ApJ, 786, 108

Ogiya, G. & Burkert, A. 2015, MNRAS, 446, 2363

Oh, S.-H., de Blok, W. J. G., Brinks, E., Walter, F., & Kennicutt, Jr., R. C. 2011, AJ, 141, 193

Oh, S.-H., Hunter, D. A., Brinks, E., et al. 2015, AJ, 149, 180

Olano, C. A., Walmsley, C. M., & Wilson, T. L. 1988, A&A, 196, 194

Olave-Rojas, D., Torres-Flores, S., Carrasco, E. R., et al. 2015, MNRAS, 453, 2808

Onishi, T., Mizuno, A., Kawamura, A., Ogawa, H., & Fukui, Y. 1996, ApJ, 465, 815

Oort, J. H. & Spitzer, Jr., L. 1955, ApJ, 121, 6

Opik, E. 1922, ApJ, 55, 406

Ostriker, J. 1964a, ApJ, 140, 1529

Ostriker, J. 1964b, ApJ, 140, 1056

Padoan, P., Juvela, M., Goodman, A. A., & Nordlund, Å. 2001, ApJ, 553, 227

Palmeirim, P., André, P., Kirk, J., et al. 2013, A&A, 550, A38

Panter, B., Jimenez, R., Heavens, A. F., & Charlot, S. 2007, MNRAS, 378, 1550

Papastergis, E., Giovanelli, R., Haynes, M. P., & Shankar, F. 2015, A&A, 574, A113

Pawlowski, M. S., Kroupa, P., & de Boer, K. S. 2011, A&A, 532, A118

Peacock, J. A. 1999, Cosmological Physics

Peacock, J. A., Cole, S., Norberg, P., et al. 2001, Nature, 410, 169

Peebles, P. J. E. 1993, Principles of Physical Cosmology

Peretto, N., Fuller, G. A., Duarte-Cabral, A., et al. 2013, A&A, 555, A112

Perret, V., Renaud, F., Epinat, B., et al. 2014, A&A, 562, A1

Peter, A. H. G., Rocha, M., Bullock, J. S., & Kaplinghat, M. 2013, MNRAS, 430, 105

Petraki, K. & Volkas, R. R. 2013, International Journal of Modern Physics A, 28, 30028

Pettini, M., Steidel, C. C., Adelberger, K. L., Dickinson, M., & Giavalisco, M. 2000, ApJ, 528, 96

Planck Collaboration, Ade, P. A. R., Aghanim, N., et al. 2014, A&A, 571, A16

Planck Collaboration, Ade, P. A. R., Aghanim, N., et al. 2013, A&A, 550, A134

Planck Collaboration, Ade, P. A. R., Aghanim, N., et al. 2015, ArXiv: 1502.01589

Pon, A., Johnstone, D., & Heitsch, F. 2011, ApJ, 740, 88

Pontzen, A. & Governato, F. 2012, MNRAS, 421, 3464

Pontzen, A. & Governato, F. 2014, Nature, 506, 171

Pontzen, A., Read, J. I., Teyssier, R., et al. 2015, MNRAS, 451, 1366

Pounds, K. A. & Page, K. L. 2006, MNRAS, 372, 1275

Press, W. H. & Schechter, P. 1974, ApJ, 187, 425

Primack, J. 2012, Annalen der Physik, 524, 535

Pudritz, R. E. & Kevlahan, N. K.-R. 2013, Philosophical Transactions of the Royal Society of London Series A, 371, 20248

Quillen, A. C. & Comparetta, J. 2010, ArXiv: 1002.4870

Rand, R. J. & Kulkarni, S. R. 1990, ApJ, 349, L43

Randall, S. W., Nulsen, P. E. J., Jones, C., et al. 2015, ApJ, 805, 112

Rawle, T. D., Egami, E., Bussmann, R. S., et al. 2014, ApJ, 783, 59

Read, J. I. & Gilmore, G. 2005, MNRAS, 356, 107

Recchi, S., Hacar, A., & Palestini, A. 2013, A&A, 558, A27

Reddy, N. A. & Steidel, C. C. 2009, ApJ, 692, 778

Rees, M. J. 1984, ARA&A, 22, 471

Rees, M. J. & Ostriker, J. P. 1977, MNRAS, 179, 541

Renaud, F., Bournaud, F., Emsellem, E., et al. 2013, MNRAS, 436, 1836

Ribas, I., Jordi, C., Vilardell, F., et al. 2005, ApJ, 635, L37

Riess, A. G., Filippenko, A. V., Challis, P., et al. 1998, AJ, 116, 1009

Roberts, W. W. 1969, ApJ, 158, 123

Robertson, B. E. & Kravtsov, A. V. 2008, ApJ, 680, 1083

Rocha, M., Peter, A. H. G., Bullock, J. S., et al. 2013, MNRAS, 430, 81

Rodighiero, G., Daddi, E., Baronchelli, I., et al. 2011, ApJ, 739, L40

Rodrigues, I., Dottori, H., Brinks, E., & Mirabel, I. F. 1999, AJ, 117, 2695

Romano-Díaz, E., Shlosman, I., Hoffman, Y., & Heller, C. 2008, ApJ, 685, L105

Roos, O., Juneau, S., Bournaud, F., & Gabor, J. M. 2015, ApJ, 800, 19

Rosse, T. E. O. 1850, Philosophical Transactions of the Royal Society of London Series I, 140, 499

Rubin, K. H. R., Prochaska, J. X., Koo, D. C., & Phillips, A. C. 2012, ApJ, 747, L26

Rubin, K. H. R., Weiner, B. J., Koo, D. C., et al. 2010, ApJ, 719, 1503

Rubin, V. C. & Ford, Jr., W. K. 1970, ApJ, 159, 379

Rubin, V. C., Ford, Jr., W. K., Thonnard, N., & Burstein, D. 1982, ApJ, 261, 439

Rubin, V. C., Ford, W. K. J., & . Thonnard, N. 1980, ApJ, 238, 471

Rupke, D. S., Veilleux, S., & Sanders, D. B. 2005a, ApJ, 632, 751

Rupke, D. S., Veilleux, S., & Sanders, D. B. 2005b, ApJS, 160, 115

Saha, K. 2015, ApJ, 806, L29

Saintonge, A., Kauffmann, G., Kramer, C., et al. 2011a, MNRAS, 415, 32

Saintonge, A., Kauffmann, G., Wang, J., et al. 2011b, MNRAS, 415, 61

Sakamoto, K., Aalto, S., Wilner, D. J., et al. 2009, ApJ, 700, L104

Salomé, P., Combes, F., Edge, A. C., et al. 2006, A&A, 454, 437

Salomé, Q., Salomé, P., & Combes, F. 2015, A&A, 574, A34

Salpeter, E. E. 1955, ApJ, 121, 161

Sandage, A. 1961, The Hubble atlas of galaxies

Sanders, D. B., Soifer, B. T., Elias, J. H., et al. 1988, ApJ, 325, 74

Sanders, R. H. 1996, ApJ, 473, 117

Sanders, R. H. 1999, ApJ, 512, L23

Sanders, R. H. & McGaugh, S. S. 2002, ARA&A, 40, 263

Sanders, R. H. & Noordermeer, E. 2007, MNRAS, 379, 702

Sanders, R. H. & Verheijen, M. A. W. 1998, ApJ, 503, 97

Sanduleak, N. 1969, AJ, 74, 47

Santini, P., Fontana, A., Grazian, A., et al. 2009, A&A, 504, 751

Sargent, M. T., Béthermin, M., Daddi, E., & Elbaz, D. 2012, ApJ, 747, L31

Scalo, J. M. 1986, Fund. Cosmic Phys., 11, 1

Schaller, M., Frenk, C. S., Bower, R. G., et al. 2015, MNRAS, 451, 1247

Schinnerer, E., Meidt, S. E., Pety, J., et al. 2013, ApJ, 779, 42

Schive, H.-Y., Liao, M.-H., Woo, T.-P., et al. 2014, Physical Review Letters, 113, 261302

Schlegel, D. J., Finkbeiner, D. P., & Davis, M. 1998, ApJ, 500, 525

Schmidt, M. 1959, ApJ, 129, 243

Schneider, A. 2015, MNRAS, 451, 3117

Schneider, A. & Moore, B. 2011, MNRAS, 415, 1569

Schneider, A., Smith, R. E., Macciò, A. V., & Moore, B. 2012, MNRAS, 424, 684

Schneider, S. & Elmegreen, B. G. 1979, ApJS, 41, 87

Schödel, R., Ott, T., Genzel, R., et al. 2003, ApJ, 596, 1015

Schruba, A., Leroy, A. K., Walter, F., et al. 2011, AJ, 142, 37

Schuster, K. F., Kramer, C., Hitschfeld, M., Garcia-Burillo, S., & Mookerjea, B. 2007, A&A, 461, 143

Schweizer, F. 1976, ApJS, 31, 313

Scoville, N., Sheth, K., Aussel, H., et al. 2015, ArXiv: 1505.02159

Scoville, N. Z., Polletta, M., Ewald, S., et al. 2001, AJ, 122, 3017

Sérsic, J. L. 1963, Boletin de la Asociacion Argentina de Astronomia La Plata Argentina, 6, 41

Sersic, J. L. 1968, Atlas de galaxias australes

Shandarin, S. F. & Zeldovich, Y. B. 1989, Reviews of Modern Physics, 61, 185

Shankar, F., Lapi, A., Salucci, P., De Zotti, G., & Danese, L. 2006, ApJ, 643, 14

Shao, S., Gao, L., Theuns, T., & Frenk, C. S. 2013, MNRAS, 430, 2346

Shapiro, K. L., Genzel, R., Quataert, E., et al. 2009, ApJ, 701, 955

Shapley, A. E., Steidel, C. C., Pettini, M., & Adelberger, K. L. 2003, ApJ, 588, 65

Shapley, H. 1918, PASP, 30, 42

Sharon, C. E., Baker, A. J., Harris, A. I., & Thomson, A. P. 2013, ApJ, 765, 6

Shen, J., Rich, R. M., Kormendy, J., et al. 2010, ApJ, 720, L72

Shi, Y., Helou, G., Yan, L., et al. 2011, ApJ, 733, 87

Silk, J. 2005, MNRAS, 364, 1337

Silk, J. & Norman, C. 2009, ApJ, 700, 262

Silk, J. & Rees, M. J. 1998, A&A, 331, L1

Simon, R. 1963, Annales d'Astrophysique, 26, 224

Singer, D. W. 1950, Giordano Bruno - His Life and Thought. With annotated translation of his work "On the Infinite Universe and Worlds"

Smith, B. J., Struck, C., Hancock, M., et al. 2008, AJ, 135, 2406

Smith, S. 1936, ApJ, 83, 23

Solomon, P. M. & Barrett, J. W. 1991, in IAU Symposium, Vol. 146, Dynamics of Galaxies and Their Molecular Cloud Distributions, ed. F. Combes & F. Casoli, 235

Solomon, P. M., Downes, D., Radford, S. J. E., & Barrett, J. W. 1997, ApJ, 478, 144

Solomon, P. M., Rivolo, A. R., Barrett, J., & Yahil, A. 1987, ApJ, 319, 730

Somerville, R. S., Hopkins, P. F., Cox, T. J., Robertson, B. E., & Hernquist, L. 2008, MNRAS, 391, 481

Songaila, A., Cowie, L. L., Hu, E. M., & Gardner, J. P. 1994, ApJS, 94, 461

Sparke, L. S. & Gallagher, III, J. S. 2007, "Galaxies in the Universe: An Introduction" (Cambridge University Press)

Spergel, D. N. & Steinhardt, P. J. 2000, Physical Review Letters, 84, 3760

Springel, V., Wang, J., Vogelsberger, M., et al. 2008, MNRAS, 391, 1685

Springel, V., White, S. D. M., Jenkins, A., et al. 2005, Nature, 435, 629

Stahler, S. W., Shu, F. H., & Taam, R. E. 1980, ApJ, 241, 637

Stanek, K. Z., Mateo, M., Udalski, A., et al. 1994, ApJ, 429, L73

Stark, D. P., Swinbank, A. M., Ellis, R. S., et al. 2008, Nature, 455, 775

Stecher, T. P. & Williams, D. A. 1967, ApJ, 149, L29

Steinmetz, M. & Navarro, J. F. 1999, ApJ, 513, 555

Stepnik, B., Abergel, A., Bernard, J.-P., et al. 2003, A&A, 398, 551

Stodólkiewicz, J. S. 1963, Acta Astron., 13, 30

Strickland, D. K. & Heckman, T. M. 2009, ApJ, 697, 2030

Strigari, L. E., Bullock, J. S., Kaplinghat, M., et al. 2006, ApJ, 652, 306

Sturm, E., González-Alfonso, E., Veilleux, S., et al. 2011, ApJ, 733, L16

Swaters, R. A., Sanders, R. H., & McGaugh, S. S. 2010, ApJ, 718, 380

Swinbank, A. M., Papadopoulos, P. P., Cox, P., et al. 2011, ApJ, 742, 11

Swinbank, A. M., Smail, I., Longmore, S., et al. 2010, Nature, 464, 733

Swinbank, A. M., Smail, I., Sobral, D., et al. 2012, ApJ, 760, 130

Tacconi, L. J., Genzel, R., Neri, R., et al. 2010, Nature, 463, 781

Tacconi, L. J., Neri, R., Genzel, R., et al. 2013, ApJ, 768, 74

Tachihara, K., Mizuno, A., & Fukui, Y. 2000, ApJ, 528, 817

Tatematsu, K., Umemoto, T., Kameya, O., et al. 1993, ApJ, 404, 643

Taylor, G. I. 1938, Proceedings of the Royal Society of London A: Mathematical, Physical and Engineering Sciences, 164, 476

Tennekes, H. 1975, Journal of Fluid Mechanics, 67, 561

Teyssier, R. 2002, A&A, 385, 337

Teyssier, R., Chapon, D., & Bournaud, F. 2010, ApJ, 720, L149

Teyssier, R., Pontzen, A., Dubois, Y., & Read, J. I. 2013, MNRAS, 429, 3068

Tielens, A. G. G. M. 2013, Reviews of Modern Physics, 85, 1021

Tilley, D. A. & Pudritz, R. E. 2007, MNRAS, 382, 73

Tiret, O. & Combes, F. 2007, A&A, 464, 517

Tiret, O. & Combes, F. 2008, in Astronomical Society of the Pacific Conference Series, Vol. 396, Formation and Evolution of Galaxy Disks, ed. J. G. Funes & E. M. Corsini, 259

Tomisaka, K. 1995, ApJ, 438, 226

Tomisaka, K. 1996, PASJ, 48, 701

Tonini, C., Lapi, A., & Salucci, P. 2006, ApJ, 649, 591

Toomre, A. 1964, ApJ, 139, 1217

Toomre, A. & Toomre, J. 1972, ApJ, 178, 623

Torres-Flores, S., Scarano, S., Mendes de Oliveira, C., et al. 2014, MNRAS, 438, 1894

Tosa, M. & Hamajima, K. 1975, PASJ, 27, 501

Truelove, J. K., Klein, R. I., McKee, C. F., et al. 1997, ApJ, 489, L179

Tully, R. B., Courtois, H., Hoffman, Y., & Pomarède, D. 2014, Nature, 513, 71

Turnshek, D. A., Rao, S. M., Nestor, D. B., et al. 2004, ApJ, 609, L53

Utomo, D., Blitz, L., Bolatto, A., Wong, T., & Vogel, S. 2015, IAU General Assembly, 22, 57914

van Albada, T. S., Bahcall, J. N., Begeman, K., & Sancisi, R. 1985, ApJ, 295, 305

van den Bergh, S. 1964, ApJS, 9, 65

van den Bergh, S. 1976, ApJ, 206, 883

van den Bergh, S., Abraham, R. G., Ellis, R. S., et al. 1996, AJ, 112, 359

van den Bosch, F. C. & Swaters, R. A. 2001, MNRAS, 325, 1017

van der Marel, R. P., Besla, G., Cox, T. J., Sohn, S. T., & Anderson, J. 2012, ApJ, 753, 9

Vasiliev, E. 2013, MNRAS, 434, 3174

Veilleux, S., Cecil, G., Bland-Hawthorn, J., et al. 1994, ApJ, 433, 48

Viel, M., Becker, G. D., Bolton, J. S., & Haehnelt, M. G. 2013, Phys. Rev. D, 88, 043502

Viel, M., Branchini, E., Cen, R., et al. 2005, MNRAS, 360, 1110

Vogelsberger, M., Genel, S., Springel, V., et al. 2014, MNRAS, 444, 1518

Walch, S. K., Whitworth, A. P., Bisbas, T., Wünsch, R., & Hubber, D. 2012, MNRAS, 427, 625

Walker, M. G. & Peñarrubia, J. 2011, ApJ, 742, 20

Wang, J., Frenk, C. S., Navarro, J. F., Gao, L., & Sawala, T. 2012, MNRAS, 424, 2715

Ward-Thompson, D., Kirk, J. M., André, P., et al. 2010, A&A, 518, L92

Warren, M. S., Quinn, P. J., Salmon, J. K., & Zurek, W. H. 1992, ApJ, 399, 405

Weinberg, M. D. 1996, ApJ, 470, 715

Weiner, B. J., Coil, A. L., Prochaska, J. X., et al. 2009, ApJ, 692, 187

Weinzirl, T., Jogee, S., Khochfar, S., Burkert, A., & Kormendy, J. 2009, ApJ, 696, 411

White, S. D. M. 1976, MNRAS, 174, 19

White, S. D. M. & Rees, M. J. 1978, MNRAS, 183, 341

Whitmore, B. C., Brogan, C., Chandar, R., et al. 2014, ApJ, 795, 156

Widrow, L. M., Perrett, K. M., & Suyu, S. H. 2003, ApJ, 588, 311

Wilczek, M. & Narita, Y. 2012, Phys. Rev. E, 86, 066308

Wilczek, M., Xu, H., & Narita, Y. 2014, Nonlinear Processes in Geophysics, 21, 645

Williams, J. P., Blitz, L., & McKee, C. F. 2000, Protostars and Planets IV, 97

Wilman, R. J., Gerssen, J., Bower, R. G., et al. 2005, Nature, 436, 227

Winters, J. M. & Neri, R. 2011, An introduction to the IRAM Plateau de Bure Interferometer

Wong, T. & Blitz, L. 2002, ApJ, 569, 157

Wuyts, S., Förster Schreiber, N. M., Lutz, D., et al. 2011a, ApJ, 738, 106

Wuyts, S., Förster Schreiber, N. M., van der Wel, A., et al. 2011b, ApJ, 742, 96

Wyder, T. K., Martin, D. C., Barlow, T. A., et al. 2009, ApJ, 696, 1834

Young, J. S. & Scoville, N. Z. 1991, ARA&A, 29, 581

Zamora-Avilés, M. & Vázquez-Semadeni, E. 2014, ApJ, 793, 84

Zamora-Avilés, M., Vázquez-Semadeni, E., & Colín, P. 2012, ApJ, 751, 77

Zavala, J., Vogelsberger, M., & Walker, M. G. 2013, MNRAS, 431, L20

Zel'dovich, Y. B. 1970, A&A, 5, 84

Zernickel, A., Schilke, P., & Smith, R. J. 2013, A&A, 554, L2

Zhao, D. H., Jing, Y. P., Mo, H. J., & Börner, G. 2003, ApJ, 597, L9

Zhao, D. H., Jing, Y. P., Mo, H. J., & Börner, G. 2009, ApJ, 707, 354

Zhao, H., Spergel, D. N., & Rich, R. M. 1995, ApJ, 440, L13

Zhu, Q., Marinacci, F., Maji, M., et al. 2015, ArXiv: 1506.05537

Zolotov, A., Brooks, A. M., Willman, B., et al. 2012, ApJ, 761, 71

Zwicky, F. 1933, Helvetica Physica Acta, 6, 110

Résumé. Les observations montrent qu'il y a dix milliards d'années, les galaxies formaient bien plus d'étoiles qu'aujourd'hui. Comme les étoiles se forment à partir de gaz moléculaire froid, cela signifie que les galaxies disposaient alors d'importants réservoirs de gaz, et c'est ce qui est observé. Mais les processus de formation d'étoiles pourraient aussi avoir été plus efficaces : qu'en est-il ? Les étoiles se forment dans des nuages moléculaires géants liés par leur propre gravité, mais les toutes premières étapes de leur formation demeurent relativement mal connues. Les nuages moléculaires sont eux-mêmes fragmentés en différentes structures, et certains scénarios suggèrent que les filaments interstellaires qui y sont observés aient pu constituer la première étape de la formation des coeurs denses dans lesquels se forment les étoiles. En quelle mesure leur géométrie filamentaire affecte-t-elle les coeurs pré-stellaires ? Des phenomènes de rétroaction liés à l'évolution des étoiles, comme les vents stellaires et les explosions de supernovae, participent à la régulation de la formation d'étoiles et peuvent aussi perturber la distribution de matière noire supposée entourer les galaxies. Cette thèse aborde l'évolution des galaxies et la formation des étoiles suivant trois perspectives : (i) la caractérisation des processus de formation d'étoiles à des échelles sous-galactiques au moment de leur pic de formation ; (ii) la formation des coeurs pré-stellaires dans les structures filamentaires du milieu interstellaire ; et (iii) les effets rétroactifs de la formation et de l'évolution des étoiles sur la distribution de matière noire des galaxies.
Mots-clés : *Formation des étoiles ; Galaxies à haut-redshift ; Evolution des galaxies ; Milieu interstellaire ; Halos de matière noire ; Hydrodynamique.*

Abstract. Observations show that ten billion years ago, galaxies formed their stars at rates up to twenty times higher than now. As stars are formed from cold molecular gas, a high star formation rate means a significant gas supply, and galaxies near the peak epoch of star formation are indeed much more gas-rich than nearby galaxies. Is the decline of the star formation rate mostly driven by the diminishing cold gas reservoir, or are the star formation processes also qualitatively different earlier in the history of the Universe? Ten billion years ago, young galaxies were clumpy and prone to violent gravitational instabilities, which may have contributed to their high star formation rate. Stars indeed form within giant, gravitationally-bound molecular clouds. But the earliest phases of star formation are still poorly understood. Some scenarii suggest the importance of interstellar filamentary structures as a first step towards core and star formation. How would their filamentary geometry affect pre-stellar cores? Feedback mechanisms related to stellar evolution also play an important role in regulating star formation, for example through powerful stellar winds and supernovae explosions which expel some of the gas and can even disturb the dark matter distribution in which each galaxy is assumed to be embedded. This PhD work focuses on three perspectives: (i) star formation near the peak epoch of star formation as seen from observations at sub-galactic scales; (ii) the formation of pre-stellar cores within the filamentary structures of the interstellar medium; and (iii) the effect of feedback processes resulting from star formation and evolution on the dark matter distribution.
Keywords: *Star formation; High-redshift galaxies; Galaxy evolution; Interstellar medium; Dark matter haloes; Hydrodynamics.*